

# Important Notice

This copy may be used only for the purposes of research and private study, and any use of the copy for a purpose other than research or private study may require the authorization of the copyright owner of the work in question. Responsibility regarding questions of copyright that may arise in the use of this copy is assumed by the recipient.

UNIVERSITY OF CALGARY

Oil Reservoir Assessment Using Multicomponent Seismic Data

By

Chuangdong Xu

A THESIS

SUBMITTED TO THE FACULTY OF GRADUATE STUDIES  
IN PARTIAL FULFILMENT OF THE REQUIREMENTS FOR THE  
DEGREE OF DOCTOR OF PHILOSOPHY

DEPARTMENT OF GEOSCIENCE

CALGARY, ALBERTA

JANUARY, 2011

© Chuandong Xu 2011

UNIVERSITY OF CALGARY

FACULTY OF GRADUATE STUDIES

The undersigned certify that they have read, and recommend to the Faculty of Graduate Studies for acceptance, a thesis entitled "Oil Reservoir Assessment Using Multicomponent Seismic Data" submitted by Chuandong Xu in partial fulfilment of the requirements of the degree of Doctor of Philosophy.

---

*Supervisor, Dr. R. R. Stewart  
Department of Earth and Atmospheric Sciences, University of Houston*

---

*Dr. L. R. Lines, Department of Geoscience*

---

*Dr. D. C. Lawton, Department of Geoscience*

---

*Dr. S. A. Mehta, Department of Chemical and Petroleum Engineering*

---

*External Examiner, Dr. P. W. Cary, Sensor Geophysical Ltd.*

---

January 2011

*Date*

## Abstract

The multicomponent seismic method has been recognized as a useful tool to enhance the traditional  $P$ -wave seismic method for hydrocarbon exploration and exploitation. In this dissertation, a workflow of multicomponent seismic interpretation has been proposed. Using multicomponent seismic data, two oilfields (Ross Lake heavy-oil field in Canada and Cantarrel/Sihil carbonate oilfield in Mexico) are assessed. Checking the  $V_p$ - $V_s$  relationship and other rock properties and carefully correlating synthetic seismograms, VSP (zero-offset and offset) and surface seismic data for both  $PP$ -wave and  $PS$ -wave are essential for interpreting multicomponent seismic data. In the Ross Lake heavy-oil field, a travelttime-derived  $V_p/V_s$  map clearly delineates the channel sand and shows a shale-plug in it which is supported by the result from the horizontal well. On the  $V_p/V_s$  map derived from impedance inversions of the poststack  $PP$  and  $PS$  data, the channel sand is also suggested by a low  $V_p/V_s$  anomaly but not as crispy as that of the travelttime-derived  $V_p/V_s$  map. In the Cantarell/Sihil carbonate oilfield, the  $PS$  data provide more continuous reflections in the areas where gas effects are visible in the  $P$ -wave sections (as noted elsewhere, especially in the North Sea), which may provide useful refinement of the structure. In addition, there may be fluid contacts visible in the upper reservoir. Several new structures are interpreted on the  $PS$  data.  $V_p/V_s$  values could be interpreted as showing shaliness or less consolidation in some areas.

An empirical  $V_p$ - $V_s$  relationship has been established for deep-water siliceous shale using well data.  $Q_p$  determined using spectral-ratio method from the zero-offset VSP in Ross Lake oilfield presents an inverse linear relationship with  $V_p/V_s$  derived from  $P$ -wave and  $S$ -wave source VSP, which may help to predict attenuation from  $V_p/V_s$ . An index for indicating the quality of  $Q$  estimation from VSP data has been proposed.

## **Acknowledgements**

I would like to thank Dr. Robert Stewart, my dissertation supervisor, for his guidance, suggestions and help on the research for my PhD program. Rob's vast knowledge of the geophysical literature, specifically in all the aspects of multicomponent seismic method, VSP, rock physics and the integration between them, helped me throughout my graduate studies. I learned much through our discussions. And more important to me, constant encouragement and enthusiasm from Rob helped me get to the finish line. Without Rob, I wouldn't think I can ever get this far on the road of Geophysics. The first day when I met Rob in his University of Calgary office in 1998 is still vivid in my mind, and will stay vivid forever.

I would like to thank Dr. Larry Lines, for his support through conversations. I would like to thank a number of professors in the Geoscience department from whom I learned so much about geophysics: Dr. Don Lawton, Dr. Gary Margrave, Dr. John Bancroft and Dr. Ed Krebes.

I would like to thank CREWES students and staff for providing such a friendly environment for learning and living, in particular, Kevin Hall, Rolf Maier, Arnim Haase, Hanxing Lu and Louise Forgues, and CREWES sponsors for their financial support.

I would like to thank Larry Mewhort and Ken Hedlin from Husky Energy for providing geophysical data and information in the Ross Lake project, and useful discussions and Angela Ricci from Husky for providing a lot of geological information. Also, I would like to thank Alberto Chernikoff from Schlumberger DCS for his

tremendous geological work in the Sihil project and assistance with data mining and transfer.

The second half of my time on this study was spent working for Occidental Petroleum Corporation (OXY) as an exploration/development geophysicist. I would like to thank Kurt Neher, Geoscience Director of Oxy California, for his continuous encouragement through the last four years.

I would like to thank Dr. Sudarshan (Raj) Mehta and Dr. Peter Cary for taking time to review my dissertation and their useful suggestions.

Finally, I am thankful to my wife, Honglin, for her all-time support, and my son, Neil (Zhuangzhuang) -- his happy face is always a relief for me.

## **Dedication**

To my parents

## Table of Contents

Approval Page .....	ii
Abstract .....	iii
Acknowledgements .....	iv
Dedication .....	v
Table of Contents .....	vi
List of Tables .....	viii
List of Figures .....	ix
List of Symbols and Abbreviations .....	x

### CHAPTER ONE: INTRODUCTION

1.1 Overview of the multicomponent seismic method .....	1
1.2 Some fundamentals of rock physics .....	8
1.2.1 Velocity and elastic moduli .....	8
1.2.2 $V_p$ - $V_s$ relationship .....	10
1.2.3 Attenuation .....	13
1.3 Dissertation objectives and structure .....	15
1.4 Data used .....	16
1.5 Hardware and software .....	17

### CHAPTER TWO: INTERPRETATION OF ROSS LAKE 3D MULTICOMPONENT DATA

2.1 Introduction .....	18
2.2 Work flow for multicomponent seismic interpretation .....	18
2.3 Geology background of Ross Lake oilfield .....	21
2.4 Data available: seismic data, well logs and VSPs .....	26
2.4.1 Surface seismic data .....	26
2.4.2 VSP survey .....	28
2.4.3 Wells and $V_p$ - $V_s$ relationship .....	30
2.4.4 Examine seismic frequency content .....	35
2.5 Correlation of synthetic seismogram, VSPs and seismic data .....	36
2.6 PP data interpretation .....	38
2.6.1 Interpreting horizons on <i>PP</i> seismic .....	38
2.6.2 Time structure map and time-thickness map .....	42
2.7 PS data interpretation .....	44
2.7.1 Estimate <i>S</i> -velocity from well .....	44
2.7.2 <i>PS</i> synthetic seismogram and tie with <i>PS</i> seismic and <i>PS</i> VSP .....	44
2.7.3 <i>PS</i> time to <i>PP</i> time, a gross match .....	45

2.7.4 Picking horizons on <i>PS</i> seismic data .....	47
2.7.5 <i>PS</i> time-structure map and time-thickness map .....	48
2.8 $V_p/V_s$ map and lithology interpretation .....	50
2.9 The horizontal well result .....	51
2.10 Discussion .....	55

### CHAPTER THREE: INVERSION OF ROSS LAKE PP AND PS DATA - POSTSTACK

3.1 Introduction .....	57
3.2 Acoustic impedance inversion of <i>PP</i> data .....	60
3.2.1 The initial <i>P</i> -impedance model .....	60
3.2.2 Wavelet .....	61
3.2.3 Inversion and the result .....	61
3.3 Acoustic impedance inversion of <i>PS</i> data .....	65
3.3.1 Work flow .....	65
3.3.2 <i>PS</i> to <i>PP</i> horizon matching .....	66
3.3.3 The initial <i>S</i> -impedance model .....	68
3.3.4 Inversion and the result .....	70
3.4 $V_p/V_s$ map from impedance and comparison to travelttime derived $V_p/V_s$ .....	72
3.5 Summary and discussion .....	76

### CHAPTER FOUR: ATTENUATION AND Q FACTOR ESTIMATION FROM VSP

4.1 Introduction .....	78
4.2 Methodology of <i>Q</i> estimation .....	79
4.3 Example one: Ross Lake VSP data .....	81
4.3.1 Introduction .....	81
4.3.2 Examine the amplitude spectrum .....	81
4.3.3 VSP data preparation and checking .....	84
4.3.4 Estimating <i>Q</i> .....	87
4.3.5 $Q_p$ versus $V_p$ , $V_s$ and $V_p/V_s$ .....	91
4.4 Example two: Pikes Peak VSP data .....	96
4.4.1 Introduction of Pikes Peak oilfield .....	96
4.4.2 VSP and well logs .....	97
4.4.3 Data preparation and <i>Q</i> estimation .....	99
4.4.4 Crossplotting $Q_p$ versus $V_p$ , $V_s$ and $V_p/V_s$ .....	104
4.4.5 Discussion .....	107
4.5 Discussion .....	110
4.5.1 Intrinsic and extrinsic .....	110
4.5.2 Well bore structure and cement bond in cased hole .....	110
4.5.3 Near field effects .....	111

4.5.4 Consistency of VSP source .....	111
4.5.5 $Q$ compensation for $P$ -, $S$ - and $PS$ -wave seismic data .....	111
4.6 Conclusion .....	112
CHAPTER FIVE: INTERPRETATION OF 3D MULTICOMPONENT DATA ON CANTARELL-SIHIL STRUCTURE, GULF OF MEXICO	
5.1 Introduction .....	114
5.2 Regional geology and stratigraphy .....	115
5.3 Data available .....	121
5.3.1 Seismic data .....	121
5.3.2 Well logs .....	123
5.3.3 VSP data .....	127
5.4 Methodology .....	128
5.5 Estimating shear velocity .....	129
5.6 Synthetic seismogram and correlation with VSPs and seismic data:	
$PP$ and $PS$ .....	136
5.7 Matching $PS$ seismic to $PP$ seismic data.....	143
5.8 Horizon interpretation, structure, time thickness and $V_p/V_s$ maps .....	149
5.9 Value of the $PS$ data .....	165
5.10 Summary .....	166
5.11 Recommendations .....	167
CHAPTER SIX: INTERPRETATION OF A LAND 2D MULTICOMPONENT SEISMIC DATA	
6.1 Introduction .....	168
6.2 Well log and $V_p$ - $V_s$ relationship .....	169
6.3 Checking $PP$ and $PS$ seismic data .....	175
6.4 $PP$ and $PS$ synthetic seismograms .....	180
6.5 Interpretation and analysis .....	181
6.6 Conclusion .....	184
CHAPTER SEVEN: CONCLUSIONS AND FUTURE WORK	
7.1 Conclusions .....	185
7.2 Future work .....	188
REFERENCES .....	190
APPENDIX A: SEISMIC TOMOGRAPHY OF MAYA PYRAMIDS .....	197

## List of Tables

Table 2.1 Ross Lake 3C-3D seismic <i>PP</i> data processing flow. ....	27
Table 2.2 Ross Lake 3C-3D seismic <i>PS</i> data processing flow. ....	28
Table 2.3 The source parameters of the multi-offset VSP survey in well 11-25. ....	29
Table 2.4 Average GR value of the horizontal portion of well 5-25 in each projected seismic bin and the seismic $V_p/V_s$ in the same bin. ....	54
Table 3.1 Summary of rock properties of the channel sand and shales around. $V_s$ is calculated from measured $V_p$ and VSP-derived $V_p/V_s$ . ....	60
Table 4.1 $Q_p$ , $Q_s$ , $V_p/V_s$ and $V_p$ for the main geological formations in Ross Lake.....	91
Table 4.2 Comparison of fitting quality for crossplotting $Q_p$ versus $V_p$ , $V_s$ and $V_p/V_s$ in well 11-25 of Ross Lake.....	95
Table 4.3 $Q_p$ , $V_p/V_s$ and $V_p$ for the main geological formations in Pikes Peak.....	105
Table 5.1 The data detail of the offset VSP in well Sihil-19. ....	128
Table 5.2 Intervals for crossplotting measured $V_p$ versus $V_s$ in four wells. ....	134
Table 5.3 Name of formation tops and horizons from seismic data. ....	149
Table 6.1 The definition, thickness and average value of GR, density, $V_p$ and $V_p/V_s$ for the five zones in well J28. ....	171
Table 6.2 The result of linear regression of $V_p$ versus $V_s$ for five zones in well J28.....	172

## List of Figures and Illustrations

Figure 1.1 (a) A converted-wave (PS) reflection at its conversion point (CP), compared with a pure PP-wave at its middle point (MP) in a one-layer model. (b) The location of the P-S conversion point moves from the receiver towards to the Asymptotic Conversion Point (ACP) with increasing depth. (after Stewart et al. 2002). ....	4
Figure 1.2 A composite plot of $V_p/V_s$ versus $V_p$ trend for various lithologies (after Castagna, 1985), modified by adding the grid lines. ....	12
Figure 2.1 The work flow for multi-component seismic data interpretation. ....	19
Figure 2.2 The location of Ross Lake oilfield. ....	22
Figure 2.3. Stratigraphic chart of southwest Saskatchewan (from <a href="http://www.ir.gov.sk.ca">www.ir.gov.sk.ca</a> )....	23
Figure 2.4 Diagram illustrating the stratigraphic relationship of the upper Jurassic and Lower Cretaceous, southwestern Saskatchewan (from Christopher, 1974). ....	25
Figure 2.5 Diagram showing the stratigraphic relationship of the formations within the Mannville Group. (from Vanbeselaere, 1995). ....	25
Figure 2.6 Source location map of VSP survey in well 11-25 (after Schlumberger). ....	29
Figure 2.7 Logs from well 11-25. The $V_p/V_s$ curve is calculated from the P-source and S-source VSP in the same well. ....	30
Figure 2.8 GR log and measured $V_p$ , $V_s$ from the dipole sonic log in well 2-15-19-18....	31
Figure 2.9 GR log and measured $V_p$ , $V_s$ from the dipole sonic log in well 2-33-13-19....	32
Figure 2.10 GR, density and measured $V_p$ , $V_s$ from dipole sonic in well 3-16-17-21. ....	32
Figure 2.11 GR log and measured $V_p$ , $V_s$ from the dipole sonic log in well 9-33-16-19....	33
Figure 2.12 Crossplot of measured $V_p$ and $V_s$ from four regional wells. The linear regression (red solid line) is calculated excluding the colored zone (grey and light yellow) due to questionable spikes of shear log in well 2-15-19-18. Mudrock line (pine dash line) and three constant $V_p/V_s$ lines (1.5, 2.0 and 3.0) are posted. ....	35

Figure 2.13 Average amplitude spectrum of vertical <i>PP</i> (upper panel), the radial <i>PS</i> (lower left panel) and transverse <i>PS</i> (lower right panel) data volumes of Ross Lake 3C-3D seismic. ....	36
Figure 2.14 GR, density and $V_p$ Logs, <i>PP</i> synthetic, <i>PP</i> seismic and zero-offset VSP corridor stack (a 5/10-70/80 Hz bandpass filter applied) in well 11-25. There is no stretch or squeeze applied to the synthetic seismogram. ....	38
Figure 2.15 East-west xline 11 crossing well 11-25 with <i>P</i> -velocity curve inserted at the well location. <i>PP</i> data horizons are interpreted. ....	39
Figure 2.16 North-south inline 41 of <i>PP</i> data across well 11-25 with interpreted horizons. ....	40
Figure 2.17 Zoom-in of the interval of interest on crossline 11 with GR log posted at the well 11-25. The blue circle indicates the reservoir sand. ....	41
Figure 2.18 Time slices of <i>PP</i> data: 1120 ms (top), 1140 ms (bottom left) and 1160 ms (bottom right). Red color is positive value and blue color is negative value. ....	42
Figure 2.19 <i>PP</i> time structure map of horizon IHACM (left) and Rush Lake (right). Red color is structure high, and blue color is structure low. ....	43
Figure 2.20 <i>PP</i> time thickness map between the horizon of IHACM and Rush Lake with color bar. Hot color means thick, and black color means thin. ....	43
Figure 2.21 Composite display of logs, <i>PP</i> synthetic seismograms, <i>PP</i> seismic, <i>PS</i> synthetic seismograms and <i>PS</i> seismic section for well 11-25. ....	45
Figure 2.22 The correlation between <i>PP</i> seismic, <i>PS</i> seismic, 700m-offset <i>PP</i> -VSP and 700m-offset <i>PS</i> -VSP. All data are plotted in <i>PP</i> time. The surface seismic data have a 5/10-50/60 Hz bandpass filter applied. ....	47
Figure 2.23 Crossline 11 of <i>PS</i> seismic in <i>PS</i> time. The blue horizons are picked on <i>PS</i> data while the red horizons are the same horizons on <i>PP</i> data but converted in <i>PS</i> time using the constant $V_p/V_s=2.35$ and a bulk shift of 125 ms. ....	48

Figure 2.24 <i>PS</i> time structure map of horizon IHACM (left) and Rush Lake (right). Red color is structure high, and blue color is structure low. ....	49
Figure 2.25 <i>PS</i> time-thickness map between the horizon IHACM and Rush Lake with color bar. Hot color means thick, and black color means thin. Note thicker interval but higher $V_s$ are fighting each other respecting the traveltime. ....	49
Figure 2.26 $V_p/V_s$ map between the horizon IHACM and Rush-Lake. Hot color is low $V_p/V_s$ and black color represents high value. The yellow and green colors are interpreted as sands while the black and grey as shale or shaly sands. ....	50
Figure 2.27 Xline 11 error analysis. $\Delta T_{pp}$ and $\Delta T_{ps}$ are the isochrons in ms between IHACM and Rush Lake with $\pm 2\%$ and $\pm 4\%$ error, respectively. $\pm 6\%$ error for $V_p/V_s$ .....	51
Figure 2.28 The “striplog” of the horizontal well 5-25 with GR log showing the sand. Seismic bins along the trajectory of the horizontal portion of the well are schematically illustrated. ....	52
Figure 2.29 Seismic $V_p/V_s$ map with trace bins containing the trajectory of the horizontal well (small squares filled by grey color). Hot color is low $V_p/V_s$ (sandy) and black color is high $V_p/V_s$ (Shaly). ....	53
Figure 2.30 Comparison of the normalized average GR from the horizontal well 5-25 in the well trajectory passed seismic bins and seismic traveltime derived $V_p/V_s$ in the same bins. ....	55
Figure 3.1 Logs in well 11-25. The $V_p/V_s$ is derived from zero-offset <i>P</i> -source and <i>S</i> -source VSP. The $V_s$ is calculated from the log measured $V_p$ and VSP-derived $V_p/V_s$ . ....	59
Figure 3.2 Crossline 11 of the <i>PP</i> -wave data (wiggly traces) with the smoothed initial <i>P</i> -impedance model (color background). The <i>P</i> -impedance log of well 11-25 is inserted at the well location. ....	61
Figure 3.3 Results of the model-based <i>P</i> -impedance inversion of crossline 11. Purple color is high impedance and green color is low impedance. ....	63

Figure 3.4 Zoom-in of the inverted $P$ -impedance (color). Yellow color is low impedance, and blue color is high impedance. Wiggles traces are $PP$ data. $P$ -impedance log is inserted at the well location. Notice the channel sand is a low impedance block surrounded by higher impedance shale. ....	64
Figure 3.5 $P$ -impedance horizon slices based on Rush Lake horizon: up 10ms (upper-left), up 14ms (upper-right), up 18ms (lower-left) and up 22ms (lower-right). ....	65
Figure 3.6 The flow chart of PS-wave seismic impedance inversion. ....	66
Figure 3.7 A composite display of well logs, $PP$ and $PS$ synthetic seismograms, $PP$ and $PS$ seismic traces for well 11-25. ....	67
Figure 3.8 $PS$ (right) to $PP$ (left) horizon-matching in $PP$ time. The interval $V_p/V_s$ calculated from event matching is displayed as a color background on $PS$ data. The $V_p/V_s$ color bar is shown at the right. ....	68
Figure 3.9 The smoothed initial $S$ -impedance model in color. The wiggle traces are $PS$ data in $PP$ time. ....	69
Figure 3.10 The result of $PS$ data inversion at crossline 11. The inserted curve at well location is $S$ -impedance log. ....	70
Figure 3.11 Zoom-in of the $PS$ data inversion result around the reservoir in well 11-25. Wiggle traces are $PS$ seismic. ....	71
Figure 3.12 $S$ -impedance time slices: Rush Lake horizon up 10ms (upper-left), 14ms (upper-right), 18ms (lower-left) and 22ms (lower-right). ....	72
Figure 3.13 The average $P$ -impedance over a 8ms time window centered at 14ms above the Rush Lake horizon. ....	73
Figure 3.14 Average $P$ -impedance (left) over a 8ms window indicates the sand has low $P$ -impedance value (dark color) while the average $S$ -impedance (right) shows a high $S$ -impedance. ....	74
Figure 3.15 Comparison of $V_p/V_s$ derived from impedance (left) and $V_p/V_s$ derived from the traveltimes (right). ....	75

Figure 3.16 Inversion analysis of $PP$ (left) and $PS$ (right) trace at the well location. The arrow indicates the interval between IHACM and Rush Lake. The X-axis is time and right direction going deeper. ....	77
Figure 4.1 A schematic layered earth model for $Q$ factor. ....	80
Figure 4.2 The amplitude spectrum of vertical component for all geophone levels from the $P$ -source zero-offset VSP in well 11-25 of Ross Lake. Color indicates the amplitude (red is high), and numbers show the dB down. ....	82
Figure 4.3 The amplitude spectrum of horizontal component for all geophone levels from $S$ -source zero-offset VSP in well 11-25 in Ross Lake. Color indicates the amplitude (red is high), and numbers show the dB down. Notice the left edge of the peak is not a straight vertical line. ....	83
Figure 4.4 Raw vertical component records from $P$ -wave source (left) and horizontal component records from $S$ -wave source (right). Blue dots are picked $P$ -wave first arrivals. Red dots are picked $S$ -wave first arrivals. ....	84
Figure 4.5 Aligned downgoing $P$ wavefield from the $P$ -source (left) and downgoing $S$ wavefield from the $S$ -source (right) using a single amplitude scalar.....	85
Figure 4.6 Downgoing $P$ - and $S$ -wave at station #3 (214 m depth, blue line), station #66 (685 m depth, red line) and station #129 (1157.5 m depth, green line) indicating amplitude loss and some phase change. ....	86
Figure 4.7 The amplitude spectrum of the sweep (blue line), station #4 (220 m, black line) and station #129 (1157.5 m, red line) for the $P$ -source (left) and $S$ -source (right). Amplitude and frequency loss with depth is evident. ....	87
Figure 4.8 Average $Q_p$ (blue) and $Q_s$ (red) curves from VSP in well 11-25 at Ross Lake oilfield. ....	88
Figure 4.9 Attenuation quality indicator for $Q_p$ (blue) and $Q_s$ (red), with formation tops posted. ....	89
Figure 4.10 Average $Q_p$ with 10 (black line), 20 (red line) and 30 (blue line) samples smoothing, and derived interval $Q_p$ . ....	90

Figure 4.11 Average $Q_s$ calculated using spectral ratio method between station #28 to #56 (400m - 610m, left plot) and station #91 to #115 (870m - 1050m, right plot).....	91
Figure 4.12 $V_p$ from VSP (red) is generally slower than $V_p$ from log (black). This is evidence of velocity dispersion (left panel). The smoothed interval $Q_p$ (blue), VSP-derived $V_s/V_p$ (red, scaled) and $V_p$ from sonic log (black) are grossly correlated. The $V_p/V_s$ (red) and GR log (blue) are plotted on the right. ....	92
Figure 4.13 Interval $Q_p$ plotted versus VSP-derived $V_p$ (blue) and $V_s$ (red). $V_s$ shows a better linear relationship with VSP-derived $V_p/V_s$ than $V_p$ . ....	93
Figure 4.14 Interval $Q_p$ plotted versus VSP-derived $V_p/V_s$ shows a nice linear inverse relationship . ....	94
Figure 4.15 $1/Q_p$ plotted versus VSP-derived $V_p/V_s$ to show a positive relationship. ....	95
Figure 4.16 Map of major heavy-oil deposits of Alberta and Saskatchewan with the location of Pikes Peak field (after Watson, 2004). ....	97
Figure 4.17 Logs of well A15-06. The magenta curves are $V_s$ derived from $V_p$ using mudrock line and the resulting $V_p/V_s$ . The arrow indicates the discrepancy between the measured $V_s$ , $V_p/V_s$ and derived $V_s$ , $V_p/V_s$ by the mudrock line. ....	99
Figure 4.18 Raw zero-offset VSP record in well A15-06 with the first break picks posted (red). Arrows indicate the 8 problematic receiver stations. ....	100
Figure 4.19 A15-06 zero-offset VSP raw record frequency and phase analysis: (a) AGC applied raw record; (b) the average frequency spectrum of all traces in time window 0 – 600 ms; (c) the spectrum of each individual trace, red is high; (d) the phase spectrum. ....	101
Figure 4.20 The calculated average $Q$ factor at each station (left) and the QC curve of $T_{fb}/Q_{ave}$ (right ) from VSP of well A15-06. ....	103
Figure 4.21 Calculated $Q_{p-int}$ from 11-, 21- and 31-point smoothed $Q_{p-ave}$ (left panel) and 3-point median filtered $Q_{p-int}$ (right panel). ....	103
Figure 4.22 The up-scaled log $V_p$ , $V_s$ and $V_p/V_s$ , and $Q_p$ plotted in depth, with formation tops posted. ....	105

Figure 4.23 $Q$ versus depth calculated from VSP survey using geophones of 90 m separation (after Hedlin et al. 2002). .....	106
Figure 4.24 Crossplot of $Q_p$ versus $V_p/V_s$ of well A15-06. ....	107
Figure 4.25 Crossplot of $V_s$ versus $V_p$ log of well A15-06, with mudrock line and a few constant $V_p/V_s$ lines posted. Color denotes the depth. ....	108
Figure 4.26 Crossplot of $V_p/V_s$ versus $V_p$ (left) and $V_p/V_s$ versus $S$ -wave slowness (right). ....	109
Figure 5.1 Location map of the Cantarell oilfield in the Gulf of Mexico. ....	116
Figure 5.2 Schematic diagram of the Cantarell field indicating five blocks and the saturation conditions in them. Note the gas cap and ring of oil (Hernandez et. al., 2005). ....	117
Figure 5.3 Simplified structural evolution of the Cantarell area: (a) extension in lower Cretaceous. (b) NNE over-thrust in lower to middle Miocene. (c) duplex overridding. (d) listric normal faulting in Pliocene-Pleistocene (Hernandez et. al., 2005). ....	118
Figure 5.4 Cross-section with interpreted faults, indicating the 3 main structure events: Mesozoic extension represented by the normal “half graben” type feature (black fault); Miocene compression represented by low angle thrust (red and purple faults); and the Plio-Pleistocene extension (blue fault). (Hernandez et. al., 2005). ....	119
Figure 5.5 Stratigraphy, lithology and deposition facies (after Chernikoff, 2006) with log responses from five wells. JSK stands for Jurassic Kimmeridgian. ....	120
Figure 5.6 Base map for the 4C-3D seismic survey with in-line and cross-line directions annotated. Several key wells are also shown. ....	122
Figure 5.7 (a) Log curves in Well C-3068. ....	124
Figure 5-7 (b) Log curves in Well Sihil-19. ....	125
Figure 5.7 (c) Log curves in Well C-98. There is a 300 m bad data zone in the middle.	125

Figure 5.7 (d) Log curves in Well C-3026D. ....	126
Figure 5.7 (e) Log curves in Well C-3045D. ....	126
Figure 5.7 (f) Log curves of the shallow Well Utan-1. ....	127
Figure 5.8 The geometry of offset VSPs in Well Sihil-19 (after Chernikoff, 2006).....	128
Figure 5.9 Crossplot of log measured $V_s$ versus $V_p$ in Well C-3026D. Note the somewhat linear relationship within considerable scatter. Color represents GR value. ....	131
Figure 5.10 Predicted $V_s$ versus actual $V_s$ from VSP in Well Sihil-19.....	132
Figure 5.11 Crossplot of $V_p$ versus $V_s$ in Well C-98. The green circle is for the shallow interval and the orange circle is for the deep interval. ....	133
Figure 5.12 Crossplot of $V_p$ and $V_s$ in the shallow Well Utan-1. ....	134
Figure 5.13 Compilation of various possibilities for the $V_p$ and $V_s$ relationship. The Castagna limestone equation fits most of the actual log data reasonably well.....	135
Figure 5.14 Composite plot for $P$ -waves including log, synthetic, and VSP data from Well C-3068 and S-19. Note the excellent tie between the synthetic and VSP data. The VSP data is reversed in polarity from the other data. ....	138
Figure 5.15 Well Sihil-19, 2500m offset VSP profiles in depth domain with GR curve and the major formation tops marked: $PP$ (left) and $PS$ (right). ....	139
Figure 5.16 Correlation between $PS$ synthetic seismogram and 2500 m offset VSP PS-CDP map. ....	140
Figure 5.17 Correlation between $PS$ synthetic with $PS$ seismic, inline and crossline. ...	140
Figure 5.18 Correlating $PP$ synthetic with $PP$ seismic data in Well C-3026D. ....	142
Figure 5.19 Correlating $PS$ synthetics with $PS$ seismic data in Well C-3026D. ....	142
Figure 5.20 Wavelet extracted from $PP$ seismic at well location C-3026D. ....	143

Figure 5.21 <i>PP</i> and <i>PS</i> synthetic seismograms in their raw <i>PP</i> and <i>PS</i> time domain in Well C-3068. ....	144
Figure 5.22 The <i>PS</i> and <i>PP</i> events on the synthetic seismograms have been matched and the <i>PS</i> synthetic has been mapped to <i>PP</i> time. The matching $V_p/V_s$ values are shown in the Table (on the right) and also compared to the averaged log $V_p/V_s$ values. .	144
Figure 5.23 An example (crossline 1289) of the <i>PS</i> data (left) mapped into <i>P</i> -wave time using the calculated $V_p/V_s$ and compare with <i>PP</i> data (right). The background color is $V_p/V_s$ . ....	145
Figure 5.24 An example (Inline 2667) of the <i>PS</i> data (left) mapped into <i>P</i> -wave time using the single $V_p/V_s$ mapping function. The Upper row is original and the lower row is bandpass (5/10-15/20) filtered. ....	146
Figure 5.25 <i>P</i> -wave synthetic seismogram inserted into the <i>PP</i> section, in <i>PP</i> time...	147
Figure 5.26 The converted-wave ( <i>PS</i> ) synthetic seismogram is inserted into the <i>PS</i> section. Data displayed in <i>PS</i> time. ....	147
Figure 5.27 Approximate tie of the <i>PP</i> and <i>PS</i> synthetic and seismic sections, using one $V_p/V_s$ value to stretch the <i>P</i> -wave section, at the top of the Cretaceous. ....	148
Figure 5.28 Shallow <i>PS</i> (top) and <i>PP</i> (bottom) sections with a horizon pick annotated. Both sections are in their native times. ....	150
Figure 5.29 <i>PP</i> and <i>PS</i> time structure maps of the shallow horizons. ....	151
Figure 5.30 $V_p/V_s$ value from the shallow horizon to the ocean bottom. ....	152
Figure 5.31 Comparison of the time-mapping $V_p/V_s$ values from the synthetic analysis in this study and previous work. The values are roughly similar. ....	152
Figure 5.32 Interpretation of a north-south <i>PP</i> line from the Sihil data set (from Chernikoff, 2006). ....	153
Figure 5.33 Top of the Cretaceous event as interpreted on the <i>PP</i> and <i>PS</i> seismic data.	154

Figure 5.34 A Cretaceous event traced on the <i>PS</i> section and transferred to the <i>PP</i> section to check the similarity of the structures. ....	154
Figure 5.35 <i>PP</i> time structure at the allochthonous Cretaceous. Color is <i>PP</i> time. ....	155
Figure 5.36 <i>PS</i> time structure at the allochthonous Cretaceous. Color is <i>PS</i> time. ....	155
Figure 5.37 Interval $V_p/V_s$ map as calculated from ratio of the <i>PP</i> and <i>PS</i> time thicknesses between the shallow marker and top of the Cretaceous. ....	156
Figure 5.38 Amplitude map (RMS value from a 150 ms window) above the Cretaceous (from Chernikoff, 2006). We observe that the low amplitude values (in blue) correlate with the low $V_p/V_s$ values from Figure 30. This is an indication of gas saturation. ....	156
Figure 5.39 <i>PP</i> and <i>PS</i> sections over the Akal anticlinal structure. Note the washed-out area (circled) on the <i>P</i> -wave section over the poorly defined anticlinal peak. The top of the Cretaceous is more definitive on the <i>PS</i> section. This is the classic signature of a “gas chimney”. ....	157
Figure 5.40 <i>PP</i> and <i>PS</i> sections indicating the possible effects of gas. A possible gas-oil contact is annotated. ....	158
Figure 5.41 <i>PP</i> section (inline 2667) with horizons annotated. ....	159
Figure 5.42 <i>PS</i> section (inline 2667) with horizons annotated. ....	159
Figure 5.43 <i>PP</i> and <i>PS</i> time structures interpreted on the top of the allochthonous Kimmeridgian. Color represents time in ms. ....	160
Figure 5.44 Interval $V_p/V_s$ map between allochthonous Cretaceous and Kimmeridgian horizons. ....	161
Figure 5.45 Possible deeper structure in evidence on the <i>PS</i> section (inline 2667). ....	162
Figure 5.46 Trace of the <i>PS</i> horizon superposed on the <i>P</i> -wave section. The structure is not as well developed on the <i>PP</i> section (inline 2667). ....	162

Figure 5.47 Time structures on the top of the autochthonous Cretaceous. Note the possible closure on the <i>PS</i> time structure. ....	163
Figure 5.48 <i>PP</i> section (inline 2627) with an ambiguous area in the autochthonous region. ....	164
Figure 5.49 <i>PS</i> section (inline 2627) indicating a dim area over a sub-horizontal region. ....	164
Figure 5.50 Interpreting the dim area in the previous figure as a salt structure. ....	165
Figure 6.1 The basemap of three 3C-2D lines and location of well J28. Each grid is one section, which is one mi <sup>2</sup> . ....	169
Figure 6.2 Log curves in well J28 with formation tops posted. Notice the five different zones by log responses. ....	170
Figure 6.3 Crossplot of $V_p$ versus $V_s$ in well J28. The shallow and deep zones show different regression relationship. The Mudrock line and three constant $V_p/V_s$ lines are also posted for reference. The color key is measured depth. ....	173
Figure 6.4 Crossplot of $P$ -impedance versus $V_p/V_s$ in well J28. The five zones are easy to recognize in this plot. The color key is measured depth. ....	174
Figure 6.5 <i>PP</i> section of 2D line 13S. Well J28 is projected on this line. ....	176
Figure 6.6 <i>PS</i> section of 2D line 13S. ....	176
Figure 6.7 <i>PP</i> section of 2D line 13N. ....	177
Figure 6.8 <i>PS</i> section of 2D line 13N in its native <i>PS</i> time domain. ....	177
Figure 6.9 <i>PP</i> section of 2D line 12N. ....	178
Figure 6.10 <i>PS</i> section of 2D line 12N in its native <i>PS</i> time domain. ....	178
Figure 6.11 Amplitude spectrum of the <i>PP</i> data (a) line 13S, (b) line 13N and (c) line 12S, and <i>PS</i> data (d) line 13S, (e) line 13N and (f) line 12S. ....	179

Figure 6.12 Log curves in well J28, the *PP* synthetic and *PP* seismic section. ....180

Figure 6.13 Log curves in well J28, the *PS* synthetic and *PS* seismic section. ....181

Figure 6.14 *PP* and *PS* horizon matching of line 13S, in *PP* time domain. The left panel is *PP* data overlapped with color representing  $V_p/V_s$ . The right panel is *PS* data.. 182

Figure 6.15 *PP* data of line 13S. Background color is  $V_p/V_s$  from horizon matching. ..183

Figure 6.16 *PS* data of line 13S. Background color is  $V_p/V_s$  from horizon matching...183

## List of Symbols and Abbreviations

3C	three-component
3D	three-dimensional
AVO	amplitude versus offset
<i>P</i> -wave	compressional wave
<i>PP</i>	reflected compressional wave from an incident compressional wave
<i>PS</i>	reflected shear wave from an incident compressional wave
<i>Q</i>	quality factor (attenuation)
<i>Q<sub>p</sub></i>	quality factor of compressional wave
<i>Q<sub>s</sub></i>	quality factor of shear wave
<i>S</i> -wave	shear wave
VSP	vertical seismic profiling
$\mu$	shear modulus (rigidity)
<i>K</i>	bulk modulus
$\lambda$	Lamé parameter
<i>V</i>	seismic velocity
<i>V<sub>p</sub></i>	compressional wave velocity
<i>V<sub>s</sub></i>	shear wave velocity
$\theta$	incident angle
$\rho$	bulk density

## **Chapter One: Introduction**

### **1.1 Overview of the multicomponent seismic method**

The multicomponent seismic method has been in practice for resource exploration and hydrocarbon exploitation in the oil and gas industry for about 30 years. Numerous efforts by dedicated researchers in geophysical service companies, oil companies, universities and research institutes have been made investigating the full range of this geophysical method -- from geophones and instrumentation of acquisition, data processing to data analysis and interpretation. Over the years, the multicomponent seismic method has been industry-widely recognized as a very useful tool, in addition to the conventional *P*-wave seismic method, to understand the subsurface Earth better and characterize different types of oil and gas reservoirs more precisely. It's also widely used in earth-quake seismology and occasionally archaeology (see Appendix).

#### *Definition of multicomponent:*

The multicomponent seismic method records vibrational energy using more than one sensing element. On land, this normally amounts to geophones containing three orthogonal (three-component or 3C) motion sensors, which differs from the traditional single motion sensor geophone, to detect and record the surface particle movement caused by a wavelet traveled down from an artificial source like dynamite or vibrator and reflected back to the ground surface. It directly records the full wavefield or elastic wavefield.

For marine surveys, it could be a geophone with three motion sensors plus a hydrophone (four-component or 4C) receiving the water bottom vibrations from an

airgun. Usually those geophones and hydrophones are put in either a cable (Ocean Bottom Cable or OBC) or an individual seismometer (Ocean Bottom Seismometer or OBS).

If oriented sources (e.g. vertical and horizontal vibrators) are used, the recording of 3C sources by 3C geophones would generate nine gathers for each shot, and called nine-component or 9C survey. There were discussions on the acquisition, logistics, statics, signal to noise ratio (S/N) to compare the 3C versus 9C seismic surveys (Cary 2001, Simmons and Backus 2003, Gaiser and Strudley 2004). However, the 9C survey is not in the scope of this dissertation.

*Definition of converted-wave:*

The term converted-wave implies a particular wave mode conversion in the Earth: a down-going  $P$ -wave incident to an interface and reflect back to an up-going  $S$ -wave, which is commonly denoted as  $PS$ -wave or  $C$ -wave. In this dissertation,  $PS$ -wave is used to represent  $P$ -to- $S$  converted wave.

Modeling and field measurements show that the primary  $P$ -to- $S$  reflection generally has much higher amplitudes than other transmitted or multiple conversions (Rodriguez, 2000).

*Reflection coefficient*

For a plane wave homogeneous isotropic elastic media with the discontinuity in welded contact on a plane boundary, Aki and Richards (1980) simplified the Zoeppritz

equation for the reflection coefficients of the incident  $P$ -wave to reflected  $P$ -wave and reflected  $S$ -wave, by assuming the two half-spaces have similar properties so that the ratios of  $\Delta\rho/\rho$ ,  $\Delta\alpha/\alpha$  and  $\Delta\beta/\beta$  have magnitudes much less than one (where  $\Delta\rho$ ,  $\Delta\alpha$  and  $\Delta\beta$  are the difference, and  $\rho$ ,  $\alpha$  and  $\beta$  are the mean values of density, compressional and shear velocities of the two half-spaces):

The reflection coefficient of incident  $P$ -wave to reflected  $P$ -wave is:

$$R_{PP} = \frac{1}{2}(1 - 4\beta^2 p^2) \frac{\Delta\rho}{\rho} + \frac{1}{2\cos^2 i} \frac{\Delta\alpha}{\alpha} - 4\beta^2 p^2 \frac{\Delta\beta}{\beta} \quad (1.1)$$

And the reflection coefficient of incident  $P$ -wave to reflected  $S$ -wave is:

$$R_{PS} = \frac{-p\alpha}{2\cos j} \left[ \left( 1 - 2\beta^2 p^2 + 2\beta^2 \frac{\cos i \cos j}{\alpha \beta} \right) \frac{\Delta\rho}{\rho} - \left( 4\beta^2 p^2 - 4\beta^2 \frac{\cos i \cos j}{\alpha \beta} \right) \frac{\Delta\beta}{\beta} \right], \quad (1.2)$$

where the ray parameter  $p = \frac{\sin i}{\alpha} = \frac{\sin j}{\beta}$  (Snell's Law),  $i$  is the incidence angle of  $P$ -wave,  $j$  is the reflected angle of  $S$ -wave.

Equation (1.2) shows that the  $PS$  reflection coefficient is not directly related to the  $P$ -wave velocity change but only  $S$ -wave velocity and density changes. Also, when the incident angle is zero, there is no converted  $S$ -wave, and  $R_{ps(0)} = 0$ .

There are two basic aspects of  $PS$ -wave propagation: asymmetric ray path governed by Snell's Law (Figure 1.1), and sinusoidal amplitude variation with offset described by the Zoeppritz equations.

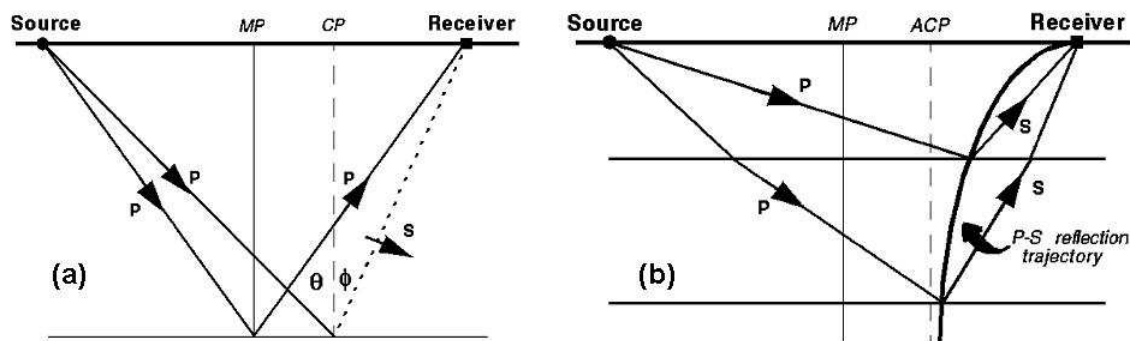


**Figure 1.1 (a) A converted-wave (PS) reflection at its conversion point (CP), compared with a pure PP-wave at its middle point (MP) in a one-layer model. (b) The location of the P-S conversion point moves from the receiver towards to the Asymptotic Conversion Point (ACP) with increasing depth. (after Stewart et al. 2002).**

*Why multicomponent seismic or converted-wave seismic?*

The conventional seismic method (*P*-wave reflection seismic) has dramatically changed the way of petroleum exploration. There are continuous needs to require crisper and more informative geological information of the subsurface. Stewart (2009) summarized a list of those needs: a better structural picture; further Stratigraphic details, indications of rock type; petrophysical properties; a description of faults/fractures/cracks; a notion of the stress regime; an estimate of the fluid content; an idea of rock and fluid changes with production. Using only *P*-wave seismic data is unlikely to fulfill all those needs. Multicomponent seismic, which measures the *S*-wave information, can be a help to meet the challenges.

Stewart (2009) also states that “the goal of this method is to more fully generate and record complete vibrations in the earth; then, use these recordings to enhance traditional *P*-wave arrivals and create complementary shear- and surface-wave pictures.”

*Where we've been to and where are we now?*

In late 1980s and the entire 1990s, consortia from universities and government (CREWES project of University of Calgary, Edinburgh Anisotropy Project, the Delphi project of Delft University, etc), and some geophysical service companies (CGG, Veritas, WesternGeco, Sensor Geophysical, etc) established and developed variety of algorithms and full flow of converted wave processing. From the end user's point of view, the unquestionable examples that the PS-wave provided extra information on top of *P*-wave are imaging through gas clouds in the North Sea (Berg, 1994), imaging sand channels and OWC (oil-water contact) at the Alba field in the North Sea (MacLeod et al., 1999), and delineating channels in the Blackfoot field in the Western Canadian Sedimentary Basin (Margrave et al., 1998).

In 2000, SEG/EAGE held a summer research workshop on multicomponent seismic method in Boise, Idaho (Gaiser et al., 2001). From the poll of evaluating the attendees' assessment of the applications, most were proven and possible, particularly on imaging below gas cloud, imaging targets of poor *PP* reflectivity, lithology delineation in clastics, and increasing shallow resolution. Nevertheless, it also concluded that much work still remained before it became financially viable for both contractors and oil companies.

Stewart et al. (2002, *ibid*, 2003) wrote an excellent tutorial and mid-term review of the method and applications. They summarized eight major applications supported by examples, which are: see through gas zone; structure imaging; near-surface imaging; discriminate sand/shale; discriminate anhydrate/dolomite; anisotropy analysis; describe formation fluids: flat spot on *PP* but not on *PS* indicates OWC; monitor reservoir.

In 2005, the second SEG/EAGE summer research workshop on multicomponent seismic methods was held in Pau, France (Lynn and Spitz, 2006). In addition to the fact that the list of issues in 2000 workshop had been successfully addressed and further established, one of the changes was that both number and data quality of case histories far exceeded those on the 2000 workshop. *P*-wave image had been improved through multicomponent data by de-multiple (PZ combination OBC) and ground roll filtering (land survey). However, it's noted that "it is quite evident that the full potential from these data is not yet fulfilled in practice, primarily due to bottlenecks in processing and interpretation" (Lynn and Spitz, 2006). In 2006, Canadian SEG published a special issue of Recorder on the multicomponent seismic methodology to foresee the future.

Stewart (2009) recently gave another review. Looking at the road ahead, he stated that the further advance would be to link rock physics to the multicomponent seismic expression and vice versa. Also, better statics, anisotropy, *Q* compensation, noise reduction, suppression or use of multipaths and multimodes, and more general anisotropic prestack depth migration need to be improved.

#### *Interpretation of converted-wave seismic data*

Under the background of all the rapid development of instrumentation, acquisition, processing and application of multicomponent seismic method in the research and service providers side, the interpretation and application in the data user side become the weak points in the chain, which may be partially due to the limited relevant training on theory and practice on multicomponent seismic method among the end users.

There are a number of reasons that increase the degree of difficulty for multicomponent seismic data interpretation. First, the interpreter would deal with multiple data volumes, which literally increases the work time. Second, the converted-wave has different travel time than *P*-wave. Third, the reflection on *PS* data could be different than *P*-wave's, because the rocks may have different *P*-wave impedance and *S*-wave impedance. Forth, the *S*-wave information, like *S*-wave log and offset VSP, may not be available. All above factors could affect the interpreter's ability to correctly describe the subsurface from *P*-wave and *PS*-wave together.

#### *PP and PS event registration*

*S*-wave travels with a different speed than *P*-wave in the Earth. The same formation at certain depth will appear at its *PS* two-way time different from the *PP* two-way time. Therefore, to determine the same formation on both *PP* and *PS* section is a critical step of multicomponent seismic interpretation, which is called event registration. Several event correlation techniques have been developed to do the automatic *PP-PS* event correlation. Lawton et al. (1992) used forward modeling to create the *PP*- and *PS*-wave offset stacks from velocity and density logs, then correlate them, followed by the correlation between *PP* seismic and *PP* synthetic stack, and correlation between *PS* seismic and *PS* synthetic stack. Gaiser (1996) developed a robust multicomponent correlation analysis to obtain average and interval  $V_p/V_s$  values. Chan (1998) suggested a method of log-stretching the *PP* and *PS* time into the logarithmic time, and search/apply a bulk shift. Those techniques are good for long wavelength component of  $V_p/V_s$ .

Although, under some circumstances, event registration could be done or partly be done by automatic program, in many cases, it needs to be interpreted manually by interpreters using synthetic seismograms and VSP data.

## **1.2 Some fundamentals of rock physics**

The variation of seismic reflection amplitude with offset is dependent on intrinsic rock parameters such as compressional-wave velocity ( $V_p$ ), shear-wave velocity ( $V_s$ ), density and attenuation. An understanding of the inter-relationships among these parameters and rock properties such as lithology, porosity and pore fluid content is needed for the quantitative extraction of rock properties for formations (Castagna, 1993). To utilize seismic waves fully, it is vital to understand what seismic waves can tell about reservoir rocks and how to extract such information from seismic waves.

Rocks are usually considered to be low-loss, acoustic or elastic media. When vibrations travel through the rocks, their deformation will be small and can be restored after the wave passes. The compressional-wave velocity ( $V_p$ ), shear-wave velocity ( $V_s$ ), density ( $\rho$ ) and attenuation ( $Q$ ) are the basic rock parameters.

### ***1.2.1 Velocity and elastic moduli***

Common elastic properties of rocks are defined in elastic moduli:

$$V_p = \sqrt{\frac{k + \frac{4}{3}\mu}{\rho}} \quad (1.3)$$

$$V_s = \sqrt{\frac{\mu}{\rho}} \quad , \quad (1.4)$$

where  $V_p$  is compressional-wave velocity;  $V_s$  is shear-wave velocity;  $k$  is rock bulk modulus (incompressibility), the ratio of volumetric stress to volumetric strain;  $\mu$  = rock shear modulus (rigidity), the ratio of shear stress to shear strain.

As  $k = \lambda + \frac{2}{3}\mu$ , equation 1.1 also has the form of

$$V_p = \sqrt{\frac{\lambda + 2\mu}{\rho}} \quad , \quad (1.5)$$

where  $\lambda$  and  $\mu$  are the Lamé parameters.

Equations 1.3 (or 1.5) and 1.4 provide the fundamental links between seismic velocities and rock properties. The rock bulk modulus may be strongly dependent on the pore fluid bulk modulus while the rock shear modulus may be less affected by the fluids. Hence, when a compressible free gas replaces liquids in the pore space, the rock  $P$ -wave velocity will decrease significantly, whereas the rock  $S$ -wave velocity might be slightly increased due to the decreasing bulk rock density. Consequently, the ratio of compressional- to shear-wave velocity ( $V_p/V_s$ ) is expected to be an excellent indicator of free gas in the pore space. The rigidity  $\mu$  gives us information about the rock matrix;  $k$  gives us additional information about the pore fluid.

For a rock's mechanical properties, the elastic constants are related by:

$$E = 2\mu(1 + \nu) = 3k(1 - 2\nu) \quad , \quad (1.6)$$

where  $E$  is Young's modulus,  $\mu$  is shear modulus,  $k$  is bulk modulus and  $\nu$  is Poisson's ratio. Combining with equation 1.3 and 1.4, if  $V_p$ ,  $V_s$  and density  $\rho$  are known, all the elastic moduli ( $k$ ,  $E$ ,  $\lambda$ ,  $\mu$ ,  $\nu$ ) can be calculated.

Poisson's ratio ( $\nu$ ) is another important rock property which measures incompressibility in porous rocks. For a homogeneous isotropic material which is deforming elastically under uniaxial compression, Poisson's ratio ( $\nu$ ) is defined as the negative fractional change in width divided by the fractional change in length (ratio of transverse to axial strain). Poisson's ratio is directly related to  $V_p/V_s$  by

$$\nu = \frac{0.5\left(\frac{V_p}{V_s}\right)^2 - 1}{\left(\frac{V_p}{V_s}\right)^2 - 1} \quad (1.6)$$

Poisson's ratio mostly varies from 0 to 0.5. It can be negative for some materials. The value 0 corresponds to a  $V_p/V_s = 1.41$ . Water, which is incompressible, has the Poisson's ratio of 0.5 as  $V_p/V_s$  is infinity due to fluid having no shear strength ( $V_s = 0$ ).

### ***1.2.2 $V_p$ - $V_s$ relationship***

The  $V_p$ - $V_s$  relationship can be theoretically derived by combining equation 1.3 and 1.4 as:

$$V_p^2 = \frac{k}{\rho} + \frac{4}{3}V_s^2 \quad (1.7)$$

However, a linear empirical  $V_p$ - $V_s$  relationship has been established from lab experiments and wireline logging measurements which holds very well in different sedimentary lithologies. Generally,  $V_s$  is nearly linearly related to  $V_p$  for sandstones and shales in clastic environment. The mudrock line obtained exclusively from in-situ measurements by Castagna et al. (1985) predicts fairly realistic  $V_s$  for shales:

$$V_s = 0.862069V_p - 1.1724 \quad (1.8)$$

where the units for  $V_p$  and  $V_s$  are km/s.

Further more, Castagna et al. (1993) show a set of similar trend equations but separated for sandstone and shale, which is

$$V_s = 0.8042V_p - 0.8559 \quad (1.9)$$

for sandstone, and

$$V_s = 0.7700V_p - 0.8674 \quad (1.10)$$

for shale. The  $V_p$  and  $V_s$  are in km/s.

For carbonate rocks, Pickett (1963) suggested that  $V_p = 1.9 V_s$ . Castagna et al. (1993) also described the  $V_p$ - $V_s$  relationship for limestone as a second-order polynomial fit:

$$V_s \text{ (km/s)} = -0.05509V_p^2 + 1.0168V_p - 1.0305 \quad (1.11)$$

And a linear fit is adequate for dolomites over a limited range:

$$V_s \text{ (km/s)} = 0.5832V_p - 0.0776 \quad (1.12)$$

They observe that for  $V_s$  greater than 1.5 km/s, Pickett's relation holds extremely well. At low velocities, there is a substantial deviation from this trend as  $V_p$  approaches 1.5 km/s (water velocity) while  $V_s$  approaches zero. Also, from laboratory experiments, they observed that gas sands have a  $V_p/V_s$  varying from under 1.4 to over 1.8 with average of about 1.5, which matches Gregory (1977)'s  $V_p/V_s = 1.5$  for gas sand.

Based on the abstracted composite plot of  $V_p/V_s$  versus  $V_p$  (Figure 1.2), Castagna (1993) concluded about the use of  $V_p/V_s$  to ascertain lithology that "Lithology discrimination is best at high velocities where the rule of thumb that  $V_p/V_s$  is equal to 1.6 for sandstone, 1.8 for dolomite and 1.9 for limestone is most nearly correct ... At high

velocity the difference in  $V_p/V_s$  between gas- and brine-saturated rocks will be relatively small. For low velocity rocks, lithology discrimination is also difficult; however, the difference in  $V_p/V_s$  between gas and brine saturated rocks will be relatively large. As a consequence, AVO analysis for hydrocarbons will be more robust for lower velocity targets.”

Another conclusion from this more conceptual plot (Figure 1.2) is that using  $V_p/V_s$  to discriminate sand from shale is relatively easy for both low and high velocity rocks, because the shale line is always above the sandstone line which suggests that shale always has higher  $V_p/V_s$  than sandstone under the condition of shale’s  $P$ -wave velocity being close to sandstone’s.

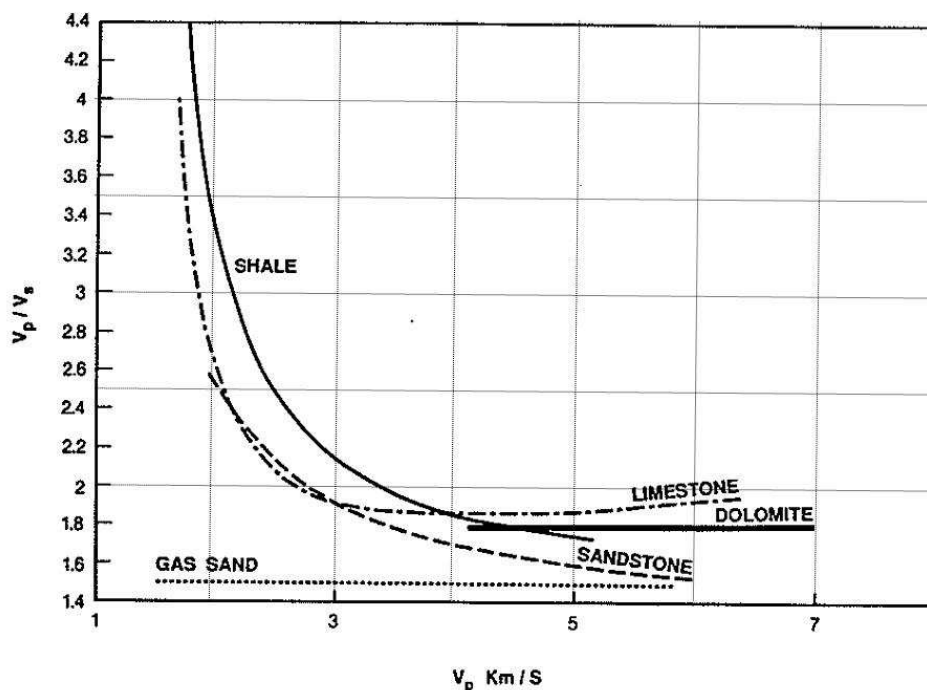


**Figure 1.2** A composite plot of  $V_p/V_s$  versus  $V_p$  trend for various lithologies (after Castagna, 1985), modified by adding the grid lines.

### 1.2.3 Attenuation

Seismic waves traveling through the subsurface of the Earth are attenuated by the conversion of seismic energy into heat. The attenuation property, associated with anelastic absorption, is a fundamental rock property (Kjartansson, 1979; Johnston and Toksöz, 1981). Attenuation is most commonly measured by the attenuation coefficient  $\alpha$ , and/or quality factor  $Q$  (or its inverse  $Q^{-1}$ ). High  $Q$  value corresponds to less attenuation.

By definition, the intrinsic quality factor  $Q$  is a measurement of the amount of energy lost per cycle or a ratio of stored energy to dissipated energy:

$$Q = 2\pi \frac{W}{\Delta W} = \frac{\omega E}{-dE/dt}, \quad (1.13)$$

where  $W$  is the elastic energy stored at maximum stress and strain and  $\Delta W$  is the energy loss per cycle of a harmonic excitation,  $E$  is the instantaneous energy in the system,  $dE/dt$  is the rate of energy loss.

The attenuation of a seismic plane wave can be expressed as

$$A(x) = A_0(x)e^{-\alpha x}, \quad (1.14)$$

where  $A(x)$  is the amplitude as a function of position  $x$ ,  $A_0(x)$  is the initial amplitude,  $\alpha$  is attenuation coefficient.  $\alpha$  can be rewritten as:

$$\alpha = -\frac{1}{A(x)} \frac{dA(x)}{dx} = -\frac{d}{dx} \ln A(x). \quad (1.15)$$

For two different positions,  $x_1$  and  $x_2$ , with respect amplitudes  $A(x_1)$  and  $A(x_2)$ , we have

$$\alpha = \frac{1}{x_2 - x_1} \ln \left[ \frac{A(x_1)}{A(x_2)} \right] \quad (1.16)$$

The attenuation coefficient  $\alpha$  is related to the quality factor  $Q$  by:

$$\alpha = \frac{\pi f}{Qv}, \quad (1.17)$$

where  $v$  is velocity and  $f$  is frequency.

Theoretical models of attenuation mechanism have been proposed, e.g., Biot global flow model (1956), Squirt local flow model (Mavko and Nur, 1975, O'Connell and Budiansky, 1977, Dvorkin and Nur, 1993). Constant  $Q$  theory (Kjartansson, 1979) considered a linear description of attenuation in which  $Q$  is exactly independent of frequency. In fact, we might expect a fairly constant level of attenuation over wide frequency bands, i.e. attenuation is independent of frequency in seismic frequency bands.

Attenuation (seismic waves are always attenuated as they travel through rocks) and velocity dispersion (velocity increase with frequency) are considered to be related (Futterman, 1962). Velocity dispersion associated with attenuation can cause up to 7.0 ms/1000 ft delay of the VSP traveltimes with respect to the integrated sonic log (Stewart et al, 1984).

Comparing with elastic properties, the anelastic properties – attenuation – is much more complex in terms of explicit analysis, mechanism, laboratory and field measurements. Small amounts of condition change can result in big change in measurement (Johnston and Toksöz, 1981). It has been widely accepted that the VSP experiments are the best for a reliable in-situ  $Q$  estimation (Stainsby and Worthington, 1985, Tonn, 1991). The accuracy of  $Q$  estimated from downhole seismic is generally higher than that from surface seismic (White, 1992).

The quality factor  $Q$  can be used for applying inverse  $Q$  filtering to surface seismic data to minimize the effect of dispersion and attenuation, and hence to increase the seismic resolution (Hargreaves and Calvert, 1991, Wang, 2002). Another application is that, because seismic attenuation ( $Q$ ) strongly depends on lithology and pore fluid properties (Batzle et al, 1996), it might help to detect gas or the change of pore fluid. Klimentos (1995) used the ratio of compressional to shear attenuations as hydrocarbon indicator based on well log data. Seismic attenuation anomalies can help to monitor the steam injection from time-lapse seismic (Hedlin and Mewhort, 2002).

### **1.3 Dissertation objectives and structure**

The objectives of the dissertation are to continue assessing the multicomponent seismic method in hydrocarbon exploration and exploitation, to develop a more complete structural and stratigraphic picture of the subsurface via multicomponent seismic data, to present the integration of the well log, VSP and multicomponent seismic data for assessing the oilfield, and to use seismic attributes to predict rock properties. They are accomplished by:

- Propose and optimize a practical work flow for interpreting the multicomponent seismic data – Chapter 2.
- Investigate and verify the  $V_p$ - $V_s$  relationship using three data examples from clastic sand-shale, carbonate and deep-water siliceous shale – Chapter 2, 5 and 6.
- Interpret the Ross Lake multicomponent seismic dataset from Western Canadian Sedimentary Basin – Chapter 2.
- Use two methods – travelttime and impedance ratio – to estimate the  $V_p/V_s$  from Ross Lake multicomponent seismic data, then compare and discuss the results – Chapter 2 and 3.

- In-situ attenuation calculation from VSP – optimize the algorithm to reduce the error and uncertainty of attenuation estimation – Chapter 4.
- Interpret the Cantarell/Sihil multicomponent seismic dataset from offshore Gulf of Mexico – Chapter 5.
- Interpret a land 2D multicomponent dataset from US – Chapter 6.

#### **1.4 Data used**

Ross Lake 3C-3D project:

- Processed 3D multicomponent seismic datasets, including post-stack time migrated vertical component (*PP*) volume and post-stack time migrated horizontal radial component (*PS*) volume;
- Zero-offset vertical vibrator sourced VSP
- Zero-offset horizontal vibrator sourced VSP
- Multi-offset vertical vibrator sourced VSP
- Well logs with  $V_p$  and  $V_s$

Cantarell/Sihil 4C-3D project:

- Processed 3D multicomponent seismic dataset, including pre-stack time migrated vertical component (*PP*) volume and pre-stack time migrated horizontal radial component (*PS*) volume;
- Zero-offset VSPs
- Well logs with  $V_p$  and  $V_s$

The US 3C-2D project:

- Processed 2D multicomponent seismic datasets, including post-stack time migrated vertical component (*PP*) volume and post-stack time migrated horizontal radial component (*PS*) volume;
- Well logs with  $V_p$  and  $V_s$

### **1.5 Hardware and software**

The work presented in this dissertation is mainly done on a SUN MICROSYSTEMS network operated by the CREWES Project of the Department of Geoscience at the University of Calgary, and PCs provided by the CREWES Project.

Hampson-Russell's (now a division of CGGVeritas) geophysical application software suite has been used to accomplish the most work in this study. *GeoView* is a well database tool to show the logs; *ProMC* is the package to do the multicomponent seismic interpretation, including *PP* and *PS* synthetic seismograms creating, *PP* and *PS* event matching, horizon picking, attributes map generating etc. *Strata* is used to do the seismic impedance inversion.

*ProMAX* from Landmark Graphics Corporation (a division of Halliburton) has been used to do the seismic data processing related procedures, mainly for VSP processing, i.e. to separate downgoing and upgoing wavefields using median filter.

*MATLAB* programming language is used to estimate  $Q$  factor from VSP data using adapted spectral-ratio method. A number of MATLAB codes by Dr. Gary Margrave from University of Calgary are also utilized in this research.

## Chapter Two: Interpretation of Ross Lake 3D multicomponent seismic data

### 2.1 Introduction

Multicomponent seismic data, combining *PP*-wave and *PS*-wave wavefields, provide independent measurement of rock and fluid properties. Unlike *P*-waves, converted (*PS*) waves are minimally affected by changes in pore fluids. Rapid advancements in multicomponent acquisition methods and processing techniques have led to numerous applications for converted wave data that are increasingly used for exploration and exploitation of oil and gas. However, the increased prevalence of multicomponent seismic applications means that interpreters must face many difficult challenges: how to register *PS*-wave time to *PP*-wave time, determine the best methodology for interpreting *PS*-wave data, and how to apply the *PS*-wave interpretation in assessing the risk of exploration and exploitation prospects.

In this chapter, an approximate 7.5 km<sup>2</sup> 3D multicomponent seismic dataset from Ross Lake oilfield in Saskatchewan, Canada is interpreted and analyzed guided by well logs and VSP. The purposes of this study are: (1) to propose a practical work flow for multicomponent seismic data interpretation using the Ross Lake data as an example; (2) to assess the Ross Lake oil reservoir, achieve a full reservoir description and evaluate the potentials for further development by combining well-logs, VSP and the 3C-3D surface seismic data.

### 2.2 Work flow for multicomponent seismic data interpretation

Although, the *PP*-wave and *PS*-wave seismic data are actually reflections of different aspects of the same subsurface objective, an interpreter has to face two separate data volumes – the *PP* volume and the *PS* volume. The obstacles for interpreting *PS* data mainly arise from three complexities: (1) different *PS* and *PP* travel time; (2) sometimes different *P*-impedance and *S*-impedance, and impedance contrast; and (3) different apparent frequency contents. All mean that, in most cases, *PS* section is NOT just simply a stretched version of *PP* seismic section. A lot of times, visual correlations could be misleading the horizon identification on *PS* data because of the above reasons combining with the time-variant  $V_p/V_s$ .

The general work flow for multi-component data interpretation is schematically shown in Figure 2.1, for either 2D or 3D seismic data.

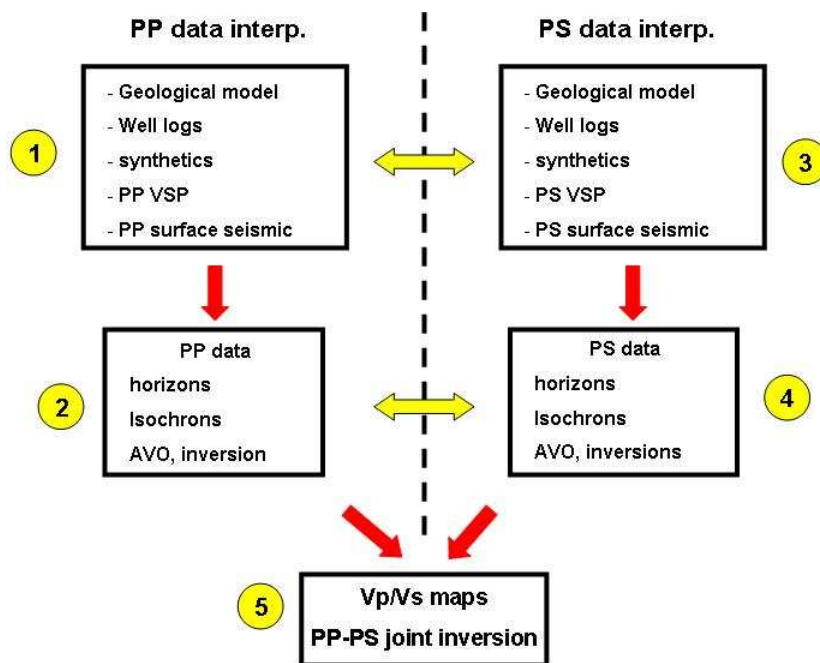


**Figure 2.1** The work flow for multi-component seismic data interpretation.

The conventional *PP* data interpretation is conducted first. To identify the geological formations on seismic sections, the synthetic seismogram is generated (at well location when *P*-wave velocity and density logs are available) to tie with seismic traces around the well. Whenever possible, the VSP, either zero-offset corridor stack or offset migrated profile, should be used to correlate with surface seismic to have more confidence in time-depth relationship and recognition of seismic character for certain formations.

Based on a reasonable correlation of synthetic seismogram, VSPs and surface seismic at well locations, the key horizons and/or geological markers are picked on *P*-wave seismic data to build the framework of the seismic interpretation. Hence, the *P*-wave time structure map of certain horizon, time-thickness (isochron/isochore) map between horizons and other horizon-based attributes are mapped and computed. Amplitude inversion for impedance (and velocity) may also be conducted. This is a fairly routine job.

Next, the same set of steps as the *PP* interpretation is followed but with the *PS* seismic data. When interpreting *PS* data, the most difficult part is often the *PS* event registration, which is to match/tie the *PS* seismic events with *PP* seismic events. This is the result of a few complexities including the *PP* time domain versus *PS* time domain and difference in *PS* reflection character and *PP* reflection. Different statics solutions of *PP* and *PS* data in processing of land surveys may put the data on different datum, partly because the near surface shear-wave velocity is not available. In the interpreter's mind, the *PS* image could be in vast difference with *PP* image in terms of the seismic character, i.e. a peak on *PP* data may correspond to a zero-crossing or a slope on *PS* data. For the

above reasons, the correlation of *PS* seismic traces with *PS* synthetic seismogram (and/or with *PS*-wave VSPs) is more critical for *PS* seismic interpretation.

Guided by *PS* synthetics and *PS* VSPs, the same set of horizons defined on *PP* data is picked on *PS* volumes. Then, the *PS* time-structure maps and time-thickness maps can be extracted.

The *PP* and *PS* time-thickness maps are used to calculate a  $V_p/V_s$  map. It is this map that typically provides an indication of the horizontal variation of lithology. For two given formations, the traveltime difference of *PP* and *PS* data comes from the  $V_p$  and  $V_s$  difference between them. Because different lithology has its own  $V_p/V_s$ , the  $V_p/V_s$  map derived from *PP* and *PS* time-thickness (isochron/isochore) maps indicates the variation of lithology between these horizons. And this information is more helpful to distinguish sands from shale background for a typical clastic deposition environment.

### **2.3 Geology background of Ross Lake Oilfield**

The Ross Lake oilfield, owned and operated by Husky Energy Inc, is located in south-west part of Saskatchewan, Canada in Township 13 Range 17, west of 3rd Meridian (Figure 2.2). The producing formation is a lower Cretaceous incised valley (channel) sand in the Dimmock Creek member of the Cantuar formation of Mannville Group.



**Figure 2.2 The location of Ross Lake oilfield.**

Up until the end of 2003, there are 4 vertical wells, namely 10-25, 11-25, 14-25 and 15-25, and one horizontal well that have been drilled and produced. The reservoir sand is over 30 m thick in well 11-25 with 12-13 m of net pay, and has porosity of about 30% and very high permeability -- in the 3 Darcy range. In the middle of the sand, pyrite cement giving low porosity is resulting in high velocity and density. This pyrite cemented layer is varying in thickness (absence in well 15-25) in different wells, and seems not a maker. The produced oil is heavy, about 13° API. There is no gas cap. The pool is on its primary production and hasn't had enhanced recovery methods applied. Husky is observing the horizontal well to see if it is economically feasible. If so, there would be more horizontal wells to drill.

The regional stratigraphic column in south-western Saskatchewan is displayed in Figure 2.3.

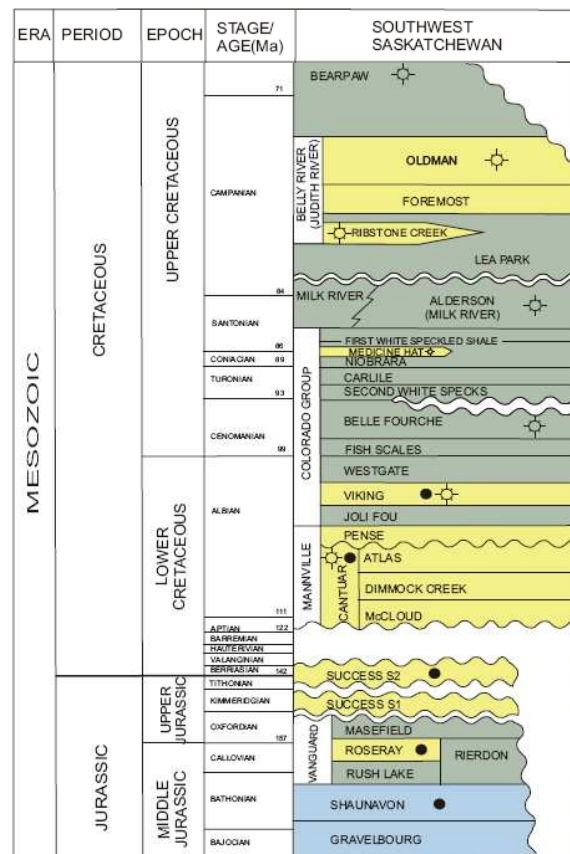


**Figure 2.3. Stratigraphic chart of southwest Saskatchewan (from [www.ir.gov.sk.ca](http://www.ir.gov.sk.ca))**

In the upper middle and lower upper Jurassic, the formation above the Shaunavon limestone is the Vanguard Group, consisting of the basal Rush Lake shale, the middle Roseray sandstone and sandy mudstone, and the upper Masefield shale. Above the unconformity between Jurassic and Cretaceous is the Mannville Group, which is the main hydrocarbon bearing formation over almost all the Western Canadian Sedimentary Basin. Three sub-divisions in Mannville Group, from oldest to youngest, are the Success Formation, Cantuar Formation and Pense Formation. The Cantuar Formation also has three subdivisions (oldest to youngest): McCloud Member, Dimmock Creek Member and Atlas Member.

A high-relief erosion surface is carved through Jurassic and Mississippian strata and is in turn filled in with Cantuar sediments. The McCloud Member occupies the base of the erosional relief, the Dimmock Creek Member (DCM) infills much of the remainder, and the Atlas Member forms the regional blanket (Figure 2.4, Christopher, 1974, and Figure 2.5, Vanbeselaere, 1995).

The Dimmock Creek Member comprises “olive-green and dark grey, argillaceous sandstones, sandy mudstones and shales, locally mottled with red, inter-bedded, and interrupted by massive quartzose sandstones expanded to nearly the full thickness of the member.” (Christopher, 1974)

One important marker in the following study is called IHACM, an acronym for the Index Horizon Above Cantuar Marker. On the conventional *P*-wave seismic sections, it is a stable and spatially wide spread small peak on a regional sense.

By correlating the wireline logs from about 370 wells in a study area of about 12 townships, Li et al. (2004) constructed ten cross sections displaying the stratigraphic complexity of the Cantuar incised-valley fill and interfluvies. The resulting regional isopach map of Cantuar Formation is about 30-50 m thick in the Ross Lake seismic covered area. They concluded that the major hydrocarbon trapping mechanism is the valley sediments of relatively low permeability sealing the permeable flanks of the Roseray-Success buttes and mesas.

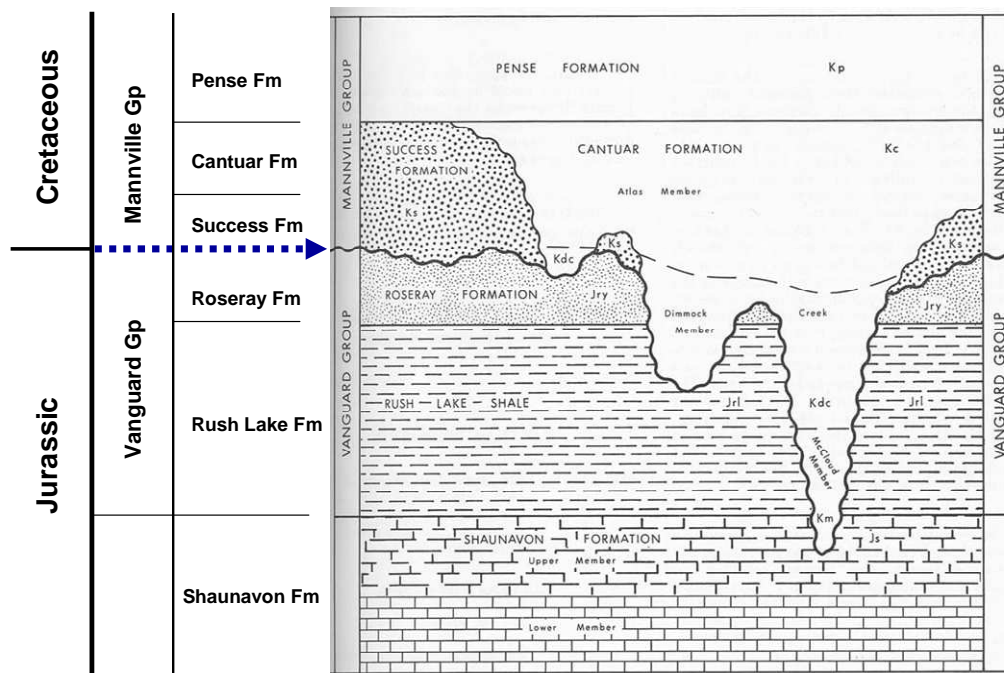


Figure 2.4 Diagram illustrating the stratigraphic relationship of the upper Jurassic and Lower Cretaceous, southwestern Saskatchewan (from Christopher, 1974).

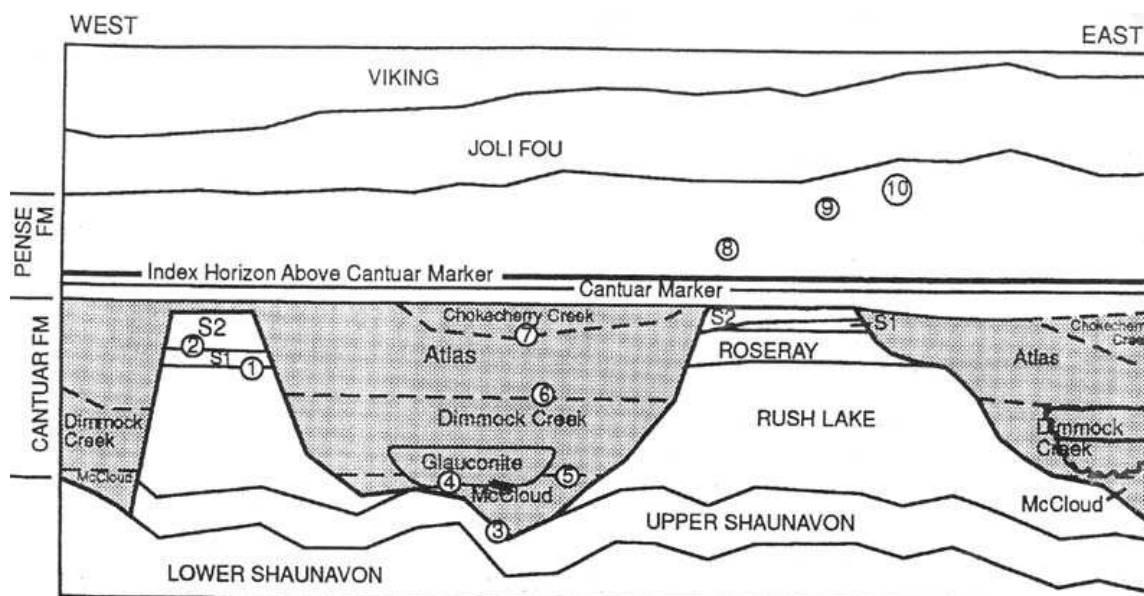


Figure 2.5 Diagram showing the stratigraphic relationship of the formations within the Mannville Group. (from Vanbeselaere, 1995).

## **2.4 Data available: seismic data, wells logs and VSPs**

### ***2.4.1 Surface seismic data***

A 3D multi-component single station VectorSeis<sup>®</sup> seismic survey was shot by Veritas Geophysical in Ross Lake area in May 2002. The total 13 receiver lines are in east-west direction with 180 m line spacing. The receiver point interval is 50 m. The shot lines are in north-south direction with 325 m line spacing. There are 11 shot lines in total. The shot point interval is 50 m. The source type is 0.5 kg dynamite at 15 m depth. There were about 484 shots and 858 receivers in this 7.5 km<sup>2</sup> 3D survey. The seismic natural bin size is 25 m × 25 m with the nominal fold of 45. The record length is 5 second at 2 ms sample rate.

Veritas Canada processed this 3C-3D data. A post-stack Kirchhoff time migration has been applied to the vertical, radial and transverse component. The migrated vertical (denoted as *PP*) and the migrated radial (denoted as *PS*) datasets are analyzed in this thesis.

The *P*-wave processing flow was as follows:

Demultiplex
High amplitude and ground roll noise attenuation, amplitude recovery
Minimum phase surface consistent deconvolution
Amplitude equalization structure statics (short wave) - 2 layer drift
Datum: 950m replacement velocity: 2000 m/s, weathering velocity: 950 m/s
Interactive trace edits
Preliminary velocity analysis - NMO from surface
Statics - automatic surface consistent (2 passes)
Final velocity analysis - NMO from surface
Spectrum balance, first break mutes
Structure statics (long wave) - 2 layer drift statics - CDP trim
Stack, FXY poststack noise attenuation
Post-stack Kirchhoff migration: 100% stacking velocity
Filter: time variant
Scaling: 600 ms window

**Table 2.1 Ross Lake 3C-3D seismic *PP* data processing flow.**

The converted-wave processing flow is as follows:

Demultiplex
High amplitude and ground roll noise attenuation, <i>PS</i> amplitude recovery
Minimum phase surface consistent deconvolution
Amplitude equalization structure statics (short wave) - 2 layer drift
Shot (P-wave) statics applied
Interactive trace edits
Preliminary $V_p/V_s$ analysis - NMO from datum
Statics - automatic surface consistent (2 passes)
Final $V_p/V_s$ analysis - NMO from datum
Tau-p shot-based noise attenuation
Spectral balance, ACP trim
CCP depth variant binning
Stack, FXY post-stack noise attenuation
Post-stack Kirchhoff migration
Filter: 2/4 - 50/70 Hz.
Mean scaling: 500 ms window

**Table 2.2 Ross Lake 3C-3D seismic *PS* data processing flow.**

#### **2.4.2 VSP survey**

In June 2003, a multi-offset Vertical Seismic Profile (VSP) survey was conducted in well 11-25-013-17W3 by Husky Energy in partnership with the CREWES project, University of Calgary. The source locations are shown in Figure 2.6. The survey parameters are in Table 2.4:

	Zero-offset	Offset		Walkaway			
	#1	#4	#6	#2	#3	#5	#7
<b>Offset (m)</b>	53.67	399.12	698.72	149.99	250.66	558.08	996.80
<b>Azimuth</b>	N16.34	N337.23	N301.54	N336.15	N337.63	N310.50	N319.52
<b>Source type 1</b>	Litton 315 P-vibe						
<b>Sweep</b>	8-180Hz, 12s, linear						
<b>Source type 2</b>	Inline IVI S-mini-vibe	N/A					
<b>Sweep</b>	5-100Hz, 12s, linear	N/A					

**Table 2.3** The source parameters of the multi-offset VSP survey in well 11-25.

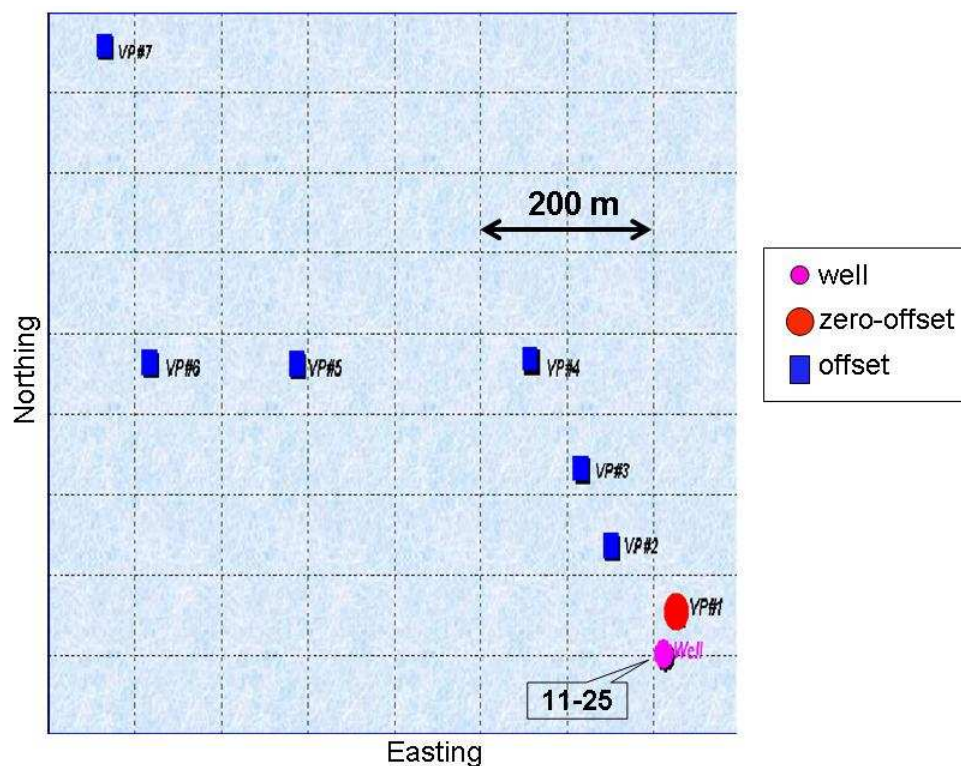


**Figure 2.6** Source location map of the VSP survey in well 11-25 (after Schlumberger).

### 2.4.3 Wells and $V_p$ - $V_s$ relationship

Four vertical wells, 10-25, 11-25, 14-25 and 15-25, and one horizontal well has been drilled in this pool. The typical well logging suite includes SP, gamma ray, resistivity, sonic, density and neutron porosity. Unfortunately, no open-hole shear velocity has been acquired in these wells.

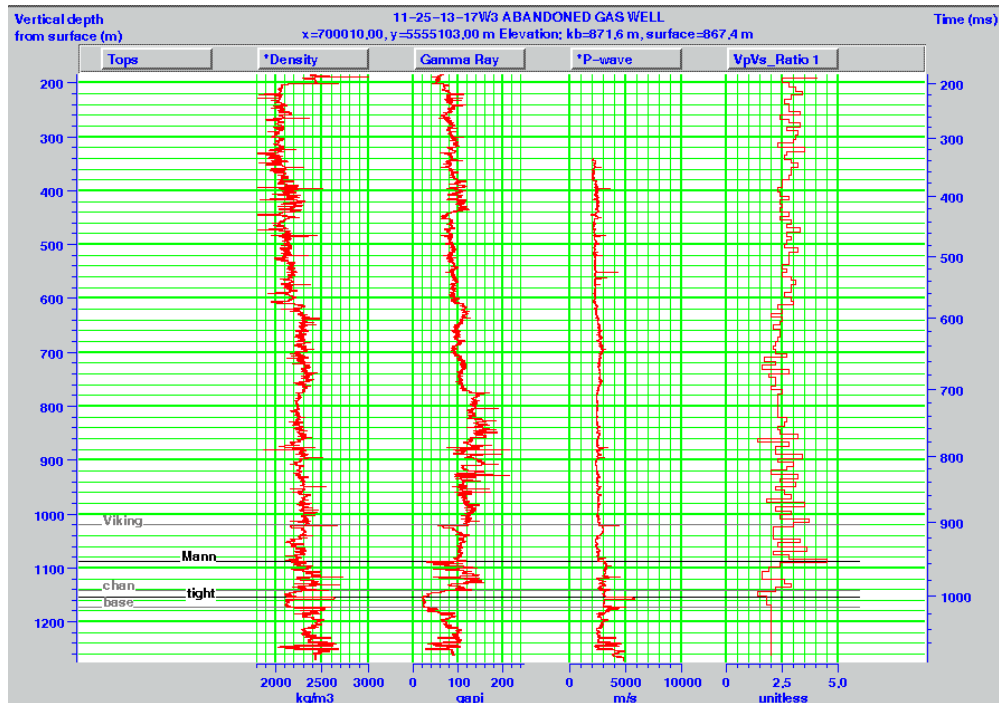


**Figure 2.7** Logs from well 11-25. The  $V_p/V_s$  curve is derived from the  $P$ -source and  $S$ -source VSP in the same well.

A dipole sonic log (DSI) was run in the cased-hole condition in well 11-25 in attempt to acquire shear wave information through casing. However, the logging results were quite poor and largely unusable.

Shear-velocity logs are helpful in interpreting converted-wave data through the construction of *PS*-wave synthetic seismograms. Unfortunately, none of the wells within this 3C-3D seismic survey had a shear-wave log. However, there are four regional wells having shear velocity log, shown in Figure 3.11 to 3.14. The nearest well is 2-33-13-19, about 24 km west of well 11-25-13-17.

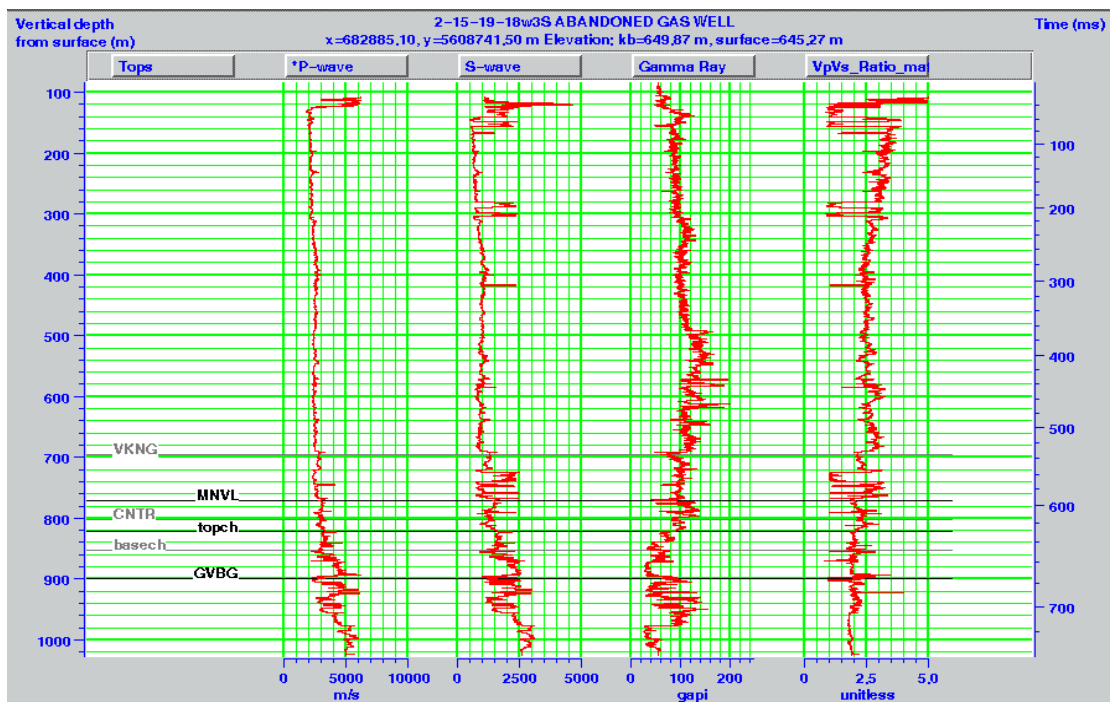


Figure 2.8 GR log and measured  $V_p$ ,  $V_s$  from the dipole sonic log in well 2-15-19-18.

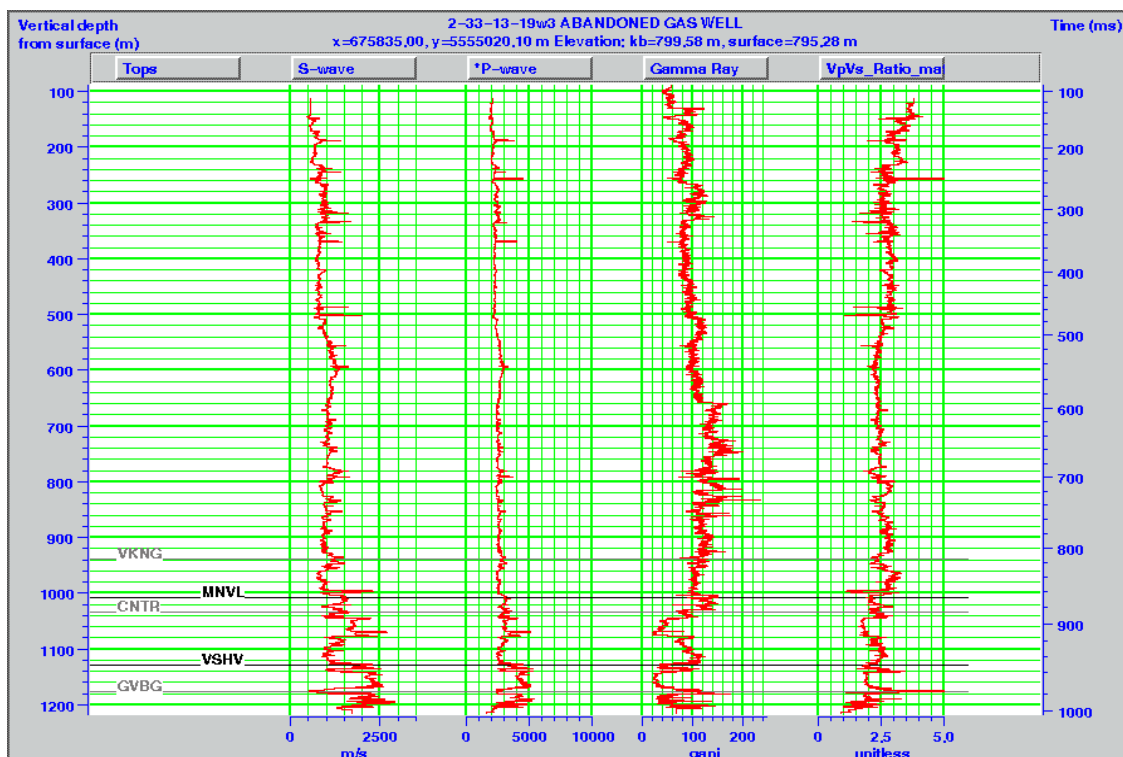


Figure 2.9 GR log and measured  $V_p$ ,  $V_s$  from the dipole sonic log in well 2-33-13-19.

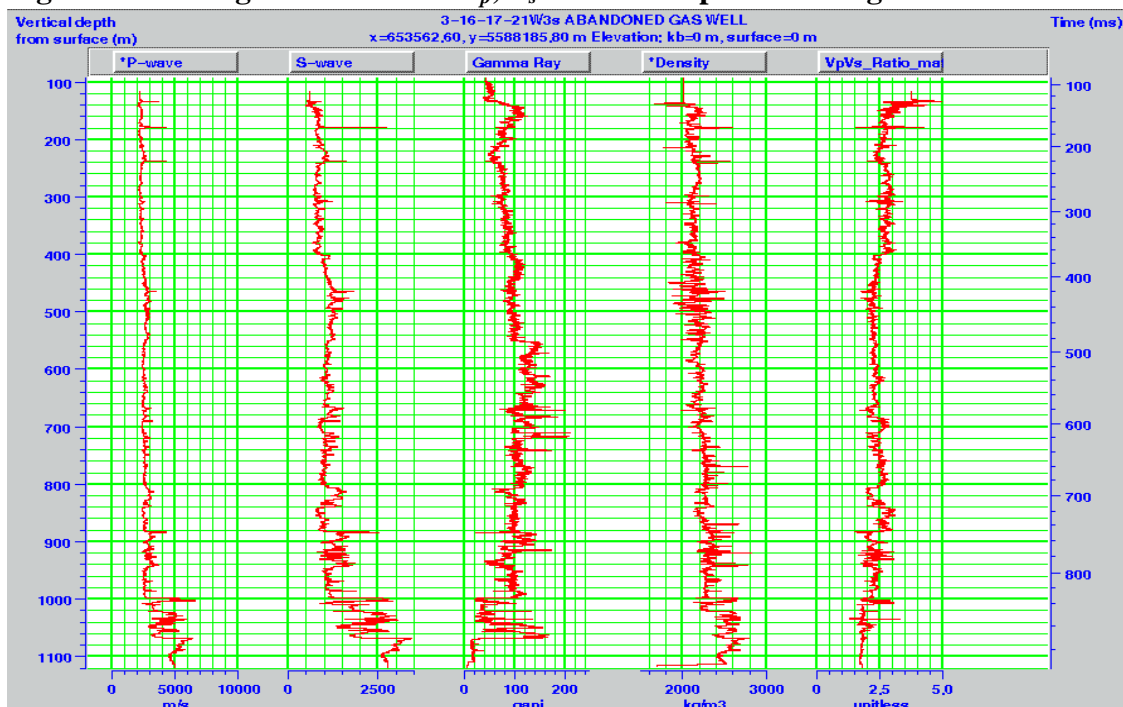
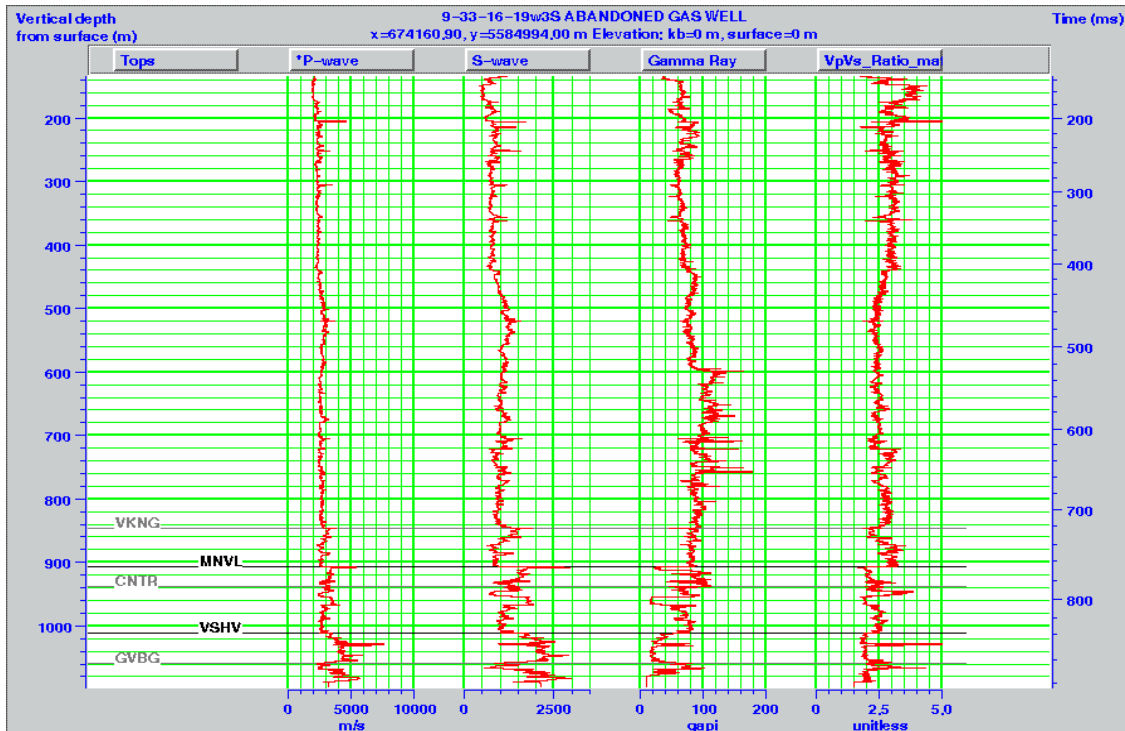


Figure 2.10 GR, density and measured  $V_p$ ,  $V_s$  from the dipole sonic log in well 3-16-17-21.



**Figure 2.11 GR log and measured  $V_p$ ,  $V_s$  from the dipole sonic log in well 9-33-16-19.**

To generate a converted-wave synthetic seismogram using well logs, knowledge of the shear-wave velocity ( $V_s$ ) is necessary. The direct measurement of formation  $V_s$  usually comes from the dipole sonic logging. Very occasionally, the shear-source VSP could provide the average shear-wave velocity between downhole geophones over a relative large interval compared with the wireline logging.

When there is no measured  $V_s$  available, empirical equations are commonly used to estimate  $V_s$  values from  $P$ -wave velocity or sonic log. A thorough study on local petrophysical model and geostatistical method using more logs, i.e. GR, resistivity, porosity, etc, could reveal more accurate  $S$ -wave velocity estimation.

Mentioned in Chapter 1, the mudrock line (Castagna, 1985) predicts a fairly reasonable  $V_s$  from  $V_p$  in the most cases of a sand-shale clastic environment:

$$V_s = 0.8621 V_p - 1.1724 \quad , \quad (2.1)$$

$$\text{or, } V_p = 1.16 V_s + 1360 \quad , \quad (2.2)$$

where the units for  $V_p$  and  $V_s$  are km/s.

Thus, we need to utilize or develop an empirical relationship between  $V_p$  and  $V_s$ , which can be used to derive  $V_s$  from  $V_p$  in wells in the Ross Lake 3C-3D seismic survey covered area. Those four regional wells with measured  $V_p$  and  $V_s$  logs are used to verify the empirical  $V_p$  - $V_s$  relationship (Figure 2.12). The channel sands have  $P$ -wave velocities in the 3000 m/s range. A regression line (red) fitting the points (excluding the unreliable grey zones which came from a very shallow region in one well) gives us the local  $V_p$ - $V_s$  relationship as:

$$V_p = 1.416 V_s + 1070 \quad , \quad (2.3)$$

where the units for  $V_p$  and  $V_s$  are m/s.

The reservoir sands generally show  $V_p/V_s$  values between 1.7 and 2.0. The shallow formations have  $V_p/V_s$  from 1.8 ~ 3.0.

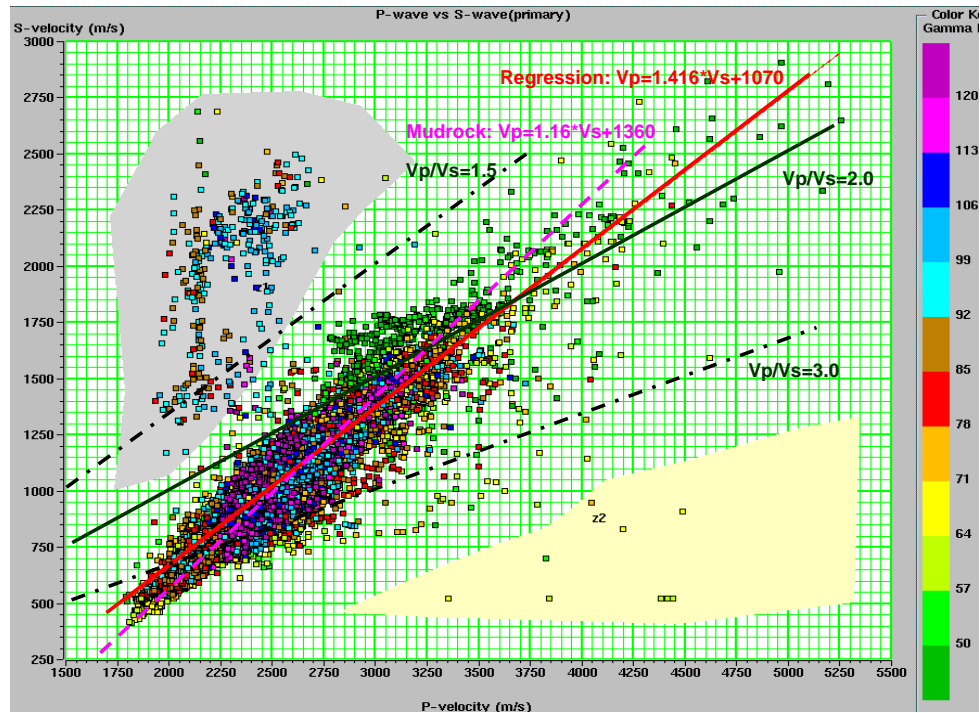


**Figure 2.12** Crossplot of measured  $V_p$  and  $V_s$  from four regional wells. The linear regression (red solid line) is calculated excluding the colored zone (grey and light yellow) due to questionable spikes of shear log in well 2-15-19-18. The mudrock line (pink dash line) and three constant  $V_p/V_s$  lines (1.5, 2.0 and 3.0) are posted.

#### 2.4.4 Examine seismic frequency content

The  $PS$  data usually have a low frequency content compared to  $PP$  data for a number of possible reasons: the longer travel time initially, shorter wavelengths and absorption. Known frequency is a guide for well-seismic correlation and  $PP$ -to- $PS$  seismic tie.

The  $PP$  data show an average signal bandwidth of about 8-100 Hz in the 800-1400 ms time window (Figure 2.13, upper panel). The radial component of  $PS$  data, in the window of 1000-2000 ms of its native  $PS$  time domain, has a narrower frequency

bandwidth of about 10-60 Hz (Figure 2.13, lower left panel). Notice that there is a platform at 60-100 Hz possibly caused by an over-boosting in the spectral balance process and most of which may be noise. The transverse component of *PS* data in the same *PS* time window shows a narrower bandwidth of 10-40 Hz (Figure 2.13, lower right panel). Only *PP* and *PS*-radial data are interpreted here as the transverse-component data were without a great deal of signal.

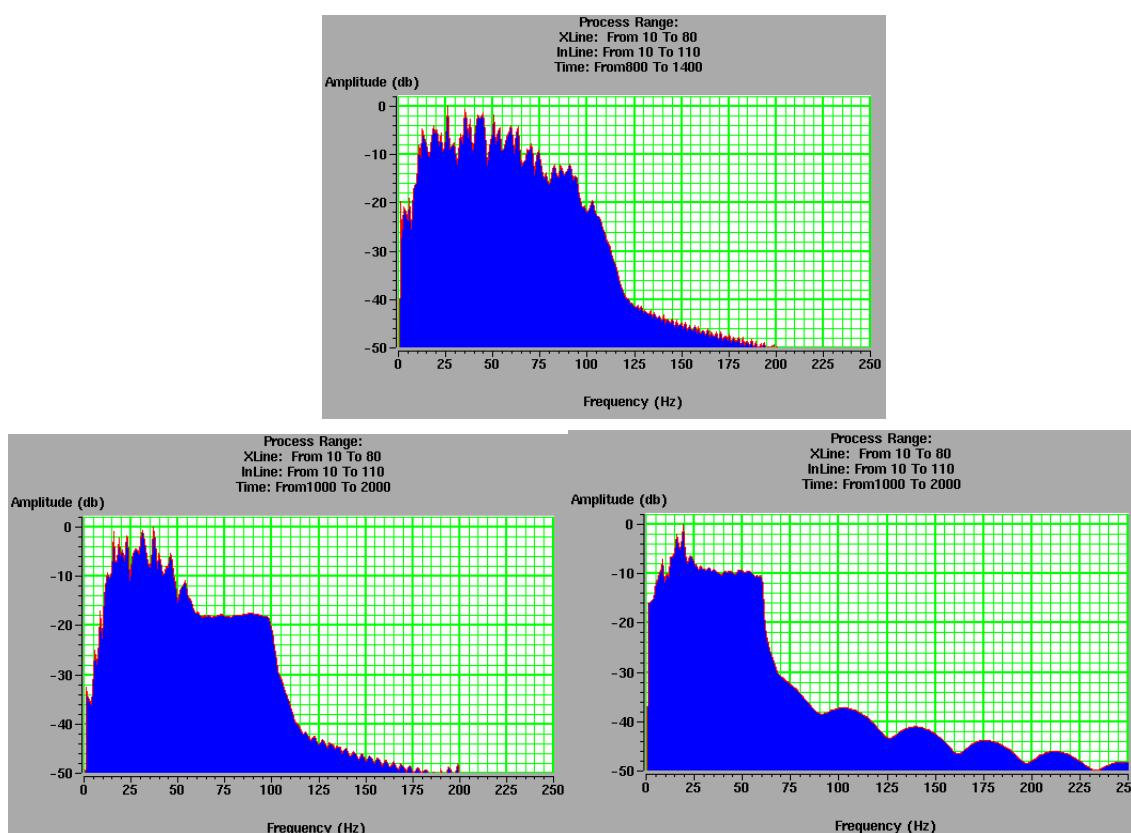


**Figure 2.13** Average amplitude spectrum of vertical *PP* (upper panel), the radial *PS* (lower left panel) and transverse *PS* (lower right panel) data volumes of Ross Lake 3C-3D seismic.

## 2.5 Correlation of P-wave synthetic seismograms, VSPs and PP seismic data

To establish the well-seismic tie is always an important step, probably the most critical step for any seismic data interpretation. In order to mark the geological formation tops from a well on seismic sections, and to know that what seismic response a certain formation or formation combination would correspond, a good and reasonable tie between the well synthetic seismogram and seismic data is essential.

Well 11-25 is used to conduct the procedure of well-seismic tie. The wavelet used here is extracted from nine *PP* seismic traces around well 11-25. Thereafter, the synthetic seismogram is created by convolving the extracted wavelet with the reflection coefficient series which is calculated from the impedance, or the product of velocity and density.

VSP data usually have higher frequency contents comparing with surface seismic. The frequency difference sometime could make the correlation ambiguous. To reduce the VSP frequency bandwidth by bandpass filtering to match the seismic frequency bandwidth can be quite helpful. To do so, a 5-10-70-80 Hz bandpass filter is applied to the zero-offset VSP corridor stack to match the surface *PP* seismic data frequency bandwidth. We see the correlation is very good.

The *PP* synthetic seismogram from well 11-25 and the zero-offset *PP* corridor stack are used to develop the correlation between geological formations and seismic events (Figure 2.14). The *PP* seismic data display a good correlation with the synthetic seismogram and zero-offset VSP.

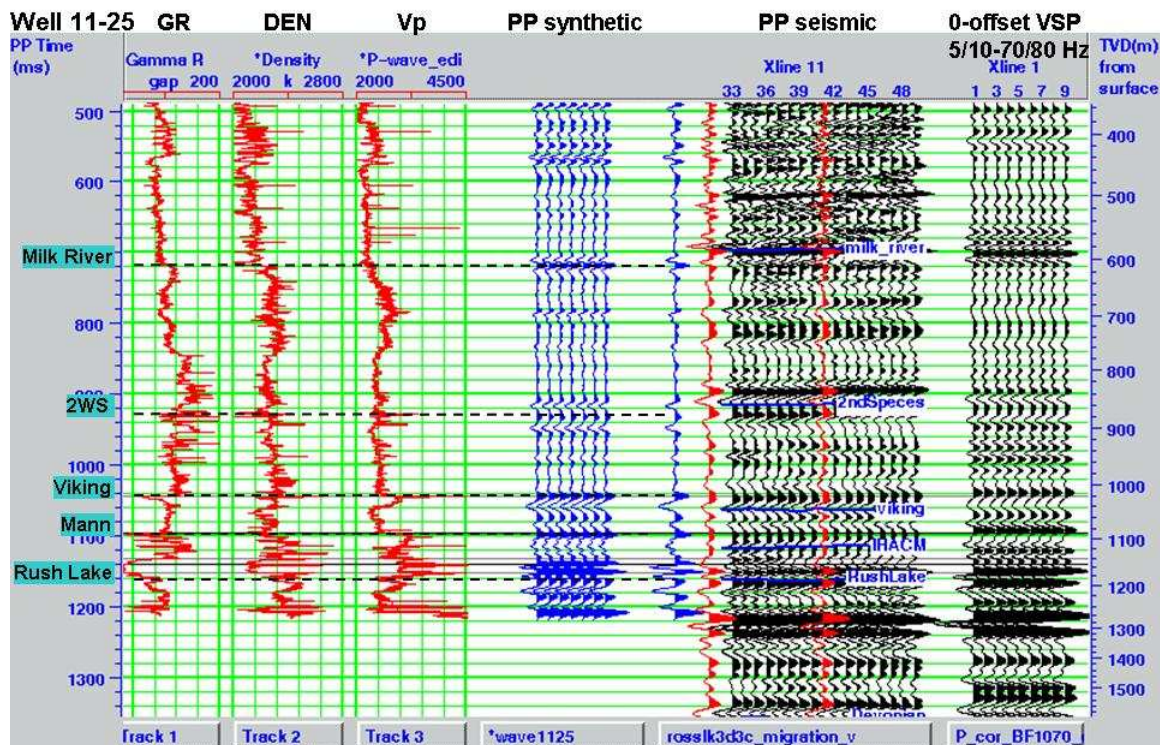


Figure 2.14 GR, density and  $V_p$  Logs, *PP* synthetic, *PP* seismic and zero-offset VSP corridor stack (a 5/10-70/80 Hz bandpass filter applied) in well 11-25. There is no stretch or squeeze applied to the synthetic seismogram.

## 2.6 *PP* seismic data interpretation

### *2.6.1 Interpreting horizons on *PP* seismic*

The quality of *P*-wave seismic data is high. There is no structure feature. All the seismic events are flat and nearly parallel with each other, partly due to the size of this 3D. There seems no obvious strata thinning or thickening. The reservoir of the channel sand is a stratigraphic play. A number of key horizons on the *PP* data volume have been interpreted by the staff of Husky, which are Milk River, 2ndSpeces, Viking, IHACM, Rush Lake, Bakken and Devonian (Figure 2.15, Figure 2.16). The zone of interest, which

is the Cantuar incised channel, is in between horizon IHACM and Rush Lake, shown as a broader trough on top of a strong peak but discontinued from surrounding events (Figure 2.17).

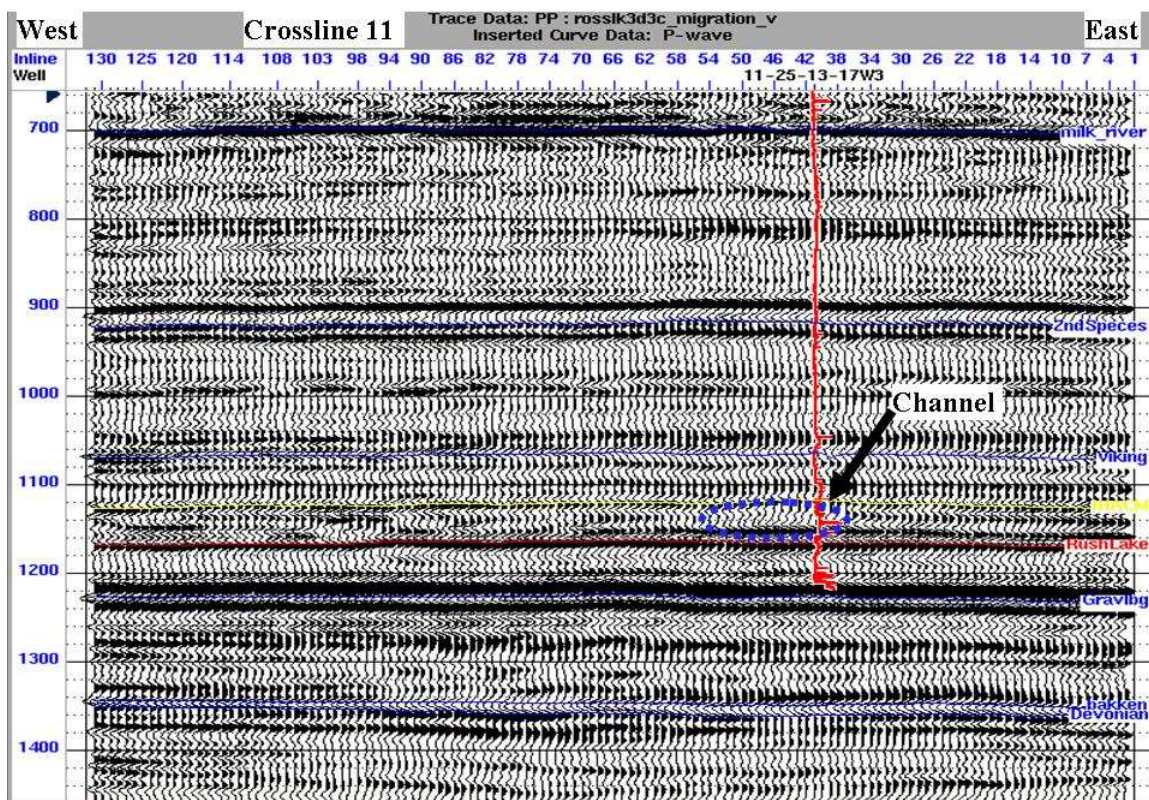


Figure 2.15 East-west xline 11 crossing well 11-25 with P-velocity curve inserted at the well location. *PP* data horizons are interpreted.

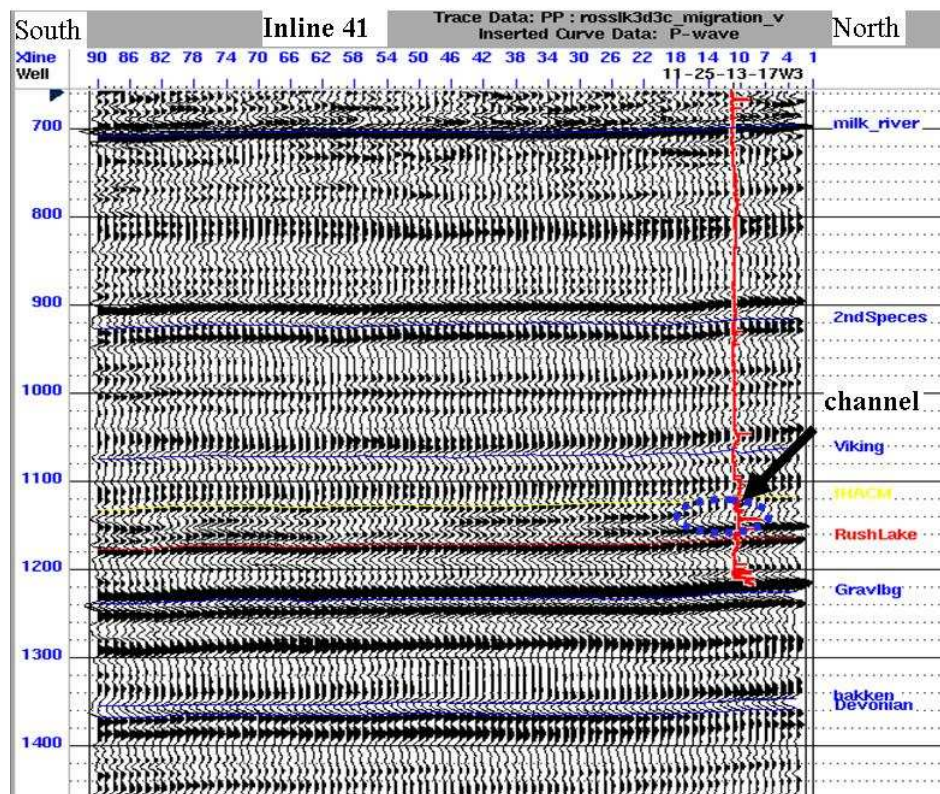
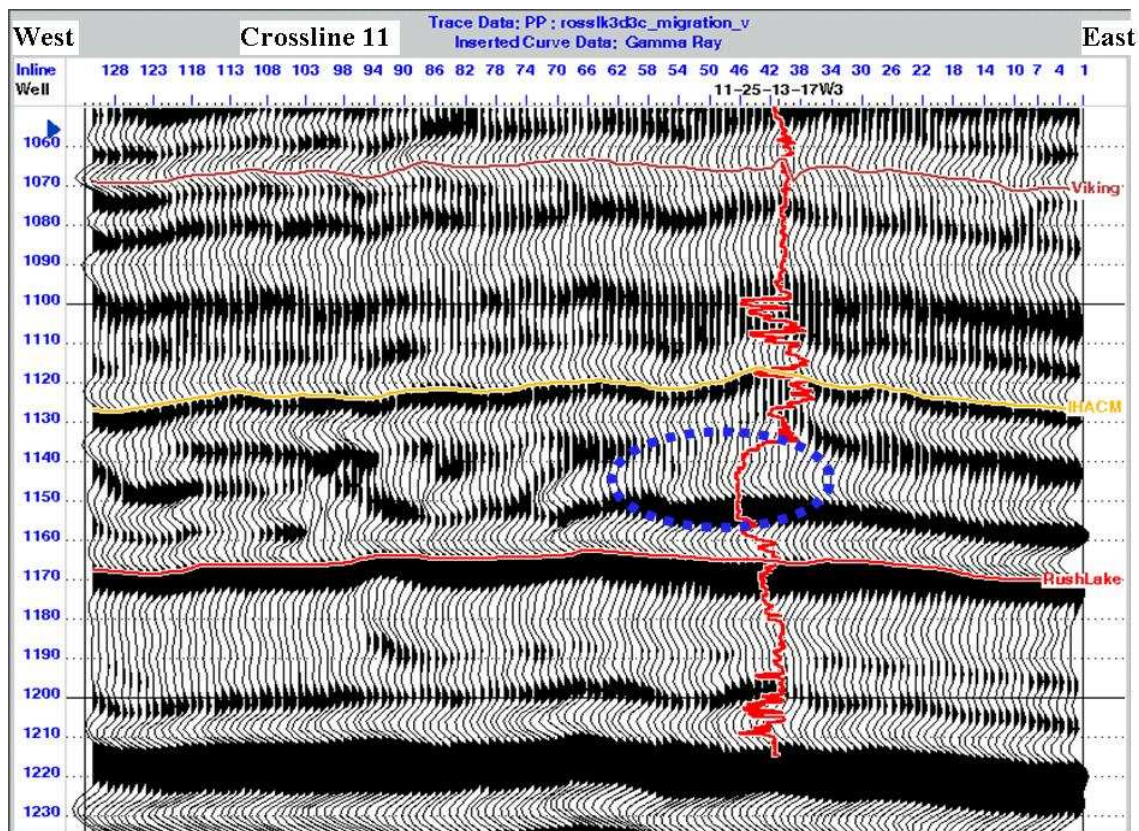


Figure 2.16 North-south inline 41 of *PP* data across well 11-25 with interpreted horizons.



**Figure 2.17** Zoom-in of the interval of interest on crossline 11 with GR log posted at the well 11-25. The blue circle indicates the reservoir sand.

The seismic feature between IHACM and Rush Lake is that (from east to west): among the two peaks starting from east, the upper peak is pulled upward and the lower peak remains similarly but stronger when get into the sand body. Continuing to the west, there are more broken events. The signatures of the reservoir sand are that there is no reflection inside and longer travel time. The pull-up/bulge on top of the channel sand may be caused by the compaction differentiation between sand and shale. The west broken seismic feature might indicate it is an abandoned channel (most likely shaly due to no pull-ups) and may cut deeper down to Rush Lake shale.

Three time slices of *PP* seismic data are shown in Figure 2.18. The slice at 1120ms shows the gentle structure at top Mannville level. The slice at 1140ms cuts the channel. The slice at 1160ms is at Rush Lake shale level and also shows the lateral variation, which might be the combination of structure and incised features.

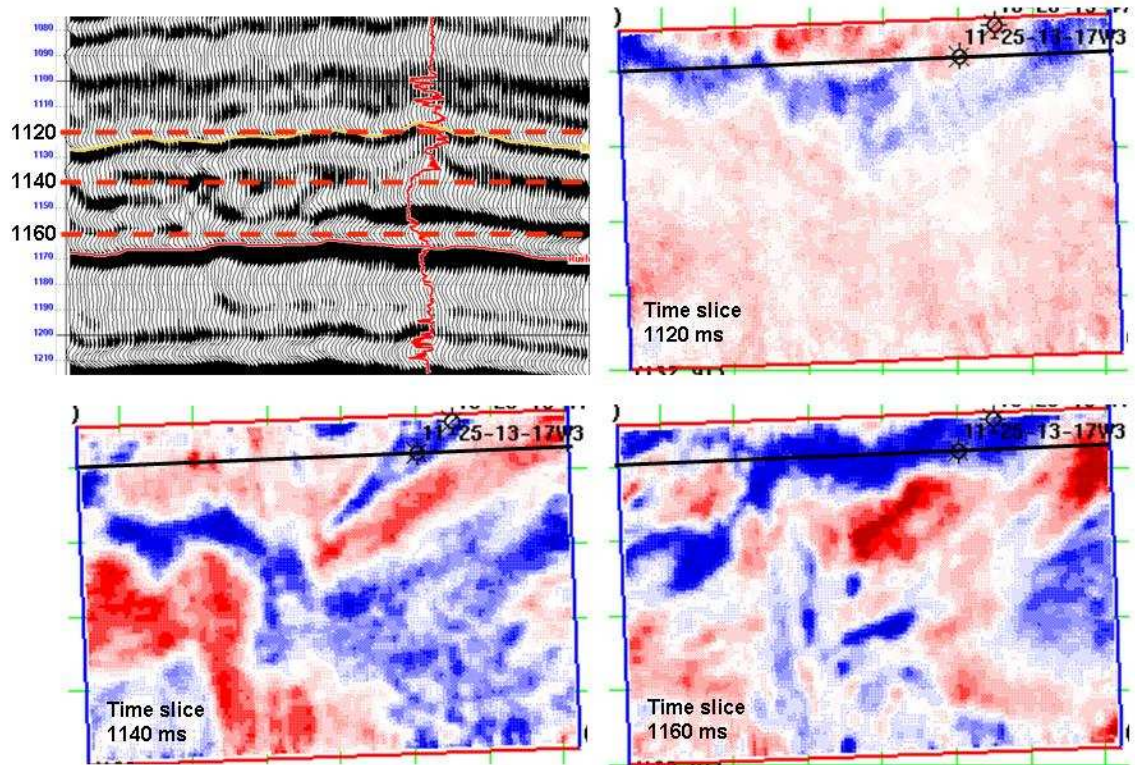


**Figure 2.18** Time slices of *PP* data: 1120 ms (top), 1140 ms (bottom left) and 1160 ms (bottom right). Red color is positive value and blue color is negative value.

### **2.6.2** *Time-structure map and time-thickness map*

The structure map for both horizon IHACM and Rush Lake are similar, showing a gentle dipping trend from northwest to southeast direction within about 30 ms amount (~ 50 m) in a distance of 3 km (Figure 2.19). The nose on IHACM map as a structure high shows the top-horizon pull-up, which indicates the shape of the sand body.

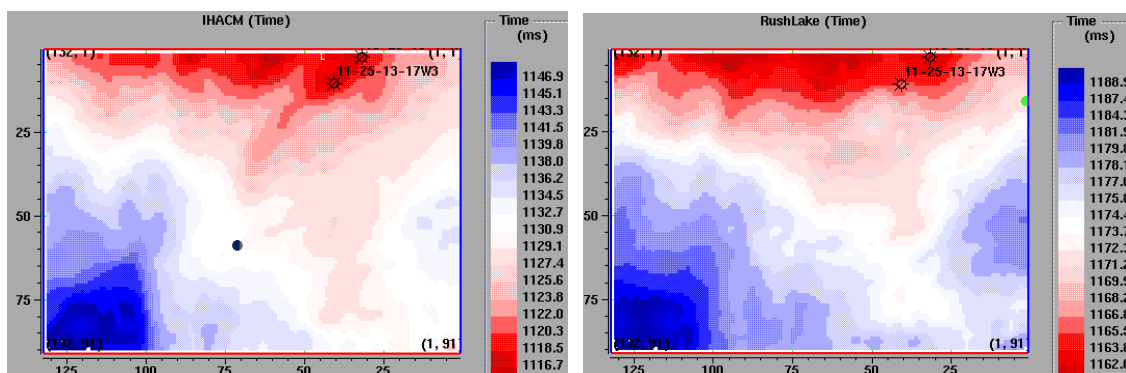


**Figure 2.19** *PP* Time structure map of horizon IHACM (left) and RushLake (right). Red color is structure high, and blue color is structure low.

From *PP* seismic data, the time thickness (isochron) map between horizon IHACM and Rush Lake clearly shows a northeast to southwest bar shape anomaly with an increased travel time (Figure 2.20). This thick anomaly is interpreted as a sand-fill channel.

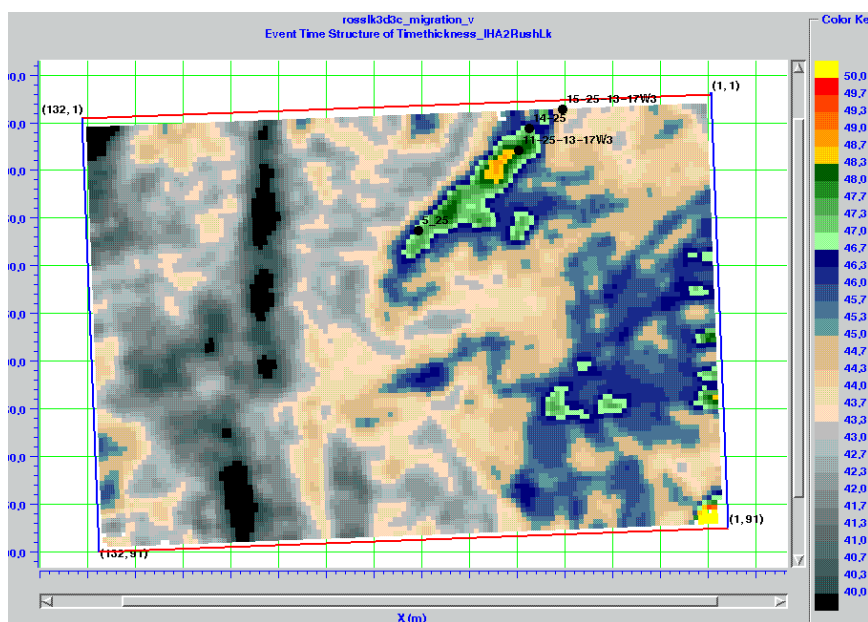


**Figure 2.20** *PP* time thickness map between the horizon of IHACM and Rush Lake with color bar. Hot color means thick, and black color means thin.

## **2.7 PS seismic data interpretation**

### ***2.7.1 Estimation of S-wave velocity***

Although there is no dipole sonic log in Ross Lake area, the zero-offset VSP in well 11-25 was conducted using two types of source: vertical vibrator (*P*-wave source) and horizontal vibrator (*S*-wave source, inline), which makes the direct measurement of  $V_s$  possible but with a larger interval compared with logging sample rate. By picking the *P*-wave and *S*-wave first-break time on the zero-offset VSP traces from 130 downhole geophones (at a 7.5 m depth interval), the interval  $V_p$  and  $V_s$  are calculated then which leads to the  $V_p/V_s$  curve. Next, we divide the *P*-velocity log by the VSP-derived  $V_p/V_s$  curve to generate a pseudo  $V_s$  log for well 11-25. This log is input to an elastic-wave synthetic seismogram package to generate the *PS* synthetic.

### ***2.7.2 PS synthetic seismogram and tie with PS seismic and PS VSP***

A *PS* wavelet is extracted from the *PS* seismic traces around well 11-25. The *PS* synthetic is generated in its native *PS* time domain, using 0 - 30 degree incident angle to stack up.

In general, there is a reasonable correlation between the *PS* synthetic and *PS* surface seismic (Figure 2.21). As often seems to be the case, however, the tie is not very obvious within the reservoir sand, especially for the *PS* data. Some stretching or further calibration of the logs may be useful.

By looking at the logs and comparing with *PP* synthetic and *PP* seismic, we find that the marker IHACM on *PS* seismic is neither a zero-crossing nor a trough, it is in between on the slope. The top of Rush Lake is a zero-crossing from positive to negative on *PS* seismic. This observation gives the guide and convention to pick horizon IHACM and Rush Lake on *PS* seismic volume.

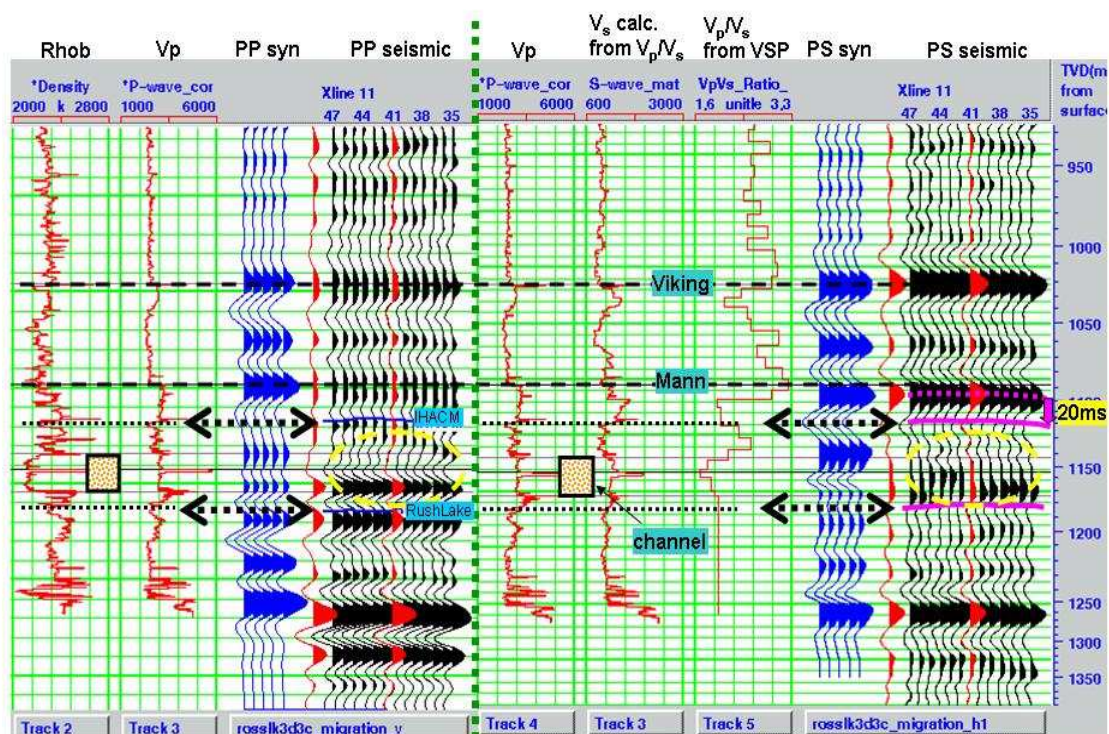


**Figure 2.21** Composite display of logs, *PP* synthetic seismograms, *PP* seismic, *PS* synthetic seismograms and *PS* seismic section for well 11-25.

### 2.7.3 *PS* time to *PP* time, a gross match

To directly compare *PS* data with *PP* data, we need a mapping from *PS* time to *PP* time. As estimated from the log and VSP data, for this flat and shallow clastic deposition, a constant  $V_p/V_s = 2.35$ , or a compressing factor of  $(1 + 2.35)/2 = 1.675$  for *PS* time is initially used here, which provides us an approximate *PS*-to-*PP* data correlation.

It's been found that an additional 125 ms time shift (upward) is also needed for the time-compressed *PS* data. This may be the result of the low *S*-wave velocities of the near(ish) surface layer giving rise to an additional static shift, or the improper *S*-wave replacement velocity being used in *PS* datuming.

In addition, this gross *PS-to-PP* time mapping using a constant  $V_p/V_s=2.35$  and 125 ms time shift (up) is assisted by comparing the 700 m offset VSP images to the *PP* and *PS* surface seismic sections in *PP* time domain (Figure 2.22). Two products result from large offset VSP: the CDP (common-depth-point) map for *PP*-wave and the CCP (common-conversion-point) map for *PS*-wave. Usually the VSP-CCP file out from processing is in *PP* time domain. A 5/10-50/60 Hz bandpass filter has been applied to VSP-CCP data and both *PP* and *PS* seismic data to reduce the frequency difference among them. The VSP-CDP data is not bandpass-filtered as its correlation with *PP* seismic data is obvious even when leaving the high frequency component there. It shows a compelling correlation among all the four datasets.

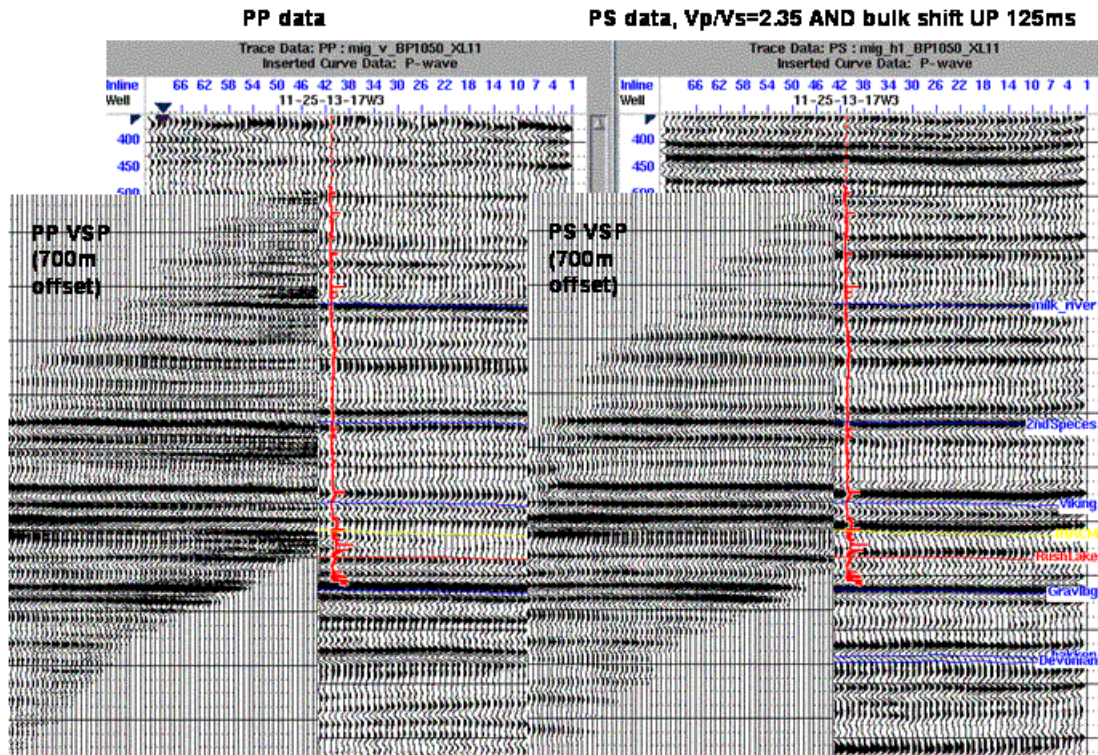


Figure 2.22 The correlation between *PP* seismic, *PS* seismic, 700m-offset *PP*-VSP and 700m-offset *PS*-VSP. All data are plotted in *PP* time. The surface seismic data and VSP-CCP data have a 5/10-50/60 Hz bandpass filter applied.

#### 2.7.4 Picking horizons on *PS* seismic data

Guided by *PS* synthetic seismogram at well 11-25 (Figure 2.21), the *PS* horizon of IHACM and Rush Lake are interpreted on *PS* seismic volume (Figure 2.23). The horizon IHACM is obtained by picking the upper nearest peak and shifting down 20 ms. To have a reference, the corresponding *PP* horizons are converted into *PS* time by  $T_{ps} = 1.675 (T_{pp} + 125)$  and displayed as red lines for cross-checking the general trend.

It's noticed that on this east-west line, the same *PP* and *PS* horizon have about 10 – 20 ms difference on the left half while they are fairly close on the right half. This may

indicate that the *PS*-wave data have slightly different solutions of refraction or long-wavelength statics than *PP*-wave data.

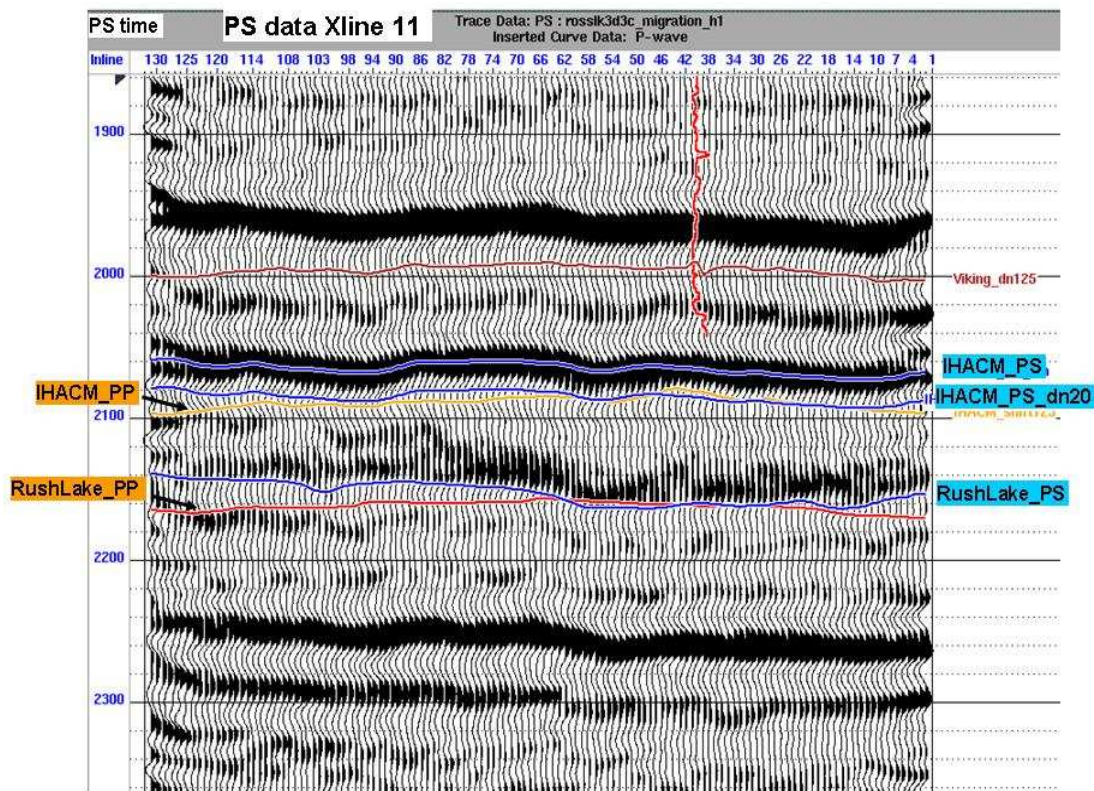


**Figure 2.23** Crossline 11 of *PS* seismic in *PS* time. The blue horizons are picked on *PS* data while the red horizons are the same horizons on *PP* data but converted in *PS* time using the constant  $V_p/V_s=2.35$  and a bulk shift of 125 ms.

### 2.7.5 *PS* time-structure map and time-thickness map

The structure maps in *PS* time for horizon IHACM and Rush Lake are shown in Figure 2.24. Compared with structure maps in *PP* time for same horizons (Figure 2.19), they show the similar northeast to southwest dipping trend in general, but the upper left corner becomes a relative high.

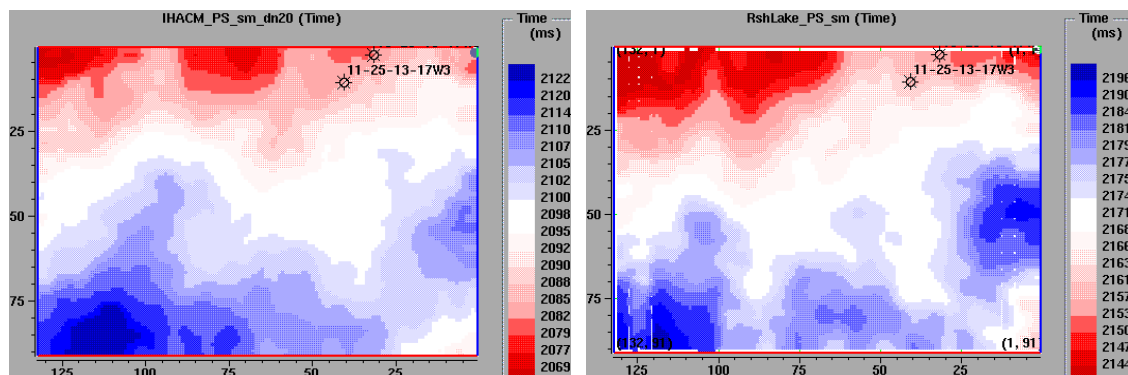


**Figure 2.24** *PS* time structure map of horizon IHACM (left) and RushLake (right). Red color is structure high, and blue color is structure low.

Similar to the *PP* data, the *PS* time-thickness (isochron) map between the IHACM and Rush Lake is calculated (Figure 2.25). Compared with the *PP* map (Figure 2.20), the *PS* isochron map has a larger time variation: 60 – 84 ms (40% change) versus 40 – 50 ms (25% change).

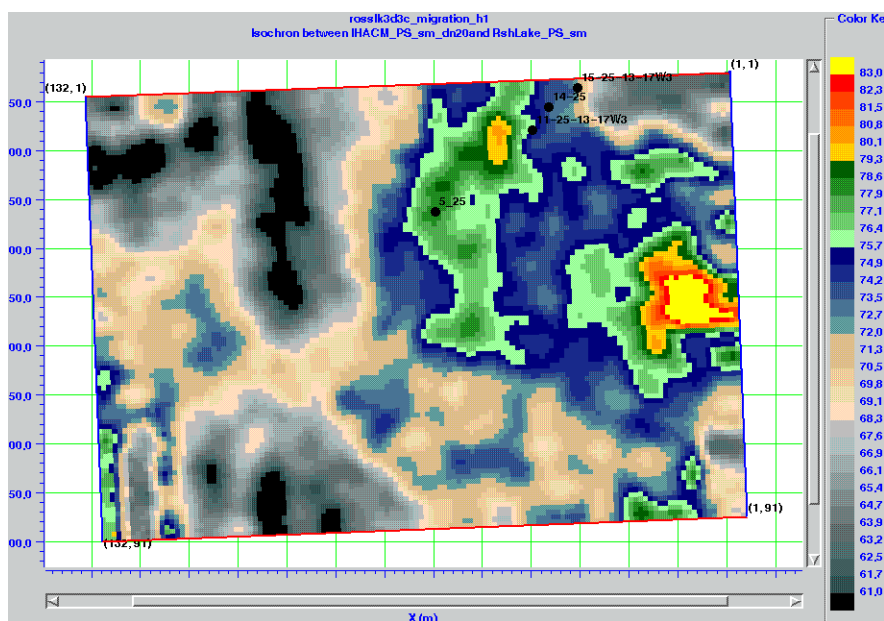


**Figure 2.25** *PS* time-thickness map between the horizon IHACM and Rush Lake with color bar. Hot color means thick, and black color means thin. Note thicker interval but higher  $V_s$  are fighting each other respecting the travelttime.

## 2.8 $V_p/V_s$ map and lithology interpretation

We use the standard *PP* and *PS* time-ratio method (Equation 2.4) to create the average interval  $V_p/V_s$  map between the IHACM and Rush Lake horizons (Figure 2.26).

$$\frac{V_p}{V_s} = \frac{2\Delta T_{ps}}{\Delta T_{pp}} - 1, \quad (2.4)$$

where  $\Delta T_{pp}$  and  $\Delta T_{ps}$  are the time-thickness (isochron) between two horizons for *PP* and *PS* data, respectively.

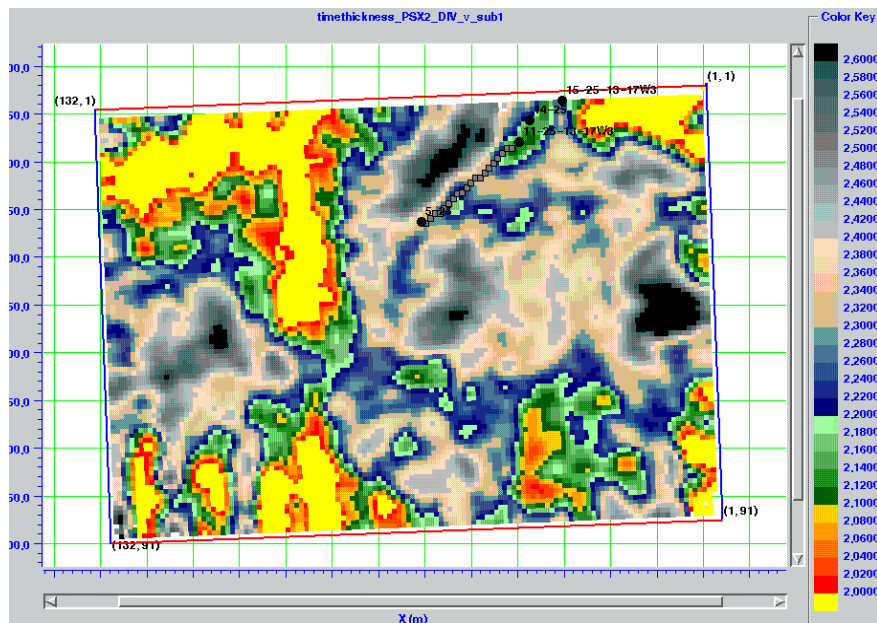


**Figure 2.26  $V_p/V_s$  map between the horizon IHACM and Rush Lake. Hot color is low  $V_p/V_s$  and black color represents high value. The yellow and green colors are interpreted as sands while the black and grey as shale or shaly sands.**

From Figure 2.26, we observe a low  $V_p/V_s$  anomaly, trending to the northeast (in the upper central area), that corresponds to the structural thick anomaly indicated on the *PP* time thickness map (Figure 2.20). This anomaly (previously interpreted as the reservoir sand body) with  $V_p/V_s$  about 2.15 ~ 2.25 is divided into two parts by a horizontal stripe with  $V_p/V_s$  about 2.3 ~ 2.4. This higher  $V_p/V_s$  value is interpreted as a shale cut or shaly-sand. The interpreted sand appears to also have an eastern extension.

A low  $V_p/V_s$  value (1.7 ~ 2.0, bright yellow color) with a north-south trend at the left half and upper right corners may be thick, tight sands or possibly other incised features not belonging to the Dimmock Creek Member. Four blackish areas with high  $V_p/V_s$  value ( $> 2.4$ ) are interpreted to be shale or shaly.

In summary, for this high-porosity, high-permeability sand play saturated with heavy oil, the hydrocarbon accumulation is correlated with: (a) large  $PP$  time thickness and (b) a middle range  $V_p/V_s$  value of about 2.15 ~ 2.25.

Considering reading errors, for example,  $\pm 2\%$  for  $PP$  data isochron and  $\pm 4\%$  for  $PS$  data isochron, the error for  $V_p/V_s$  is no greater than  $\pm 6\%$  (Figure 2.27). For  $V_p/V_s=2$ , 6% error means that  $V_p/V_s$  could range from 1.88 to 2.12. Although the absolute value has a range, the spatial trend would be same.

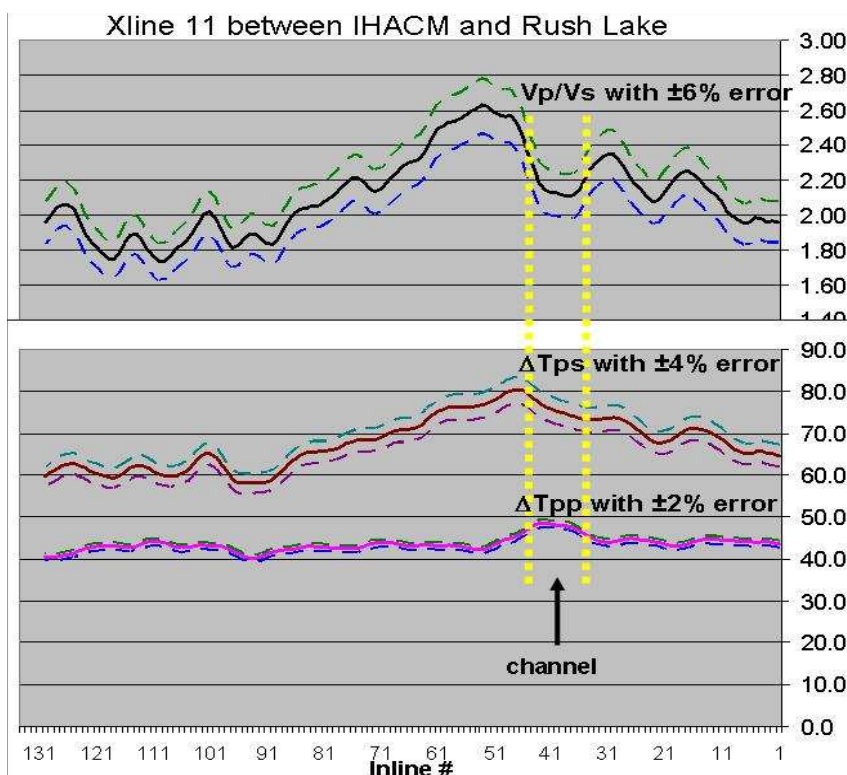


Figure 2.27 Xline 11 error analysis.  $\Delta T_{pp}$  and  $\Delta T_{ps}$  are the isochrons in ms between IHACM and Rush Lake with  $\pm 2\%$  and  $\pm 4\%$  error, respectively.  $\pm 6\%$  error for  $V_p/V_s$ .

## 2.9 The horizontal well result

Husky drilled a horizontal well 5-25-13-17W3 in August 2002, based on the *PP* time-thickness anomaly. This well has a 600 m horizontal reach and stays within the Dimmock Creek Member sand (Figure 2.28). We compared our traveltime-based  $V_p/V_s$  map (Figure 2.29, created before we had any drilling results) to the actual drilling results (as indicated by the gamma ray log).

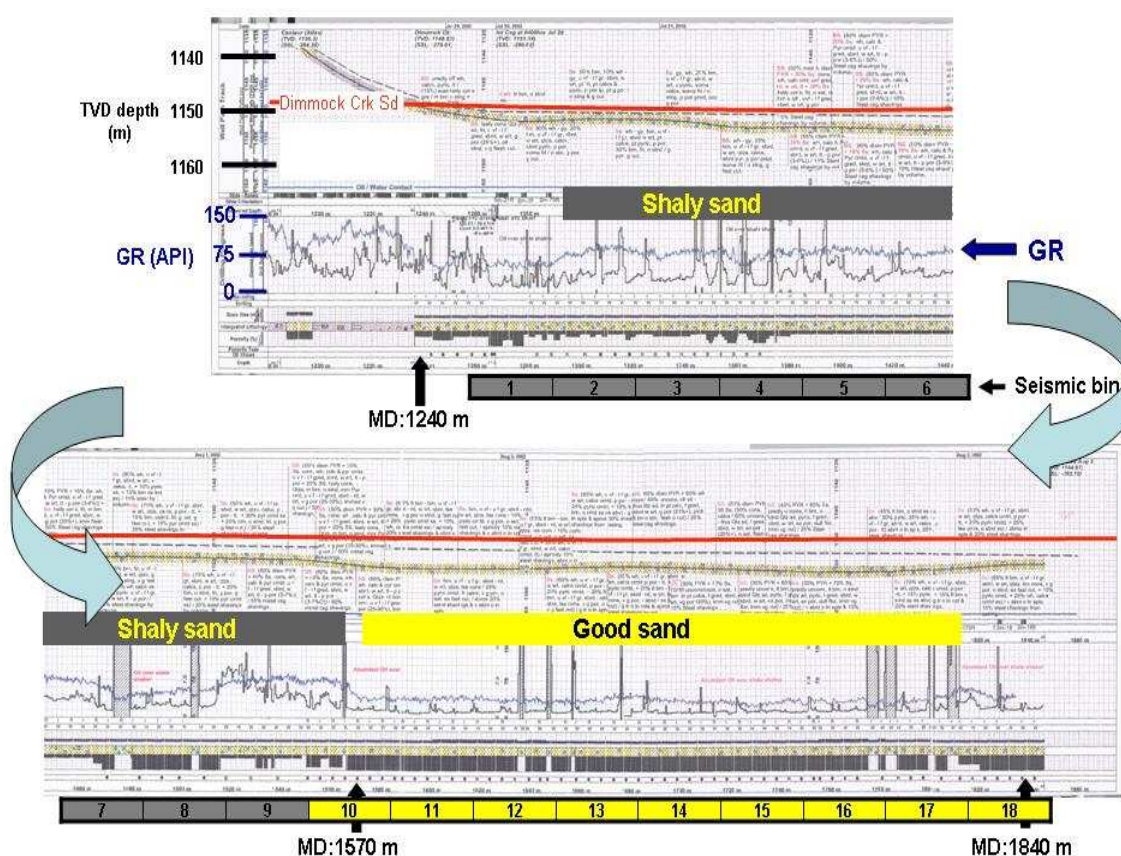
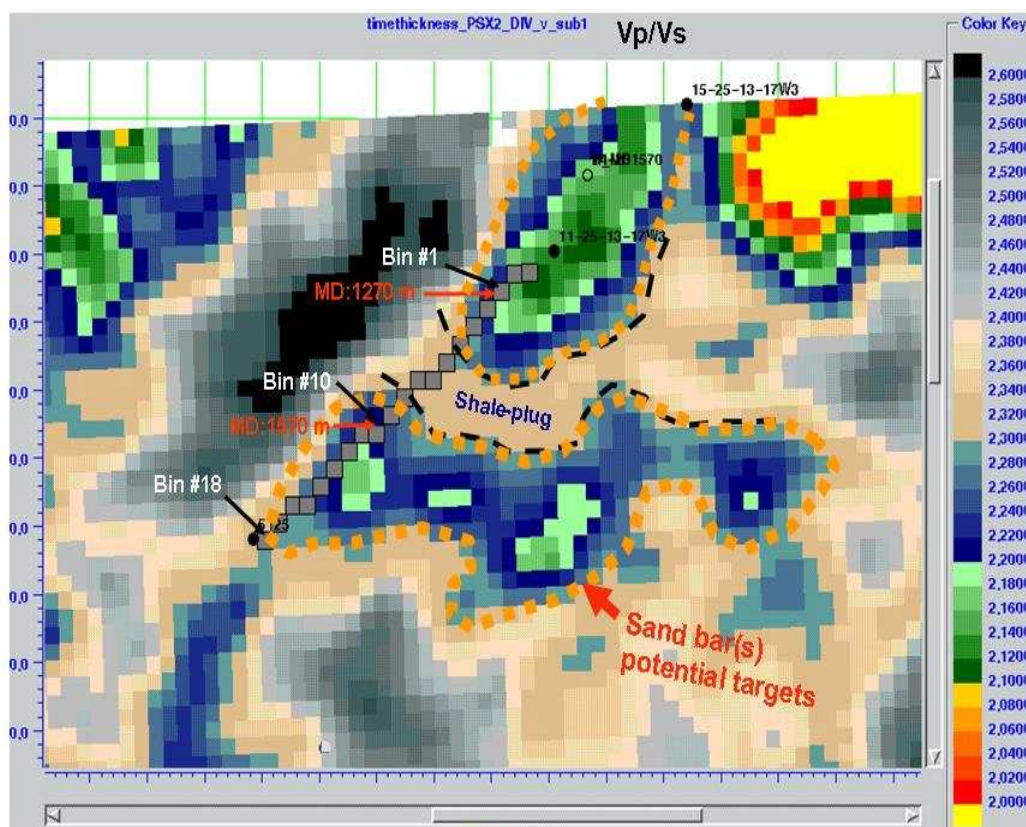


Figure 2.28 The “striplog” of the horizontal well 5-25 with GR log showing the sand. Seismic bins along the trajectory of the horizontal portion of the well are schematically illustrated.



**Figure 2.29** Seismic  $V_p/V_s$  map with trace bins containing the trajectory of the horizontal well (small squares filled by grey color). Hot color is low  $V_p/V_s$  (sandy) and black color is high  $V_p/V_s$  (Shaly).

One way to compare the GR value from log with  $V_p/V_s$  from seismic is to do a local normalization, just to highlight the relative change and trend regardless the absolute value and unit. Equations (2.5) and (2.6) show this calculation. The results are shown in Table 2.4. Figure 2.30 displays the normalized variation of the gamma ray log (a shaliness indicator) and our  $V_p/V_s$  value along the well's trajectory. The  $V_p/V_s$  map predicted a shaly interval that was indeed encountered in the well. This suggests that the  $V_p/V_s$  maps could have been useful in the drilling design and economic predictions.

$$GR_{norm} = \frac{GR - GR_{min}}{GR_{max} - GR_{min}} \quad (2.5)$$

$$V_p / V_{s \text{ norm}} = \frac{V_p / V_s - V_p / V_{s \text{ min}}}{V_p / V_{s \text{ max}} - V_p / V_{s \text{ min}}} \quad (2.6)$$

Seismic Bin #	Inline	Xline	Seismic Vp/Vs	MD in well (m)	GR (API)	Normalized GR	Normalized Vp/Vs
1	44	12	2.15	1270	65	0.58	0
2	45	13	2.18	1300	60	0.50	0.17
3	46	14	2.23	1335	90	1.00	0.46
4	47	15	2.27	1370	75	0.75	0.71
5	48	16	2.29	1400	70	0.67	0.84
6	49	17	2.30	1435	85	0.92	0.88
7	50	18	2.32	1470	75	0.75	1.00
8	51	18	2.32	1500	60	0.50	1.00
9	52	19	2.28	1532	60	0.50	0.76
10	53	20	2.24	1570	75	0.75	0.54
11	54	21	2.21	1600	45	0.25	0.35
12	55	21	2.20	1635	45	0.25	0.29
13	56	22	2.20	1670	37	0.12	0.29
14	57	23	2.22	1700	36	0.10	0.37
15	58	24	2.25	1732	37	0.12	0.55
16	59	25	2.27	1765	30	0	0.68
17	60	25	2.28	1800	32	0.03	0.78
18	61	26	2.30	1830	40	0.12	0.86

**Table 2.4 Average GR value of the horizontal portion of well 5-25 in each projected seismic bin and the seismic  $V_p/V_s$  in the same bin.**

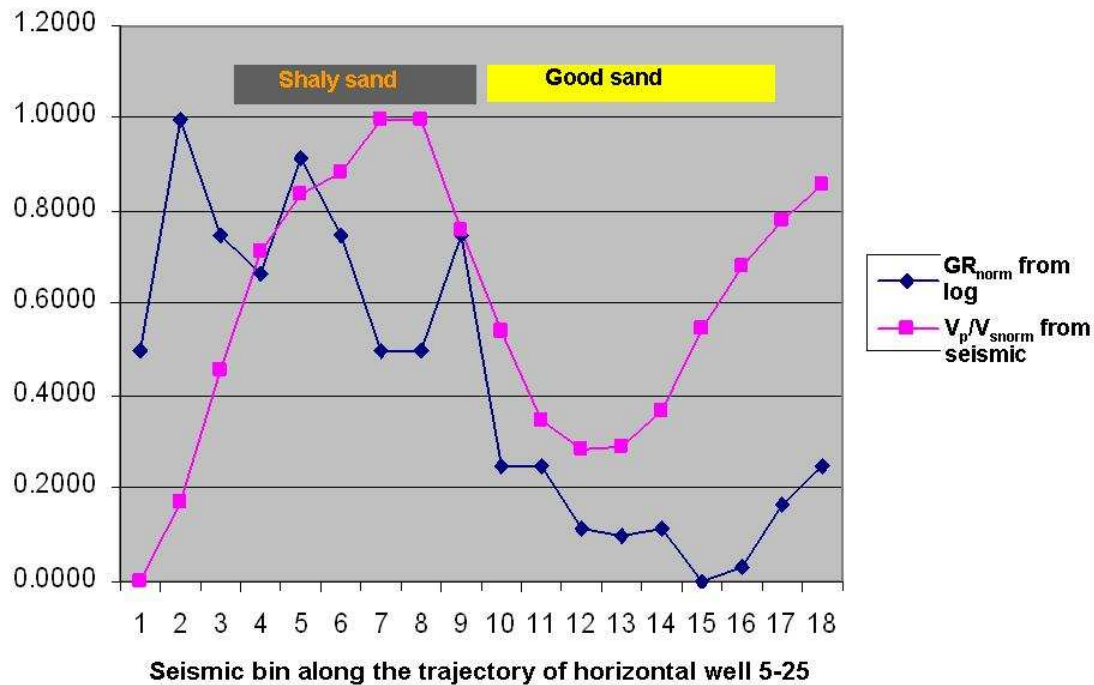


**Figure 2.30** Comparison of the normalized average GR from the horizontal well 5-25 in the well trajectory passed seismic bins and seismic traveltime derived  $V_p/V_s$  in the same bins.

## 2.10 Conclusion

A 3C-3D seismic dataset over the Ross Lake oilfield in south-western Saskatchewan has been analysed. We find a reasonable correlation among the logs, synthetic seismograms, VSP, and surface seismic volumes. *P*-wave source and *S*-wave source zero-offset VSPs provide an interval  $V_p/V_s$  curve in the well 11-25 which, in turn, helps estimate a pseudo shear-velocity log. The *PS* synthetic seismogram increases the confidence of *PS* seismic event identification and provides an essential guide to pick *PS* horizons. The far-offset VSP-CCP map helps to identify the events on the *PS* seismic section and is another bridge in correlating *PP* and *PS* seismic data.

On the *PP* time-thickness map, the target sand body clearly stands out as a thick anomaly. Combining the *PP* and *PS* horizon time-thickness maps provides a  $V_p/V_s$  map between the IHACM and Rush Lake horizons. Relatively low  $V_p/V_s$  values are interpreted as a sand indicator. A break in low  $V_p/V_s$  values suggests that there is a shale-cut or shaly part within the target sand body. This interpretation is supported by the gamma ray log from the horizontal well. Other anomalies from the  $V_p/V_s$  map also suggest further drilling targets.

## Chapter Three: Inversion of Ross Lake *PP* and *PS* data -- Poststack

### 3.1 Introduction

Inversion, in the seismic sense, is a transform from the observed wave propagation to the underlying Earth's physical properties. Under the assumption that seismic trace can be modelled using a wavelet convolve with vertical incidence reflection coefficient, the post-stack inversion is a robust process to extract the acoustic impedance information from stacked seismic data (Russell and Hampson, 1991).

Stewart and Bland (1997) find that in a small incidence angle the *PS* reflectivity and pure-shear reflectivity can be related as

$$R_{PS}(\theta) \approx 4 \frac{\beta}{\alpha} \sin(\theta) R_{SS}(0) \quad , \quad (3.1)$$

where  $\theta$  is the incidence angle,  $\alpha$  is *P*-wave velocity and  $\beta$  is *S*-wave velocity. This relationship can be used with *PS* seismic data to infer the zero-offset *S*-wave reflectivity.

To accomplish the post-stack *PS* data inversion, we make the simplifying and quite approximate assumption that the *PS* reflectivity is linearly proportional to the *SS* reflectivity. In reality, the relationship is more complicated and is dependent on the trace offsets comprising the stacked *PS* seismogram as well as the time-dependent incidence angle. Nonetheless, relative changes in the *PS* reflectivity over a small depth interval may be highlighted by the inversion procedure.

In Chapter two, both *PP*- and *PS*-wave volume of the Ross Lake 3C-3D seismic data have been interpreted by correlating the synthetic seismograms, VSPs with surface seismic data. *PP* and *PS* horizons are also properly registered.

In this chapter, the post-stack migrated *PP* and *PS* seismic volumes will be inverted into *P*-impedance and *S*-impedance individually. Then, a  $V_p/V_s$  value/map is obtained by combining the  $I_p$  and  $I_s$  around the reservoir interval, and compared with the  $V_p/V_s$  map derived from the *PP* and *PS* traveltimes in Chapter two.

Hampson-Russell Software's inversion package STRATA, which is generalized linear single trace inversion, is used to conduct the post-stack *PP*- and *PS*-wave impedance inversion.

A zoom-in look of the logs in well 11-25 is shown in Figure 3.1. An approximate 4 m thick possible pyrite cemented layer (in this well) divides the Cantuar channel in two parts: the ~12 m thick upper channel is more shaly and fining upward indicated by the increase of GR, increase of density, and decrease of porosity upward; the 15 m thick lower channel has much cleaner sand indicated by a blocky low GR value (about 25 API), low density (about 2.12 g/cc) and high porosity (about 30%). The upper channel is the net pay while the lower channel is wet. As mentioned before, the pyrite cemented layer is varying in thickness (absence in well 15-25) in different wells, and seems not a consistent layer in a large areal extent, which indicates it is unlikely a reflector on seismic section.

As mentioned in Chapter two, there is no  $V_s$  log available in this 3C-3D seismic covered area. However, in well 11-25, the zero-offset VSP has both vertical (*P*-wave) source and horizontal (*S*-wave) source. The shear wave information at each downhole

geophone level is directly measured. By picking the first arrivals on recorded  $P$ -wave and  $S$ -wave train from each level, the interval  $V_p/V_s$  is determined, and then used to derive the  $V_s$  log from the  $V_p$  log. The reservoir sand shows  $V_p/V_s$  about 1.8. Below the bottom of the lower channel at 1175 m, the  $V_p/V_s$  is set to 2.0 and extended to TD due to no VSP geophone below it.

The table 3.1 lists the reservoir properties including  $V_p$  and derived  $V_s$  of channel sand, the shale above, and the Rush Lake shale below. Treating the upper and lower channel sands as one unit, in general, the sand has nearly same  $P$ -impedance as the shale above, and lower  $P$ -impedance than Rush Lake shale below. The  $S$ -impedance of the sand is a little higher than the shale above but slightly lower than the shale below.

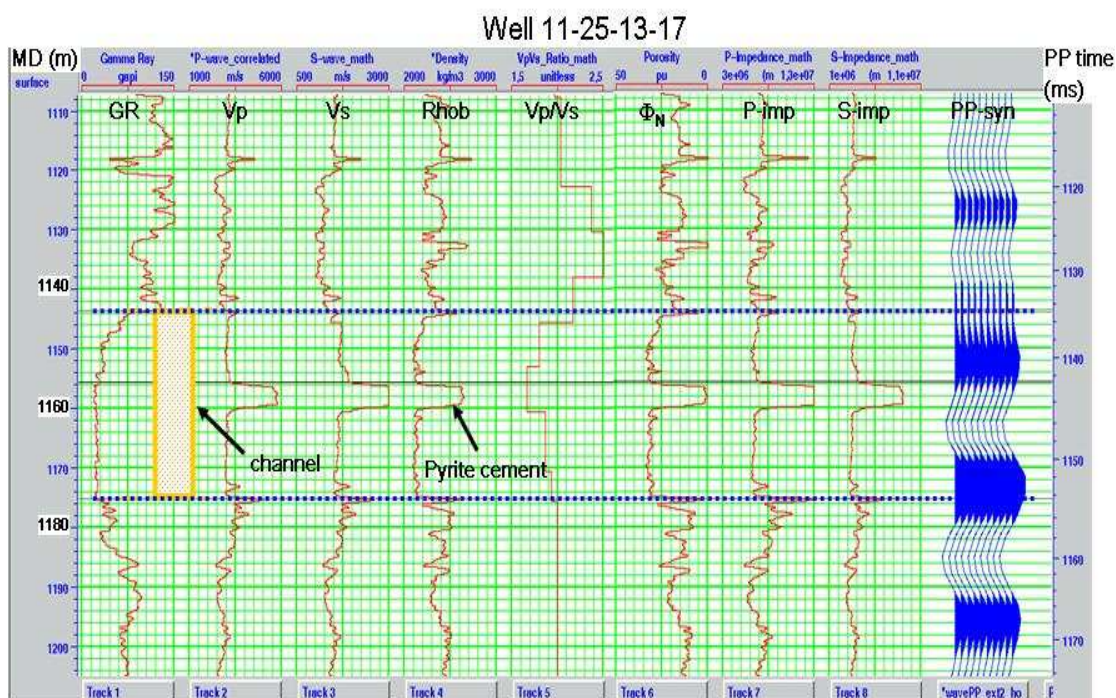


**Figure 3.1** Logs in well 11-25. The  $V_p/V_s$  is derived from zero-offset  $P$ -source and  $S$ -source VSP. The  $V_s$  is calculated from the measured  $V_p$  and VSP-derived  $V_p/V_s$ .

Well 11-25	GR (API)	$V_p$ (m/s)	$V_s$ (m/s)	Rhob (g/cc)	Phi (%)	$V_p/V_s$	$I_p$ (m.g/s.cm <sup>3</sup> )	$I_s$ (m.g/s.cm <sup>3</sup> )
Shale (above)	110	2700	1180	2.35	22	2.30	6350	2770
Upper sand	40	3100	1720	2.20	30	1.80	6820	3780
Lower Sand	25	3000	1620	2.12	32	1.85	6360	3430
Rush Lake Shale	55	3500	1750	2.45	15	2.00	8580	4290

**Table 3.1 Summary of rock properties of the channel sand and shales around.  $V_s$  is calculated from measured  $V_p$  and VSP-derived  $V_p/V_s$ .**

### **3.2 Acoustic impedance inversion of PP data**

#### ***3.2.1 The initial P-impedance model***

An initial  $P$ -impedance model is required to be the starting point. As usual, the model is made by extending the  $P$ -impedance from well log of a well or a few wells to the entire 3D seismic covered area, spatially constrained by seismic horizons. In this case, out of 3 vertical wells, only the well 11-25 is relatively away from the edge of the 3D. Therefore, constrained by four seismic horizons Viking, IHACM, Rush Lake and Gravelbourg, the  $P$ -impedance curve in well 11-25 is spatially interpolated to build the  $P$ -impedance model. The upper limit for the model is 100 ms above horizon Viking. The lower limit is 100 ms below horizon Gravelbourg. Then, a 20 Hz low-pass filter is applied to make a smoothed initial  $P$ -impedance model (Figure 3.2).

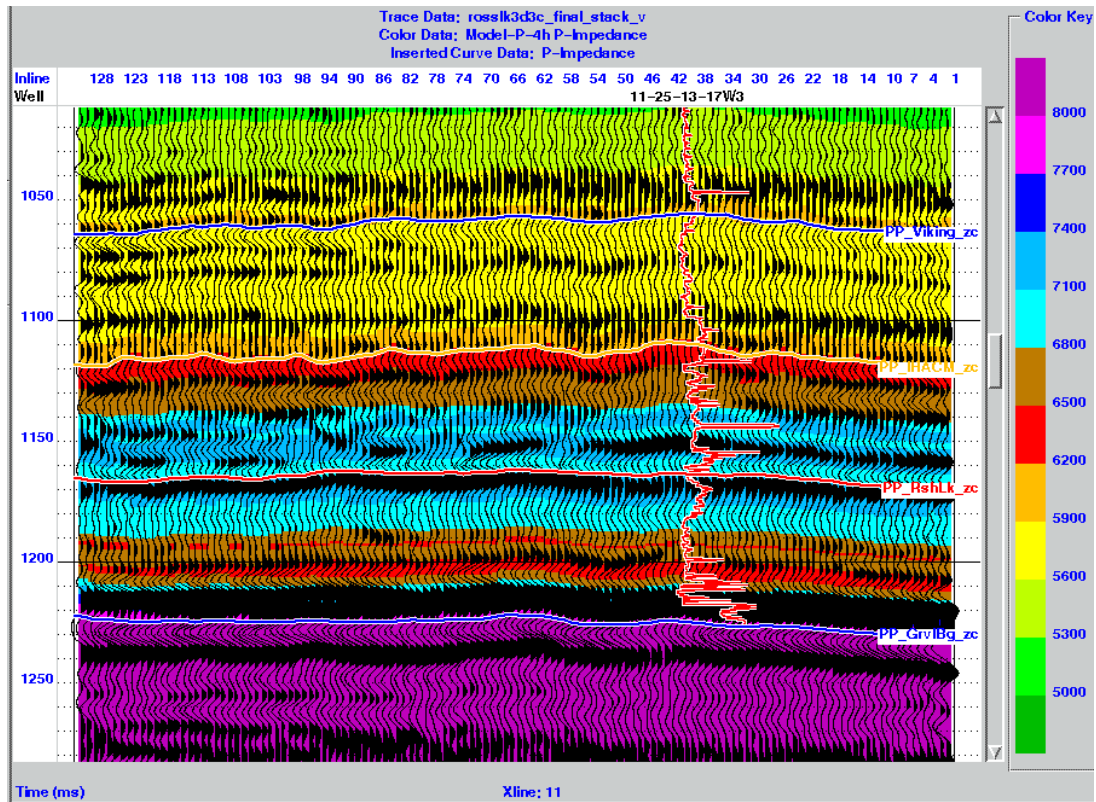


**Figure 3.2** Crossline 11 of the *PP*-wave data (wiggles traces) with the smoothed initial *P*-impedance model (color background). The *P*-impedance log of well 11-25 is inserted at the well location.

### 3.2.2 *P*-wave Wavelet

The wavelet for *P*-wave data inversion is extracted in the time window of 1000 – 1300 ms from the *PP* seismic volume excluding the edge traces.

### 3.2.3 Inversion and the result

A model-based inversion is performed to invert the *PP* seismic traces into *P*-impedance. The result of the east-west crossline 11 is shown in Figure 3.3. Although the initial model has the smoothed low-frequency trend, the final result has a lot more higher frequency contents derived from the seismic traces themselves. Also, the formation boundaries are much sharper in the impedance section compared with the raw seismic section. For instance, the top of Viking is a nice impedance contrast at about 1070 ms from high impedance ( $\sim 6200 \text{ m.g/s.cm}^3$ ) to lower impedance ( $\sim 5600 \text{ m.g/s.cm}^3$ ), indicating the unconformity; the top of Gravelbourg limestone has a very acute contact at about 1220 ms with the above Rush Lake shale.

Zoom-in the reservoir formation around the well 11-25 is shown in Figure 3.4. The channel sand is very well imaged on the P-wave inversion as a low impedance anomaly capsuled in the surrounding shales, flat bottom. The seismic enlarge or amplify the acoustic contrast between the porous channel sand with the surrounding shale, which is not that obvious on the impedance log.

Within the channel sand, the pyrite layer separates the sand into upper and lower parts. The lower sand looks to have larger lateral extension with lower impedance, which corresponding to higher production. The upper sand has slightly higher impedance and smaller lateral extension,

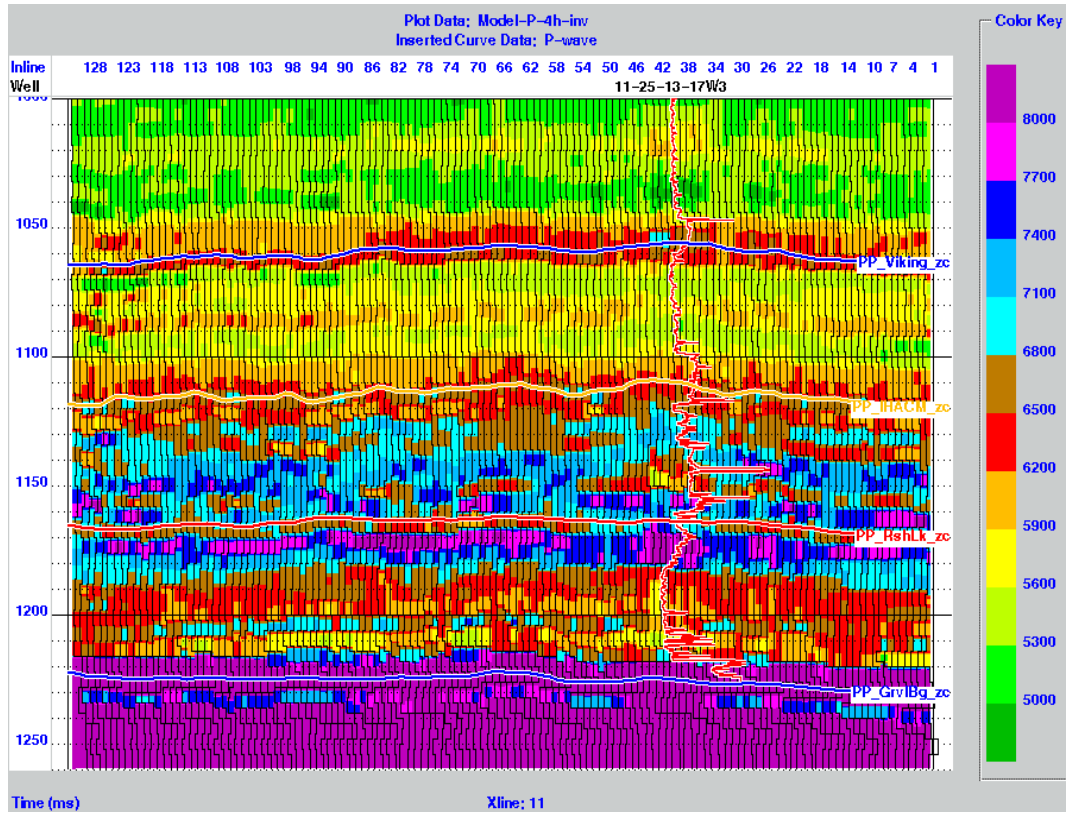


**Figure 3.3 Results of the model-based  $P$ -impedance inversion of crossline 11. Purple color is high impedance and green color is low impedance.**

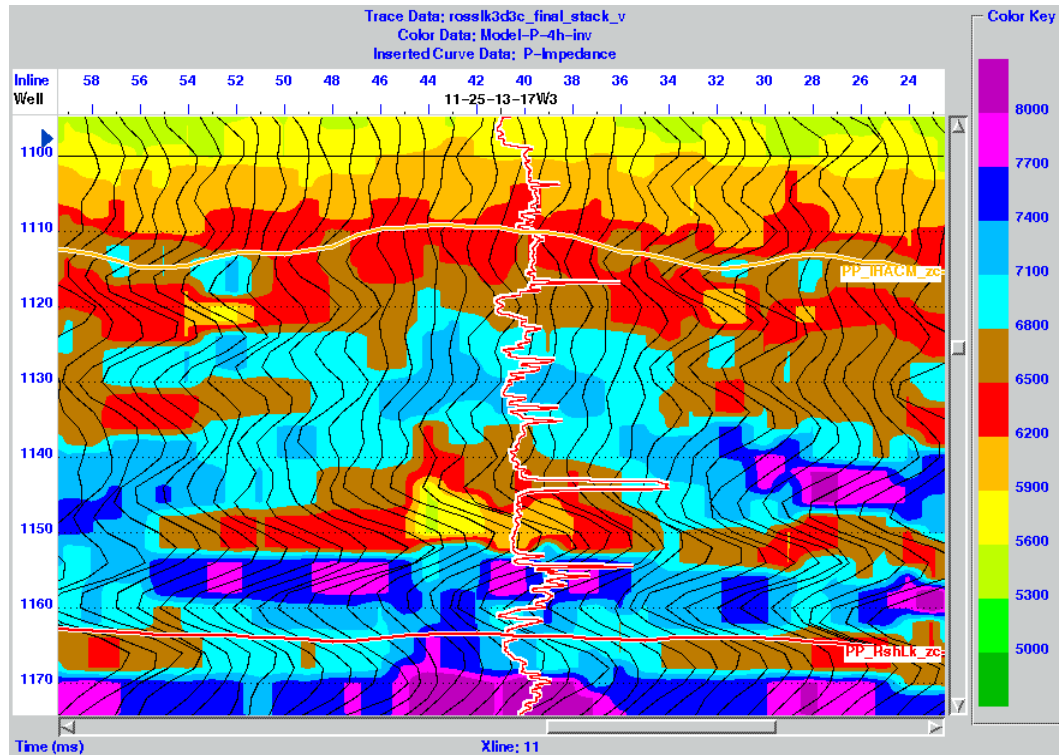


**Figure 3.4 Zoom-in of the inverted  $P$ -impedance (color). Yellow color is low impedance, and blue color is high impedance. Wiggles traces are  $PP$  data.  $P$ -impedance log is inserted at the well location. Notice the channel sand is a low impedance block surrounded by higher impedance shale.**

Horizon slices are also checked to observe the spatial trends. The Rush Lake horizon is the reference. Figure 3.5 shows the inverted  $P$ -impedance map of the Rush Lake horizon moving up 10ms, 14ms, 18ms and 22ms, respectively. The (a) and (b) show the lower channel, and (c), (d) show the upper channel. In the middle-left area on the impedance maps there is a north-south trend oblique to the channel sand. It's been interpreted as an old shale-plugged channel and acts as a lateral seal to the Ross Lake pool.

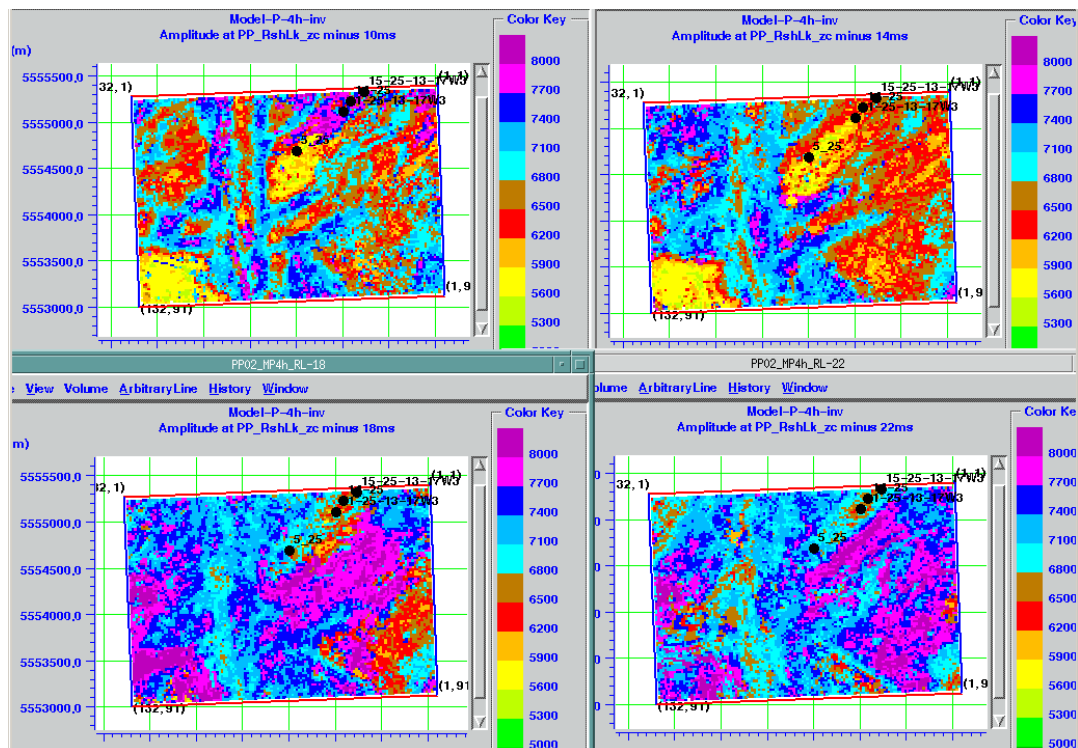
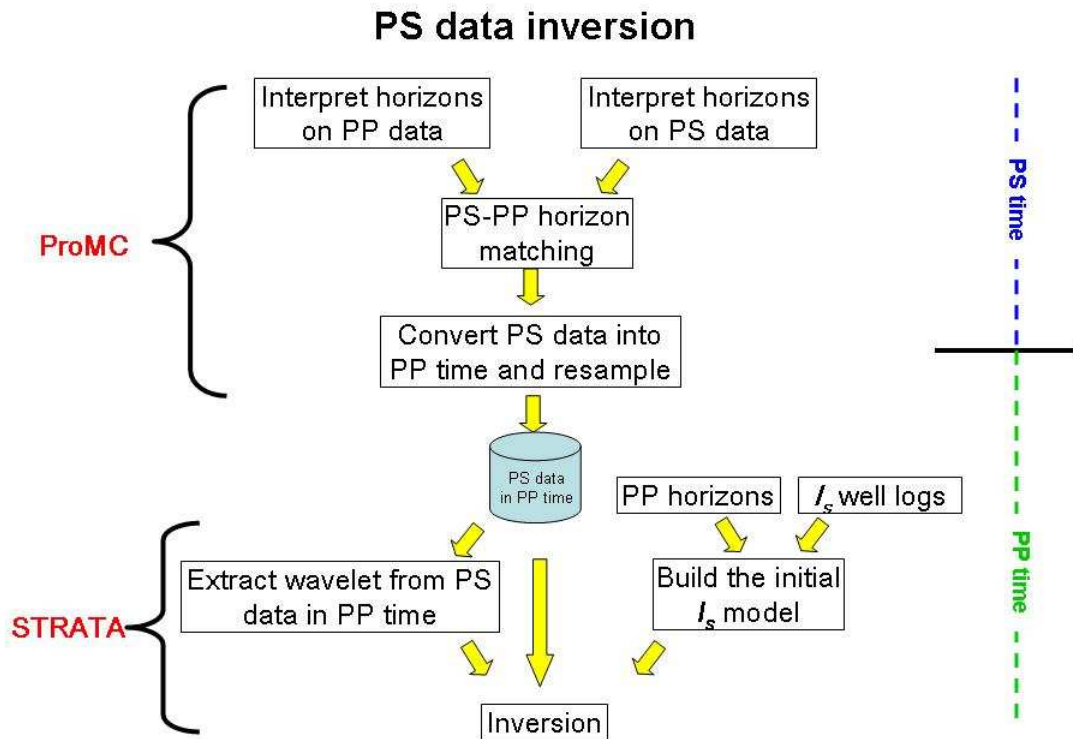


Figure 3.5 *P*-impedance horizon slices based on Rush Lake horizon: up 10ms (upper-left), up 14ms (upper-right), up 18ms (lower-left) and up 22ms (lower-right).

### 3.3 Acoustic impedance inversion of *PS* data

#### *3.3.1 Work flow*



**Figure 3.6 The flow chart of PS-wave seismic impedance inversion.**

### 3.3.2 PS to PP horizon matching

Registering *PS* and *PP* events has been done in Chapter two using Hampson-Russell's multi-component seismic data interpretation package, ProMC. The event correlation between *PP*- and *PS*-wave seismic data are guided and assisted by tying the synthetic seismograms from well to surface seismic data (Figure 3.7).

Horizon Viking, IHACM, Rush Lake and Gravelbourg are picked on *PS* seismic data.

In chapter two, the IHACM was picked as a “-to+” zero-crossing above a small peak on *PP* seismic. On *PS* seismic, due to the lack of a consistent feature to pick, the strong peak above the reservoir sand was picked and bulk-shifted 20 ms down to serve as the IHACM. A slight difference in this chapter, IHACM is picked as a “+to-” zero-crossing on *PP* seismic and also a “+to-” zero-crossing below the strong peak on *PS* seismic (Figure 3.8).

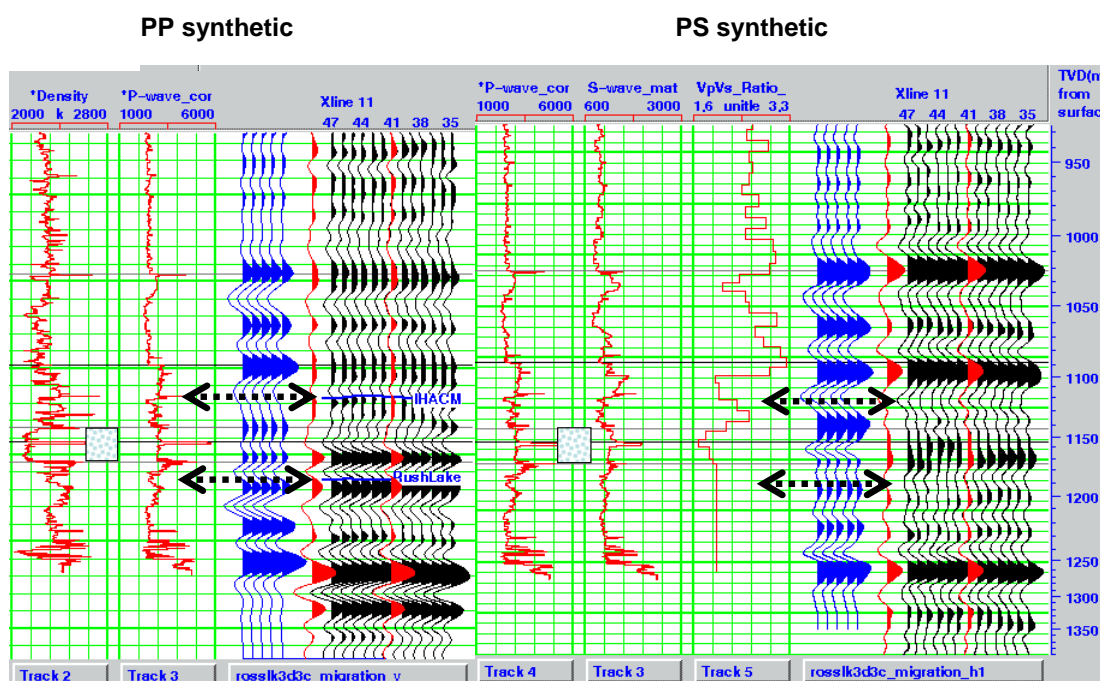


**Figure 3.7** A composite display of well logs, *PP* and *PS* synthetic seismograms, *PP* and *PS* seismic traces for well 11-25.

In the process of horizon matching, all the four *PS* horizons are forced to put at the *PP* time of the same horizons. In turn, the amount of squeeze of *PS* time at each CDP is used to calculate the interval  $V_p/V_s$  between the two horizons (Figure 3.8). Notice the lateral change of the background color, which is  $V_p/V_s$ , on the *PS* data panel (right of Figure 3.8).

After horizon matching, the  $PS$  data in its native  $PS$  time is squeezed and converted into  $PP$  time. It's then re-sampled in 2 ms sample rate and output, as the input of  $PS$  data inversion in STRATA.

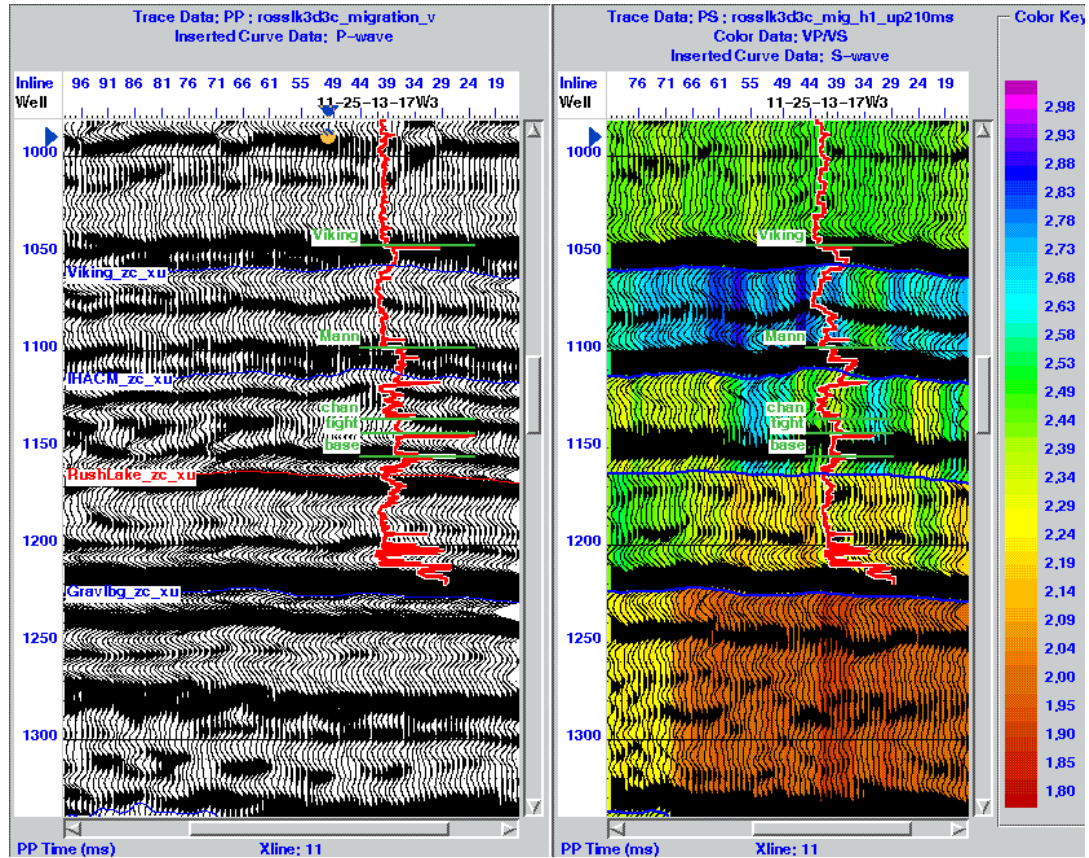


**Figure 3.8**  $PS$  (right) to  $PP$  (left) horizon-matching in  $PP$  time. The interval  $V_p/V_s$  calculated from event matching is displayed as a color background on  $PS$  data. The  $V_p/V_s$  color bar is shown at the right.

### 3.3.3 The initial $S$ -impedance model

The  $PS$  data are now in the  $PP$  time with four horizons, Viking, IHACM, Rush Lake and Gravelbourg, at the exact time as  $PP$  data, which means the same set of horizons used to create the  $P$ -impedance mode should be able to be used for constraining the  $S$ -impedance model. The same fashion as making the  $P$ -impedance model, the

$S$ -impedance log at the well 11-25 is used. Instead using an empirical  $V_p/V_s$  relationship like mudrock line, the measured blocky  $V_p/V_s$  from the special zero-offset VSP with both  $P$ -wave and  $S$ -wave source is used to calculate  $V_s$  from  $V_p$ .

Then, a 10 Hz low-pass filter is applied to the model to make the initial model smooth (Figure 3.9).

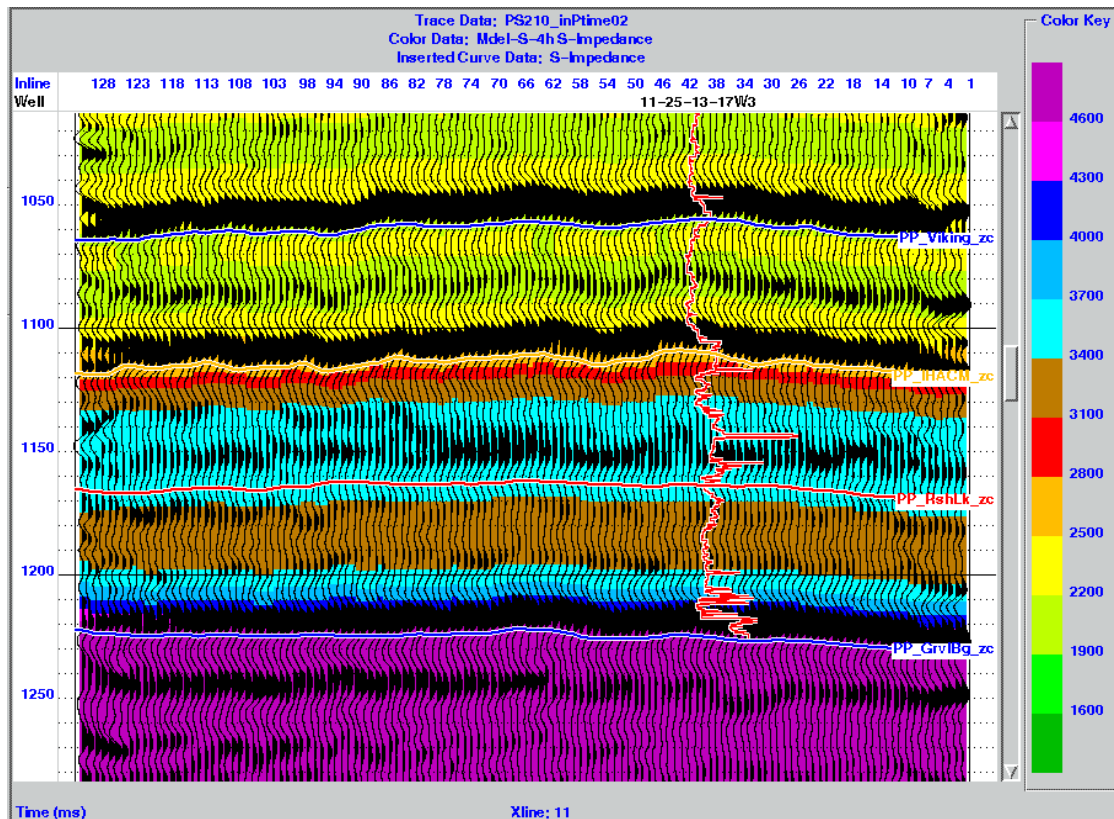


**Figure 3.9** The smoothed initial  $S$ -impedance model in color. The wiggle traces are  $PS$  data in  $PP$  time.

The wavelet for  $PS$  data inversion is then extracted from all the  $PP$ -time  $PS$  seismic traces excluding the edge traces in the time window of 800 – 1300 ms, assuming zero-phase.

### 3.3.4 Inversion and the result

Two inversion techniques are investigated here: model-based and sparse-spike. The sparse-spike inversion seems to be less noisy than the model-based inversion. The sparse-spike inversion result is chosen as the final result (Figure 3.10).

The Formation Viking at about 1060 ms shows as a high impedance layer between its surrounding shales. At near the bottom of the section at about 1220 ms, the sharp boundary of an impedance increase is Gravelbourg limestone. The Cantuar channels between the IHACM horizon and Rush Lake horizon are characterized by the lower S-impedance (red) sandwiched by shales above and below.

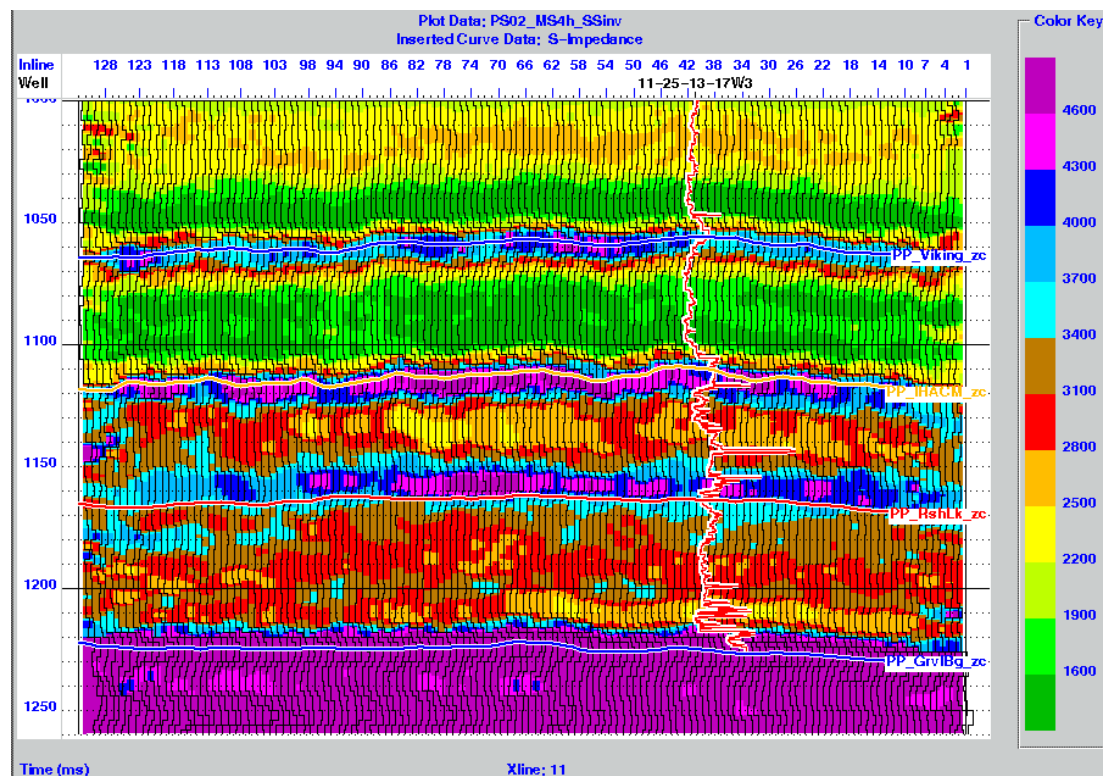
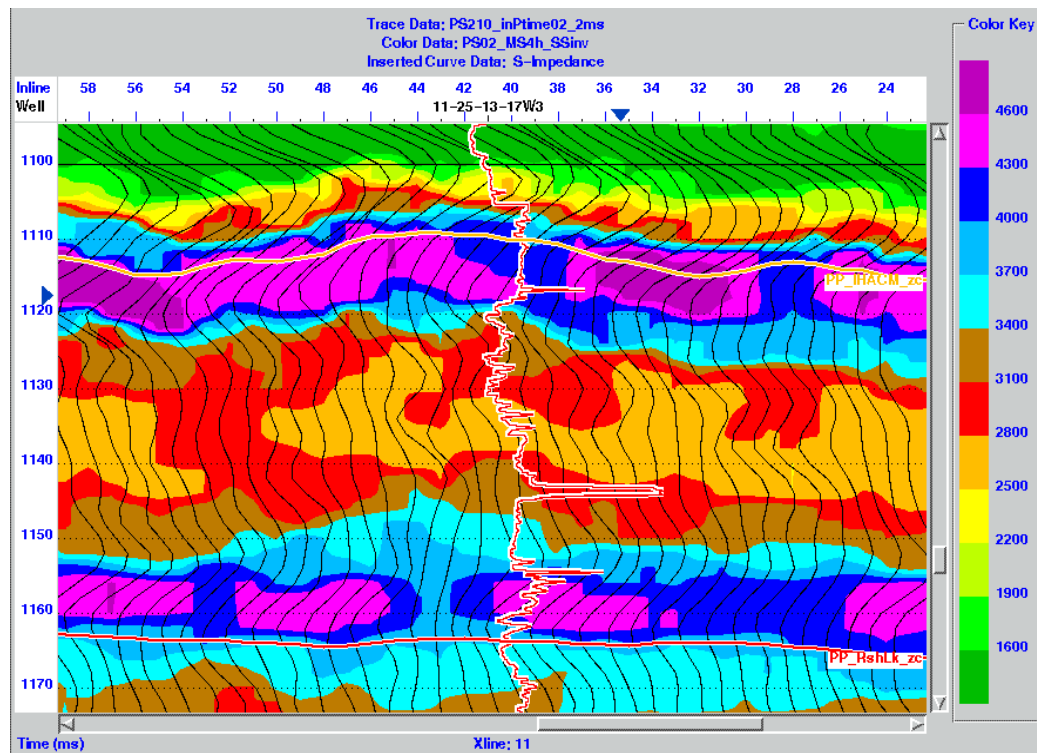


Figure 3.10 The result of *PS* data inversion at crossline 11. The inserted curve at well location is *S*-impedance log.



**Figure 3.11** Zoom-in of the *PS* data inversion result around the reservoir in well 11-25. Wiggle traces are *PS* seismic.

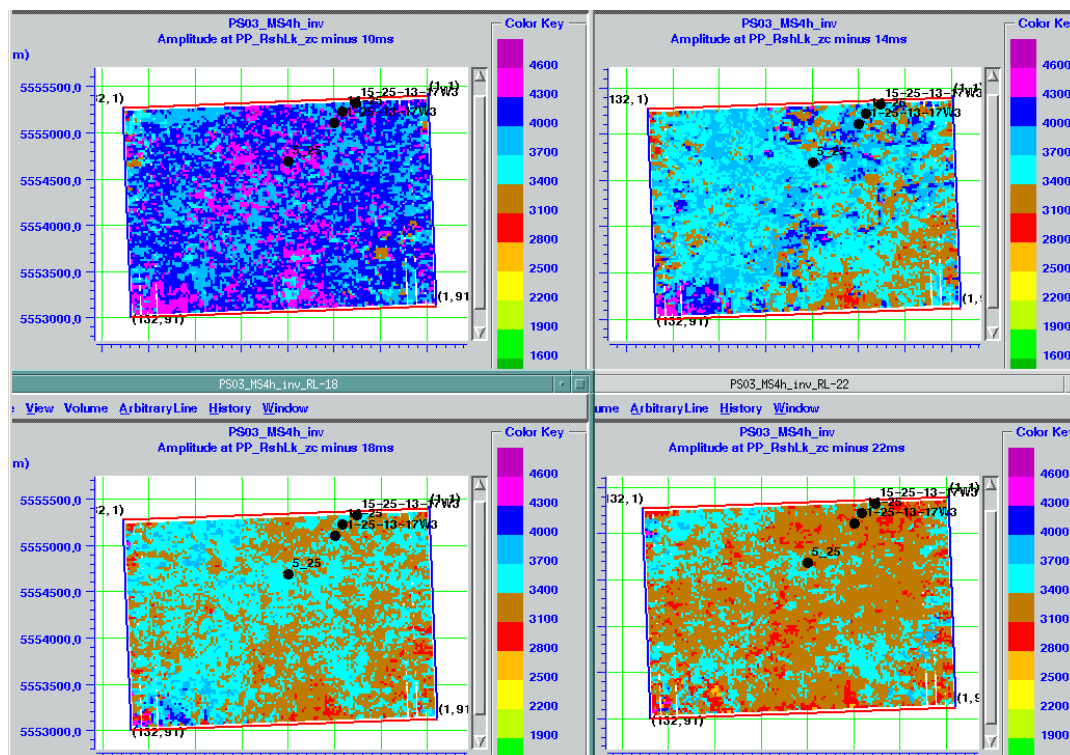


Figure 3.12 *S*-impedance horizon slices: Rush Lake horizon up 10ms (upper-left), 14ms (upper-right), 18ms (lower-left) and 22ms (lower-right).

### 3.4 $V_p/V_s$ map from impedance and comparison to travelttime-derived $V_p/V_s$

Now, we have two seismic inverted impedance volumes: the *P*-impedance and *S*-impedance. Ideally, the  $V_p/V_s$  volume can be derived by dividing the *P*-impedance by the *S*-impedance. However, the *PP* and *PS* time registration remains as a problem: by horizon matching, we only force *PS* time equal to *PP* time along the horizons. All the trace samples between horizons are not necessarily correspondent, until we have a very accurate  $V_p/V_s$  between any two adjacent samples at each CDP location, which is actually what we want to achieve.

Therefore, an average value over a certain time window is perhaps more reasonable to smooth out the un-aligned *PP* and *PS* events in small scale but still be able to catch the spatial trends in large scale.

By checking the horizon slices of the inverted *P*-impedance, starting from the Rush Lake horizon upward with 4ms increment, it's noticed that a 8ms window centered at the 14ms above Rush Lake horizon is relatively a good window. A RMS averaged *P*-impedance is calculated in this 8ms window and approximately represents the geometry of the lower channel in Ross Lake pool (Figure 3.13). The reservoir sand body associated with the low impedance has an elongated geometry in northeast to southwest direction.

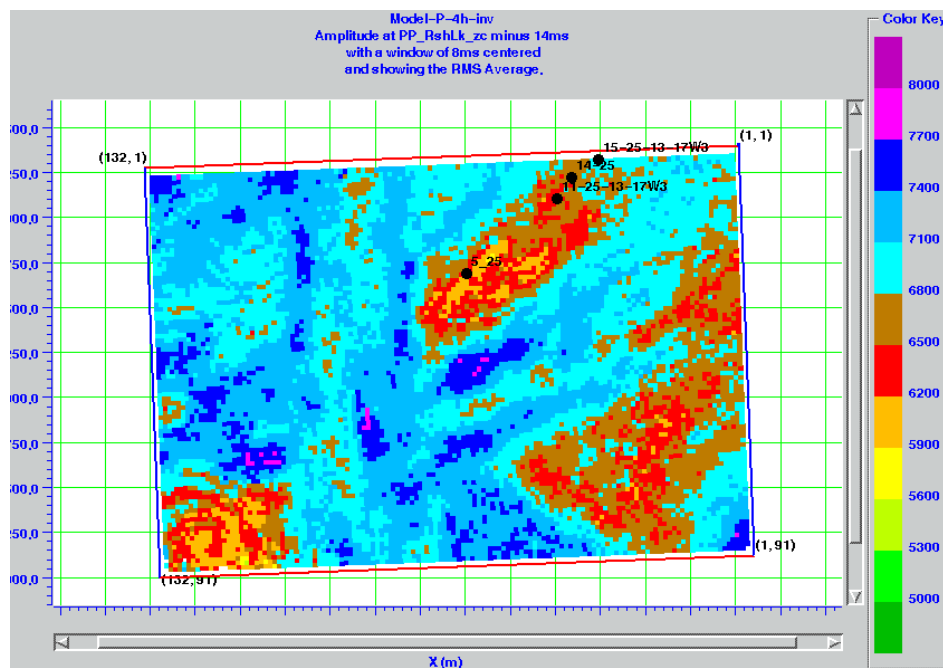


**Figure 3.13** The average *P*-impedance over a 8ms time window centered at 14ms above the Rush Lake horizon.

The average *P*-impedance and *S*-impedance over the same time window are put side-by-side for comparison (Figure 3.14), with a suitable different color scheme. The left

map in Figure 3.14 shows that the sand body is featured with low  $P$ -impedance value (in black color). The high  $P$ -impedance (in hot color) linear feature in north-south direction in the same figure is intercepted as a shale-plugged channel.

The RMS average of  $S$ -impedance is also calculated in the same 8 ms window centered at the 14 ms above Rush Lake horizon from the inverted  $S$ -impedance volume (Figure 3.14, right map). The sand body has slightly higher  $S$ -impedance than the surrounding shale. It is not as obvious and sharp as  $P$ -impedance to have the reservoir sand body stand-out, still, the  $S$ -impedance shows the similar trend as  $P$ -impedance map.

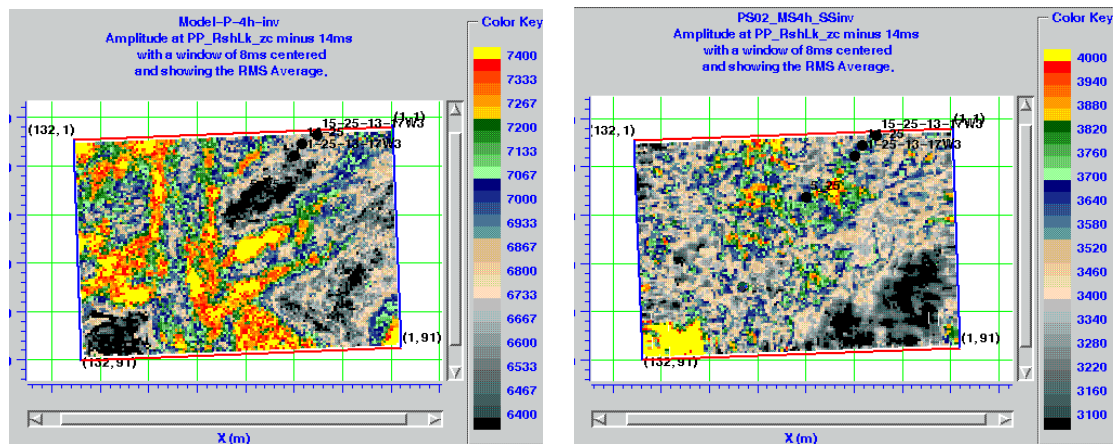


**Figure 3.14 Average  $P$ -impedance (left) over a 8ms window indicates the sand has low  $P$ -impedance value (dark color) while the average  $S$ -impedance (right) shows a high  $S$ -impedance.**

The  $V_p/V_s$  map over this 8 ms time window is calculated by dividing the average  $P$ -impedance by the average  $S$ -impedance.

The comparison of the impedance-derived  $V_p/V_s$  and travel time-derived  $V_p/V_s$  in Chapter Two is shown in Figure 3.15. Also keep in mind that using the impedance

method, the  $V_p/V_s$  is an average over 8 ms ( $PP$  time) window, meanwhile, the  $V_p/V_s$  from travel time is an average over 40~50 ms ( $PP$  time) window.

Some observations from these two  $V_p/V_s$  maps are:

1. Overall, the impedance-derived  $V_p/V_s$  map has a lower  $V_p/V_s$  value, which ranges from 1.5 ~ 2.3 with reservoir sand about 1.6~1.7, than the traveltime  $V_p/V_s$ , which ranges from 1.7~ 2.6 with reservoir sand about 2.15~2.25.
2. The low-  $V_p/V_s$  strip at the left part of traveltime  $V_p/V_s$  map disappears on the impedance  $V_p/V_s$  map.
3. The size of the sand body looks more areally extensive on the impedance  $V_p/V_s$  map.
4. The sand body has an eastern direction extension on both impedance  $V_p/V_s$  map and travel time  $V_p/V_s$  map.

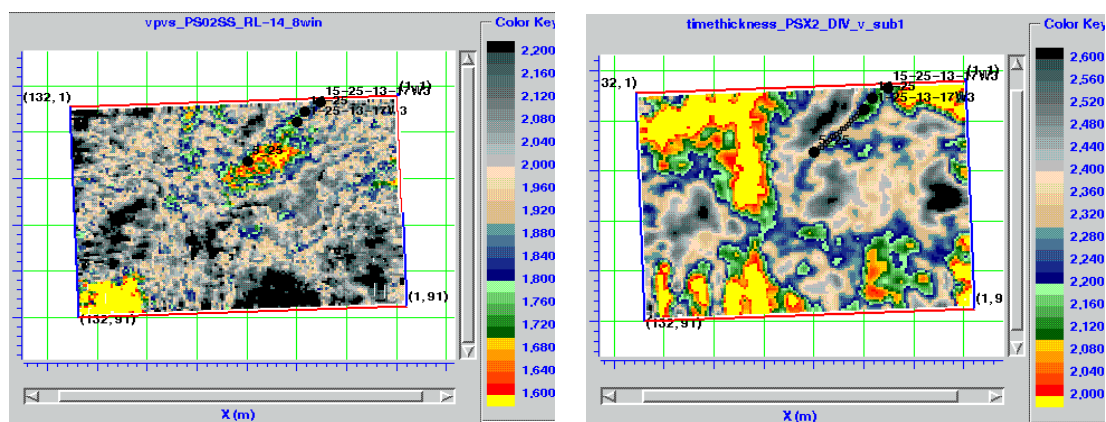


**Figure 3.15 Comparison of  $V_p/V_s$  derived from impedance (left) and  $V_p/V_s$  derived from the traveltimes (right).**

### **3.5 Summary and discussion**

The *PP* data inversion indicates that the oil-bearing sand body has a lower *P*-impedance compared with surrounding formation. In contrast, *PS* data inversion shows the sand has a slightly higher *S*-impedance. The  $V_p/V_s$  value derived from impedance inversion is generally lower than the  $V_p/V_s$  derived from the time-thickness ratios. The impedance  $V_p/V_s$  and travel time  $V_p/V_s$  values show promising anomalies.

The channel on the *PS* data inversion is not as clear and crisp as on the *PP* data inversion. First, by checking the well-seismic tie at the well location, in the zone of interest, the *PP* seismic trace shows a good correlation with *PP* synthetic. However, the *PS* seismic trace doesn't show such a nice correlation with the *PS* synthetic seismogram (Figure 3.7). Second, looking at the inversion QC plot (Figure 3.16), above IHACM and below Rush Lake horizon, the *PP* and *PS* data are correlated in terms of their seismic characters. Between these two horizons, where the zone of interest lies (indicated by the arrow), the *PP* data show several events. In contrast, *PS* section has only one wide, low-frequency, low-amplitude peak. This difference is sufficient to create the discrepancy between *PP* and *PS* inversion. The amplitude of *PS* seismic data within the reservoir channel in this round of processing may not be able to properly reflect the reality.

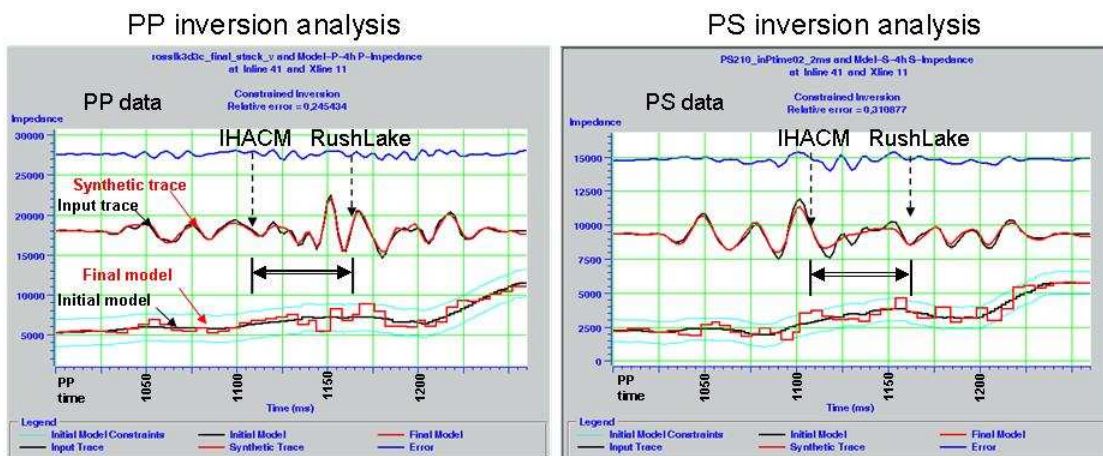


**Figure 3.16** Inversion analysis of *PP* (left) and *PS* (right) trace at the well location. The arrow indicates the interval between IHACM and Rush Lake. The X-axis is time and right direction going deeper.

## Chapter Four: Attenuation and $Q$ factor estimation from VSP

### 4.1 Introduction

Seismic attenuation is the general term given to irrecoverable energy loss as a vibration propagates. Attenuation is a rock property. It can be indicative of the rock type, and potentially discriminate pore saturant type. In seismic processing, estimating  $Q$ , then applying inverse  $Q$  to data can compensate for attenuation and enhance the general frequency content (Wang, 2002, Wang, 2003).

There are quite a few methods to estimate  $Q$  factor from seismic data, particularly from VSP data. Tonn (1991) compared 10 methods and concluded that the spectral ratio method is optimal in the “noise-free” case but no single method is generally superior.

The spectral-ratio method, which analyses different stations at various frequencies, is widely used to determine an attenuation, or  $Q$  factor from VSP data (e.g., Tonn, 1991). The calculation proceeds as follows: for two downhole receivers at depths  $d_1$  and  $d_2$ ,

$$\ln \left[ \frac{|A(\omega)_{d_2}|}{|A(\omega)_{d_1}|} \right] = \text{const.} - \frac{|\omega|}{2Q} \left( \frac{d_2}{v_2} - \frac{d_1}{v_1} \right), \quad (4.1)$$

where  $A(\omega)$  is the amplitude spectrum at different depth,  $\omega = 2\pi f$  is the angular frequency,  $v_1$  and  $v_2$  are the average velocities from the source to receiver locations  $d_1$  and  $d_2$ , respectively.

As  $t = d/v$ , expressed in time, equation (4.1) becomes:

$$\ln \left[ \frac{|A(\omega)_{d_2}|}{|A(\omega)_{d_1}|} \right] = \text{const.} - \frac{|\omega|}{2Q} (t_2 - t_1) \quad , \quad (4.2)$$

where  $t_1$  and  $t_2$  are the traveltimes from source to geophones at depths  $d_1$  and  $d_2$ .

This is a linear relation between the spectral ratio and the frequency  $\omega$  with a slope of  $p$ , where

$$p = \frac{t_2 - t_1}{2Q} \quad (4.3)$$

By choosing any two VSP downhole geophones, equation (4.1) gives the average interval  $Q$  factor of the strata between them -- assuming that the geophones are well coupled with the formation and the source is consistent. To estimate a relatively stable interval  $Q$ , a larger spacing is often selected. Averaging the amplitude spectra of a few adjacent geophones is also commonly used. If we use every adjacent geophone, the calculated interval  $Q$  could possibly oscillate or be negative. Therefore, choosing the proper spacing or averaging scheme often becomes a case of trial and error. In the following, we use a different application of the spectral ratio method to calculate  $Q$  values using each adjacent geophone, and discuss the conditions for estimating a reasonable  $Q$ .

#### **4.2 Methodology of $Q$ estimation**

The zero-offset VSP gives an almost vertical incident ray-path for a horizontal-layered model.

For a layered earth model (Figure 4.1), the effective  $Q_{eff}$  (or average  $Q_{ave}$ ) satisfy:

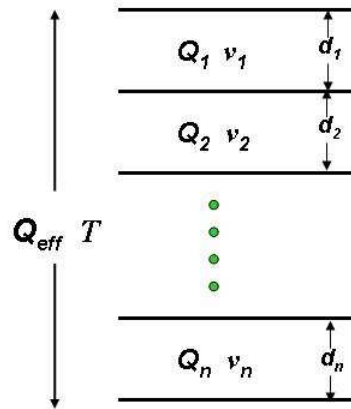


**Figure 4.1** A schematic layered earth model for  $Q$  factor.

$$\frac{T}{Q_{eff}} \equiv \sum_{n=1}^N \frac{d_n}{Q_n v_n} , \quad (4.4)$$

The interval  $Q$  ( $Q_{int}$ ) of each layer and the average  $Q$  ( $Q_{ave}$ ) of all the layers have a cumulative relationship (Bale and Stewart, 2002):

$$\frac{T(n+1)}{Q_{ave}(n+1)} = \frac{T(n)}{Q_{ave}(n)} + \frac{T(n+1) - T(n)}{Q_{int}(n+1)} , \quad (4.5)$$

where  $n=1, 2, \dots, N-1$  and  $Q_{int}(1) = Q_{ave}(1)$ .

Equation (4.5) shows that the interval quality factor  $Q_{int}$  depends on the relationship between  $\frac{T(n)}{Q_{ave}(n)}$  and  $\frac{T(n+1)}{Q_{ave}(n+1)}$  :

- To make  $Q_{int} > 0$ , we must have  $\frac{T(n+1)}{Q_{ave}(n+1)} > \frac{T(n)}{Q_{ave}(n)}$  ;
- If  $\frac{T(n+1)}{Q_{ave}(n+1)} - \frac{T(n)}{Q_{ave}(n)}$  is very small, then the  $Q_{int}$  calculation is unstable.

Therefore, the ratio of the first-arrival time and the estimated average  $Q$  factor,  $\frac{T(n)}{Q_{ave}(n)}$ , is acting as a “quality indicator” for  $Q$  estimation.

The reference level ( $n=1$ ) could be set at any depth. Here, we set the source location at the ground surface as the reference level. The spectral ratio between a down-hole recorded trace at a certain depth and the surface sweep is used to calculate the  $Q_{ave}$ . The advantage of this approach is that the surface sweep is relatively constant and designed to have a largely flat spectrum across a given band.

### **4.3 Example 1: Ross Lake VSP data**

#### ***4.3.1 Introduction***

The VSP data used in this study is from Husky Energy Inc’s Ross Lake heavy oil field in south-western Saskatchewan. There were two types of source for the zero-offset VSP: a vertical mini-vibrator with a 12-second sweep over 8-180 Hz and an inline horizontal vibrator with a 12-second sweep over 5-100 Hz. As we are using largely vertical incidence geometries with these sources, we take the simple “ $P$ -source” terminology to represent the vertical-vibrator and “ $S$ -source” for the horizontal-vibrator. There are 130 three-component geophone levels ranging from 198 m to 1165 m of measured depth at a nominal 7.5 m spacing. The VSP survey well has a  $P$ -wave sonic log and a low-quality, through-casing dipole sonic log (to measure  $V_s$ ).

#### ***4.3.2 Examine the amplitude spectrum***

After being normalized with the shallowest level trace, the amplitude spectrum of all traces from the *P*-source (Figure 4.2) clearly shows that as depth increases the amplitude decays and frequency bandwidth shrinks as well. Another observation is that above 600 m, the -20 dB contour line changes rapidly: from 140 Hz at about 200 m depth decreases to about 30 Hz at about 600 m depth. Below 600 m, the -20 dB contour line has its slope nearly unchanged. Meanwhile the -40 dB line has a nearly constant gradient for the whole measured interval. Both -20 and -40 dB lines could be extended with similar gradient to the high cut (180 Hz) of the *P*-wave vibrator sweeping frequency at the surface. This indicates that in this area, (1) different frequencies behave differently; (2) most frequency and amplitude attenuation for *P*-wave happens in the shallow few hundred meters of the Earth with a nearly linear decay rate.

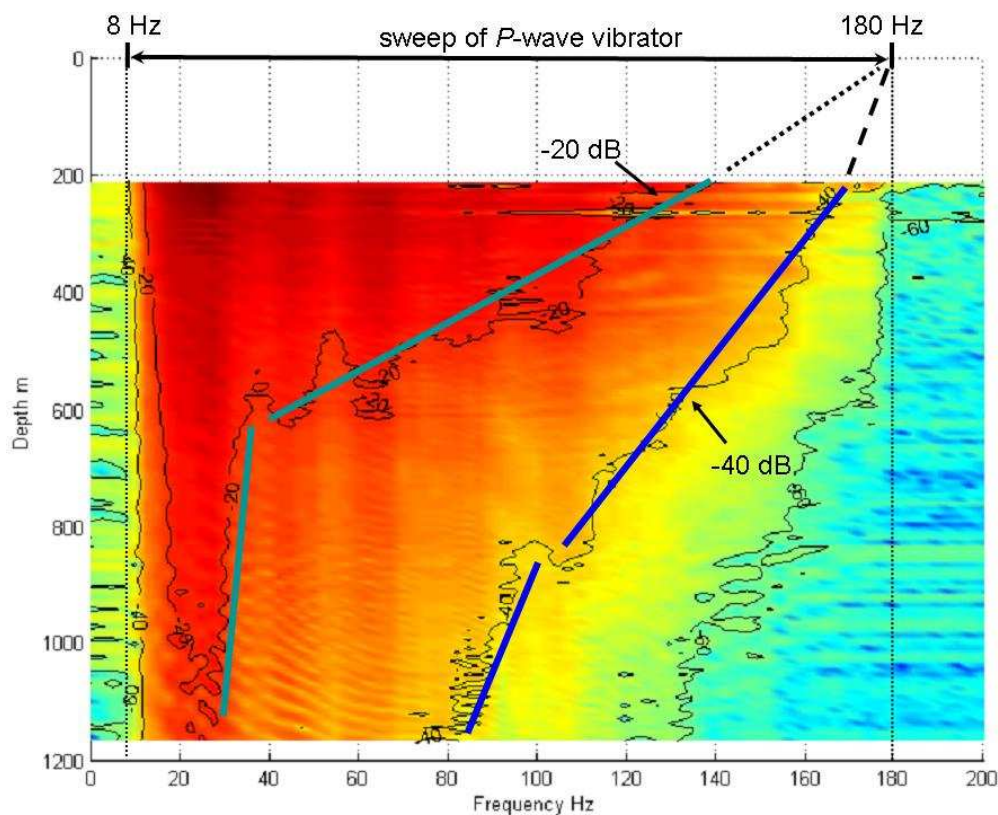


**Figure 4.2** The amplitude spectrum of vertical component for all geophone levels from the *P*-source zero-offset VSP in well 11-25 of Ross Lake. Color indicates the amplitude (red is high), and numbers show the dB down.

For recorded *S*-waves generated by the shear-wave vibrator, the -20 dB contour line vanishes below about 600 m depth (Figure 4.3). The gradient of -40 dB contour line changes at around 650 m depth. The more interesting observation is that the extension using same rate from 200 m depth to surface would only reach about 60 Hz. To get to the high-cut sweeping frequency of 100 Hz, it needs a rapid change of the gradient. So, unlike *P*-wave, the -40 dB contour line of *S*-wave is not linear. Also unlike *P*-wave, when *S*-wave propagates down in the Earth, the most severe loss of amplitude and frequency happens at the very shallow layers, less than 200 m in depth, or possibly near the surface.

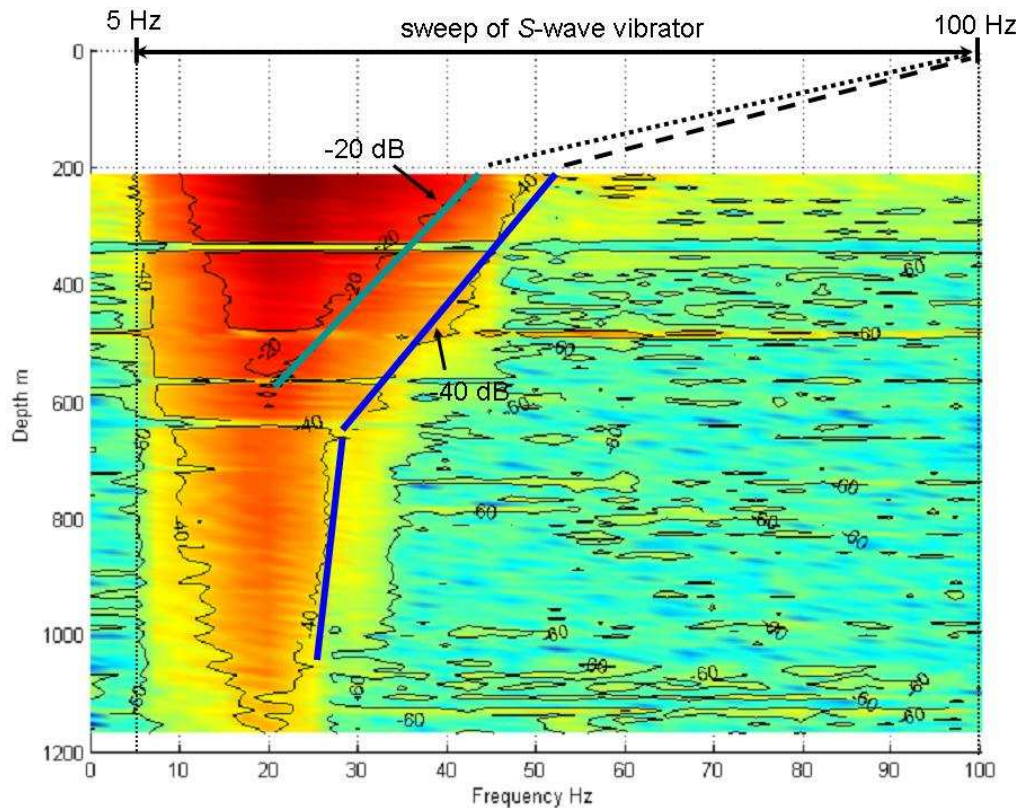


**Figure 4.3** The amplitude spectrum of horizontal component for all geophone levels from *S*-source zero-offset VSP in well 11-25 in Ross Lake. Color indicates the amplitude (red is high), and numbers show the dB down. Notice the left edge of the peak is not a straight vertical line.

### 4.3.3 VSP data preparation and checking

The raw records of vertical component from  $P$ -wave source ( $P$ - $P$  events) and horizontal component from  $S$ -wave source ( $S$ - $S$  events) are displayed in Figure 4.4 with picked  $P$ -wave and  $S$ -wave first arrivals superimposed.

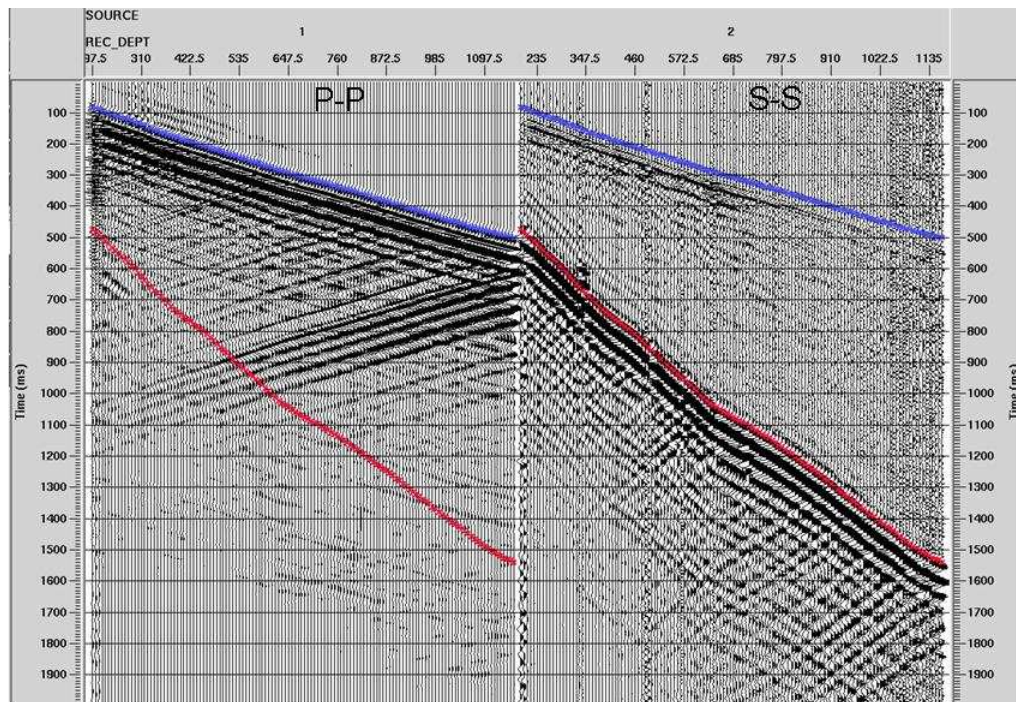


**Figure 4.4** Raw vertical component records from  $P$ -wave source (left) and horizontal component records from  $S$ -wave source (right). Blue dots are picked  $P$ -wave first arrivals. Red dots are picked  $S$ -wave first arrivals.

Both  $P$ - and  $S$ -source zero-offset VSPs are processed to extract the downgoing  $P$ - and  $S$ -wavefields. For the  $P$ -source vertical-component data, after aligning the first-arrival times, a 5-by-5 alpha-trimmed, weighted median filter is used to separate the downgoing wavefield from the total wavefield. For the  $S$ -source horizontal-component data, a rotation of the X- and Y-component to radial- and transverse-component by using hodogram analysis is first needed to align energy in the source-receiver plane. The

*S*-source radial component traces are then flattened at the first-break time, and the same median filter as used for *P*-source data is applied to extract the downgoing shear wavefield (Figure 4.5).

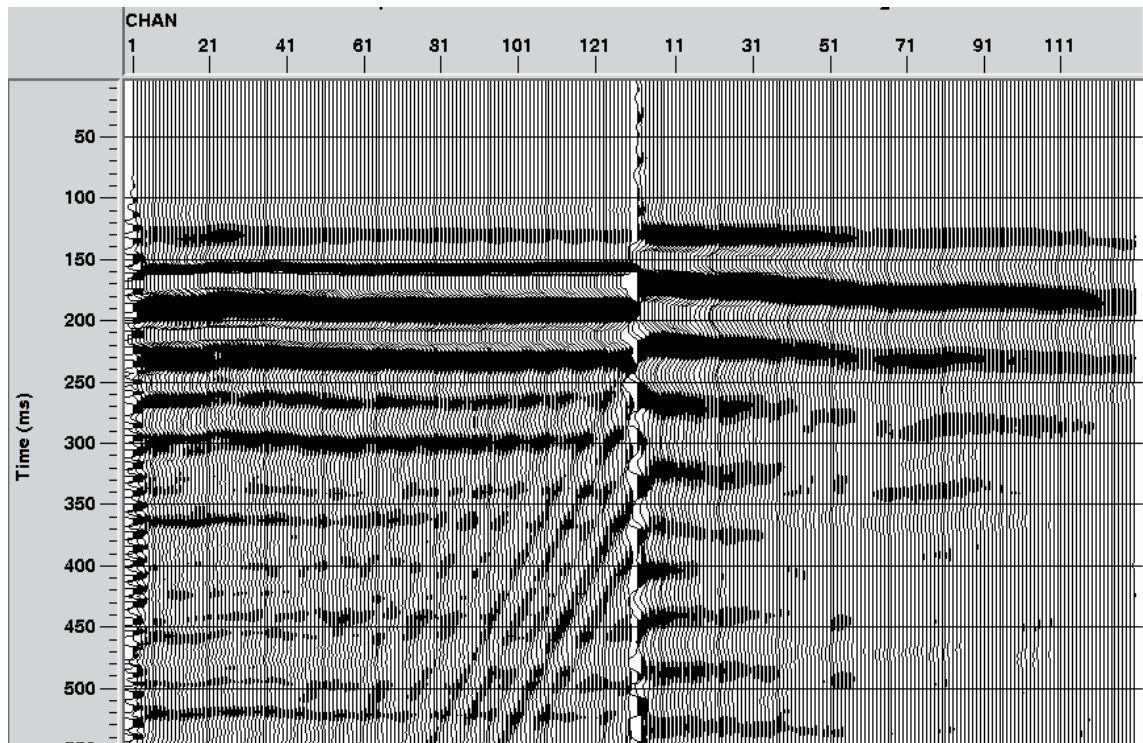


**Figure 4.5** Aligned downgoing *P* wavefield from the *P*-source (left) and downgoing *S* wavefield from the *S*-source (right) are displayed using a single amplitude scalar.

To have a more detailed comparison, the downgoing *P*- and *S*-wave traces at three different depths, 264 m, 685 m and 1157.5 m, are plotted on top of each other (Figure 4.6). The *S*-wave shows a larger amplitude loss and phase change than the *P*-wave over the same depth range.

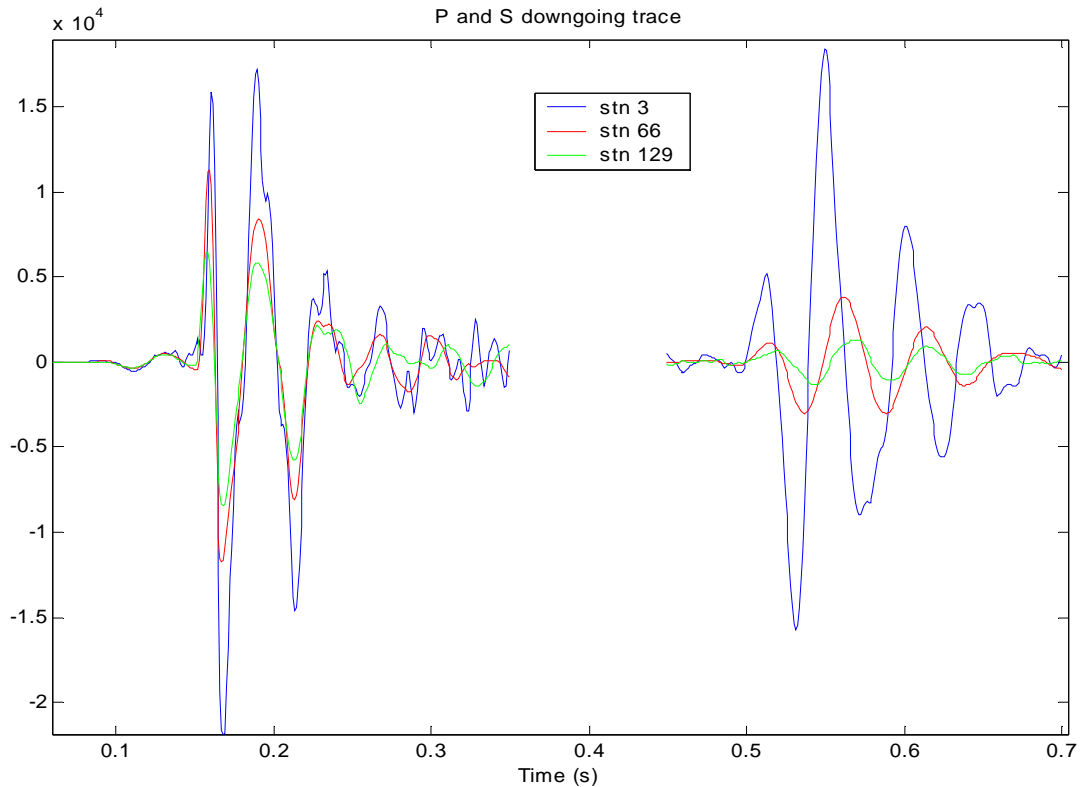


**Figure 4.6 Downgoing *P*- and *S*-wave at station #3 (214 m depth, blue line), station #66 (685 m depth, red line) and station #129 (1157.5 m depth, green line) indicating amplitude loss and some phase change.**

Figure 4.7 displays the amplitude spectrum of the raw surface sweep of both *P*- and *S*-wave sources, the spectrum of the *PP* traces and *SS* trace at a shallow station (220 m), and a deep station (1157.5 m). It shows that the *S*-wave amplitude decays faster than the *P*-wave, and has less high-frequency components.

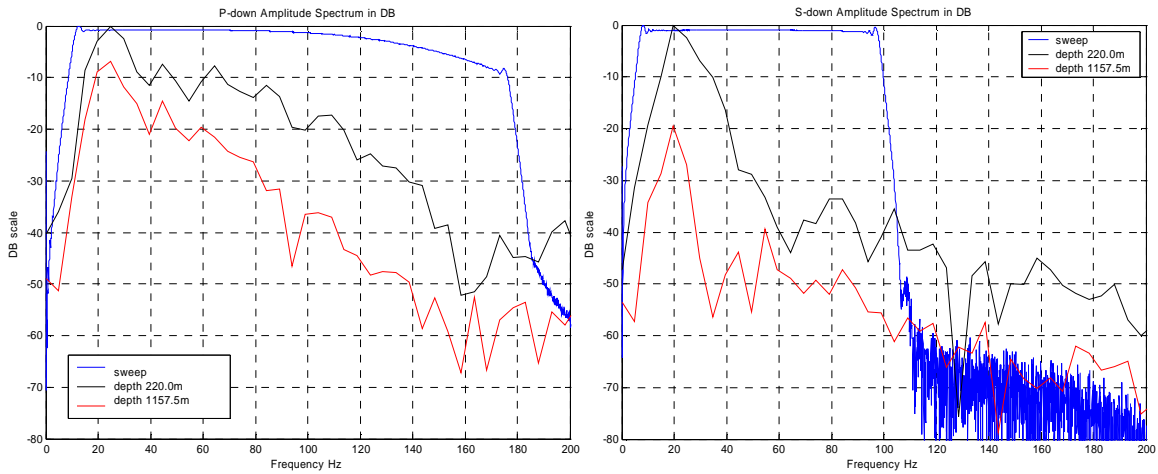


**Figure 4.7** The amplitude spectrum of the sweep (blue line), station #4 (220 m, black line) and station #129 (1157.5 m, red line) for the *P*-source (left) and *S*-source (right). Amplitude and frequency loss with depth is evident.

#### 4.3.4 Estimating $Q$

The spectral-ratio method of various levels is often used to estimate a  $Q$  factor (Xu and Stewart, 2001). Here, we set the surface as the reference level. Using equation (4.5), the  $Q_{p\_ave}$  and  $Q_{s\_ave}$  curves for the whole interval are calculated and plotted against depth (Figure 4.8). We note that  $Q_{p\_ave}$  and  $Q_{s\_ave}$  have different trends.

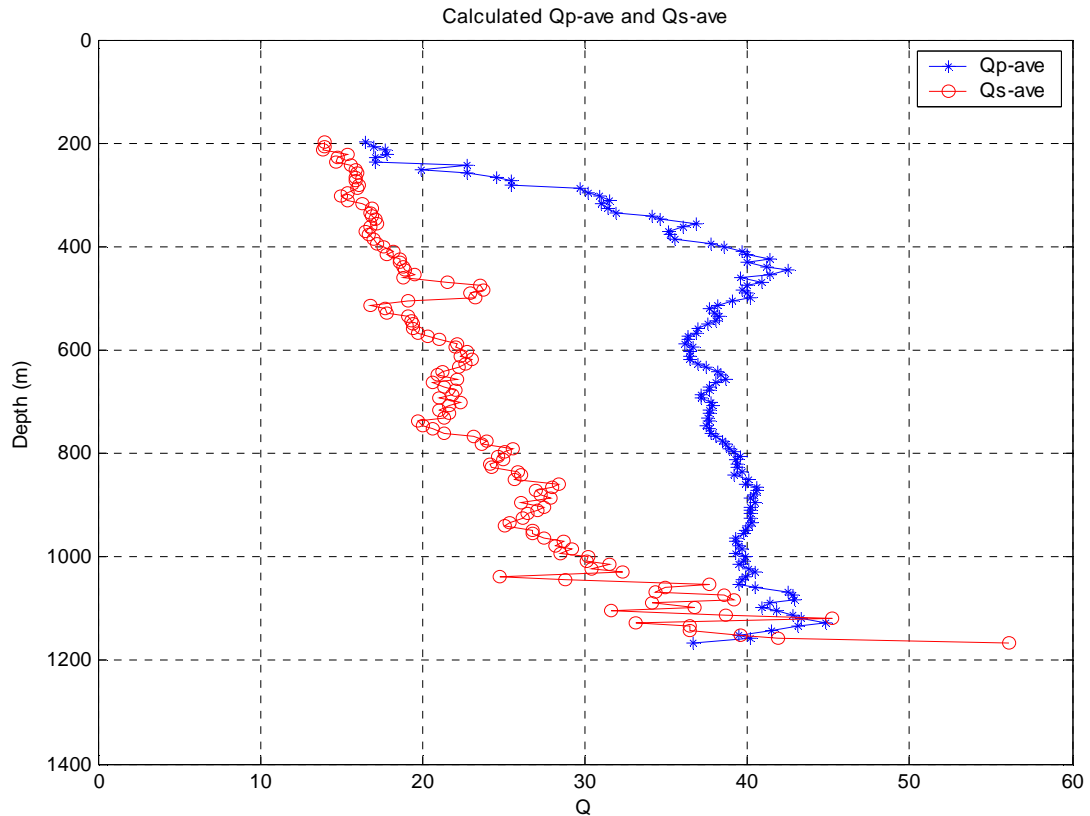


**Figure 4.8 Average  $Q_p$  (blue) and  $Q_s$  (red) curves from VSP in well 11-25 at Ross Lake.**

We observe in Figure 4.9 that the  $P$ -wave quality indicator (blue line) from about 400 m to 1050 m is well behaved – steadily increasing with a slowly changing positive slope. When this curve has a negative slope, i.e. from 200 m to 400 m, the  $Q_{p\_int}$  will be negative (which is not physically realistic). A nearly vertical line (at 600 m and 800 m) results in a very high  $Q_{p\_int}$ . Smoothing can stabilize  $Q_{int}$ , but will not change the general trend, which means we are unable to get a reasonable interval  $Q_p$  above 400 m in this case.

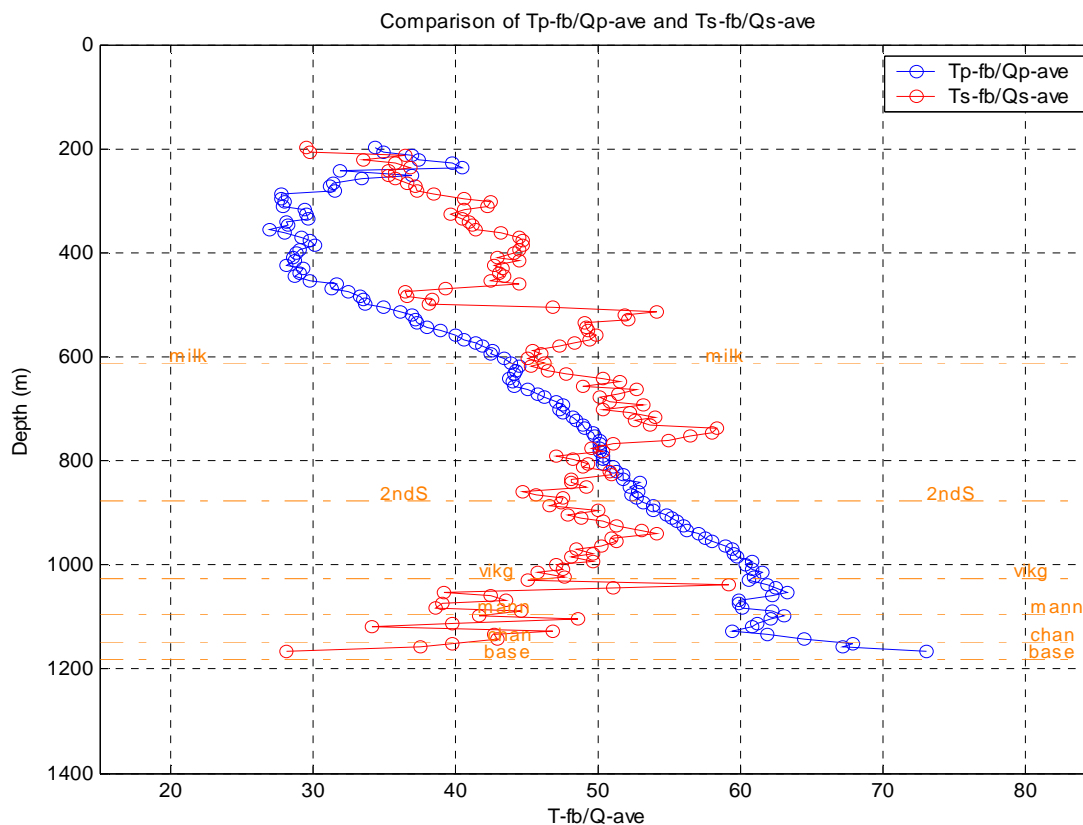


**Figure 4.9** Attenuation quality indicator for  $Q_p$  (blue) and  $Q_s$  (red), with formation tops.

The  $P$ -wave quality indicator (blue curve in Figure 4.9) suggests that a reasonable interval  $Q_p$  can be estimated from 450 m to 1050 m. To avoid an oscillatory  $Q_{int}$ , different size boxcar smoothers are used in attempt to smooth  $Q_{ave}$ . Figure 4.10 shows the results with 10-, 20- and 30-sample smoothing. The 30-sample smoothing is chosen to produce the final  $Q_{p\_int}$ .

Haase and Stewart (2006) extracted  $Q$  values from the Ross Lake VSP using an analytic signal technique. They found  $Q_p$  values of 25 to 35 over the same interval as that considered here. They also analysed a  $P$ -wave drift curve measurement, from the VSP and sonic log, which gave  $Q_p$  values of 40 to 60 over this same interval.

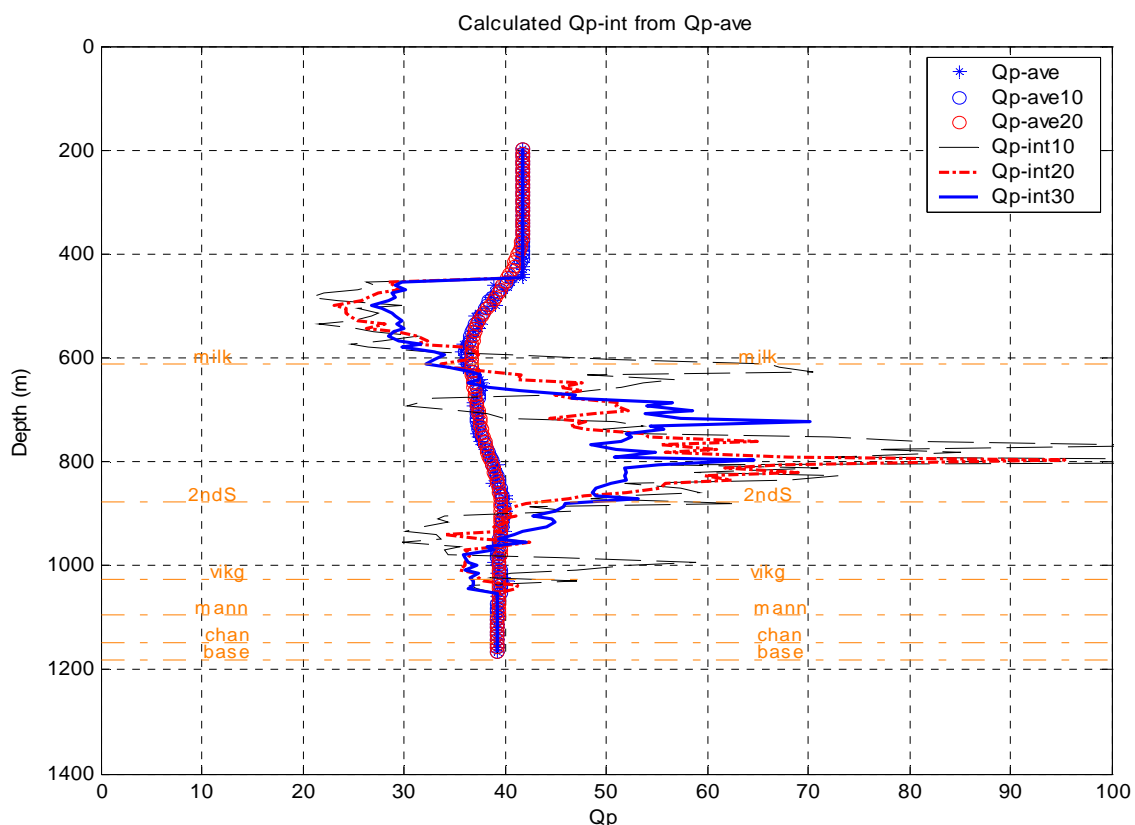


**Figure 4.10** Average  $Q_p$  with 10 (black line), 20 (red line) and 30 (blue line) samples smoothing, and derived interval  $Q_p$ .

The  $S$ -wave quality indicator (Figure 4.9, red curve) increases in certain areas which can be used for reliable estimation. Unfortunately, below 620 m, the estimation of  $Q_s$  becomes unstable if we want to achieve the interval  $Q_s$  between the adjacent geophone levels. Therefore, using spectral ratio method, the average  $Q_s$  over large intervals are calculated: 17 for surface - 400m, 16 for 400m - 610m, 37 for 610m - 870m and 26 for 870m - 1150m, which correspond to certain geological formations. Figure 4.11 shows the result of two intervals.

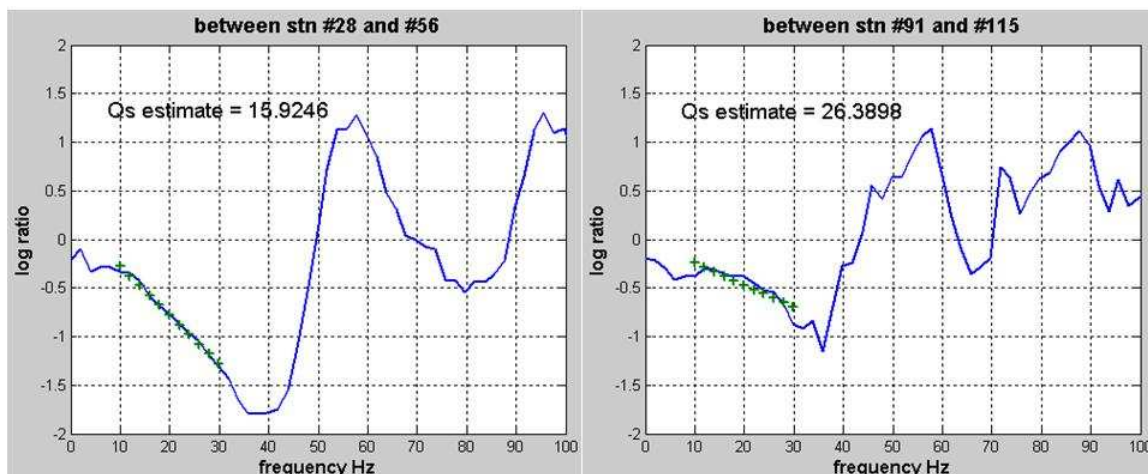


**Figure 4.11 Average  $Q_s$  calculated using spectral ratio method between station #28 to #56 (400m - 610m, left plot) and station #91 to #115 (870m - 1050m, right plot).**

Based on the above estimate, a  $Q$  model over large intervals for the Ross Lake area has been proposed (Table 4.1). For formations shallower than 600 m,  $Q_s$  is about half of  $Q_p$ . For formations deeper than 600 m,  $Q_s$  is about two thirds of  $Q_p$ .

Formation and depth	$Q_p$	$Q_s$	$V_p/V_s$	$V_p$ (m/s)
Surface - 400m	38	17	~ 3.5	~ 1800
400m - 610m (Ribstone ~ Milk River)	29	16	~ 2.8	~ 2200
610m - 870m (Milk River ~ K2WS)	54	37	~ 2.3	~ 2700
870m - 1050m (K2WS – Mannville)	40	26	~ 2.7	~ 2500

**Table 4.1  $Q_p$ ,  $Q_s$ ,  $V_p/V_s$  and  $V_p$  for the main geological formations in Ross Lake.**

#### 4.3.5 $Q_p$ versus $V_p$ , $V_s$ and $V_p/V_s$

In general, as depth increases, the rock becomes harder and more rigid. Both  $V_p$  and  $V_s$  increase,  $V_p/V_s$  decreases, and there is less attenuation (higher  $Q$  factor). The  $V_p/V_s$  values are commonly used as a lithology indicator.

Since there is no reliable  $V_s$  log in this well, the  $V_p/V_s$  curve is calculated from the zero-offset VSP by picking the first-arrivals from  $P$ - and  $S$ -wave. Both  $P$ -velocities from well logging and from VSP are plotted to check the correlation between these two types of measurement (Figure 4.12, left panel). The observation that  $V_p$  from VSP is slightly lower than the log measured  $V_p$  indicates the velocity dispersion.

In the attempt to investigate if there is any correlation between attenuation factor  $Q$  and  $P$ -velocity or  $S$ -velocity or  $V_p/V_s$ , curves of interval  $Q_p$  derived from VSP ( $Q_{p\_int30}$ ),  $V_p$  from sonic log and  $V_s/V_p$  from VSP are plotted on one canvas (middle of Figure 4.12). Generally, these three curves are following the same trend in this case.

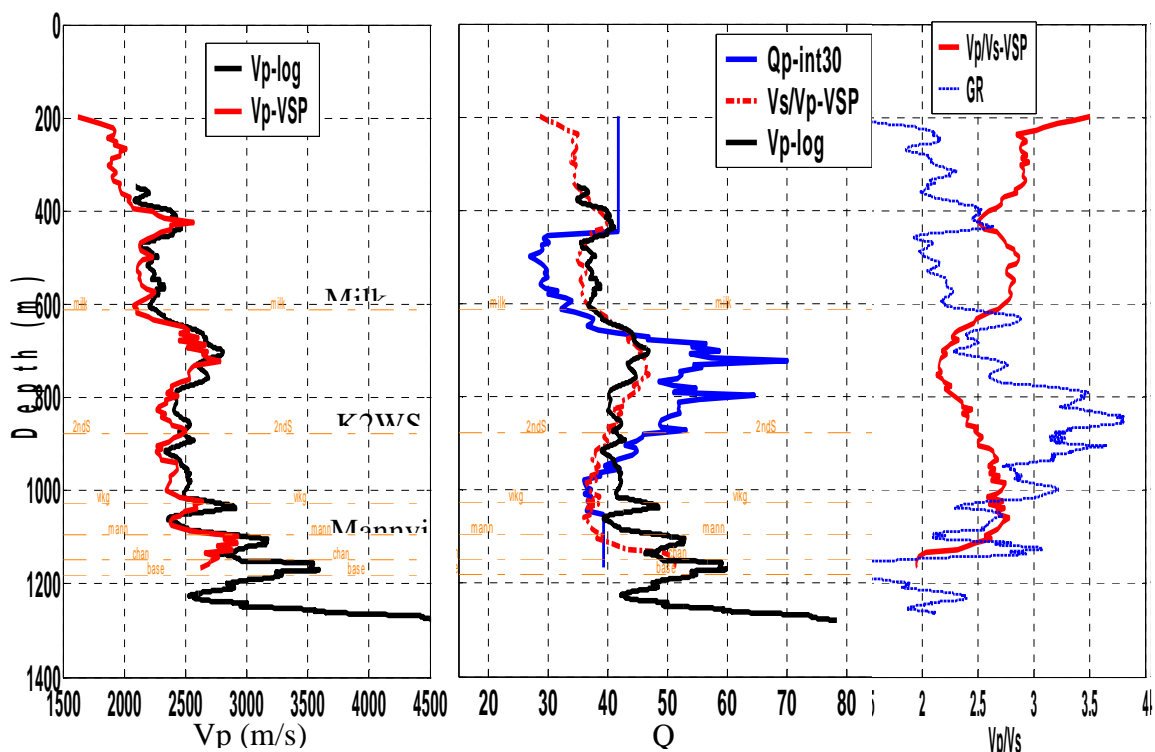


**Figure 4.12**  $V_p$  from VSP (red) is generally slower than  $V_p$  from log (black). This is evidence of velocity dispersion (left panel). The smoothed interval  $Q_p$  (blue), VSP-derived  $V_s/V_p$  (red, scaled) and  $V_p$  from sonic log (black) are grossly correlated. The  $V_p/V_s$  (red) and GR log (blue) are plotted on the right.

To further check the quantitative relationship,  $Q_p$  is crossplotted with  $V_p$  and  $V_s$ , respectively. It seems a linear regression function represents the relation between the attenuation and formation velocity quite well (Figure 4.13). The trend is that lower velocity formation, both  $P$ -wave and  $S$ -wave, corresponds to lower  $Q$  factor. In other words, waves travelling in such a soft formation attenuate more. The linear relation looks weaker for  $Q_p$  versus  $V_p$ , and stronger for  $Q_p$  versus  $V_s$ . The 95% confidence lines are also plotted to demonstrate the fitting quality.

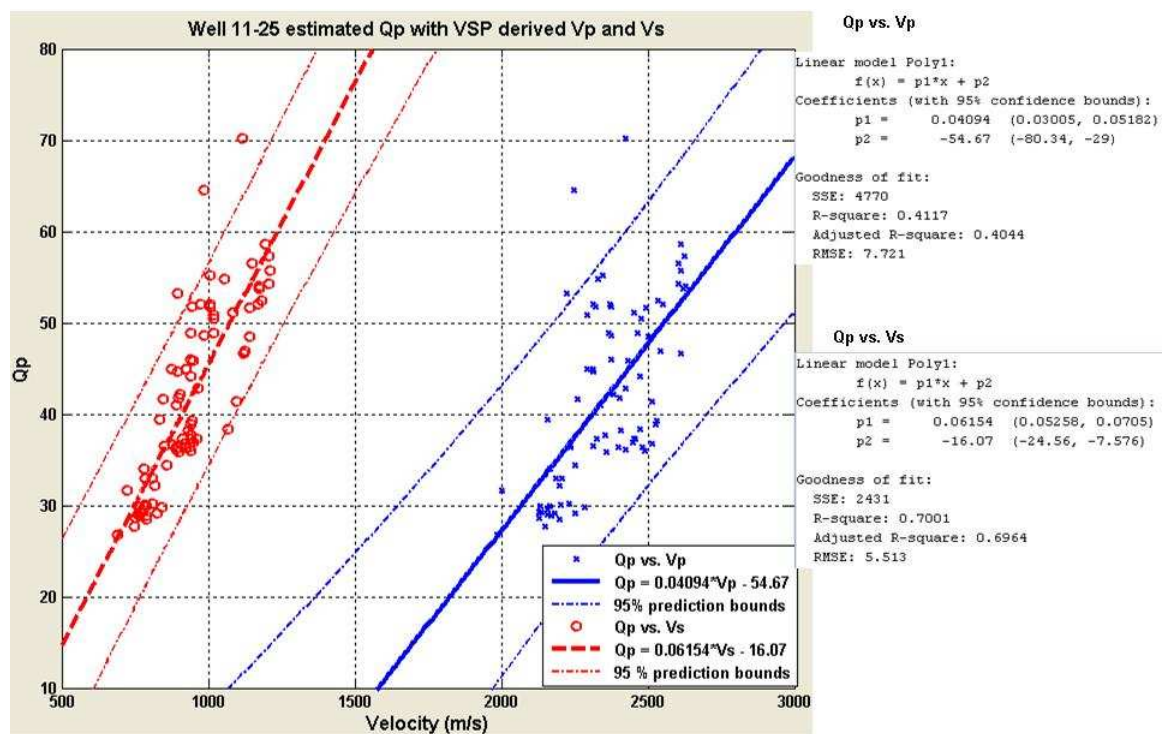


**Figure 4.13** Interval  $Q_p$  plotted versus VSP-derived  $V_p$  (blue) and  $V_s$  (red).  $V_s$  shows a better linear relationship with VSP-derived  $V_p/V_s$  than  $V_p$ .

A least-squares polynomial regression finds a reciprocal linear relationship between  $Q_p$  and  $V_p/V_s$ :

$$Q_p = -40.39 * (V_p/V_s) + 144.2 \quad , \quad (4.6)$$

which means that a high  $V_p/V_s$  value (softer formation) corresponds to a low  $Q_p$  (more attenuation) and a low  $V_p/V_s$  (harder formation) has a high  $Q_p$  (less attenuation). The 95% confidence level lines show that the 95% of the predicted  $Q_p$  value from  $V_p/V_s$  are within the range of about  $\pm 10$  of the true  $Q_p$  value (Figure 4.14).

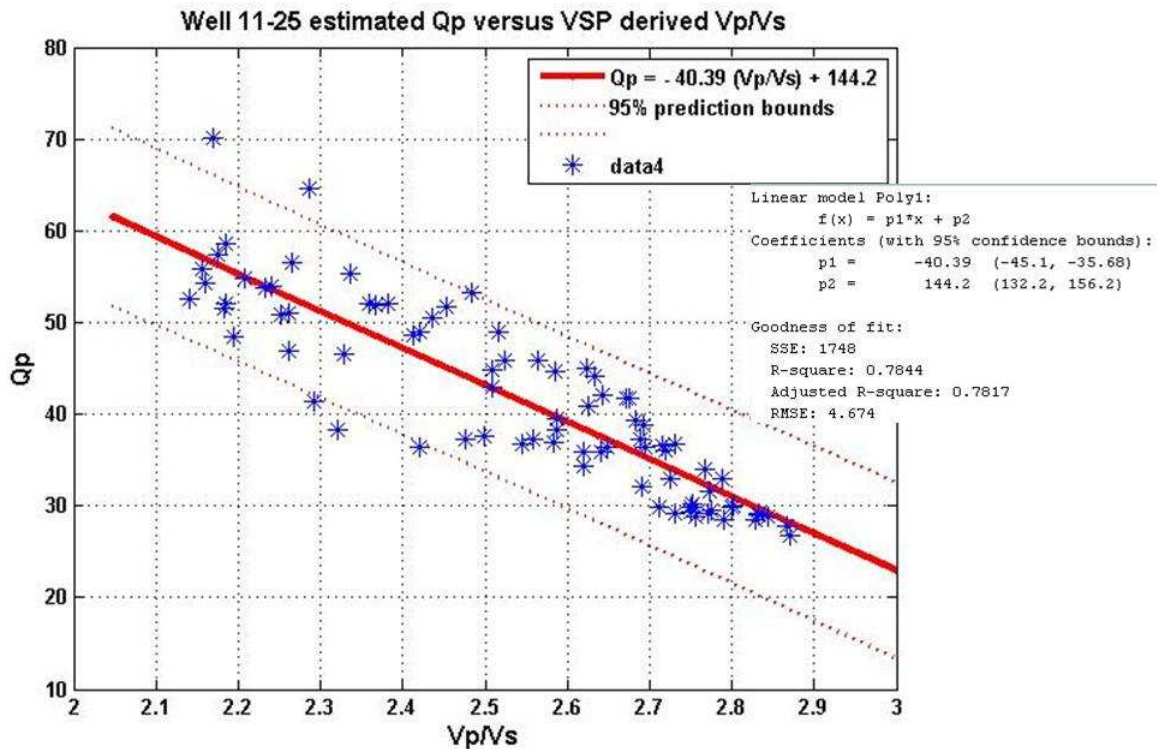


**Figure 4.14 Interval  $Q_p$  plotted versus VSP-derived  $V_p/V_s$  shows a nice linear inverse relationship.**

To show the relationship as a positive one,  $1/Q_p$  is plotted versus  $V_p/V_s$  (Figure 4.15) and the linear fitting gives:

$$1/Q_p = 0.0241 * (V_p/V_s) - 0.0375 \quad , \quad (4.6)$$

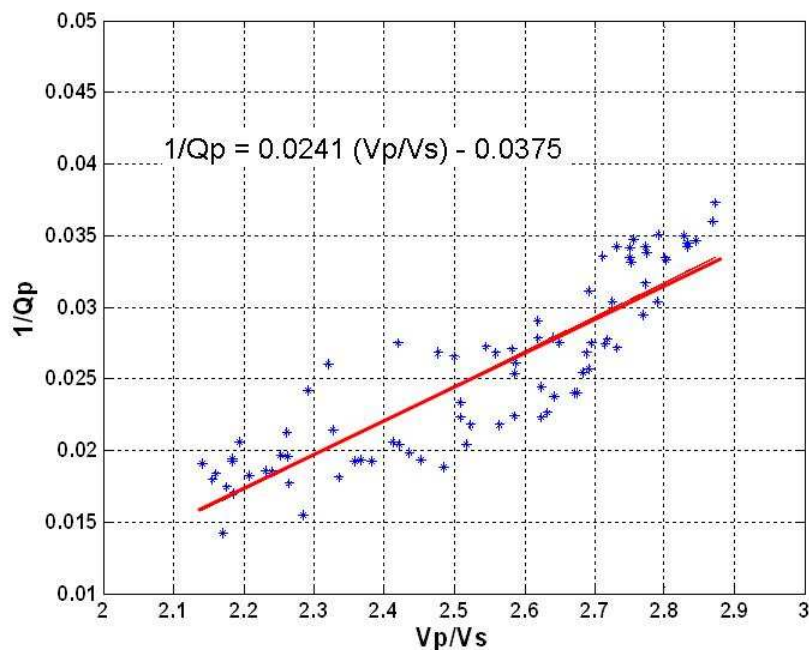


**Figure 4.15**  $1/Q_p$  plotted versus VSP-derived  $V_p/V_s$  to show a positive relationship.

By looking at the criteria of goodness for fitting, it's noticed that the linear regression of  $Q_p$  versus  $V_p/V_s$  is the best and have relative high correlation (Table 4.2), which means we might be able to predict  $P$ -wave  $Q$  factor from  $V_p/V_s$  under certain circumstances, in this case, for the shallow sand-shale dominated formations in Western Canadian Sedimentary Basin.

Variables	SSE	R-square	Adj. R-square	RMSE
$Q_p$ vs. $V_p$	4770	0.4117	0.4044	7.721
$Q_p$ vs. $V_s$	2431	0.7001	0.6964	5.513
$Q_p$ vs. $V_p/V_s$	1748	0.7844	0.7817	4.674

**Table 4.2** Comparison of fitting quality for crossplotting  $Q_p$  versus  $V_p$ ,  $V_s$  and  $V_p/V_s$  respectively in well 11-25 of Ross Lake.

## **4.4 Example two: Pikes Peak VSP data**

### ***4.4.1 Introduction of Pikes Peak oilfield***

The Pikes Peak heavy-oil field, operated by Husky Energy Ltd., is in West Central Saskatchewan, about 40 km east of city Lloydminster (Figure 4.16). The reservoir is a channel sand in Waseca formation of Mannville group of Lower Cretaceous age. The predominantly quartz, well-sorted sand has 32 - 36% porosity, 1 - 10 Darcie permeability, 5 – 30 m net pay at depth range 475 - 500 m (Wong et al., 2001). The oil has a gravity of 12° API at the reservoir temperature. A steam-driven enhanced recovery process is deployed for production. Hulten (1984) provided a comprehensive geologic description for the Waseca formation in and around the Pikes Peak field.

Considerable effort has been expended to research this steam injected heavy-oil field after the release of the Pikes Peak data to the University of Calgary. Downton (2001) performed an AVO study to map the steam chamber. Xu et al. (2001) reported on the acquisition and processing of VSP data. Hedlin et al. (2001) investigated the delineation of steam flood using the seismic attenuation. Newrick et al. (2001) presented an investigation of seismic velocity anisotropy at Pikes Peak using VSP data. Zou et al. (2002) conducted a time-lapse seismic modeling. Watson (2004) investigated the acoustic impedance inversion and showed the stratigraphy of the reservoir. Soubotcheva (2006) studied the reservoir property prediction using well logs, VSP and 2D-3C seismic data.



**Figure 4.16** Map of major heavy-oil deposits of Alberta and Saskatchewan with the location of Pikes Peak field (after Watson, 2004).

#### *4.4.2 VSP and well logs*

A walkaway VSP was conducted in well 141/15-06-50-23W3 using Schlumberger's three-component five-level ASI downhole tool. A MERTZ HD18 Buggy vertical vibrator with a linear sweep from 8 Hz to 200 Hz served as the source at zero-offset (23 m source to wellhead) as well as other five offset locations from 90 m to 450 m with 90 m increment. The downhole geophones were clamped from 514.5 m to 27 m measured from the KB with 7.5 m spacing resulting in a total of 66 receiver stations.

There are Gamma ray, density and dipole sonic logs in well A15-06 (Figure 4.17). Formation tops from top to bottom are posted as: 2WS (stands for “Second White Specs”), BFS (stands for “Base of Fish Scale”), Colony, McLaren, Weseca, Homogeneous Sand and Sparky. The top of Colony sand at around 450 m is shown on all logs, and specifically, the shear-wave velocity shows a significant step boundary. Crossing this boundary, which is from Joli Fou shale to Colony sand,  $V_p$  increases from ~ 2500 m/s to ~ 2600 m/s, about 4% increment. In contrast,  $V_s$  increased dramatically from ~ 600 m/s to ~ 1300 m/s average, about 116%. In consequence, the  $V_p/V_s$  drops from 4.0 – 5.0 (kind of marine soft sediments?) to 1.8 – 2.0 (typical sand) across this boundary.

For comparison purpose,  $V_s$  derived from the measured  $V_p$  using Castagna’s relationship (equation 1.10) is overlaid in the same track of measured  $V_s$  (track 4 of Figure 4.17). Similarly, the calculated  $V_p/V_s$  (magenta curve in track 5 of Figure 4.17) is also displayed in the same scale with the measured  $V_p/V_s$ . It’s noticed that the measured  $V_s$  and calculated  $V_s$  are quite comparable in the interval of above the anonymous top at ~ 200 m and the interval below Colony at ~ 450 m. In between, from 200 m to 450 m, the measured  $V_s$  is significantly smaller than  $V_s$  derived from the empirical relationship. As a result, the measured  $V_p/V_s$  has a higher value, i.e., 4.0 - 5.5, which may suggest there is a need to locally calibrate the mudrock line relationship of  $V_p$ - $V_s$  in this area. Another possibility is that the measured  $V_s$  from the dipole sonic log maybe is questionable.

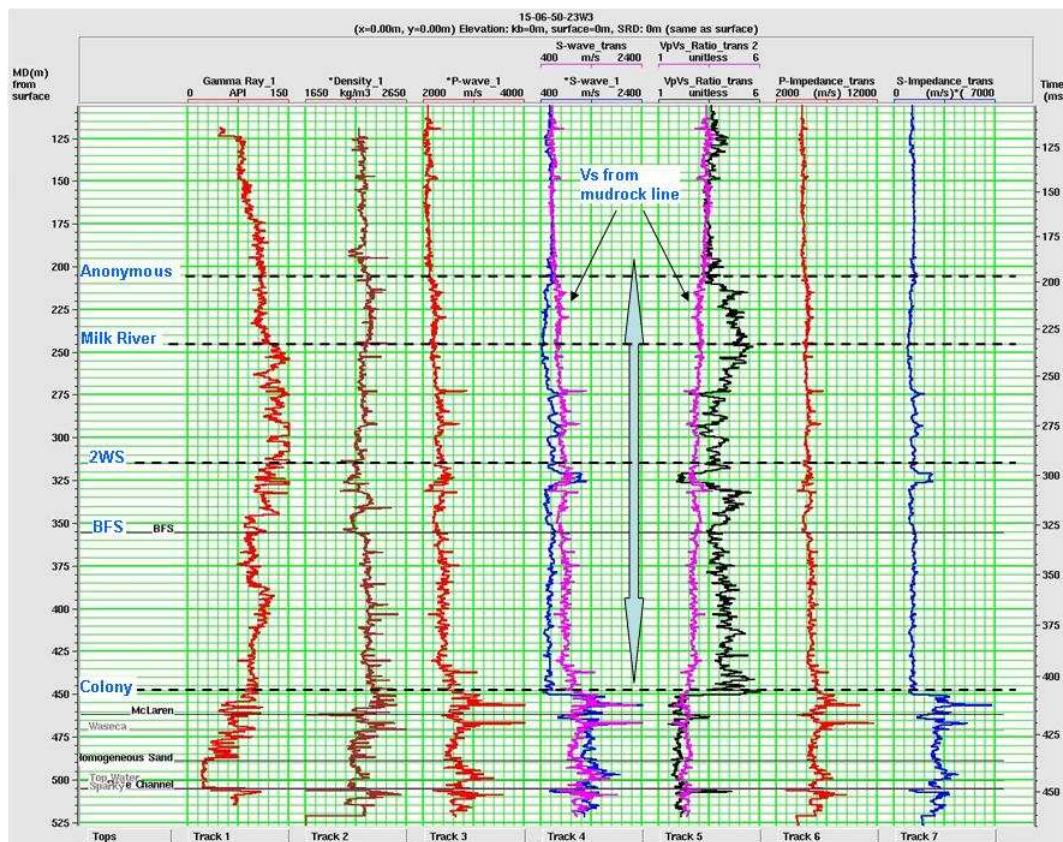


**Figure 4.17** Logs of well A15-06. The magenta curves are  $V_s$  derived from  $V_p$  using mudrock line and the resulting  $V_p/V_s$ . The arrow indicates the discrepancy between the measured  $V_s$ ,  $V_p/V_s$  and derived  $V_s$ ,  $V_p/V_s$  by the mudrock line.

#### 4.4.3 Data preparation and $Q$ estimation

First breaks are picked on the VSP raw record of station stack (Figure 4.18). The numbering convention for processing is that the shallowest station is numbered 1 and the deepest station is numbered 66 for the total 66 stations, although in logging sequence the deepest station recorded first. Four high-frequency station pairs with regular spacing are clearly observed, which may be caused by the casing or tool ringing due to bad cementing or geophone coupling.

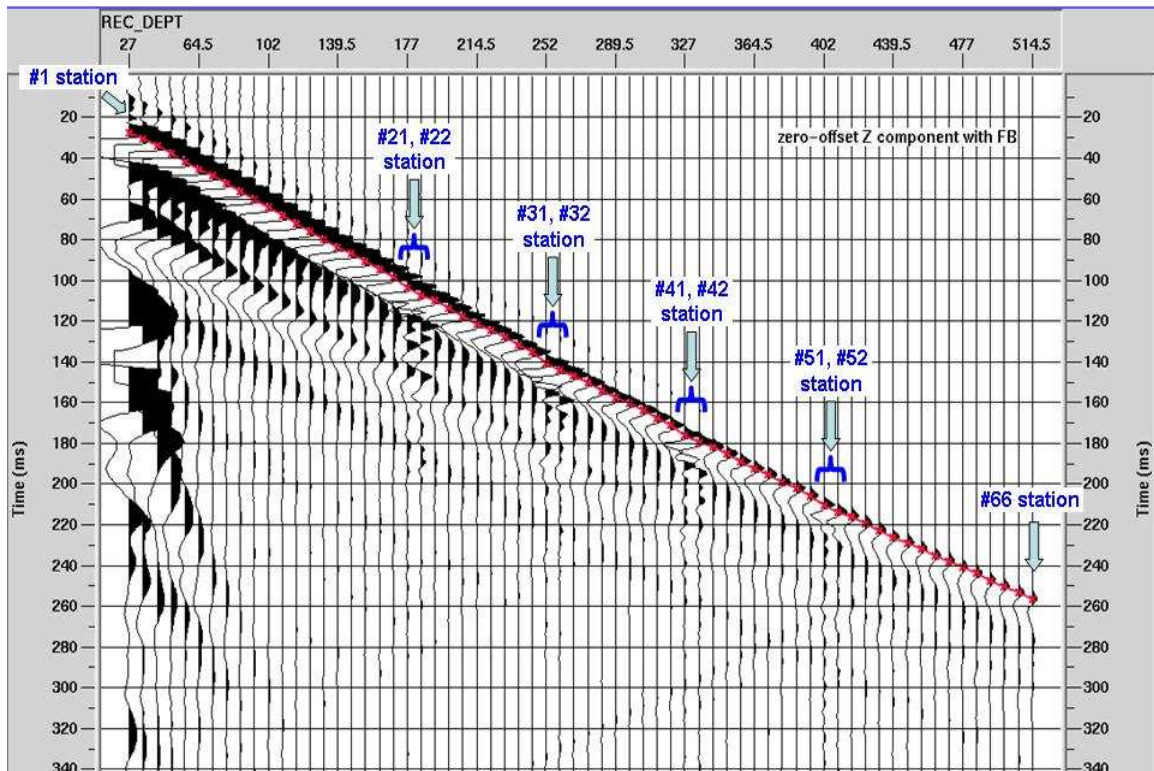


**Figure 4.18** Raw zero-offset VSP record in well A15-06 with the first break picks posted (red). Arrows indicate the 8 problematic receiver stations.

Figure 4.19 shows the amplitude spectrum of average of all traces and each individual trace. The general frequency band is from 12 Hz to 200 Hz. In the plot of spectrum for each trace (panel (c) of Figure 4.19), the four problematic station pairs demonstrate much higher frequency than other traces and could not be filtered out by a band-pass filter as it is in the signal frequency bandwidth.

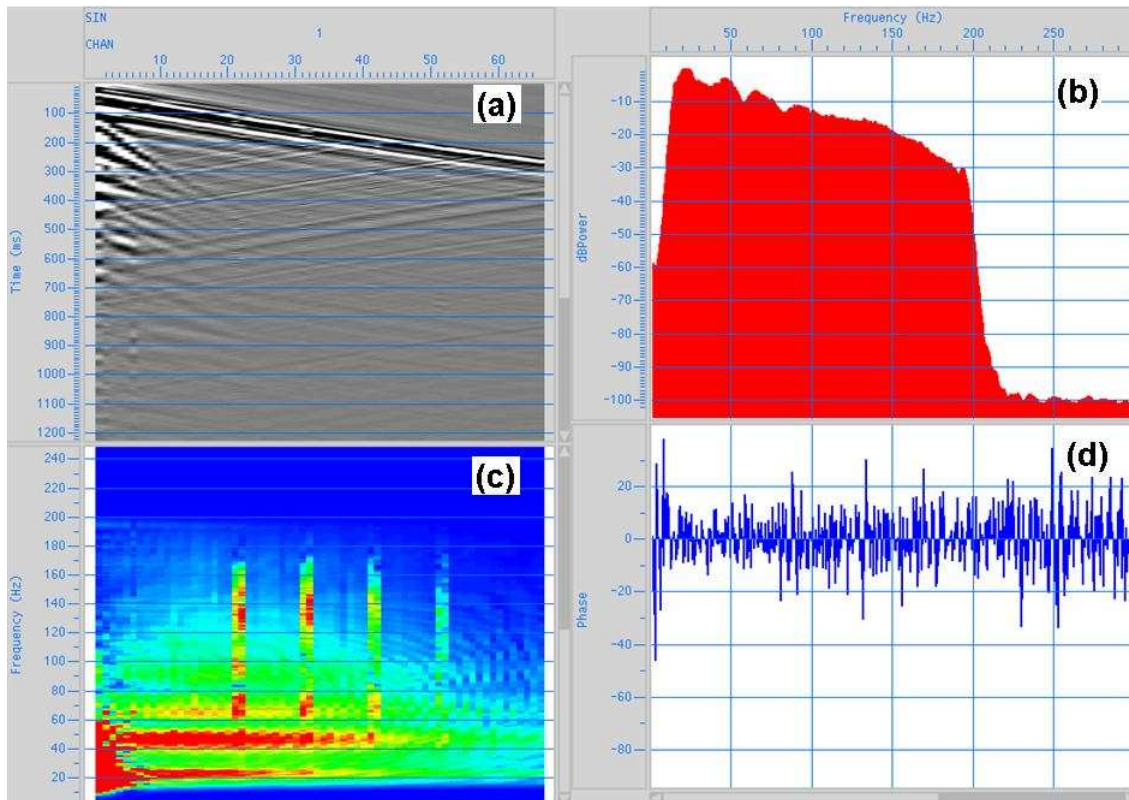


**Figure 4.19 A15-06 zero-offset VSP raw record frequency and phase analysis: (a) AGC applied raw record; (b) the average frequency spectrum of all traces in time window 0 – 600 ms; (c) the spectrum of each individual trace, red is high; (d) the phase spectrum.**

Then, the total wavefields are aligned at 100 ms by the first break time. After testing, a 3-sample by 7-trace median filter is used to separate the total wavefields into down-going and up-going wavefield.

As there is no shear-wave source in Pikes Peak VSP survey, only  $P$ -wave quality factor  $Q_p$  is calculated here. The input data for estimating  $Q$  factor are the down-going waves. As in the example of  $Q$  calculation from Ross Lake VSP data, using equation (2.5) and setting the ground surface as the reference level, the  $Q_{p\_ave}$  curve for the entire

interval is calculated and plotted against depth (Figure 4.20). The eight problematic stations are excluded from  $Q_{p-ave}$  calculation and linearly interpolated afterwards.

To have a qualitative view before going ahead to calculate the interval quality factor  $Q_{p-int}$ , the quality indicator curve, ratio of the first break time to the average  $Q$ ,  $T/Q_{p-ave}$  is also calculated and plotted in depth (the right panel in Figure 4.20). It's observed that from about 150 m to 450 m the  $T/Q_{p-ave}$  is generally increasing, with 2 different but positive slopes, although there are quite a few adjacent station pairs having negative slopes. This indicates that we could get reasonable (positive) interval  $Q$  in this depth interval. However, around the reservoir level which is below the top of Colony at 450 m, the  $T/Q_{p-ave}$  curve has generally a negative slope indicating the interval  $Q$  between the adjacent geophones will not be stable.

Different size boxcar smoothers are used in attempt to smooth  $Q_{p-ave}$ . The left panel of Figure 4.21 shows the results of the interval  $Q_p$  calculated from 11-, 21- and 31-point smoothed  $Q_{p-ave}$ . Because those interval  $Q_p$  are still oscillating, a 3-point median filter has been applied to remove the oscillated values. The 31-point smoothed and 3-point median filtered  $Q_{int}$  is chosen as the final result.

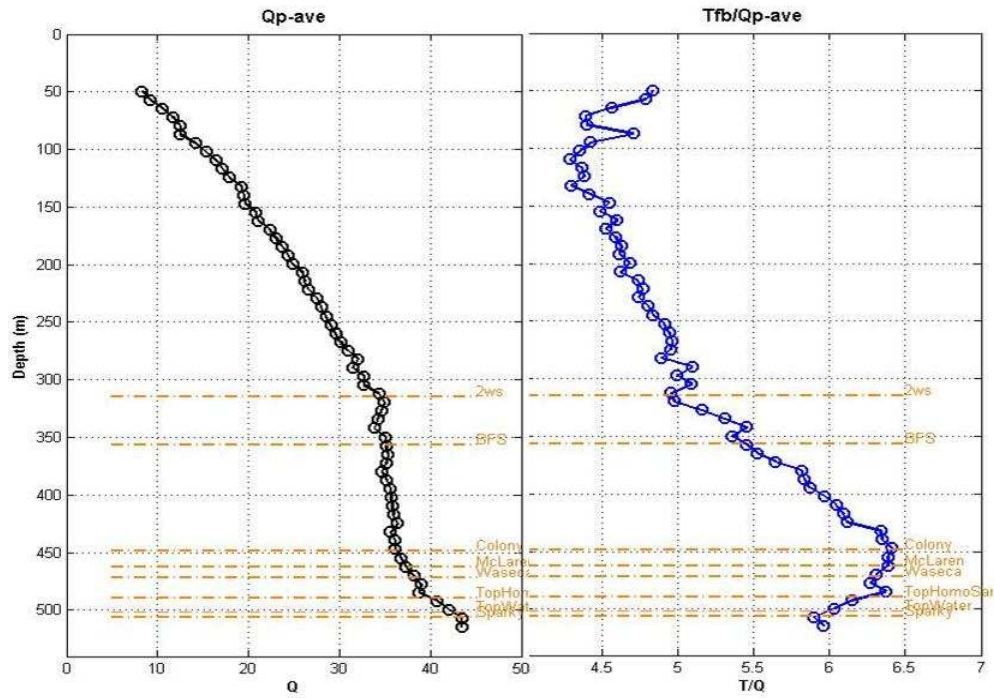


Figure 4.20 The calculated average  $Q$  factor at each station (left) and the QC curve of  $T_{fb}/Q_{ave}$  (right) from VSP of well A15-06.

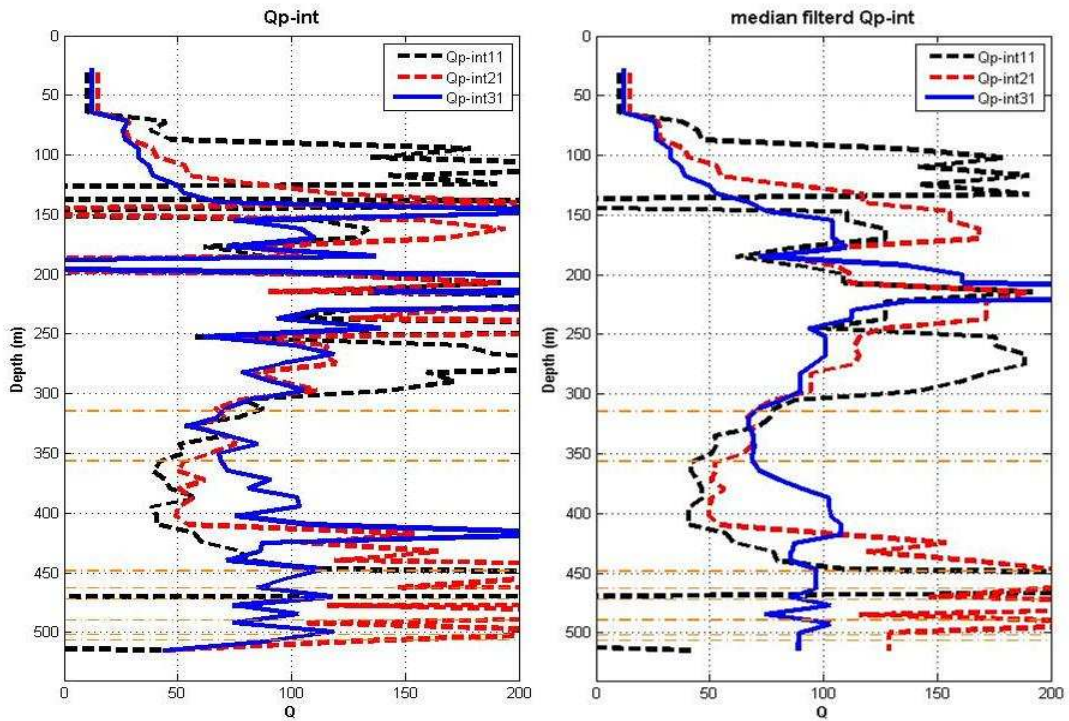


Figure 4.21 Calculated  $Q_{p-int}$  from 11-, 21- and 31-point smoothed  $Q_{p-ave}$  (left panel) and 3-point median filtered  $Q_{p-int}$  (right panel).

#### 4.4.4 Crossplotting $Q_p$ versus $V_p$ , $V_s$ and $V_p/V_s$

Now we have the VSP-derived formation quality factor for  $P$ -wave  $Q_p$  and log measured  $V_p$  and  $V_s$ . To investigate the relations between them, the log measured velocity curves with sample rate of 0.1 m need to be up-scaled to the VSP sample rate which is 7.5 m. To do so, the log curves  $V_p$  and  $V_s$  are filtered by a 11-point median filter first to remove some high frequency noise, then averaged in 7.5 m depth windows between any two adjacent VSP stations. The averaged values of  $V_p$  and  $V_s$  are put at the lower geophone depth of the two adjacent stations, called “blocked- $V_p$ ” and “blocked- $V_s$ ”. Then by dividing the blocked- $V_p$  by the blocked- $V_s$ , we get the blocked-  $V_p/V_s$ . Now the  $V_p$ ,  $V_s$ ,  $V_p/V_s$  and  $Q_p$  curves have the same sample rate (Figure 4.22).

Looking at the interval from  $\sim 200$  m to the top Colony at 450 m, the  $V_p/V_s$  swings from  $\sim 3.4$  to 5.0, and  $Q_p$  shows a single trend of decreasing, with the shallow part about  $\sim 100$  to 150 and the lower part around 50. It seems no apparent relationship between  $Q_p$  and  $V_p/V_s$  has been observed.

Below Colony formation, around the reservoir level, the  $Q_p$  is about 85 to 90, and  $V_p/V_s$  is about 2.0 with  $V_p$  around 2700 m/s, which is common for a typical sand.

The summary of  $V_p$ ,  $V_p/V_s$  and  $Q_p$  for Pikes Peak area is listed in Table 4.3.

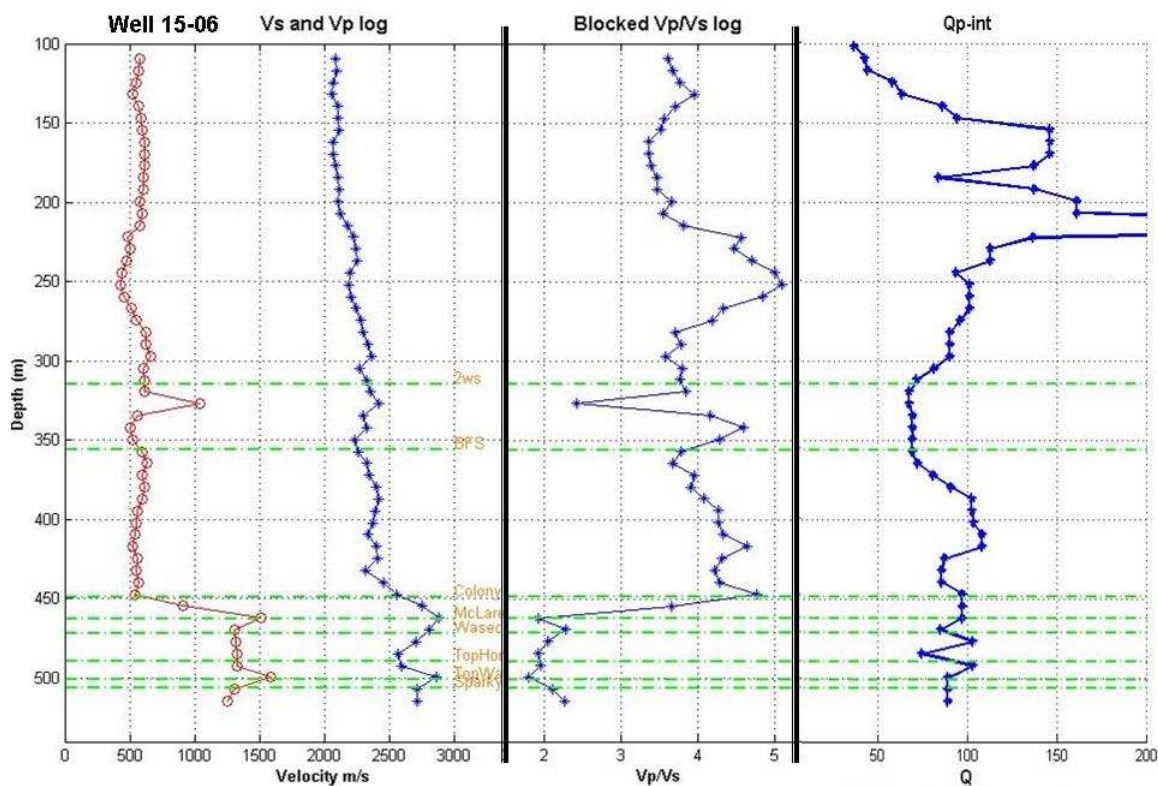


**Figure 4.22** up-scaled log  $V_p$ ,  $V_s$  and  $V_p/V_s$ , and  $Q_p$  plotted in depth, with formation tops posted.

Formation and depth	$Q_p$	$V_p/V_s$ (log)	$V_p$ (m/s)
205m - 245m (Anonymous ~ Milk River)	~ 150	~ 4.3	~ 2200
245m - 315m (Milk River ~ 2WS)	~ 85	~ 4.0	~ 2300
315m - 450m (2WS – Colony)	~ 85	~ 4.0	~ 2400

**Table 4.3**  $Q_p$ ,  $V_p/V_s$  and  $V_p$  for the main geological formations in Pikes Peak.

Nonetheless, the result from well A15-06 that the shallow part (150 m to 250 m) has a higher  $Q$  value than the deeper part (350 m to 450 m) would be contrary to what we normally think about the sedimentary rocks in subsurface: shallower  $\rightarrow$  less consolidated  $\rightarrow$  softer  $\rightarrow$  more attenuated  $\rightarrow$  smaller  $Q$  value. Hedlin et al. (2002) derived  $Q_p$  using the

spectral ratio method of 90 m separation and centroid frequency and spectral variance method from the same VSP data (Figure 4.23), which shows very similar trend compared with the estimated  $Q_p$  here.

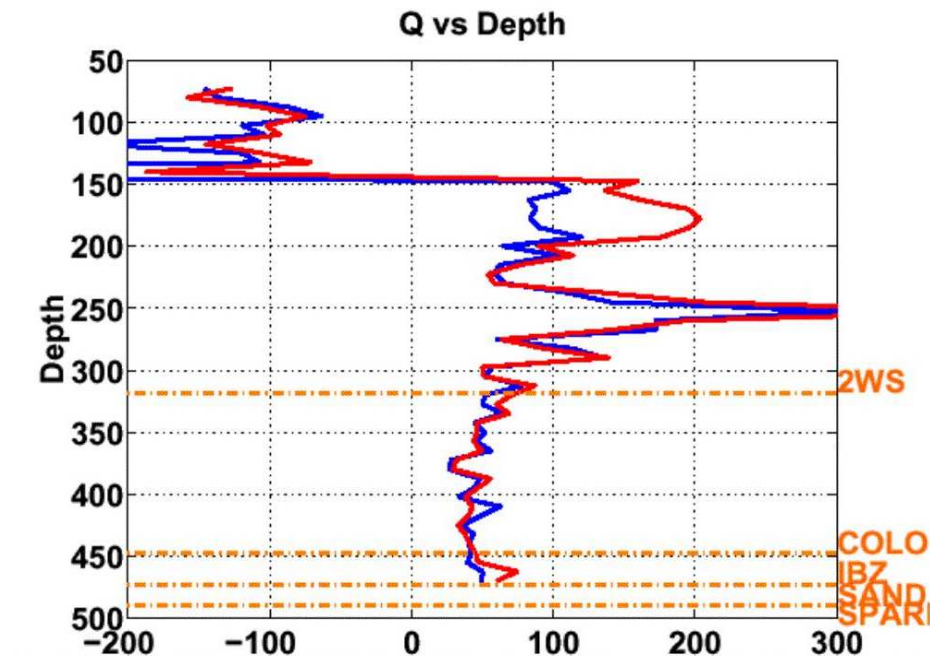


**Figure 4.23**  $Q$  versus depth calculated from VSP survey using geophones of 90 m separation (after Hedlin et al. 2002).

On the crossplot of  $Q_p$  and  $V_p/V_s$  (Figure 4.24), corresponding to the  $V_p/V_s$  range of 3.0 to 5.0, the  $Q_p$  values jump from about 50 to 150 and spread out with no observable trend.

The conclusion here is that the  $Q_p$  derived from this zero-offset VSP has no relation with the log measured  $V_p/V_s$  in the well A15-06.

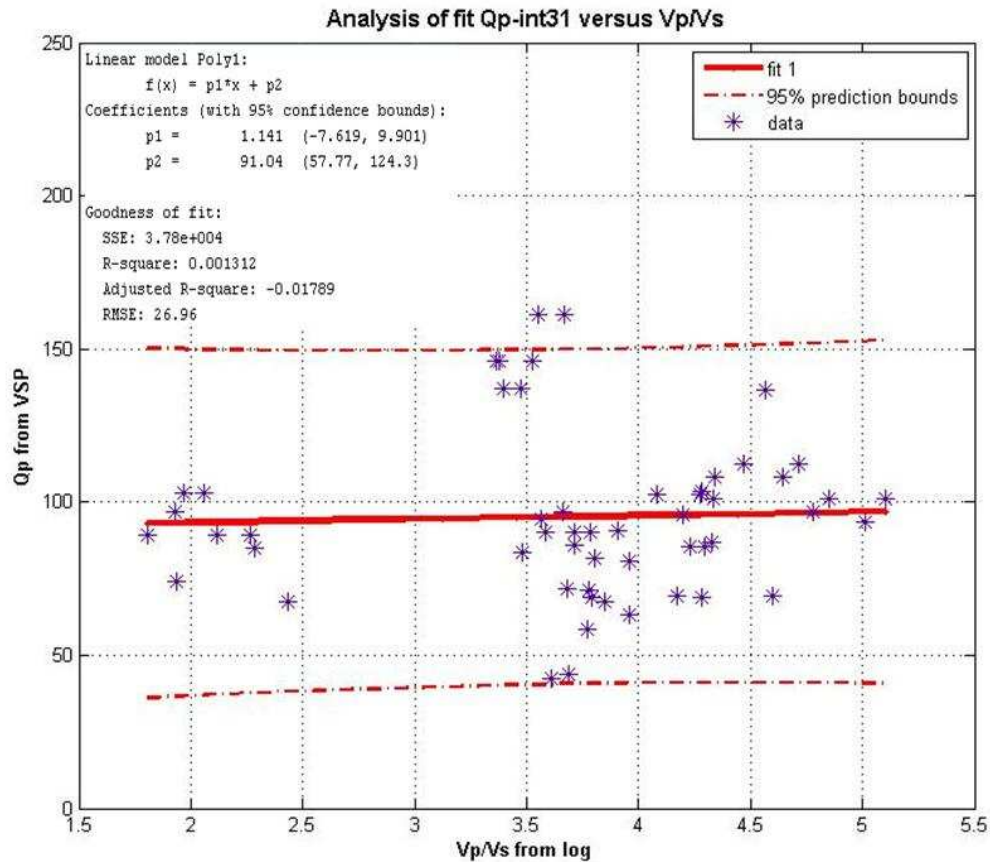


**Figure 4.24 Crossplot of  $Q_p$  versus  $V_p/V_s$  of well A15-06.**

#### 4.4.5 Discussion

To better understand the relationship between  $V_p$  and  $V_s$ , a crossplot of  $V_p$  versus  $V_s$  is generated (Figure 4.25). The mudrock line is posted as a reference. The constant  $V_p/V_s$  of 1.5, 2.0, 3.0, 4.0, and 5.0 are also overlaid. It's noticed that the data points are divided into 2 groups at the depth of 450 m or top of Colony formation. The scattered data points in whole seem not to follow the mudrock line, and also do not show any strong trend to fit a regression unless they are put into two regressions.

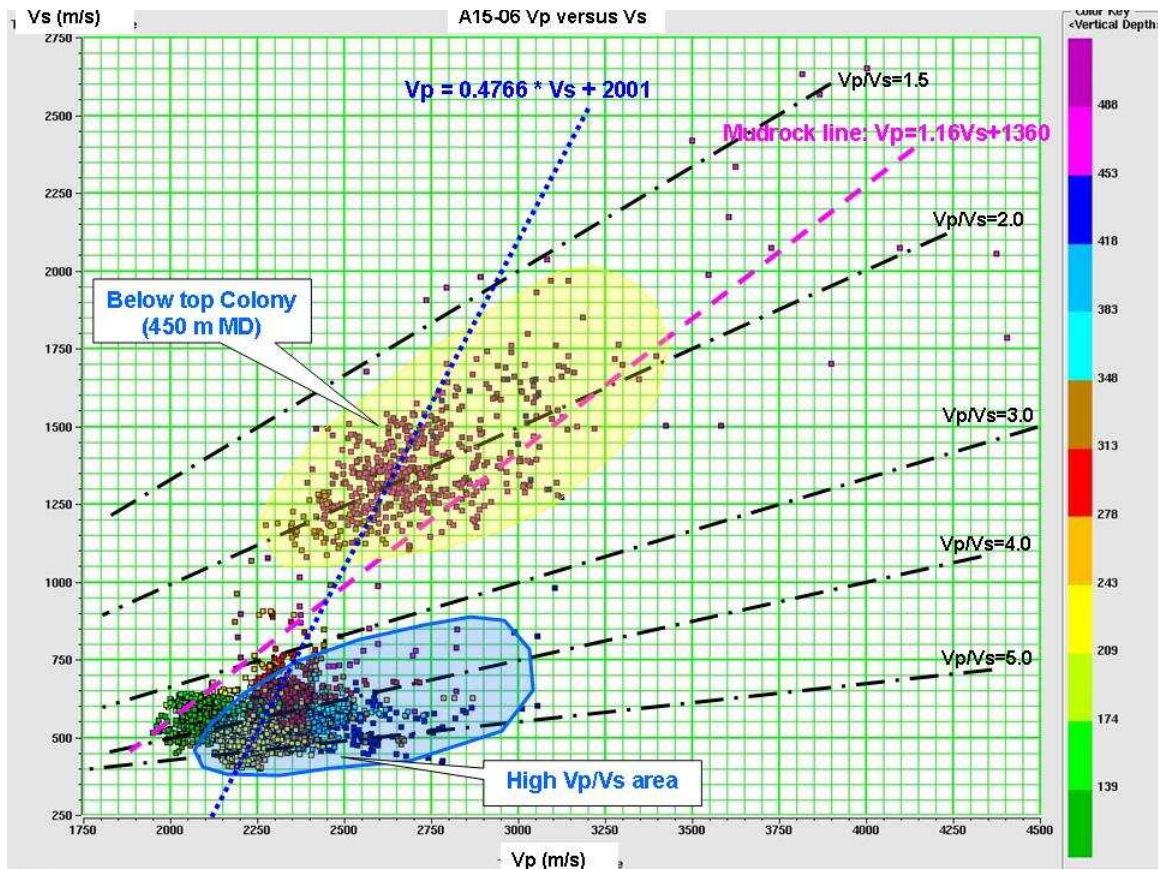


**Figure 4.25** Crossplot of  $V_s$  versus  $V_p$  log of well A15-06, with mudrock line and a few constant  $V_p/V_s$  lines posted. Color denotes the depth.

Another way to check  $V_p$ - $V_s$  relationship is to crossplot  $V_p/V_s$  versus  $1/V_s$ . Although it's the same as  $V_p$  versus  $V_s$ , the data points collapse and close to a linear relation. Crossplotting the  $V_p/V_s$  to  $V_p$  and  $V_s$ , respectively. While  $V_p/V_s$  shows no relationship with  $V_p$  (the left panel of Figure 4.26), the  $V_p/V_s$  has a very strong linear relationship with the S-wave slowness (right panel of Figure 4.26). A least-square regression fit gives:

$$V_p/V_s = 0.002001 * S\_slowness + 0.4766 , \quad (4.7)$$

where the S-wave slowness is in  $\mu\text{s}/\text{m}$ .

Substituting the  $S$ -wave slowness by  $S$ -wave velocity, the regression relationship of equation (4.7) becomes:

$$V_p = 0.4766 * V_s + 2001, \quad (4.8)$$

where both  $V_p$  and  $V_s$  are in m/s.

The  $V_p$ - $V_s$  relationship of equation (4.8) is posted on the  $V_p$  and  $V_s$  crossplot of well A16-05 as a blue dotted line (Figure 4.25). It has a much steeper slope of 0.4766 compared to the mudrock line's 1.16. This looks like an exception of Castagna's  $V_p$ - $V_s$  relationship in sand-shale sequence. Another possibility is that the  $V_s$  log in this well is not quite reliable at shallow depth.

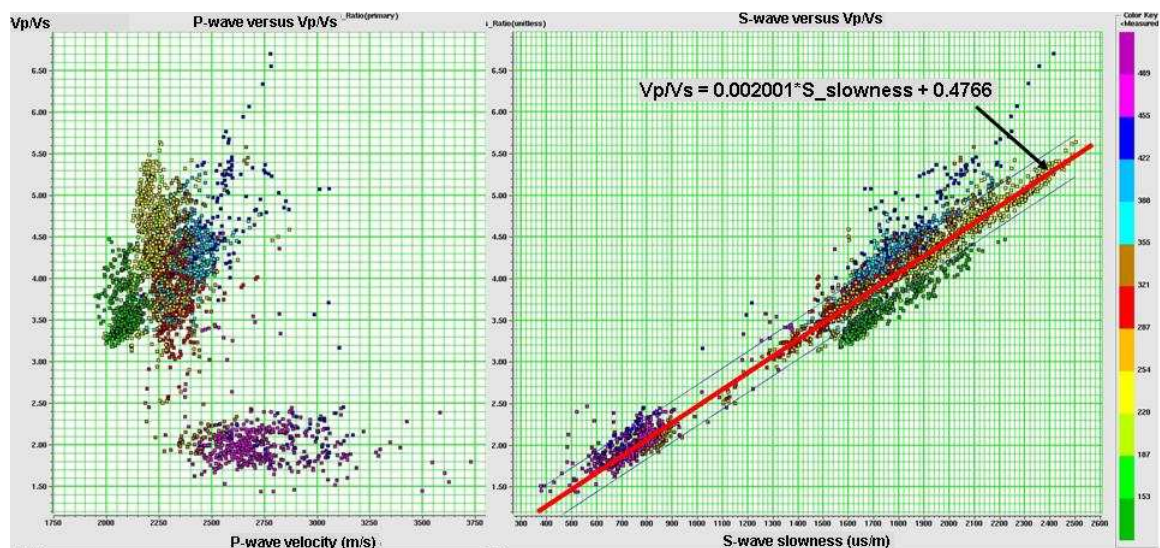


**Figure 4.26** Crossplot of  $V_p/V_s$  versus  $V_p$  (left) and  $V_p/V_s$  versus  $S$ -wave slowness (right).

The above analysis suggests that the non-correlation between  $Q_p$  and  $V_p/V_s$  in well A15-06 might be a two-fold problem: (1) some VSP calculated  $Q$  values possibly do not represent the formation  $Q$ ; (2) some log measured  $V_s$  values possibly do not represent the formation  $V_s$ .

## **4.5 Discussion**

### ***4.5.1 Intrinsic and extrinsic***

Lab measurement is more likely to be considered as measuring the intrinsic property of the sample rock. Field measurement is more likely to measure the system value in the vicinity of a sample formation, or a combination of rocks, and including the condition between casing and formation (if in a cased well-bore), the coupling condition between geophone and casing.

### ***4.5.2 Well bore structure and cement bond in cased hole***

A lot of times VSP survey is acquired in the cased-hole condition. Different from the open-hole operation, where the downhole geophone is directly clamped against the formation (although the coupling between the sonde and wellbore sometimes is an issue), the geophone in cased-hole VSP is pushed against the casing. So, when the wave travels from the surface source point down, it passed the earth layers, cement between formation and casing, and the casing, before it reaches the downhole geophone. The two material interfaces (casing-to-cement and cement-to-formation) and sometimes two annulars could affect the wave propagation, especially the amplitude and phase. In poor cement bond intervals, things are getting even worse. It's usually not a severe problem if the purpose of VSP is to get time-depth pairs and formation velocity from the first arrivals. However, to estimate the formation  $Q$  factor from amplitude information could be problematic when the annular are present.

Usually there is a surface casing for any well. So, there are commonly at least two casing strings and two cement layers at the shallow part. When a wave travels down through the shallow unconsolidated formation and hard cement and steel casing to get to the downhole geophone, depending on the bonding conditions, it would be quite complicated to determine the distribution of which part to the recorded amplitude for this steel-cement-steel-cement-formation system. This may possibly explain why Pikes Peak data has much higher  $Q$  at shallow formation which has relative high  $V_p/V_s$  value.

#### ***4.5.3 Near field effects***

Haase and Stewart (2010) point out that attenuation ( $Q$ ) determined by the spectral ratio method in the near field (first several hundred meters) is faulty. A correction term has to be used to give reasonable  $Q$  values. This might be part of what's causing the problem at shallow depth with Pikes Peak data.

#### ***4.5.4 Consistency of VSP source***

While the VSP is acquired in a well from deep to shallow, the surface condition at the source location may be changing (getting better) as the vibrator continues to shake. This may enhance the frequency contents penetrated into the earth. This, of course, violates the assumption of a constant source. It would be useful to have a monitor geophone at surface to record the source signature.

#### ***4.5.5 $Q$ compensation for P-, S- and PS-wave seismic data***

From log of well A15-06, the  $V_p/V_s$  is in the range of 3.0 - 5.0 at the near surface. This implies that the wavelength of  $S$ -wave is about 3 to 5 times shorter than the  $P$ -wave for same frequency component. In other words, given the same distance, there are more cycles for  $S$ -wave to travel and hence more energy is lost due to attenuation. Even in a medium with  $Q_p=Q_s$ , energy will eventually attenuate more for the  $S$ -wave, especially for high-frequency components. So, attenuation has a larger impact on the  $S$ -wave amplitude and phase, and it's more necessary to apply the inverse  $Q$  filter to compensate the  $S$ - and  $PS$ -wave in seismic data processing.

#### **4.6 Conclusion**

The spectral-ratio method is used to calculate the interval formation quality factor  $Q$  values from zero-offset VSP. Setting the surface sweep as the reference level, the average  $Q$  from the surface to a certain downhole station is calculated. Based on a layered model, the interval formation  $Q$  between two adjacent geophone stations is then calculated from the average  $Q$ . Meanwhile, a quality indicator, the ratio of first arrival time to the average  $Q$  factor –  $T/Q_{ave}$ , has been established for  $Q$  factor estimation. This quality indicator curve reveals where the standard spectra-ratio method could give us stable  $Q$  values and where it couldn't.

In the Ross Lake example, a reliable and continuous interval  $Q_p$  curve from about 450 m to 1050 m in well 11-25 has been calculated from the zero-offset  $P$ -wave source VSP. Known from the quality indicator  $T/Q_{ave}$ , the  $Q_s$  is not stable for the  $S$ -wave source VSP. Therefore, a high resolution continuous  $Q_s$  is unlikely achievable. Instead, an average  $Q_s$  over larger intervals corresponding to certain geological formations is estimated. Finally, the bulk value of  $Q_p$ ,  $Q_s$ ,  $V_p/V_s$  and  $V_p$  are estimated for four major

geological intervals in Ross Lake area: which are 0 (surface) – 400 m (top of Ribstone Creek member of the Belly River Formation), 400 m – 610 m (top of Milk River Formation), 610 m – 820 m (top of Second White Speckled Shale) and 870 m – 1050 m (top of Mannville). In general, at depth above 600 m,  $Q_s$  is about half of  $Q_p$ , or 16~17 comparing with 30~38. Below 600 m,  $Q_s$  is about two thirds of  $Q_p$ , or 26~37 comparing with 40~54.

The VSP-derived  $Q_p$  curve demonstrates an inverse linear relationship with the VSP-derived  $V_p/V_s$  curve (equation 4.6) from the Ross Lake example. This is a very interesting result as we may be able to predict attenuation from  $V_p/V_s$  which is usually considered as a lithology indicator.

In the Pikes Peak example, because the conventional vertical vibrator is used as the source, only  $Q_p$  has been estimated from the zero-offset VSP using the same method. In general, the  $Q$  factor is relative higher. For the formations above Colony, the log-measured  $V_s$  is quite low so that  $V_p/V_s$  is high, about 3.5 to 5.0. The  $Q_p$  doesn't show an obvious relationship with  $V_p/V_s$ .

## **Chapter Five: Interpretation of multicomponent seismic data on Cantarell-Sihil structure, Gulf of Mexico**

### **5.1 Introduction**

A 4C-3D seismic survey, using ocean-bottom seismometers, was conducted in 2003-2004 for Petroleos Mexicanos over the Cantarell oilfield in the southern Gulf of Mexico. The 4C-3D seismic data were acquired by Seabed Geophysical AS, using node receivers planted by Remotely Operated underwater Vehicle (ROV). The data were processed by CGG in France. The original motivation for the node seismic acquisition was to better image the Sihil reservoir - which lies below the super-giant Akal reservoir in the Cantarell oilfield. As the Cantarell area is heavily congested with production platforms and marine traffic, routine streamer acquisition is not readily applicable. Thus, the need to use ocean-bottom sensors was required.

The intention of this study is to interpret the converted-wave (*PS*) data that have resulted from the Sihil 4C-3D seismic survey. The two specific goals are: (1) to interpret the *PS* data volume via correlations with log, synthetic seismograms, VSP, and *P*-wave data volumes, (2) to attempt to find anomalies and exploration leads in the *PS* data which are beyond that of the *P*-wave data alone.

There is an enormous amount of data and knowledge concerning the Cantarell oilfield and Sihil seismic surveys, especially as concerns *P*-wave imaging. This present study, however, focuses on the *PS* data and uses previous *P*-wave interpretations in the analysis of the *PS* data. The full-wave sonic logs are analyzed first. Then *PP* and *PS* synthetic seismograms are generated and tied to VSP data. A *PS*-to-*PP* time relationship

has been developed to map the *PS* seismic volume to *PP* time. This considerably assists in the interpretation of the *PS* data. A number of horizons are picked on *PS* data volume, corresponding to same *PP* horizons. From these horizons, time thickness maps as well as interval  $V_p/V_s$  map are generated. There are some interesting features that arise from the *PS* data, including the interpretation of leaky gas zones above the Akal reservoir, new structural traps in the allochthonous Cretaceous, possible salt horizons in the deeper section, and some hints at lithology.

## **5.2 Regional geology and stratigraphy**

The Cantarell oilfield is located 80 kilometres northwest of Ciudad del Carmen, Campeche in the Gulf of Mexico (Figure 5.1). Discovered in 1976, it is one of the most prolific oil-producing fields in the world with a cumulative production of approximately 7.86 billion barrels of oil with 20-24° API for over 22 years (Aquino et al., 2003). The Akal block is the main producer of the five blocks that make up this super giant Cantarell oilfield complex (Figure 5.2). The Sihil block is situated below the Akal block, in a complicated structure zone, described as a sub-thrust compressive structure. The Cantarell reservoirs are mainly composed of carbonate rocks (Upper Cretaceous breccias and Jurassic dolomitized Kimmeridgian formation), which are intensely dolomitized exhibiting mainly intergranular, vuggy, and fracture porosities. The Sihil field is the latest discovery (in 1999).

Definition of allochthonous: Pertaining to materials, particularly rock masses, that formed somewhere other than their present location, and were transported by fault movements, large-scale gravity sliding, or similar processes. Autochthonous material, in contrast, formed in its present location. Landslides can result in large masses of

allochthonous rock, which typically can be distinguished from autochthonous rocks on the basis of their difference in composition. Faults and folds can also separate allochthons from autochthons.

(<http://www.glossary.oilfield.slb.com/Display.cfm?Term=allochthonous>)

Definition of autochthonous: Materials, especially rock masses, that formed in their present location and have not been transported. Fault surfaces can separate indigenous rocks from allochthonous rocks, although some allochthonous rocks are clearly delineated by their differing composition.

(<http://www.glossary.oilfield.slb.com/Display.cfm?Term=autochthonous>)

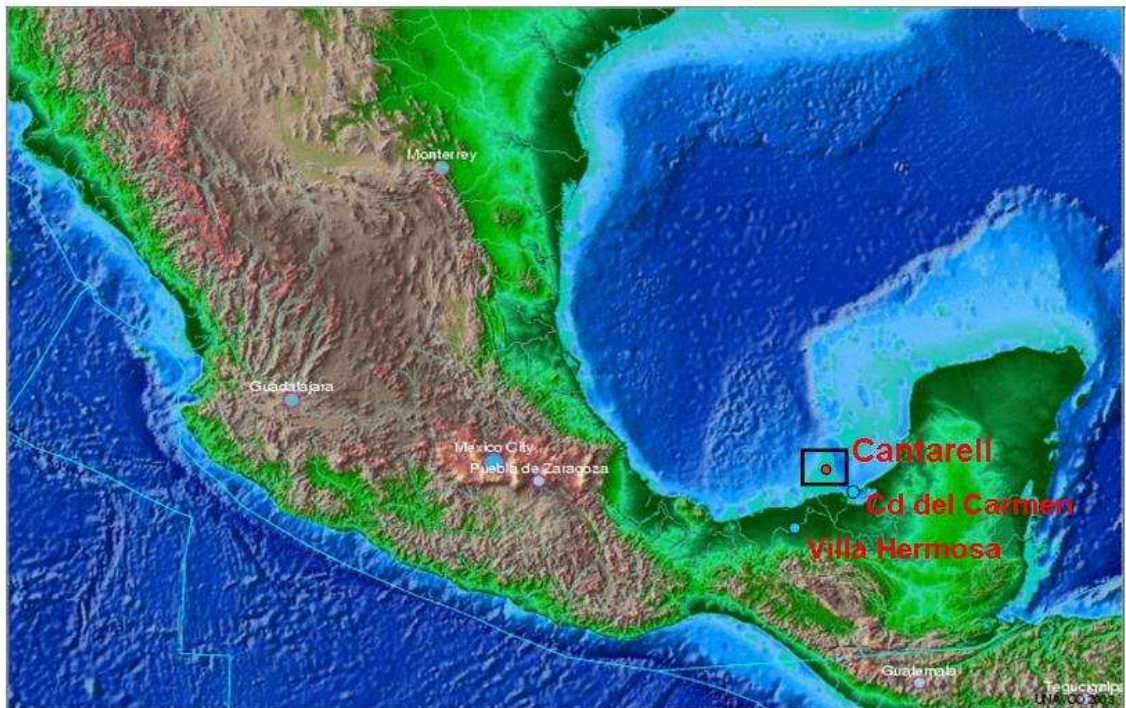


**Figure 5.1 Location map of the Cantarell oilfield in the Gulf of Mexico.**

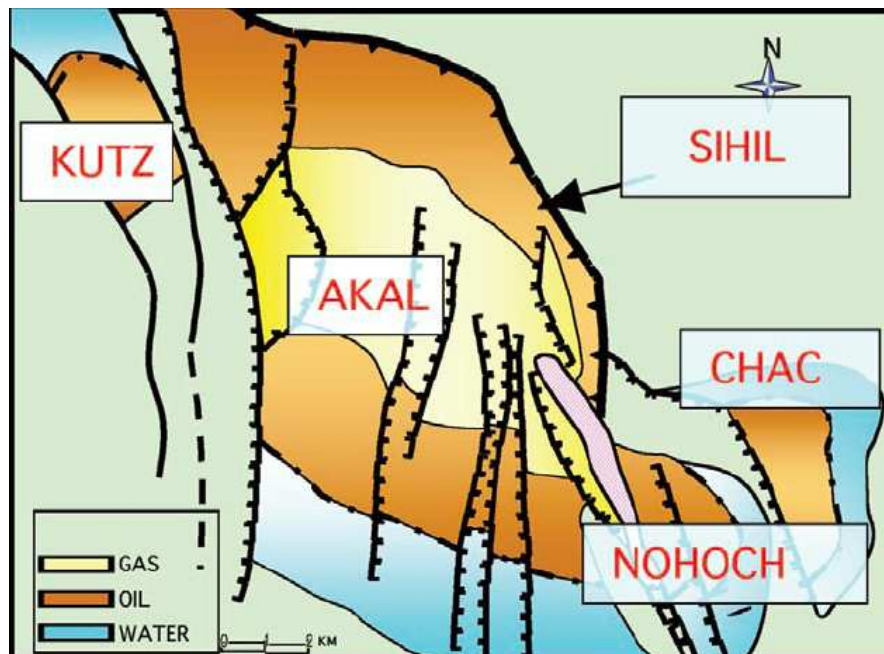


**Figure 5.2 Schematic diagram of the Cantarell field indicating five blocks and the saturation conditions in them. Note the gas cap and ring of oil (Hernandez et al., 2005).**

The geology of the Cantarell oilfield complex has been reviewed by a number of papers (Mitra et al., 2005, Hernandez et al., 2005, Chernikoff et al., 2006). The Cantarell field produces out of three separate fault-bounded allochthonous blocks: the Akal, Nohoch, and Kutz blocks. The main field is located in the Akal structure. Secondary fields in the allochthonous block include Kutz, which formed on the crest of a downthrown fault block, and Nohoch, which formed above a west-vergent backthrust. The recently discovered Sihil field is located in a subthrust-compressive structure and consists of two structural lobes formed above the sub-Sihil fault. The Chac structure is formed at the updip edge of a tilted fault block in the autochthonous block. The detailed three-dimensional structural model is being used for future production of the remaining reserves in the Cantarell field as well as for the delineation of the Sihil field.

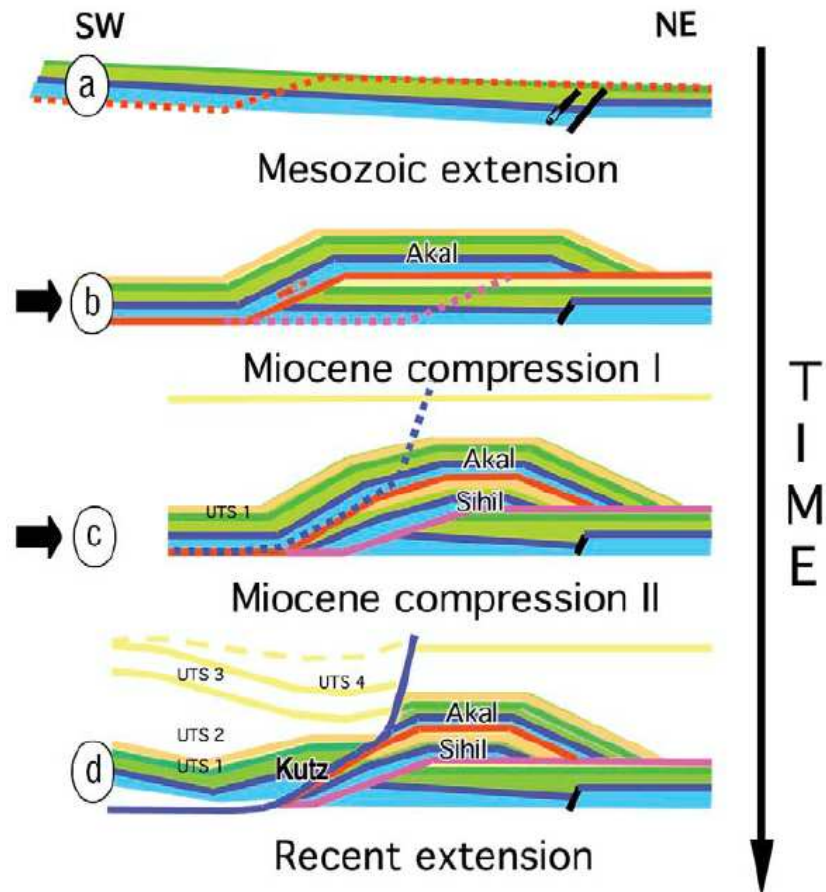


**Figure 5.3** Simplified structural evolution of the Cantarell area: (a) extension in lower Cretaceous. (b) NNE over-thrust in lower to middle Miocene. (c) duplex overthrusting. (d) listric normal faulting in Pliocene-Pleistocene (Hernandez et. al., 2005).

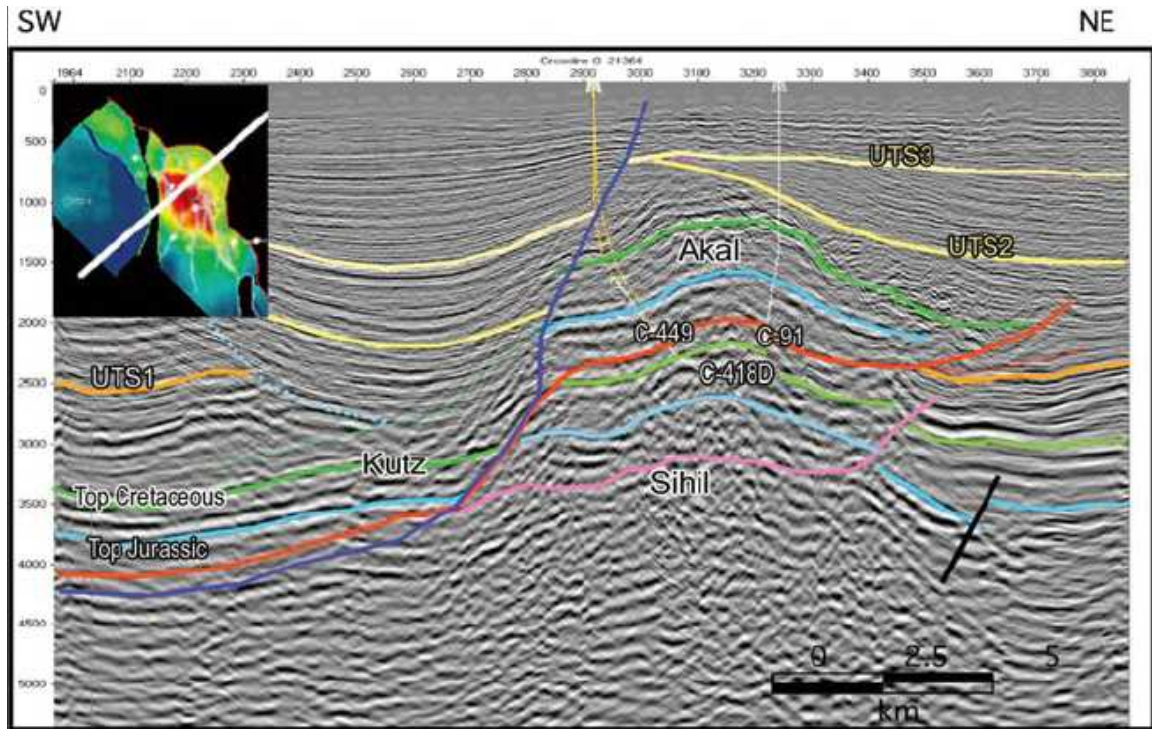


**Figure 5.4** Cross-section with interpreted faults, indicating the 3 main structure events: Mesozoic extension represented by the normal “half graben” type feature (black fault); Miocene compression represented by low angle thrust (red and purple faults); and the Plio-Pleistocene extension (blue fault). (Hernandez et. al., 2005).

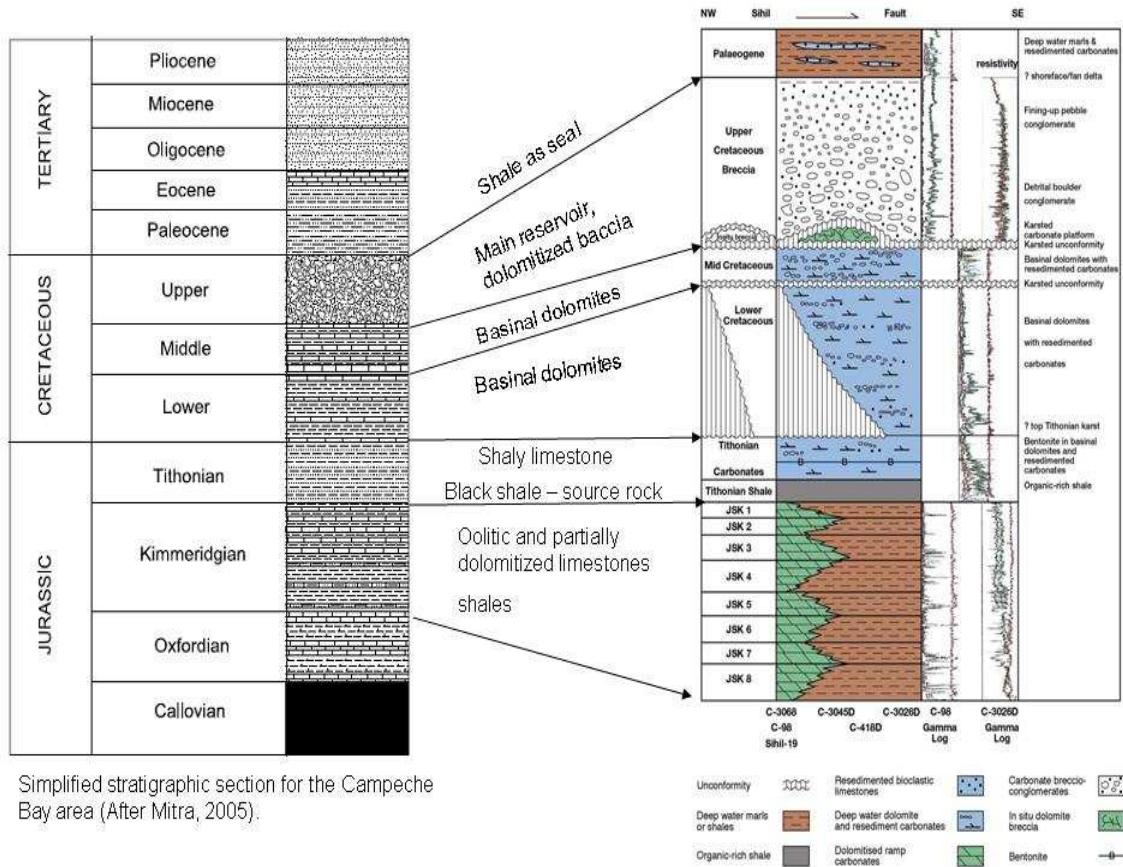


**Figure 5.5 Stratigraphy, lithology and deposition facies (after Chernikoff, 2006) with log responses from five wells. JSK stands for Jurassic Kimmeridgian.**

## **5.3 Data available**

### ***5.3.1 Seismic data***

The earliest streamer seismic data in Cantarell was acquired in late 1970s. There have been three multicomponent datasets acquired over the Sihil field since late 1990s. They include:

1. 1997 2C-3D dual-sensor, ocean-bottom-cable (OBC) survey acquired by Western Geophysical. Orthogonal shot lines to receiver lines, 650 m receiver line spacing, 50 m group interval, 250 m shot line spacing, 25 m shot interval;
2. 2000 4C-2D ocean-bottom-cable (OBC) surveys (50 m shot interval, 50 m receiver interval) by Western Geophysical;
3. 2004 4C-3D ocean-bottom-seismometer (OBS) survey by Seabed Geophysical.

The seismic data used in this study is from the 2004 4C-3D OBS survey (Vazquez et. al., 2005). The field data were acquired in 7 patches - each consisting of about 232 CASE 4C seismic nodes (with 4 channels each node). The nodes were deployed in the patches on a 400 m  $\times$  400 m grid. The mean water depth over the survey area is about 45 m. Air gun shots were recorded from a 9 km by 18 km shooting grid over each of the patches. The shot lines were about 18 km long with line spacing of 75 m and shots every 50 m. This gave rise to over 300,000 recorded shots and about 300 million traces. The CASE 4C ocean-bottom sensors used 3 Hz - 218 Hz field filters and sampling at 2 ms.

The resultant data were processed by CGG through pre-stack time migration. *PP* and *PS* data have been re-processed by CGG (March, 2006). A base map for the 3D survey, with inline and crossline numbers, is shown in Figure 5.6. We have employed the

migrated (PSTM) 3D seismic volumes of *PP* and *PS* data (processed by CGG – France) from the Seabed Geophysical 4C-3D seismic survey conducted in 2003-2004 (Vazquez et al., 2005; Maya, 2006). The inline (SW-NE direction) spacing is 18.75 m, and the crossline spacing is 25 m. The data covered area is about 220 km<sup>2</sup>, which is known the largest acquisition of this type by far.

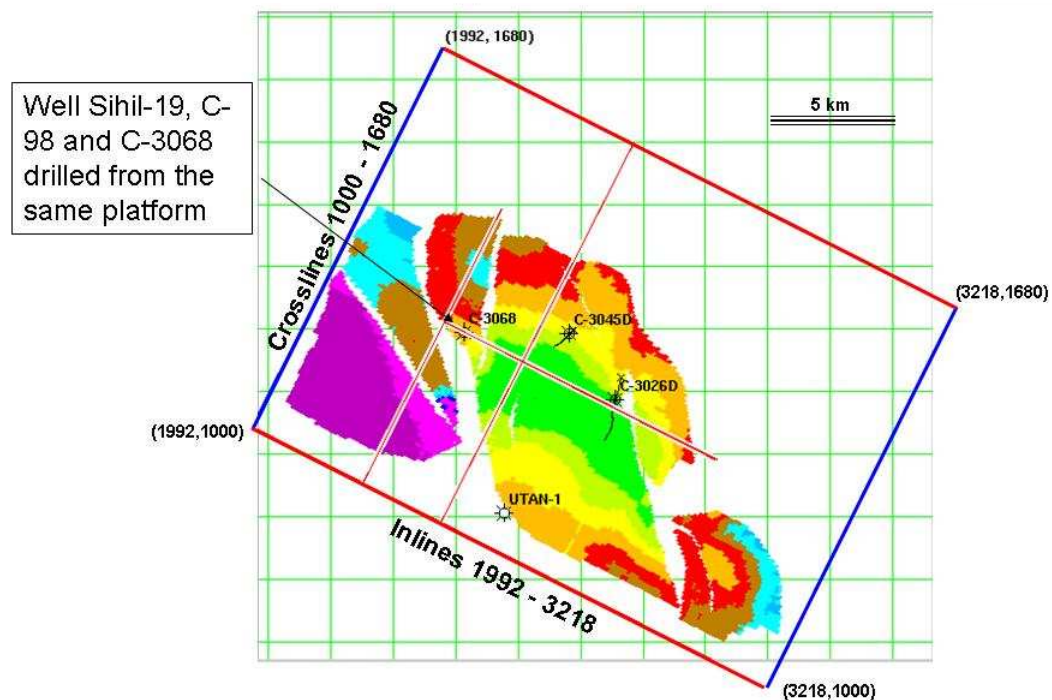


**Figure 5.6 Base map for the 4C-3D seismic survey with in-line and cross-line directions annotated. Several key wells are also shown.**

The *P*-wave data have a frequency bandwidth about 6 – 60 Hz in the shallow section and 4 - 30 Hz at depth. An initial  $V_p/V_s$  value of 2.5 was used for binning. The *PS* data (at -35 dB) is from 5 to 42 Hz. Note acquisition footprints are visible to about 1500 ms in the *PS* data (from Seabed, 2005 and our observations). We further note that it appears in Seabed Geophysical processing report that the vertical component polarity is opposite to that which is recommended by Brown et al. (2003). However, our

interpretation indicates that the *PS* and *PP* seismic data are in positive polarity (a peak corresponds to impedance increase).

### 5.3.2 Well logs

There are hundreds of wells in the Cantarell block. We have digital well logs for several wells in the Cantarell oilfield (Sihil-19, C-3026D, C-3068, C-98, C-3045D, Utan-1) as outlined in Table 5.1 and displayed in Figure 5.7 (a) to (f). The necessary logs are:

Caliper (in inch): to indicate the quality the borehole and in hence other curves

GR (in API): natural gamma ray, a lithology indicator

$V_p$  (in m/s): formation compressional-wave velocity

$V_s$  (in m/s): formation shear-wave velocity

Density (in g/cc): formation bulk density

Rt (in ohm.m): formation deep resistivity

Among these 6 wells, Utan-1 is an exceptional shallow gas well discovered the Pliocene reservoir in a small sub-basin located to the west of Cantarell. In this study, the purpose to use this well is to find a  $V_p$ - $V_s$  relationship for the shallow part (above Cretaceous allochthonous) which is not available from logs in other wells.

C-3068 is a vertical well with longest measured interval (from 500 m to 5000 m) but no  $V_s$  log. All other 4 wells have some dipole sonic ( $V_s$ ) records but are deviated. C-3026D has the longest measured  $V_p$  and  $V_s$  logs but the most deviated.

All the formation tops in these given wells are available. Four major formation boundaries are used here: top of Cretaceous allochthonous (BKS\_AL), top of Jurassic Kimmeridgian allochthonous (KIM\_AL or JSK\_AL), top of Cretaceous autochthonous (BKS\_AU) and Kimmeridgian autochthonous (JSK\_AU).

Regarding the deep Sihil field (Kimmeridgian autochthonous), well C-3068, Sihil-19 and C-98 (close to fault) encountered clean and good limestone reservoir with GR about 10 API. At the southeast of the structure, however, the GR in well C-3026D is about 100 API from Kimmeridgian autochthonous (JSK\_AU) to below, showing not a reservoir type of formation. Well C-3045D doesn't penetrate as deep to JSK\_AU.

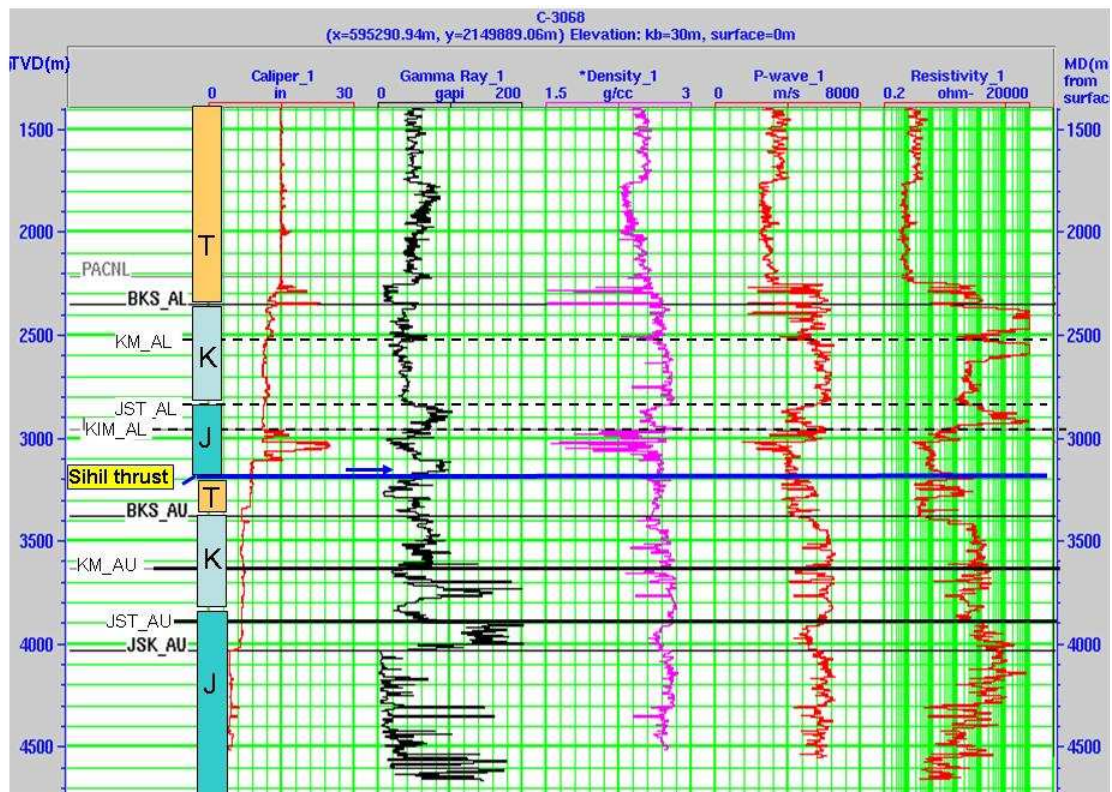


Figure 5.7 (a) Log curves in Well C-3068.

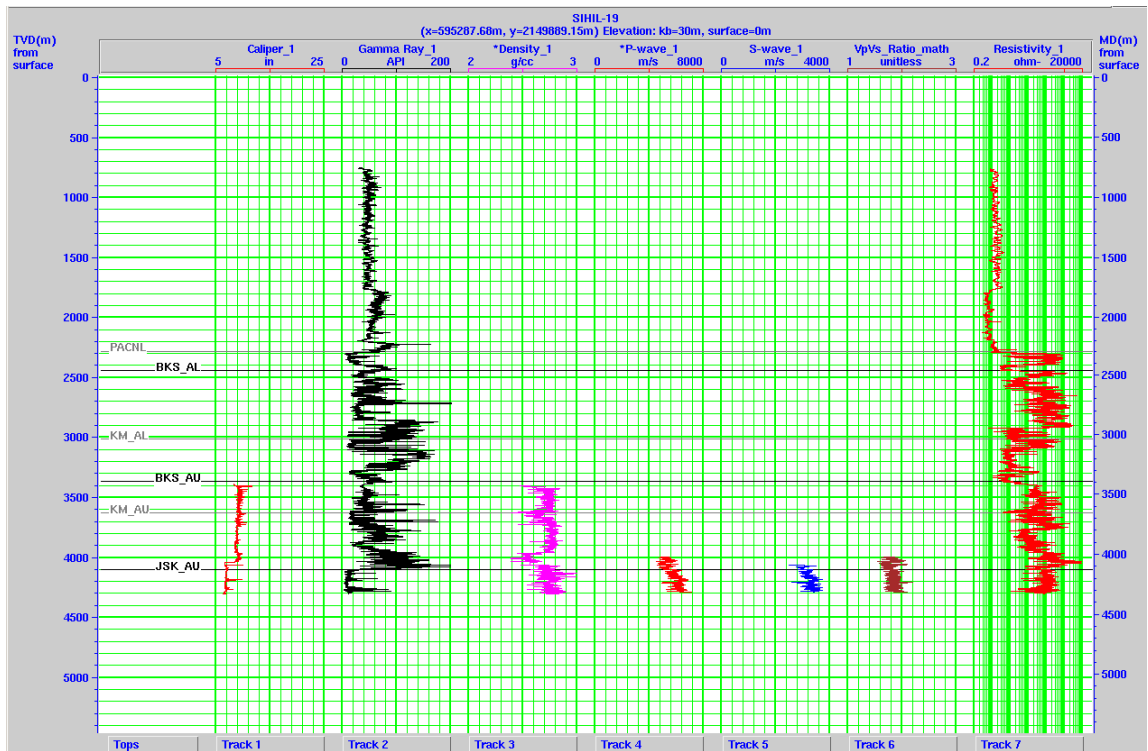


Figure 5-7 (b) Log curves in Well Sihil-19.

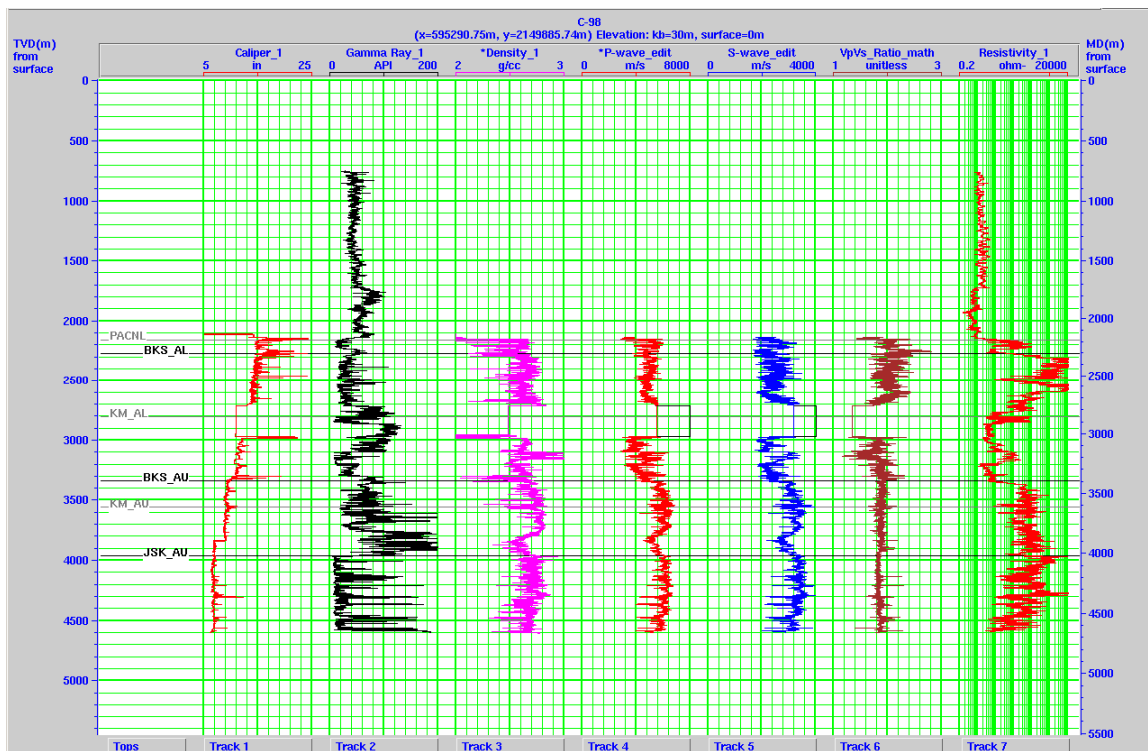


Figure 5.7 (c) Log curves in Well C-98. There is a 300 m bad data zone in the middle.

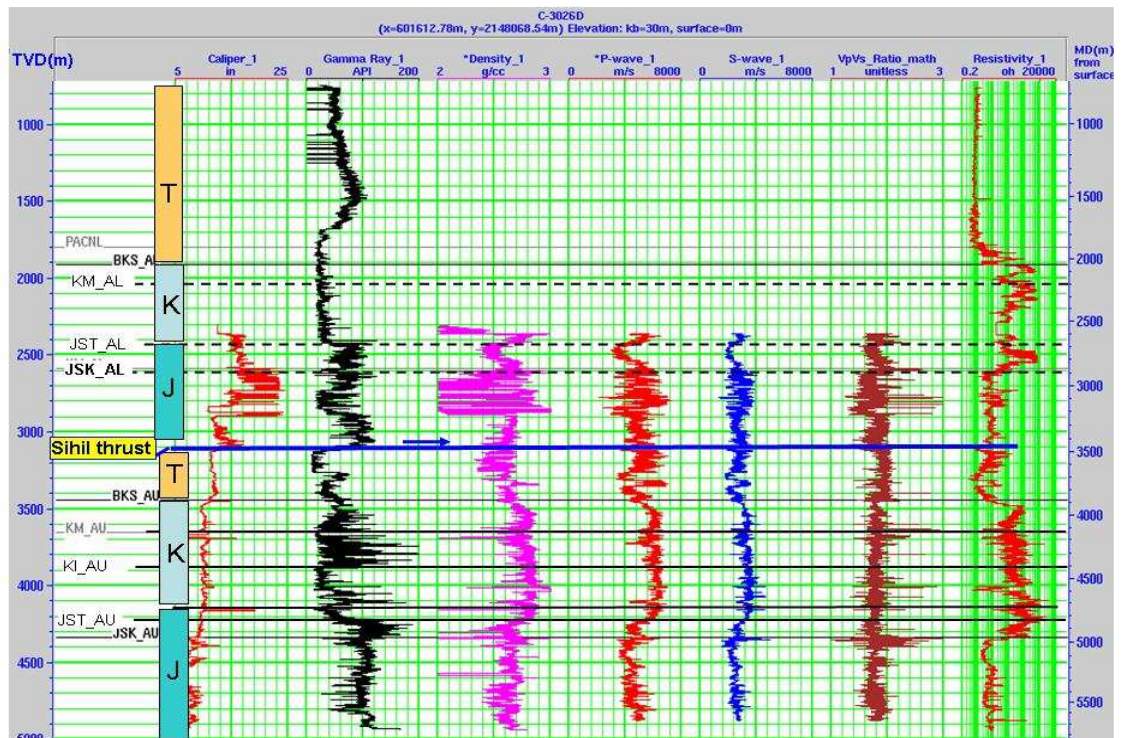


Figure 5.7 (d) Log curves in Well C-3026D.

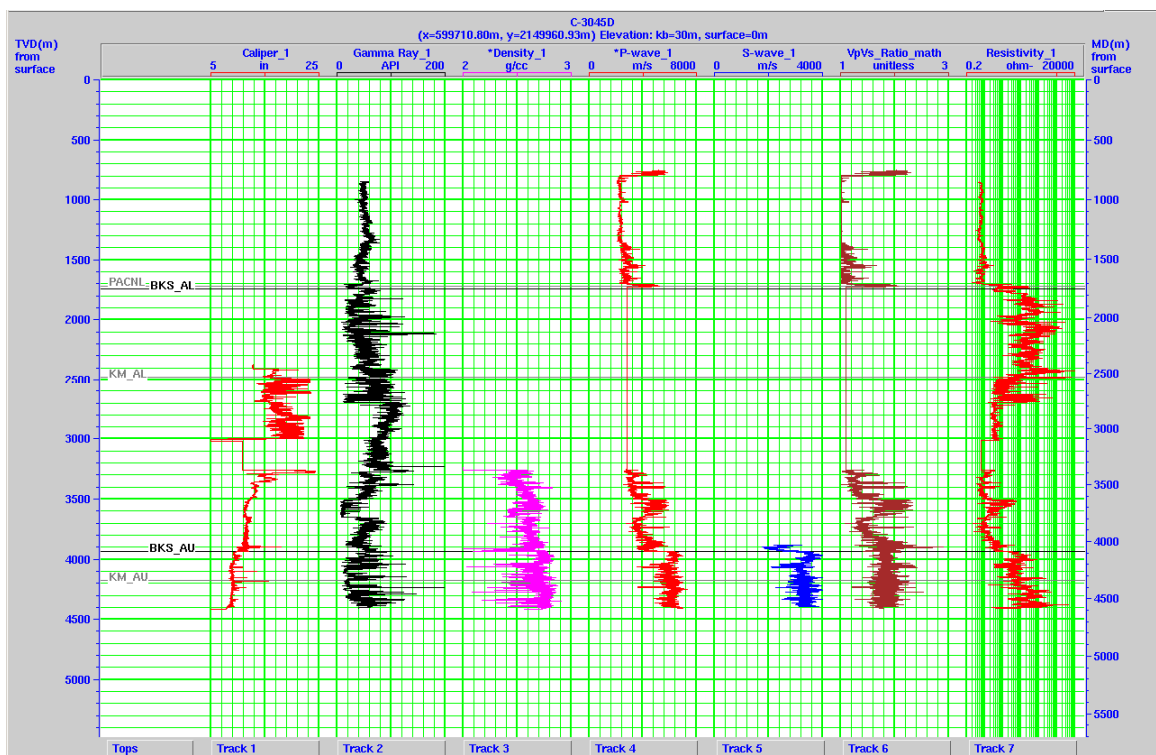
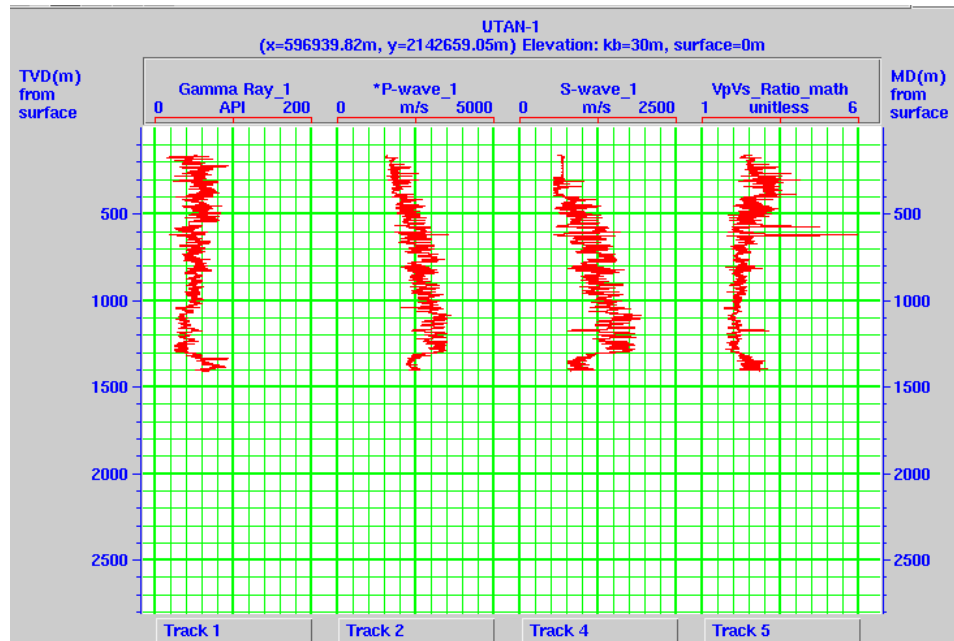


Figure 5.7 (e) Log curves in Well C-3045D.



**Figure 5.7 (f) Log curves of the shallow Well Utan-1.**

### 5.3.3 VSP data

VSP data is only available in well Sihil-19. In addition to the standard zero-offset VSP, there is one 2500 offset and one 3500 m VSP in different directions. The two offset VSPs are all processed to have both *PP* and *PS* CDP images. Table 5.1 shows the configuration and available data. Figure 5.8 shows the geometry of these two offset-VSPs.

The 2500m offset VSP line also crosses the well C-3068.

Checkshot surveys are available for well C-3068, S-19, C-2045D and C-3026D.

Offset	Direction (N clockwise)	Data	Bin size	Trace # in file	Valid trace #	Coverage
2500 m	115 deg. N	<i>PP</i>	10.0 m	1-181	1-128	1280 m
		<i>PS</i>	12.5 m	1-105	4-64	750 m
3500 m	45 deg. N	<i>PP</i>	20.0 m	1-91	4-82	1560 m
		<i>PS</i>	20.0 m	1-76	4-70	1320 m

**Table 5.1** The data detail of the offset VSP in well Sihil-19.

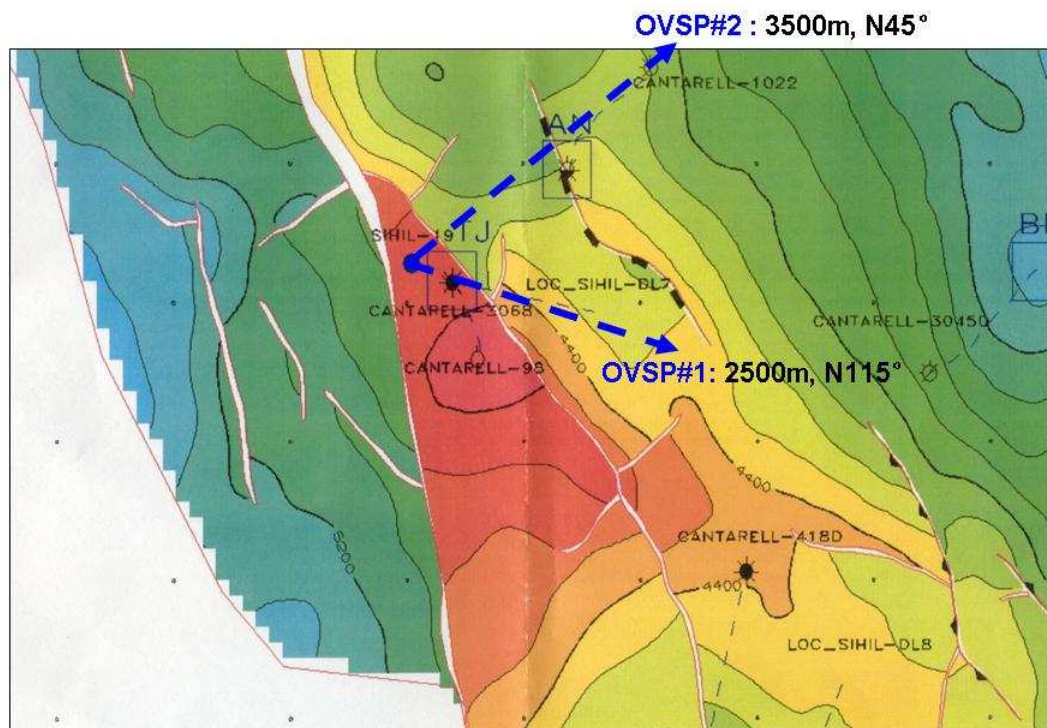


**Figure 5.8** The geometry of offset VSPs in Well Sihil-19 (after Chernikoff, 2006).

#### 5.4 Methodologies

The motivations for interpreting the *PS* seismic data are several folds including those outlined below:

- To validate and increase confidence in the *P*-wave interpretation
- Develop some new structural details (faults, compartments, closures)
- Assist with new stratigraphic features
- Provide some large-scale lithology (limestone, shales, salt) information
- Help provide information about fluid distributions

The general procedure that we follow in analyzing the converted-wave (*P*-to-*S*) seismic data volume is to first understand the *P*-wave data. To accomplish this, we generate synthetic seismograms, and correlate them with VSP and the surface seismic data. In the Sihil case, the *P*-wave horizons have already been interpreted by PeMex and Schlumberger. We use their *P*-wave interpretation as a guide for the *PS* data and accept them, as is, for *P*-wave calculations. Mr. Alberto Chernikoff of Schlumberger Data and Consulting Services has been central in the interpretation of the *P*-wave data and provided considerable assistance in our analysis of the converted-wave data.

### **5.5 Estimating shear velocity**

To generate converted wave synthetic seismogram, the knowledge of formation shear-wave velocity ( $V_s$ ) is necessary. The direct continuous in-situ measurement of  $V_s$  usually comes from the Dipole sonic log. If there is no measured  $V_s$ , it is common to use the empirical equations to predict  $V_s$  from existing logs. The empirical relationship also needs to be checked/calibrated using local data.

Greenberg-Castagna equation ( $V_p$  and  $V_s$  are in km/s):

$$V_s = 0.8042 V_p - 0.8559 \quad \text{for sandstone} \quad (5.1)$$

$$V_s = 0.7700 V_p - 0.8674 \quad \text{for shale} \quad (5.2)$$

Castagna (1985) Mudrock line

$$V_s = 0.8621 V_p - 1172.41 \quad (\text{in m/s}) \quad (5.3)$$

Castagna's equation for Carbonate:

$$V_s = -0.05509V_p^2 + 1.0168V_p - 1.0305 \quad (\text{in km/s}) \quad (5.4)$$

$$V_s = -0.00005509V_p^2 + 1.0168V_p - 1030.5 \quad (\text{in m/s}) \quad (5.5)$$

The well logs do not have full coverage with  $S$ -wave velocity values. Thus, we need to develop a relationship between  $V_p$  and  $V_s$ . We plot values from the various logs available. Figure 5.9 shows one example from well 3026D:

$$V_s = 0.5138 V_p + 200 \quad (\text{in m/s}) \quad (5.6)$$

We test the regression line relationship with known  $V_p$  and  $V_s$  values from the Sihil-19 VSP. Figure 5.10 shows that  $V_s$  can be reasonably well predicted from  $V_p$  in the VSP data using well log values.

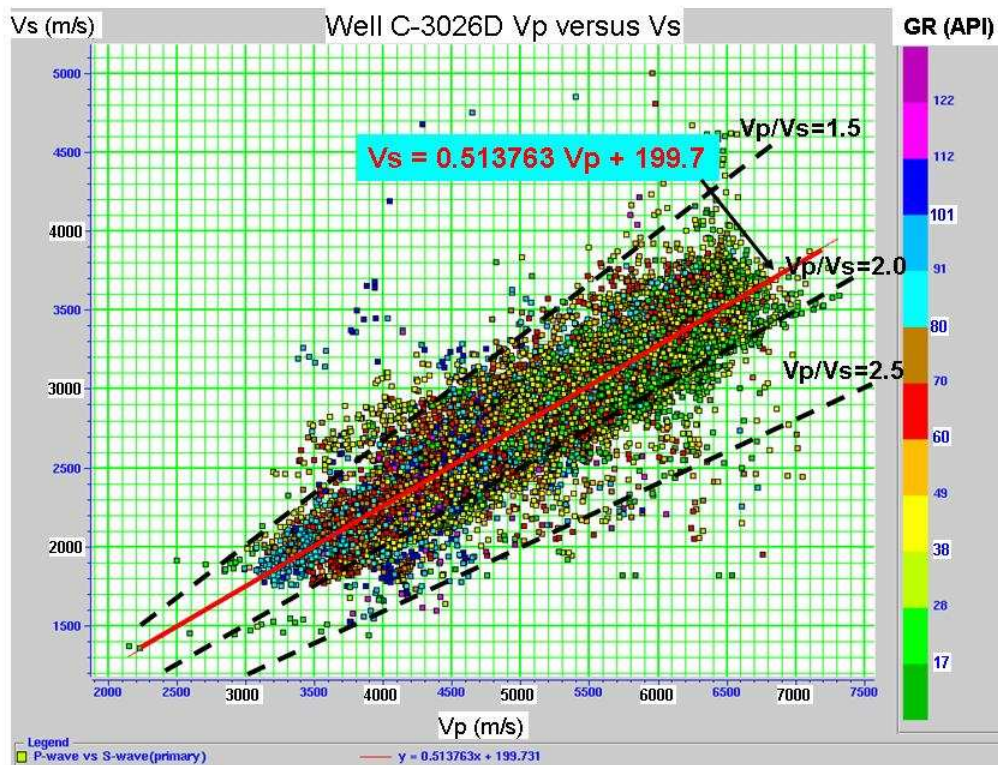
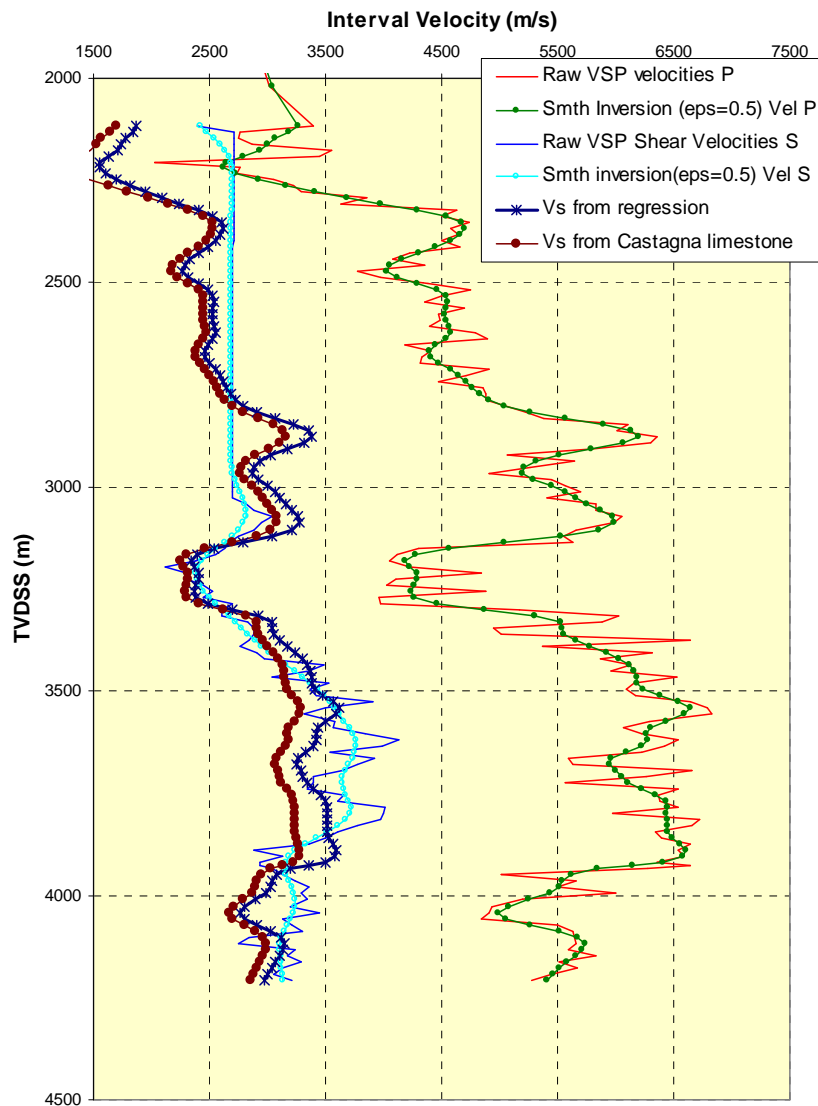


Figure 5.9 Crossplot of log measured  $V_s$  versus  $V_p$  in Well C-3026D with the regression line posted. Note the somewhat linear relationship within considerable scatter. Color represents GR value.



**Figure 5.10 Predicted  $V_s$  versus actual  $V_s$  from VSP in Well Sihil-19.**

In another well having Dipole sonic logs -- well C-98, there are two good data zones, both are carbonate, separated by a roughly 300 m bad data interval (Figure 5.7 (a)). Crossplotting the measured  $V_p$  and  $V_s$  gives us two different trends for these two intervals (Figure 5.11).

Interval 1 (shallow) 2162-2710m:

$$V_s = 0.7461 V_p - 1255 \quad (5.7)$$

Interval 2 (deep) 3000-4605m:

$$V_s = 0.5172 V_p + 127 \quad (5.8)$$

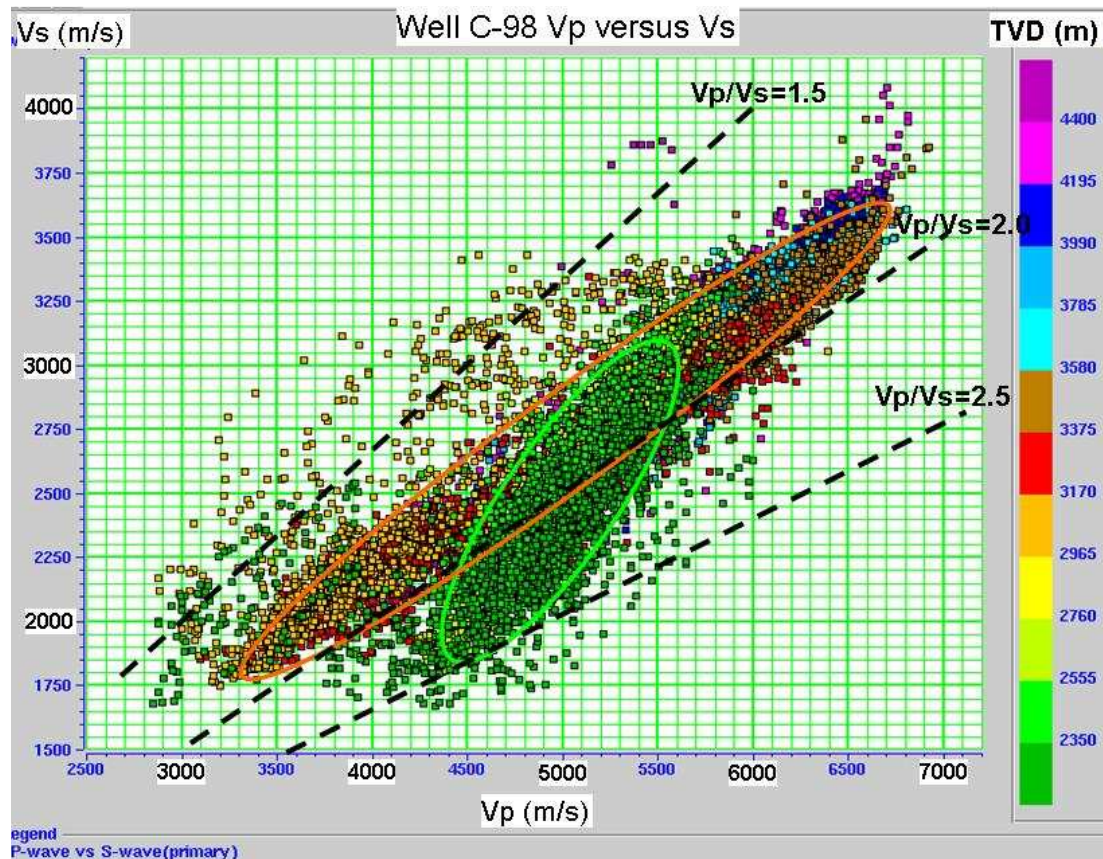


**Figure 5.11** Crossplot of  $V_p$  versus  $V_s$  in Well C-98. The green circle is for the shallow interval and the orange circle is for the deep interval.

Then, we look at the shallow well Utan-1. The linear regression for 300 – 1409 m interval gives us the following relation (Figure 5.12):

$$V_s = 0.7238 V_p - 731 \quad (\text{in m/s}) \quad (5.9)$$

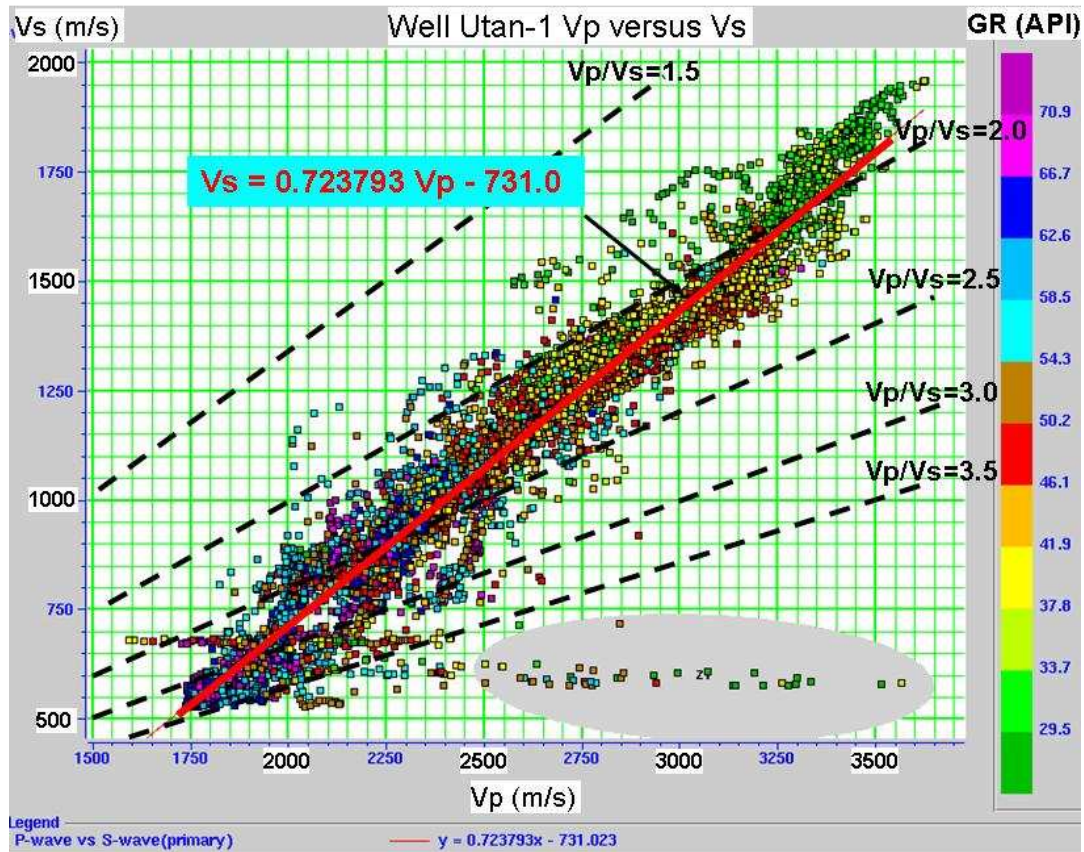


Figure 5.12 Crossplot of  $V_p$  and  $V_s$  in the shallow well Utan-1.

We crossplot the measured  $V_p$  and  $V_s$  log using four wells. Table 5.2 lists those intervals.

Well name	Start depth (m)	End depth (m)	Interval (m)
C-98 shallow	2162	2710	548
C-98 deep	3000	4602	1602
C-3026D	2370	4880	2510
Utan-1	300	1400	1100

Table 5.2 Intervals for crossplotting measured  $V_p$  versus  $V_s$  in four wells.

The various regression lines from different wells are plotted in one figure (Figure 5.13). Several constant  $V_p/V_s$  values (1.5, 2.0 and 2.5), along with Castagna's limestone relationship, are super-imposed on it to be as a reference. It is noticed that the limestone quadratic equation fits the Sihil  $V_p$  and  $V_s$  values very well. Thus, in the following, the Castagna carbonate equation is used to determine  $V_s$  from  $V_p$  when an  $S$ -wave log is not available.

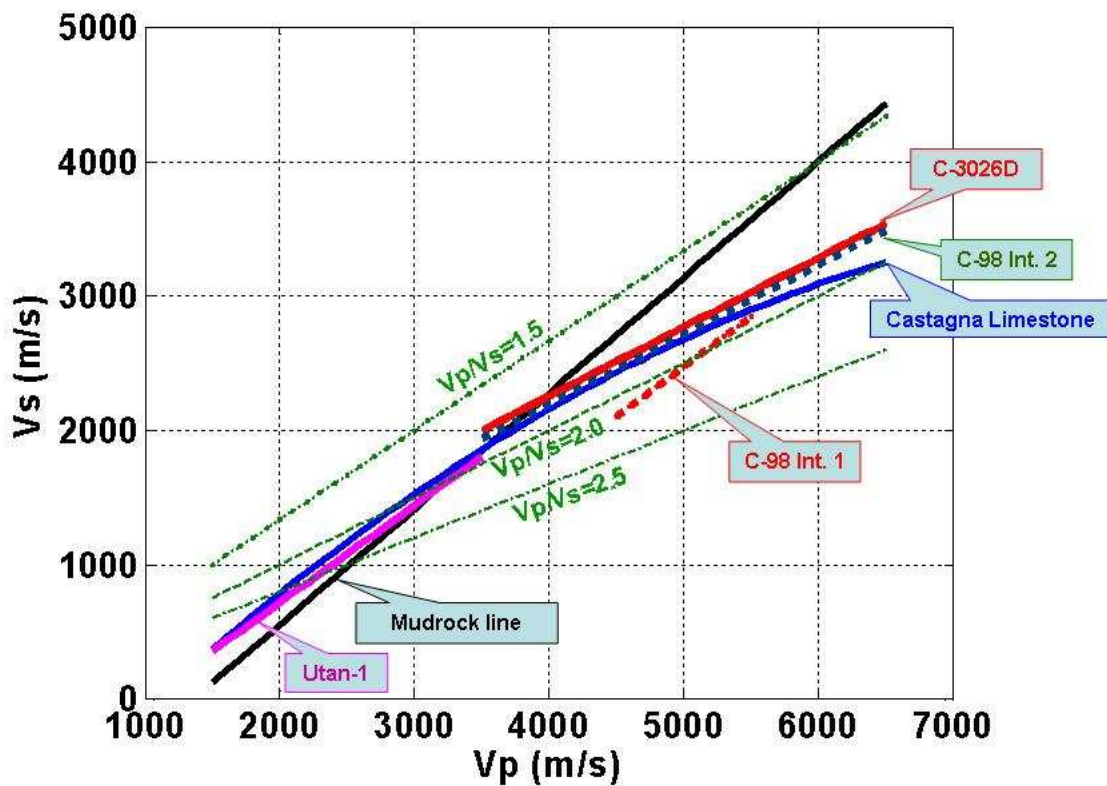


Figure 5.13 Compilation of various possibilities for the  $V_p$  and  $V_s$  relationship. The Castagna limestone equation fits most of the actual log data reasonably well.

## **5.6 Synthetics seismogram and correlation with VSPs and seismic data: PP and PS**

The *P*-wave synthetic seismogram in a well is generated using the reflection coefficient series (calculated from the velocity and density log) convolved with a wavelet. Synthetic seismograms link surface seismic time-domain information with high-resolution, depth-domain well log data.

Formation velocity (or slowness) is measured by sonic logging tool, usually in open-hole condition. Commonly, companies only run sonic log around the pay zone but not to surface. The lack of shallow depth formation velocity results in that the time zero (0) of synthetics is not the same time zero of surface seismic data. Therefore, to put synthetic at the roughly same time with surface seismic, it's recommended to correct (or calibrate) the *P*-velocity log by checkshot survey wherever it is available.

Checkshot survey is a travel-time-from-surface measurement by placing the receivers at known depths in a well. It's a simplified VSP (Vertical Seismic Profile), which just measure the first arrivals but not the full waveform. These measurements produce accurate time-depth relation and seismic velocities that can be used to calibrate well log data. Velocity survey information is presented as time-depth correlation plots and detailed velocity tables.

The difference in operating frequencies makes the correlation between log-generated synthetic seismogram and surface seismic, in some cases, more difficult.

Two wells, C-3068 (vertical well, off the structure) and C-3026D (deviated well, on the north-west slope of the structure), are used to generate the synthetic seismograms.

C-3068 has the longest  $V_p$  and density logs – about 4400 m from the autochthonous Jurassic Kimmeridgian to just below seabed, unfortunately, without  $V_s$  log. It's very close to well Sihil-19 which has zero-offset VSP and offset VSPs. So, for correlating with VSPs, we can borrow Sihil-19. C-3026D has good quality  $V_s$  log and relatively long interval. Its deviated borehole trajectory to the structure will help to correlate the synthetics with seismic data.

For each well, both *PP*-wave and *PS*-wave synthetics are generated in ProMC, the multi-component seismic interpretation software by Hampson-Russell.

Various wavelets in different dominant frequency are tried. Wavelets extracted from seismic data are also tested. A Ricker wavelet is used.

### Well C-3068

The ideal situation to do the *PP* and *PS* well-to-seismic correlation is using a well having significant longer measured  $V_p$  and  $V_s$  logs, zero-offset VSP – for *P*-wave well-to-VSP tie, and offsets VSP which have *PP* and *PS* CDP maps – for *PS*-wave well-to-VSP tie and VSP-to-seismic tie.

The first step is to generate the *P*-wave synthetic seismogram and correlate with *P*-wave corridor stack from zero-offset VSP. Then, *PS* synthetic is generated and correlated with *PS* CDP map from offset VSP.

Well C-3068 has the longest *P*-wave velocity log, but no *S*-wave velocity log, and no VSP. Well Sihil-19 has the zero-offset and two offsets VSP, but very short dipole

sonic log. Fortunately, these two wells are drilled from the same platform and only about 300 meter away at the hole bottom. C-3068 is right on the path of Sihil-19's 2500m-offset VSP. Therefore, we borrow Sihil-19's zero-offset and 2500m-offset VSP as if they were done in C-3068.

The logs, synthetic seismogram and VSP are put into a single composite plot as shown in Figure 5.14. For this *P*-wave data, we note the especially good tie between the synthetic and zero-offset VSP. This increases our confidence in the *P*-wave correlations. We note that the VSP data appear to be reversed in polarity from the other data. The synthetic seismogram is inserted into the seismic section at the well location to confirm the general times of the previous picks.

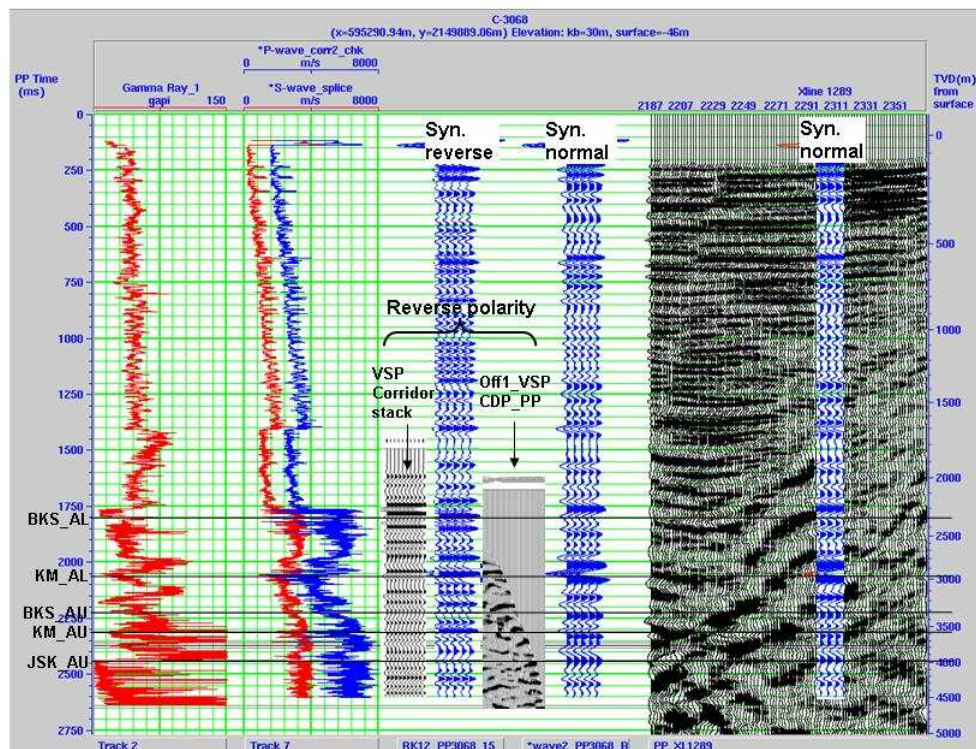


**Figure 5.14** Composite plot for *P*-waves including log, synthetic, and VSP data from well C-3068 and S-19. Note the excellent tie between the synthetic and VSP data. The VSP data is reversed in polarity from the other data.

Before moving into generating *PS* synthetics, let's look at Sihil-19's 2500m-offset VSP (Figure 5.15). They're in depth domain with GR curve and a few key formation tops are also posted.

We now proceed to the *PS*-wave synthetics. Since there is no  $V_s$  log in well C-3068, based on the analysis of  $V_p$ - $V_s$  relation from imperial and local wells, Castagna's limestone equation is used to create a  $V_s$  log from  $V_p$  log. Then, in ProMC, the *PS* synthetic is created by stacking the traces of the angle gather, with incidence angle range from 0 to 30 degree. The *PS* synthetic trace is in its native *PS* time domain (Figure 5.16, 5.17).

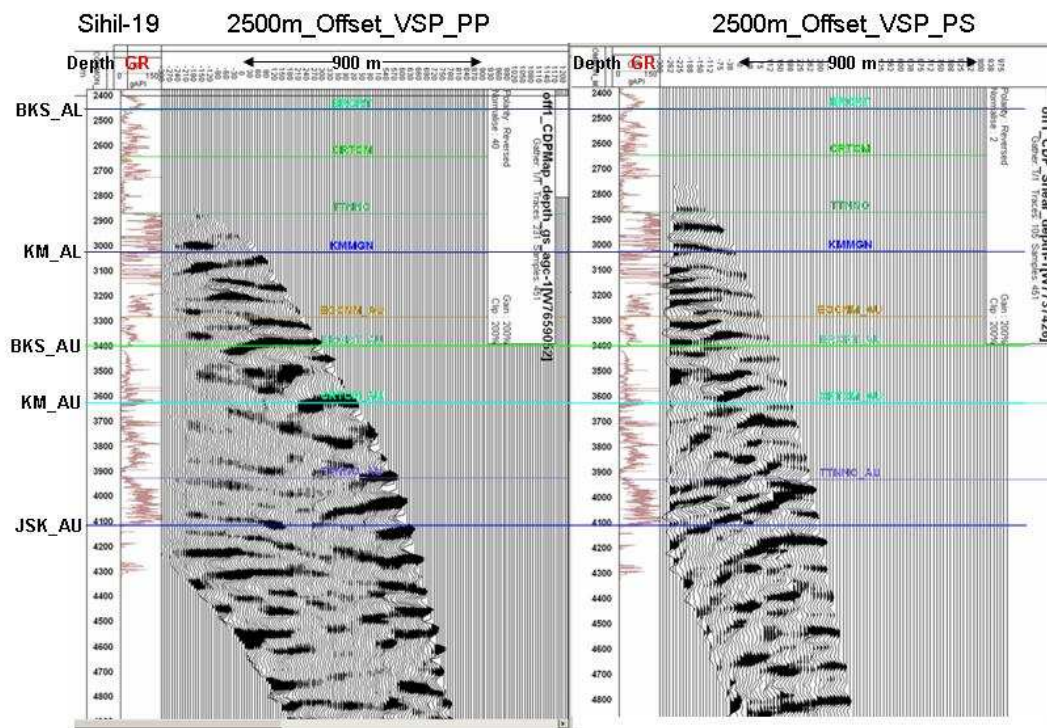


**Figure 5.15 Well Sihil-19, 2500m offset VSP profiles in depth domain with GR curve and the major formation tops marked: PP (left) and PS (right).**

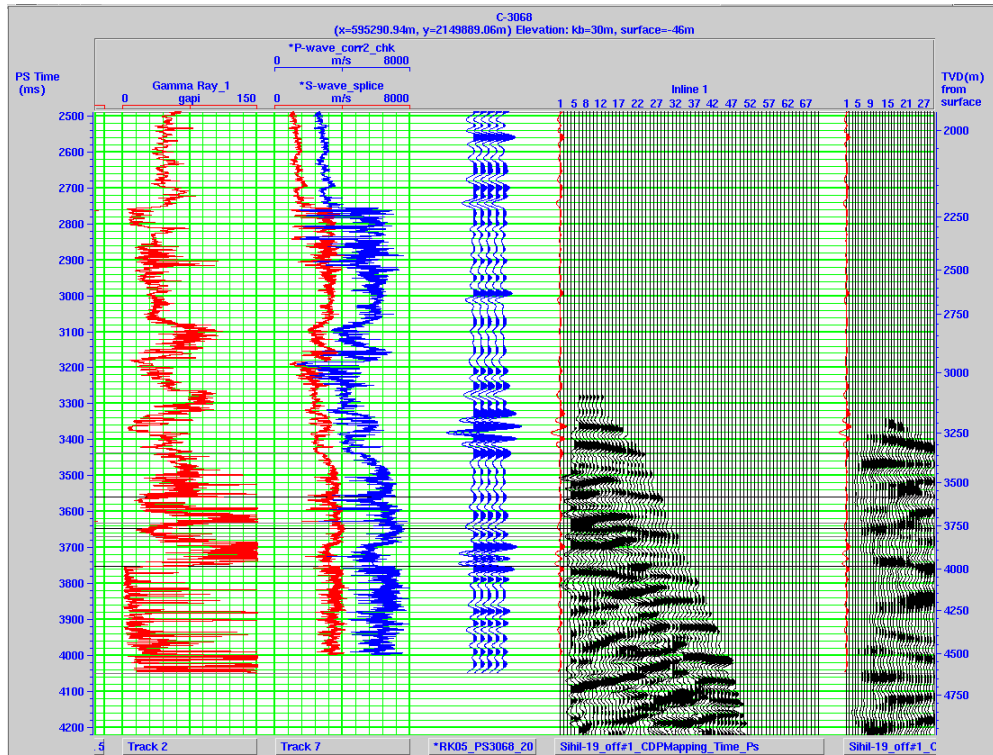


Figure 5.16 Correlation between PS synthetic seismogram and 2500 m offset VSP PS-CDP map.

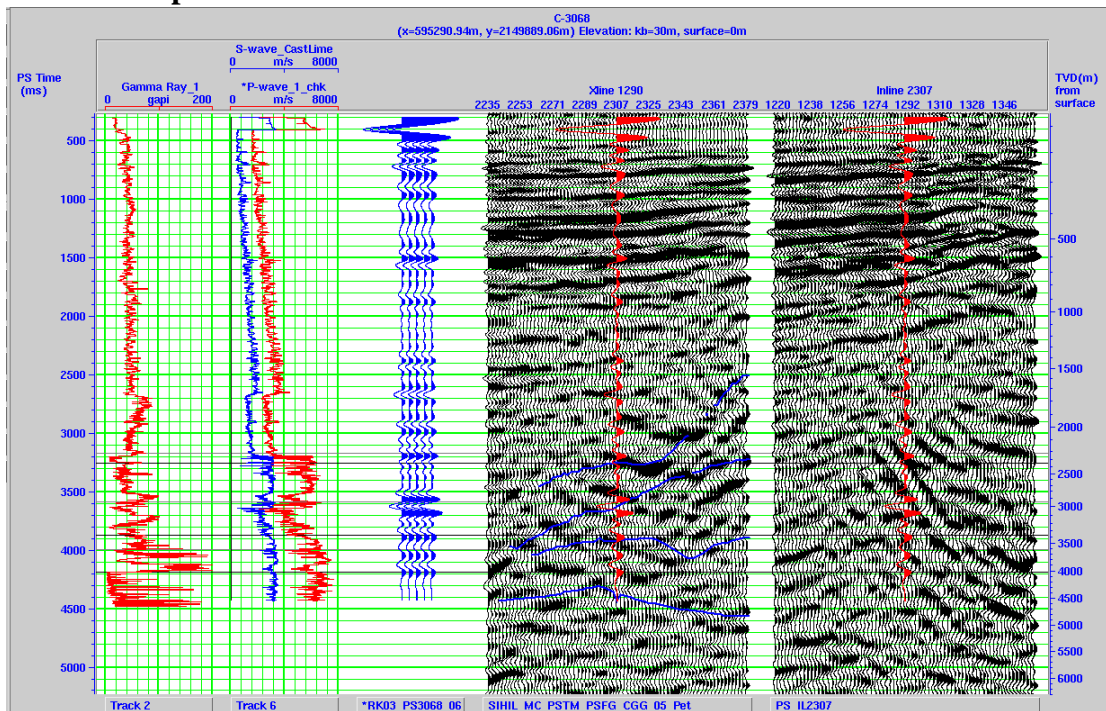


Figure 5.17 Correlation between PS synthetic with PS seismic, inline and crossline.

Well C-3026D.

It's more difficult to correlate *PS* synthetics with *PS* seismic in an intermediately to highly deviated well. First, usually there is no S-wave checkshot information for a gross calibration of the *PS* time of synthetic to *PS* time of the converted-wave seismic. The second reason comes from the geometry. In the vertical well case, correlating means sliding the synthetic trace up or down along the vertical wellbore – depth axis or 1D. In the deviated well case, the well trajectory is in a 2D plane – z (vertical) and r (horizontal), which means to move the synthetic up/down on the seismic time section is moving the well trajectory in this 2D-plane rather than sliding it along the well bore -- the well trajectory is not in the fixed position in time domain.

The ideal practice is to use *PS*-wave image from middle-offset or far-offset VSP as a bridge, and assume *PS*-VSP could tie with surface *PS*-wave seismic data very well, as they have similar type of wave propagation.

Another way to have a rough tie is to use structure as a reference. In the Sihil case, because of the highly structured area, the *PP* and *PS* seismic are similar on the size and shape of the pop-up structure. Therefore, the strong structure feature is used as a reference. Checkshot-corrected  $V_p$  gives us a reliable correlation between *PP* synthetic and *PP* seismic. Based on the position of *PP* synthetic in *PP* seismic (Figure 5.18), we moved *PS* synthetic trace into a similar position in *PS* seismic profile (Figure 5.19).

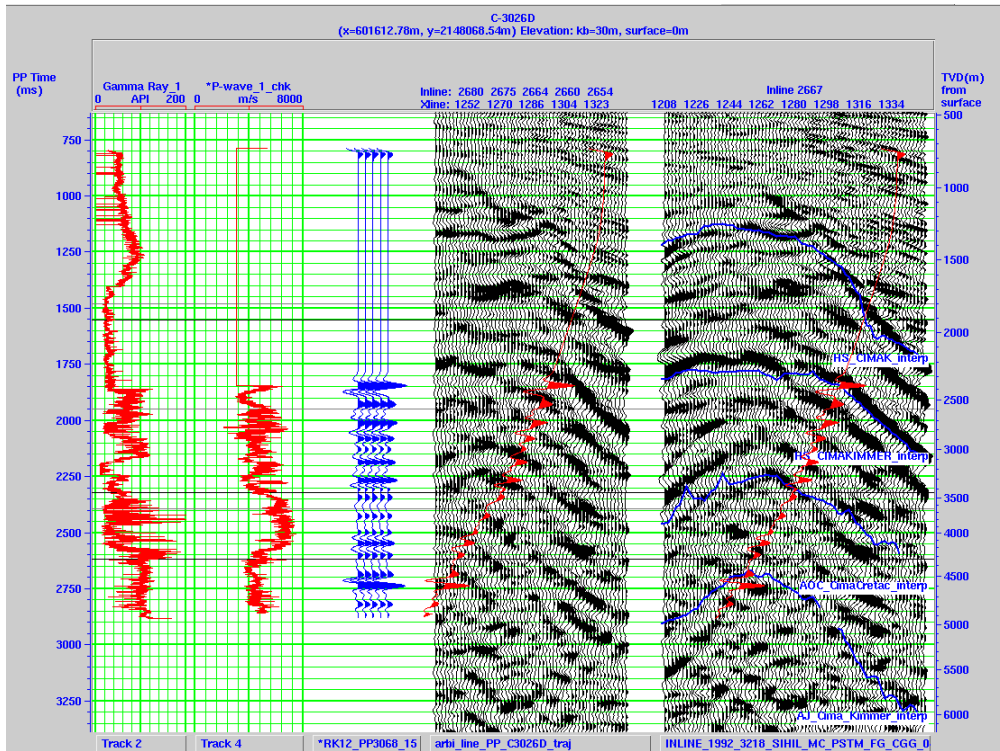


Figure 5.18 Correlating *PP* synthetic with *PP* seismic data in well C-3026D.

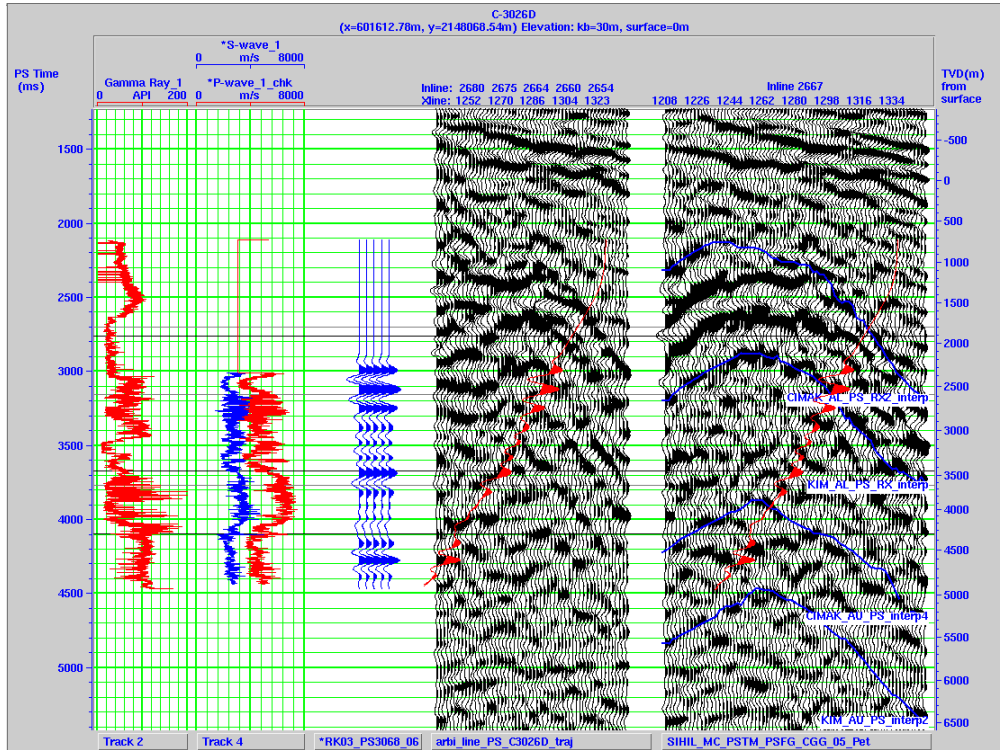
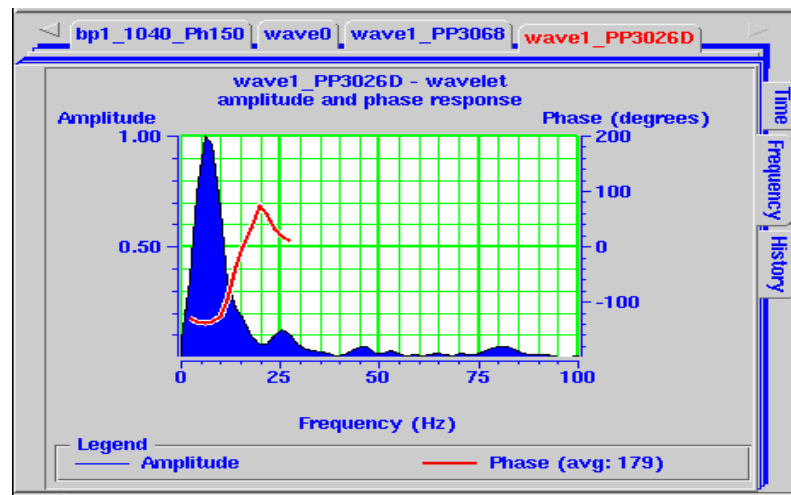


Figure 5.19 Correlating *PS* synthetics with *PS* seismic data in well C-3026D.

A wavelet extracted from the seismic data near well C-3026D has a dominant frequency of about 7 Hz and signal bandwidth from 3 - 20 Hz (Figure 5.20) – fairly low frequency seismic data!



**Figure 5.20** Wavelet extracted from *PP* seismic at well location 3026D.

### **5.7 Matching *PS* seismic to *PP* seismic data**

We matched the *PP* and *PS* synthetics in the vertical well C-3068. It's easy to correlate the events since the  $V_s$  is derived from  $V_p$  using the defined relationship and *PP* and *PS* synthetics are similar under such a low-frequency bandwidth.

We correlated the events on the *PP* synthetic with those of the *PS* synthetics (Figure 5.21). From this correlation, we find the  $V_p/V_s$  values that will map the *PS* events into the *PP* events (Figure 5.22). The  $V_p/V_s$  values that do the correct mapping range from 4.16 near the surface to 1.88 at depth. These values, determined from the synthetic seismograms, are similar to the blocked  $V_p/V_s$  values from the logs (as they should be).

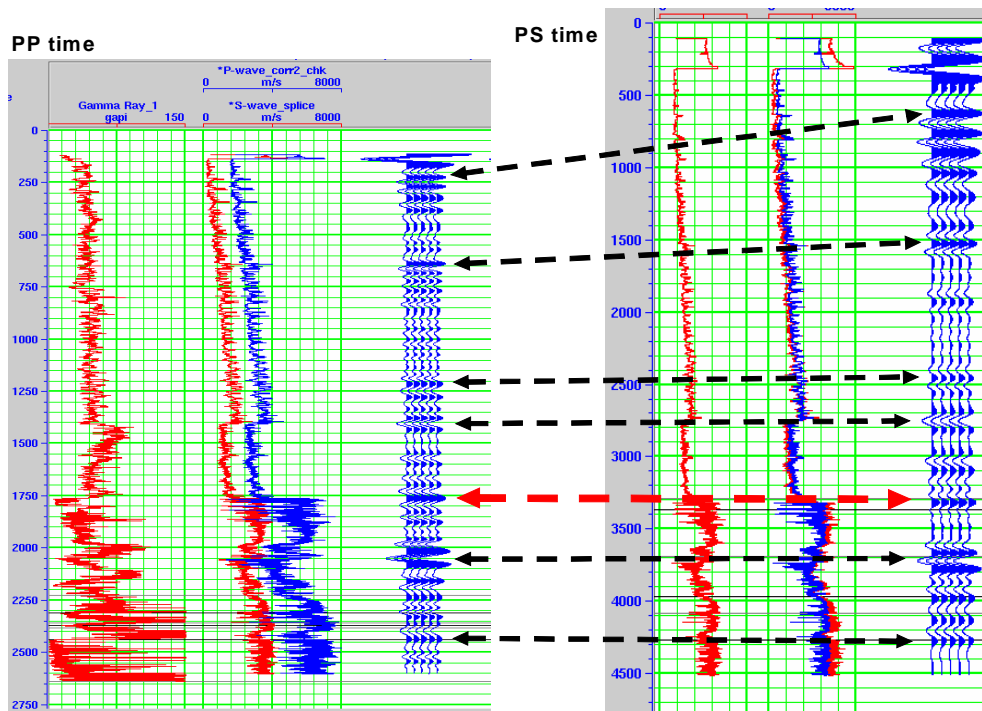


Figure 5.21 PP and PS synthetic seismograms in their raw PP and PS time domain in well C-3068.

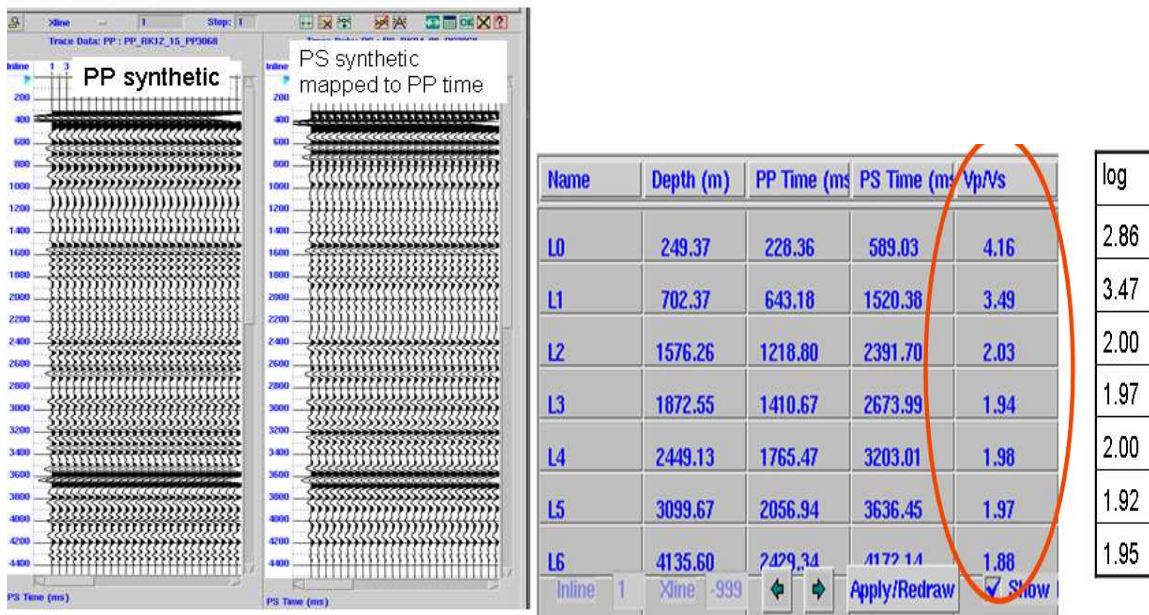
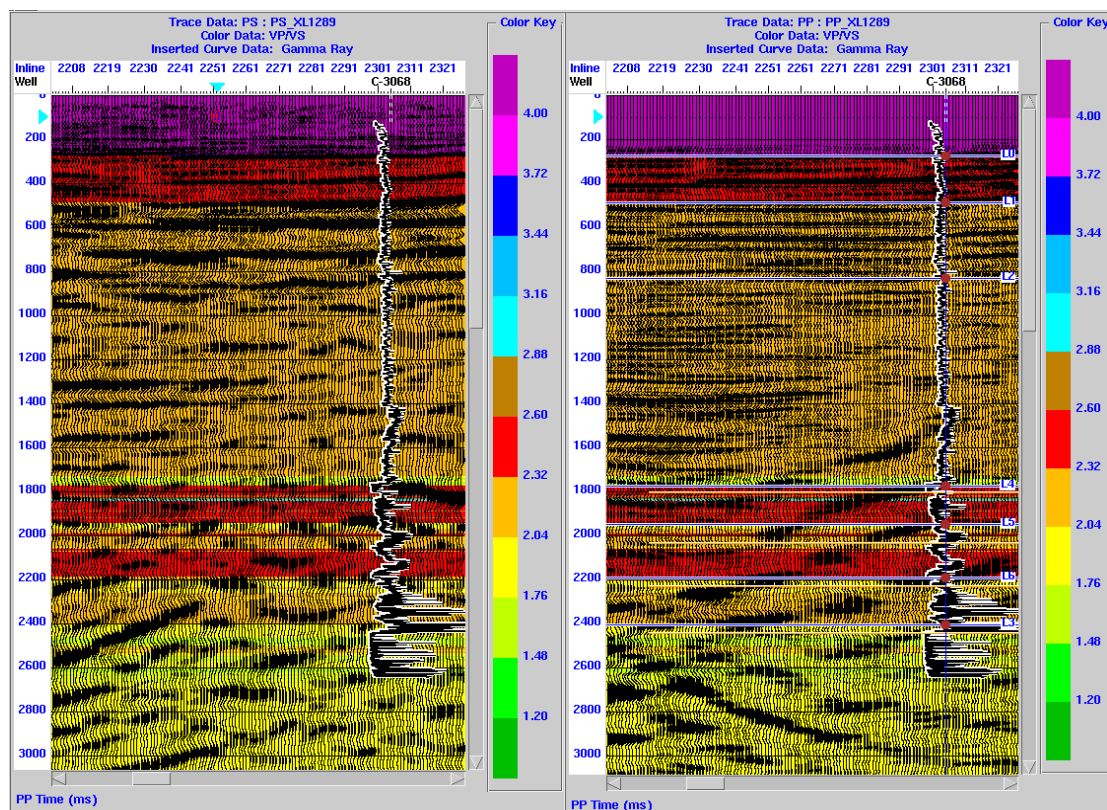


Figure 5.22 The PS and PP events on the synthetic seismograms have been matched and the PS synthetic has been mapped to PP time. The matching  $V_p/V_s$  values are shown in the Table (on the right) and also compared to the averaged log  $V_p/V_s$  values.

The  $V_p/V_s$  values in Figure 5.22 have been determined by assuming that matched events on the  $PP$  and  $PS$  traces have the same origin points in depth. Thus, from interpreted traveltimes or time-thicknesses, we can find  $V_p/V_s$  values. Conversely, from  $V_p/V_s$  values over an interval, we can find the corresponding  $PP$  or  $PS$  traveltimes. This table (Figure 5.22) provides the basis for conversion between any two of the 4 domains:  $PP$  time,  $PS$  time,  $SS$  time and Depth.

Using this table, we could immediately map the  $PS$  data into  $PP$  time and observe the correlation (Figure 5.23 and 5.24). This single mapping function brings most of the  $PS$  data into a gross alignment with the  $PP$  data. In Figure 5.24, the  $PS$  data shows a clear truncation at about 600 ms, which indicates an unconformity.



**Figure 5.23** An example (crossline 1289) of the  $PS$  data (left) mapped into  $P$ -wave time using the calculated  $V_p/V_s$  and compare with  $PP$  data (right). The background color is  $V_p/V_s$ .

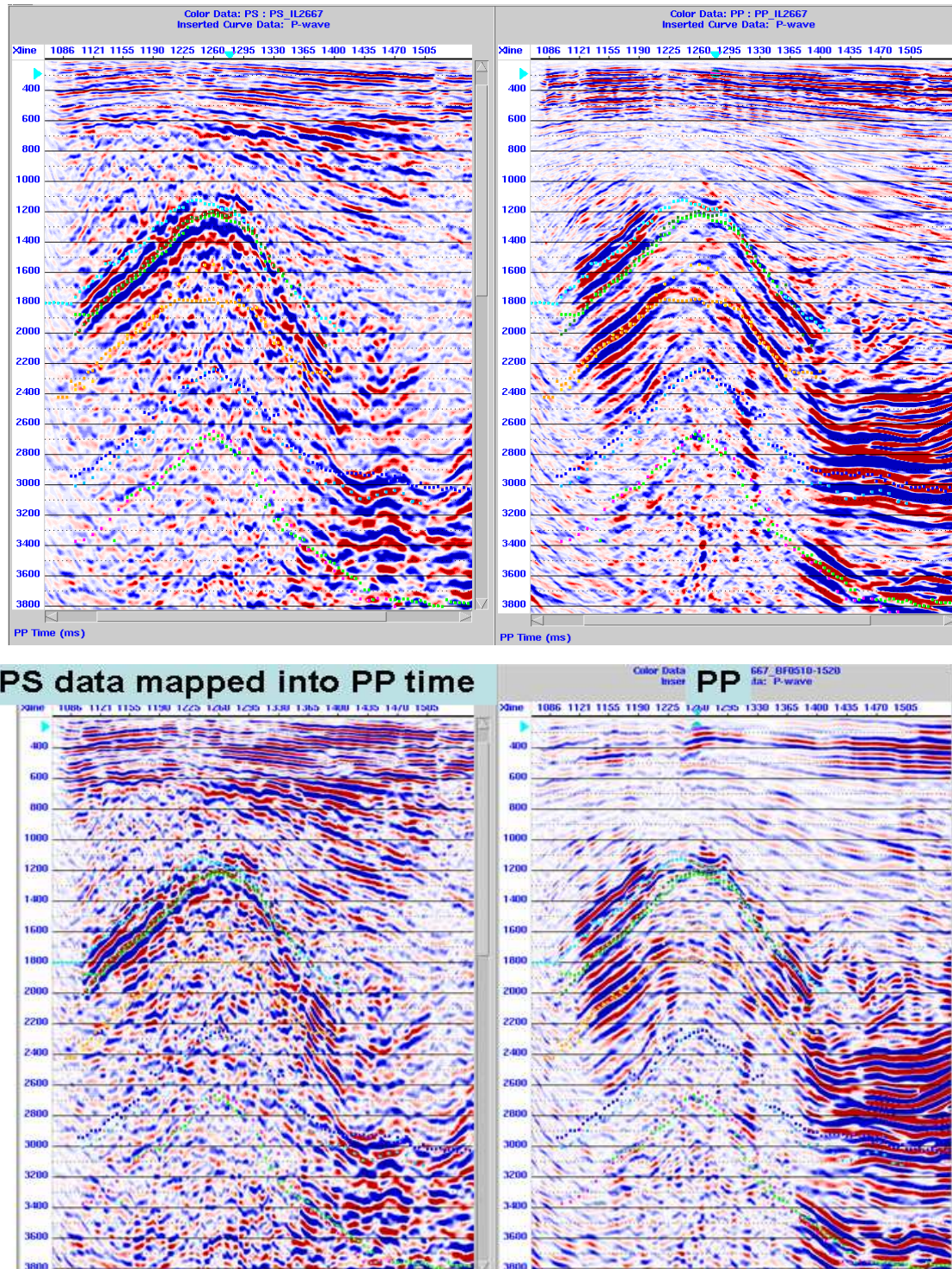


**Figure 5.24** An example (Inline 2667) of the *PS* data (left) mapped into *P*-wave time using the single  $V_p/V_s$  mapping function compare to *PP* data (right). The Upper row is original and the lower row is bandpass (5/10-15/20) filtered.

We splice the *PP* synthetic into the section to guide our picking of the horizons (Figure 5.25). We also post the *PS* synthetic on the *PS* section to pick the corresponding horizons on the *PS* data (Figure 5.26).

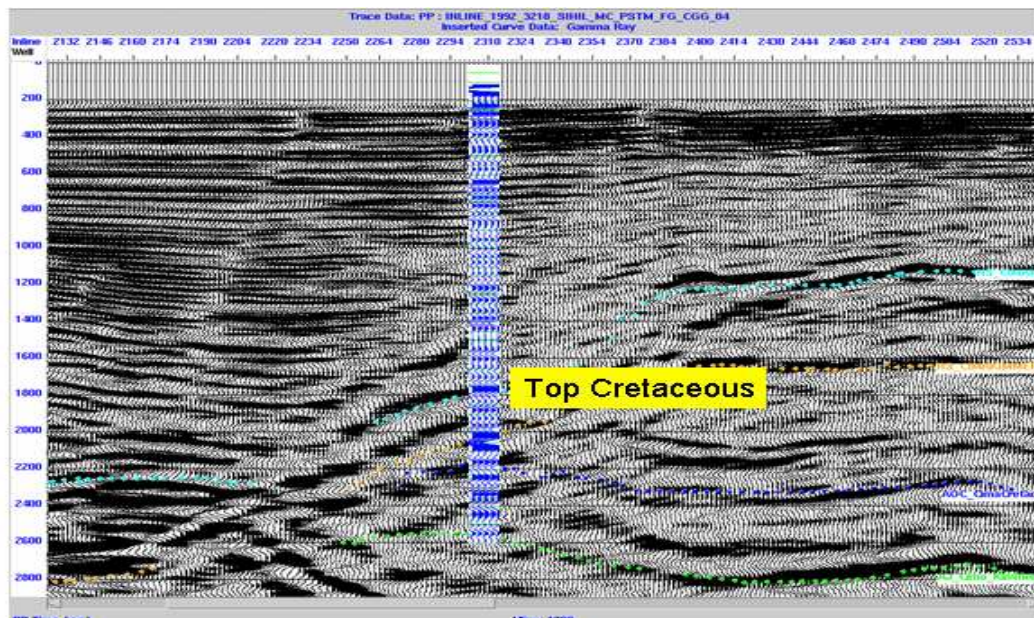


Figure 5.25 *P*-wave synthetic seismogram inserted into the *PP* section, in *PP* time.

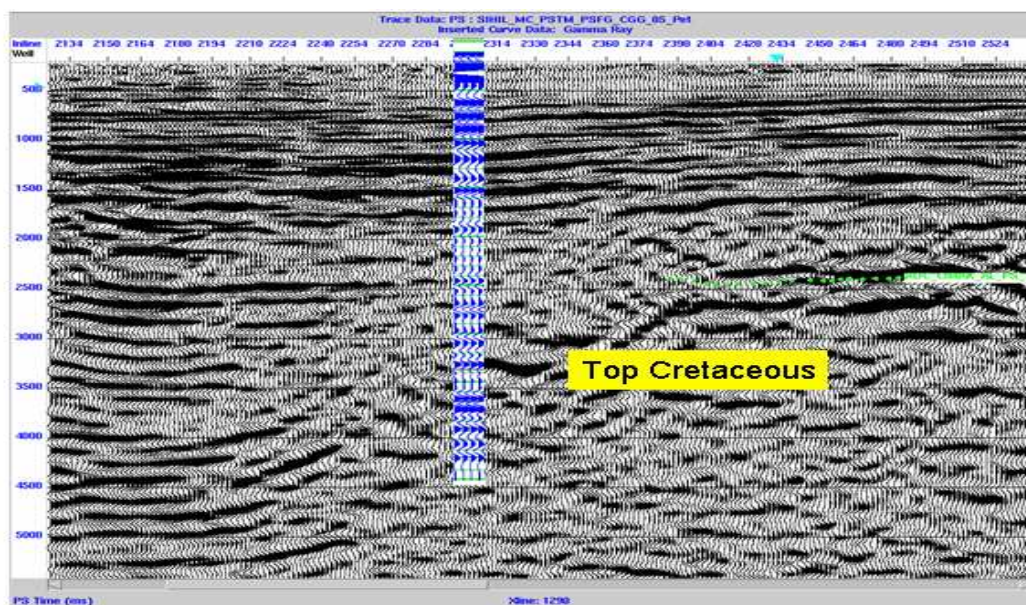
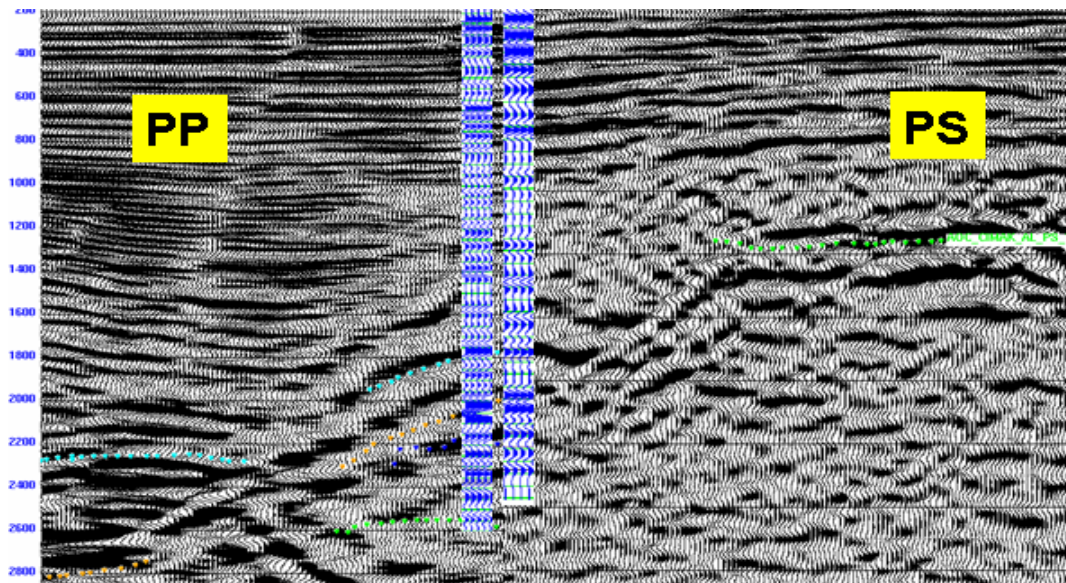


Figure 5.26 The converted-wave (*PS*) synthetic seismogram is inserted into the *PS* section. Data displayed in *PS* time.

As part of the procedure to continually refine and check our *PP* and *PS* horizon picks, we tie the two sections together at a known horizon (Cretaceous, say) and observe the correlations (Figure 5.27).



**Figure 5.27** Approximate tie of the *PP* and *PS* synthetic and seismic sections, using one  $V_p/V_s$  value to stretch the *P*-wave section, at the top of the Cretaceous.

Mapping *PS* data volume from its original *PS* time domain to *PP* time domain to have the gross alignment between *PP* and *PS* data, is considered the most critical step of *PS* data interpretation. In this case, although the *PS*-to-*PP* time mapping function is 1D and from well logs, it surprisingly shows the accuracy and consistency of the domain conversion for the entire 3D volume.

### **5.8 Horizon interpretation, structure, time-isochores and $V_p/V_s$ maps**

The *PP* seismic data has been interpreted by Schlumberger DCS in Mexico and the results of four horizon picks are imported into this project directly. Table 5.3 lists the name convention for formations/tops in well logs and horizons from seismic data.

	Tops in log	Horizons of <i>PP</i> seismic	Horizons of <i>PS</i> seismic
Top of Cretaceous allochthonous	BKS_AL	HS_CIMAK	CIMAK_AL_PS
Top of Kimmeridgian allochthonous	KIM_AL	HS_CIMAKIMMER	KM_AL_PS
Top of Cretaceous autochthonous	BKS_AU	AOC_CimaCretac	CIMAK_AU_PS
Top of Kimmeridgian autochthonous	JSK_AU	AJ_Cima_Kimmer	KIM_AU_PS

**Table 5.3 Name of formation tops and horizons from seismic data.**

The interpretation includes the allochthonous (over-thrust) block which forms the giant Akal field, and the autochthonous block for both Cretaceous and Jurassic formations. A shallow horizon on *PP* and *PS* seismic data are also picked.

The procedure of picking *PS* horizon:

- display the *PS* seismic in its native *PS* time domain
- After applying the 1D event matching, convert a *PP* horizon from *PP* time to *PS* time
- display the *PP* horizon (in *PS* time already) on the *PS* seismic data

- Guided by the *PP* horizon in *PS* time, the corresponding *PS* horizon is picked.

### Shallow horizon

With the knowledge of the approximate *PP*-to-*PS* time correlations, we pick a shallow horizon on both *PP* and *PS* volumes. The picks on the section are shown in Figure 5.28. Note that the *P*-wave pick is at about 400ms while the *PS* pick is at 1000ms. This implies a near-surface  $V_p/V_s$  value of about 4.0.

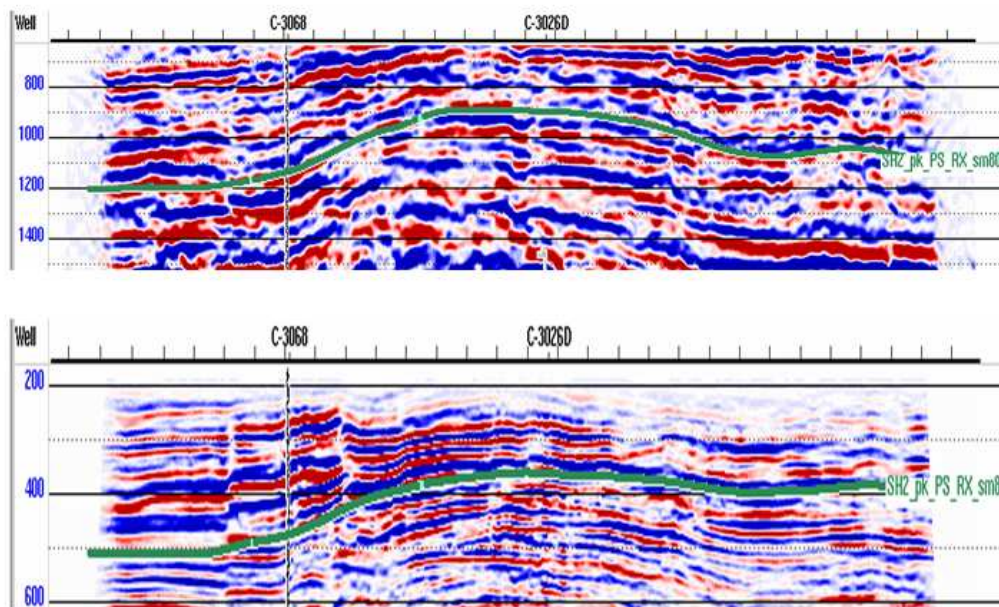


**Figure 5.28** Shallow *PS* (top) and *PP* (bottom) sections with a horizon pick annotated. Both sections are in their native times.

The time structure maps of the shallow horizon are given in Figure 5.29.

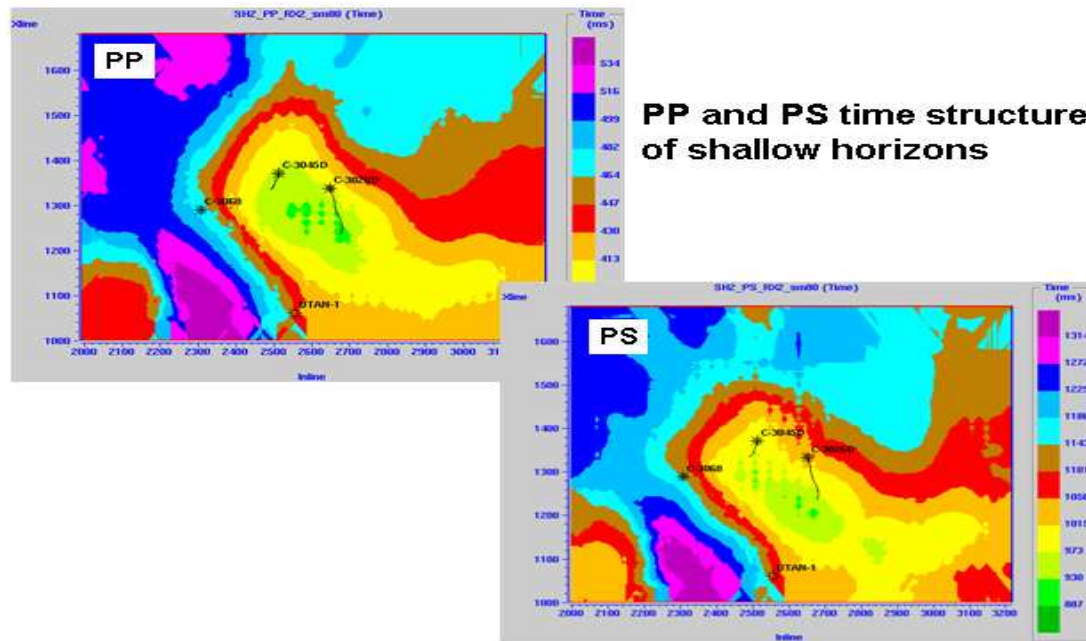


**Figure 5.29** *PP* and *PS* time structure maps of the shallow horizons.

Now using the time-thickness ratios, we can calculate the spatially variant  $V_p/V_s$  map of the near-surface as shown in Figure 5.30. These values, near 4.0, are typical for shallow marine sediments and compare reasonably well with those processing values determined from the WesternGeco 2000 survey (Figure 5.31).

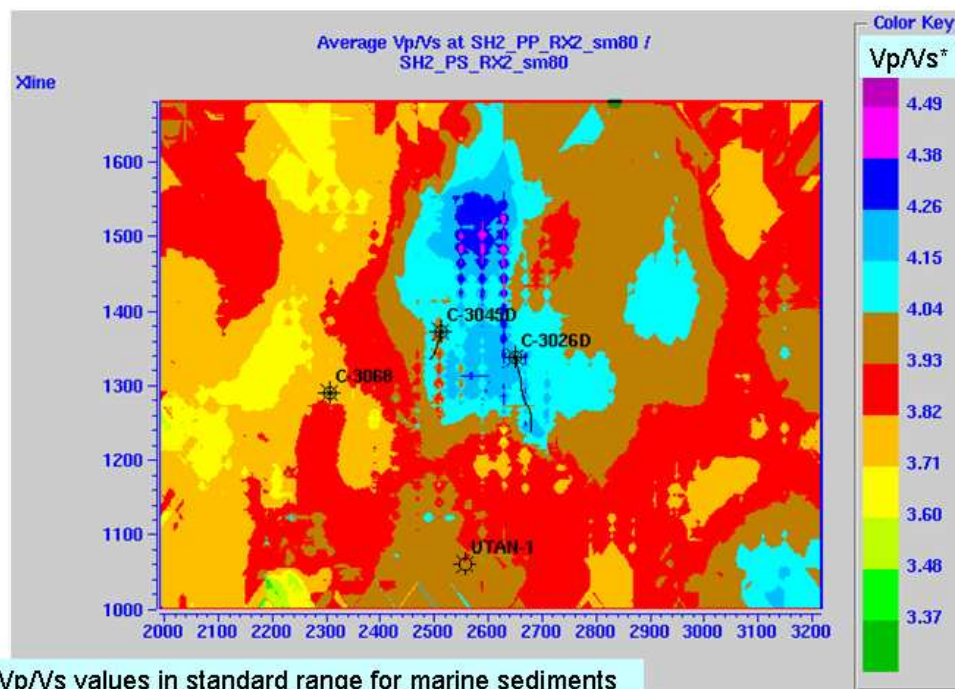


Figure 5.30  $V_p/V_s$  value from the shallow horizon to the ocean bottom.

WesternGeco PS section with  $V_p/V_s$  values  
(from RMS processing velocities)

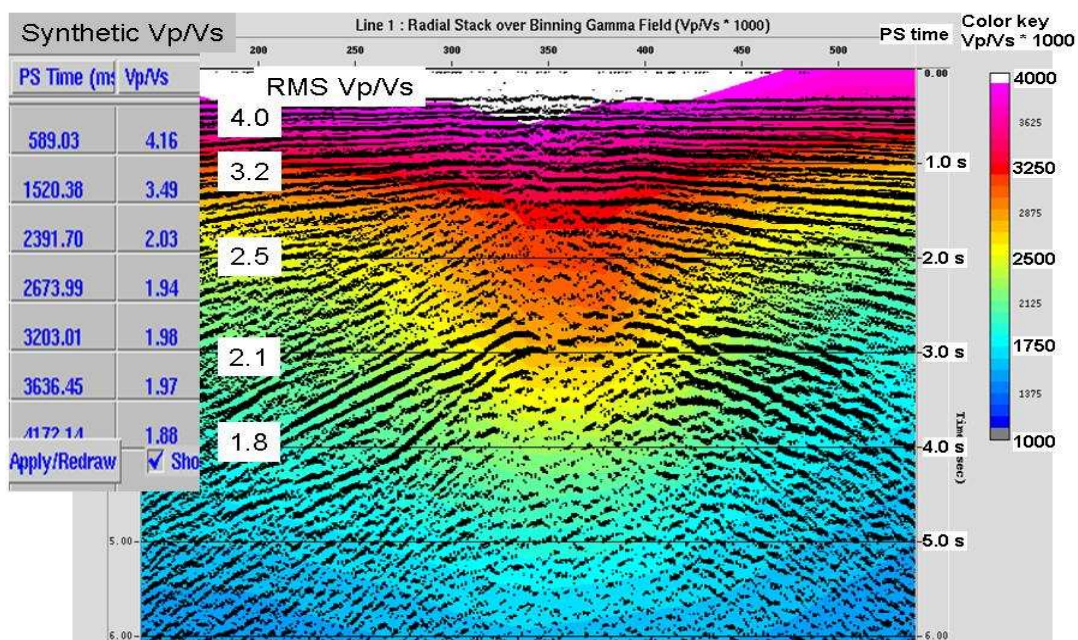
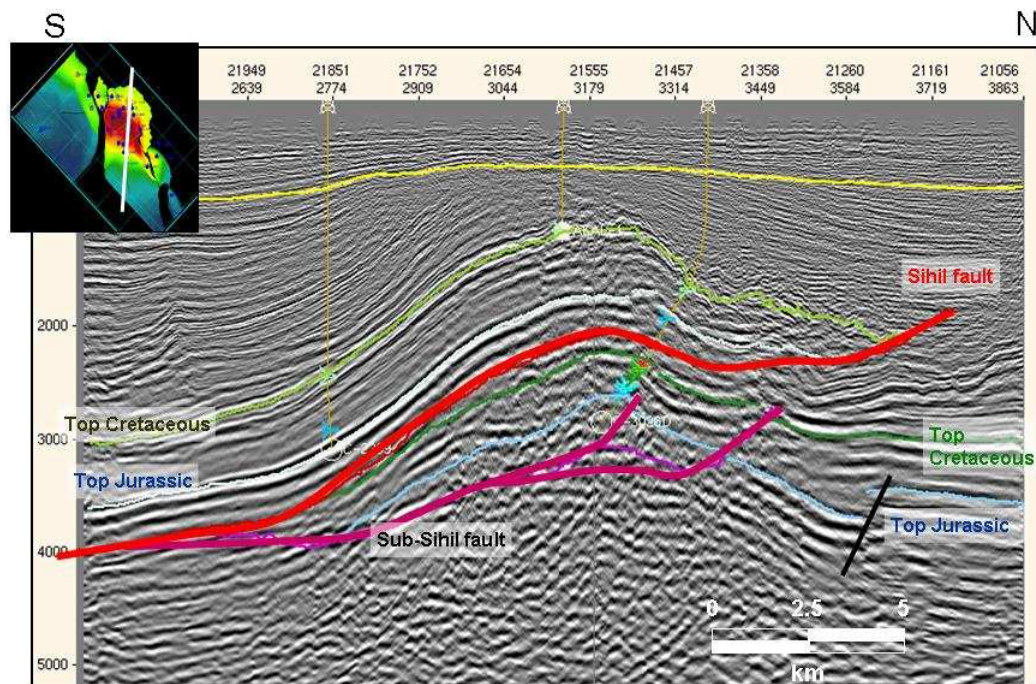


Figure 5.31 Comparison of the time-mapping  $V_p/V_s$  values from the synthetic analysis in this study and previous work. The values are roughly similar.

### *Cretaceous Allochthonous*

We now move on to the interpretation of the top of allochthonous (over-thrust) Cretaceous horizon. This important area defines the top of the super-giant Akal field. Previous work has interpreted the *P*-wave data and an example of that interpretation is shown in Figure 5.32.



**Figure 5.32** Interpretation of a north-south *PP* line from the Sihil data set (from Chernikoff, 2006).

Guided by this *P*-wave interpretation, we interpret our *PS* structure. Several examples on the *PP* and *PS* seismic sections are given in Figures 5.33 and 5.34. The top Cretaceous (or close to Cretaceous) event is very strong, relative to the *P* wave, on the converted-wave data. This is partially a result of the significant *S*-wave velocity change, evident on the sonic logs, as well as the likely deleterious effect of gas in the region on the *P*-wave data.

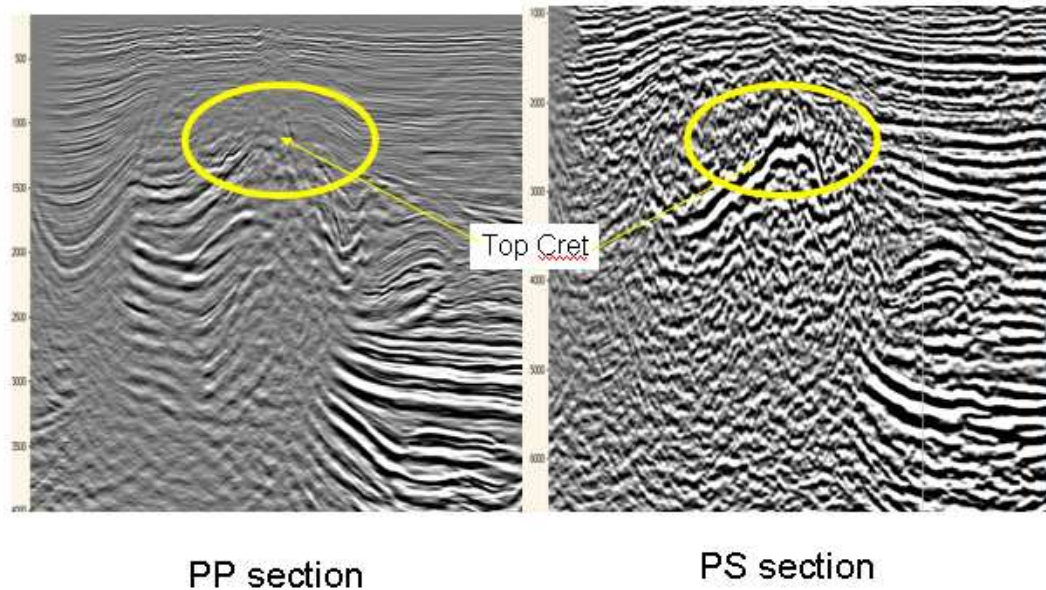
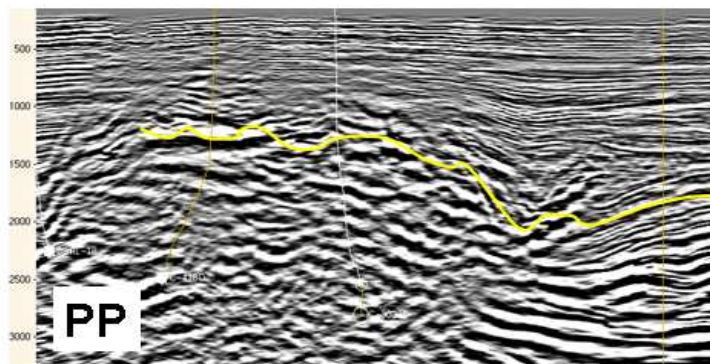


**Figure 5.33** Top of the Cretaceous event as interpreted on the *PP* and *PS* seismic data.



**Checking  
the  
interpreted  
horizons by  
copying an  
event**

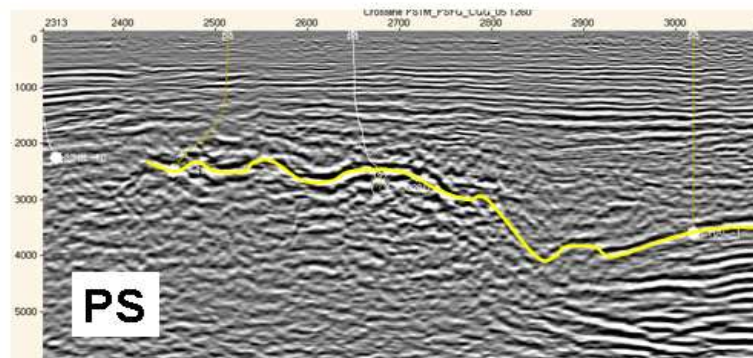


**Figure 5.34** A Cretaceous event traced on the *PS* section and transferred to the *PP* section to check the similarity of the structures.

The time structure maps for the *PP* and *PS* volumes are displayed in Figure 5.35 and 5.36. Again, from the time thicknesses between the shallow horizon and top Cretaceous, we calculate a  $V_p/V_s$  map as shown in Figure 5.37.

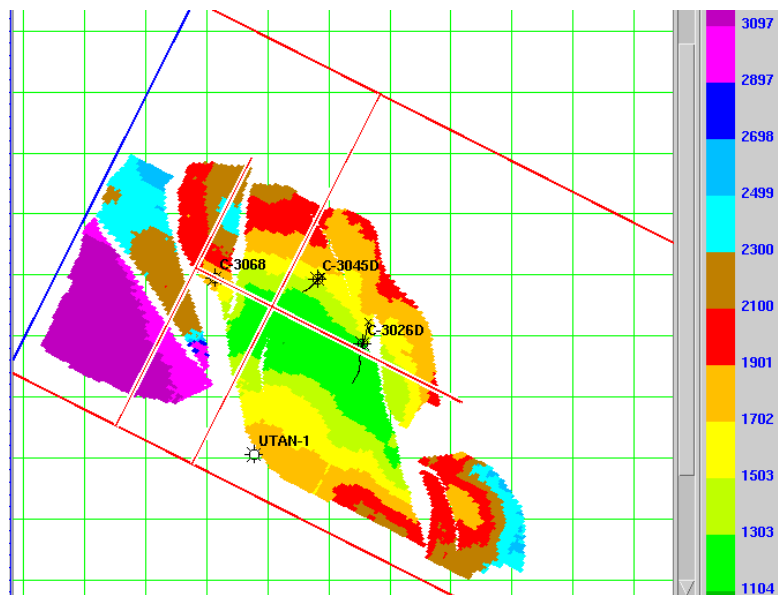


**Figure 5.35** *PP* time structure at the allochthonous Cretaceous. Color is *PP* time.

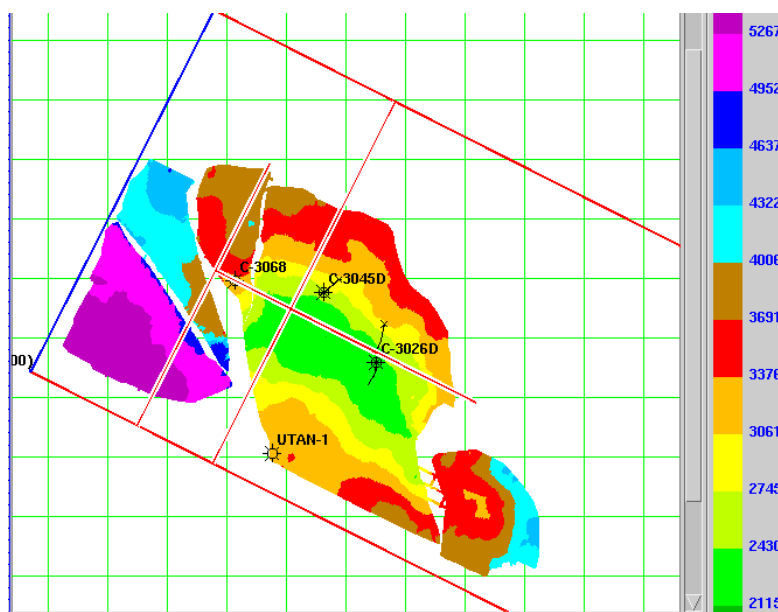


**Figure 5.36** *PS* time structure at the allochthonous Cretaceous. Color is *PS* time.

An interesting association can be observed between some of the low  $V_p/V_s$  values in Figure 5.37 and low RMS amplitudes extracted from the  $P$ -wave volume (Figure 5.38) just above the Cretaceous marker. We would interpret this correlation as a result of gas saturation.

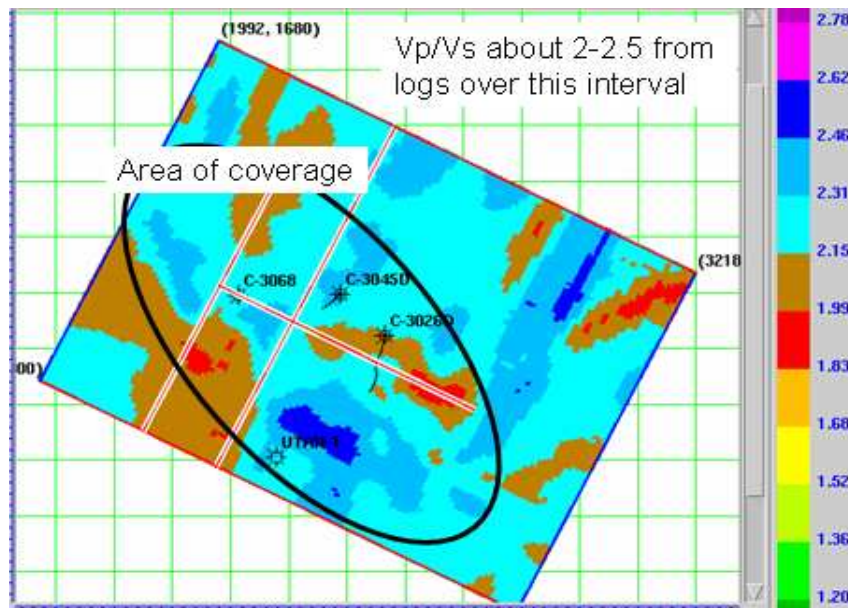


**Figure 5.37** Interval  $V_p/V_s$  map as calculated from ratio of the  $PP$  and  $PS$  time thicknesses between the shallow marker and top of the Cretaceous.

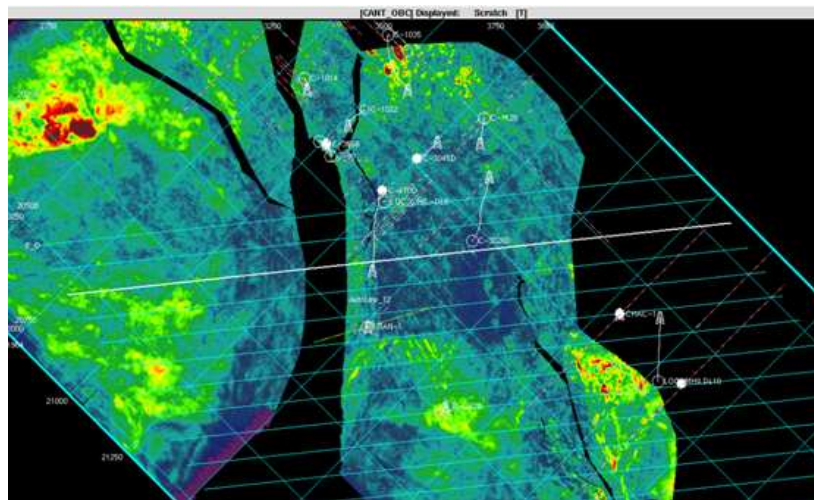


**Figure 5.38** Amplitude map (RMS value from a 150 ms window) above the Cretaceous (from Chernikoff, 2006). We observe that the low amplitude values (in

blue) correlate with the low  $V_p/V_s$  values from Figure 30. This is an indication of gas saturation.

Another view of the possible gas chimneying or leakage is evident on the two sections shown in Figure 5.39. Here again, we see a washed-out region on the  $P$ -wave data compared to a fairly crisp reflection on the  $PS$  data.

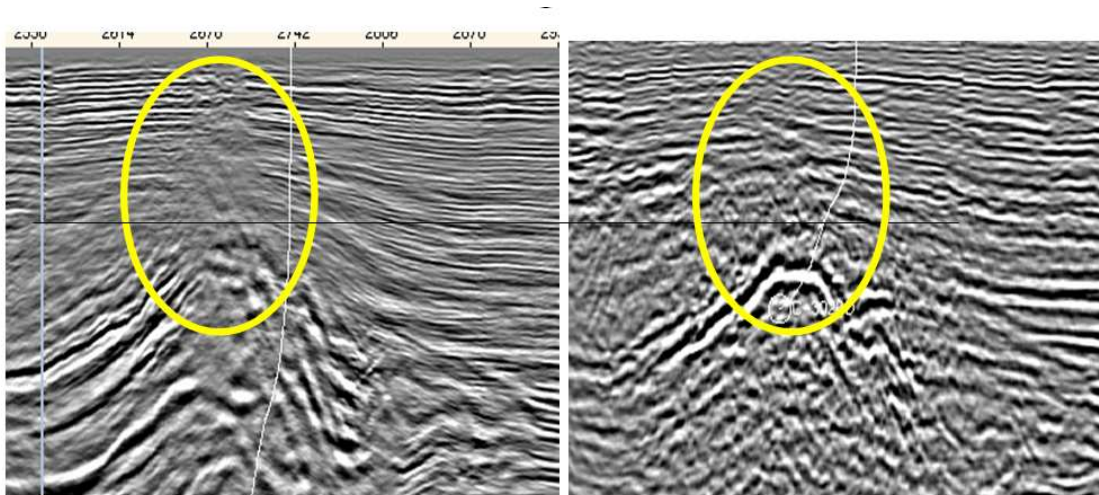


**Figure 5.39**  $PP$  and  $PS$  sections over the Akal anticlinal structure. Note the washed-out area (circled) on the  $P$ -wave section over the poorly defined anticlinal peak. The top of the Cretaceous is more definitive on the  $PS$  section. This is the classic signature of a “gas chimney”.

Figure 5.40 is another example of the possible gas effect. In addition, there is the hint of a gas-oil contact (brightness on the  $P$ -wave with no corresponding event on the  $PS$ ).

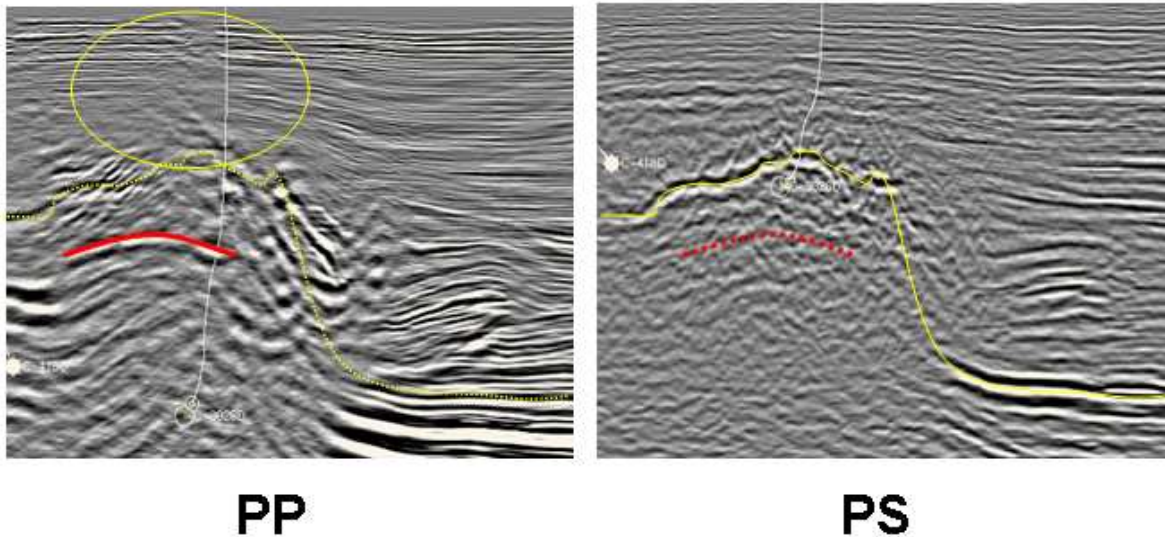


**Figure 5.40** *PP* and *PS* sections indicating the possible effects of gas. A possible gas-oil contact is annotated.

### *Kimmeridgian Allochthonous*

We continue our interpretation in depth by considering deeper reflectors. Figures 5.41 and 5.42 show inline sections with interpreted horizons. We have picked the allochthonous Kimmeridgian event and display its time structure maps in Figures 5.43 and the  $V_p/V_s$  map between the Kimmeridgian and Cretaceous in Figure 5.44.

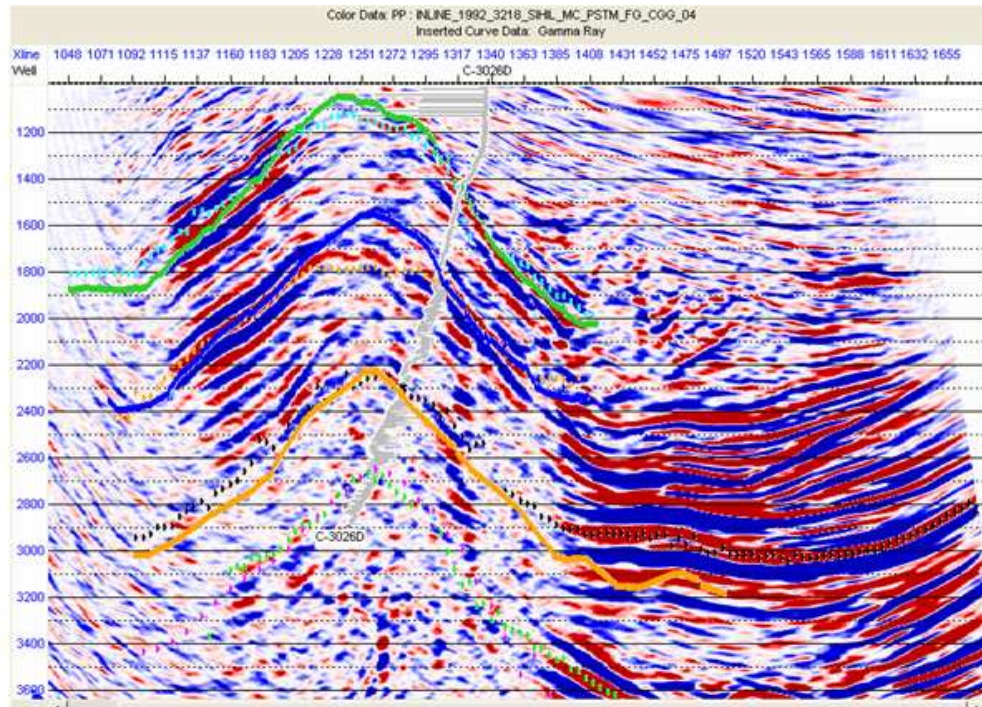


Figure 5.41 *PP* section (inline 2667) with horizons annotated.

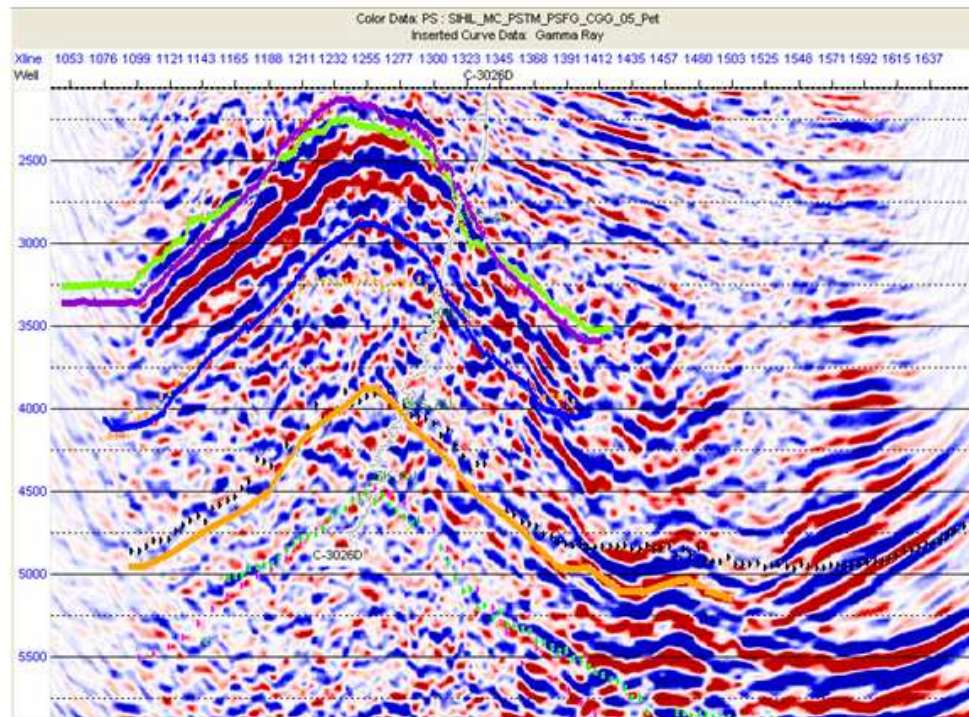
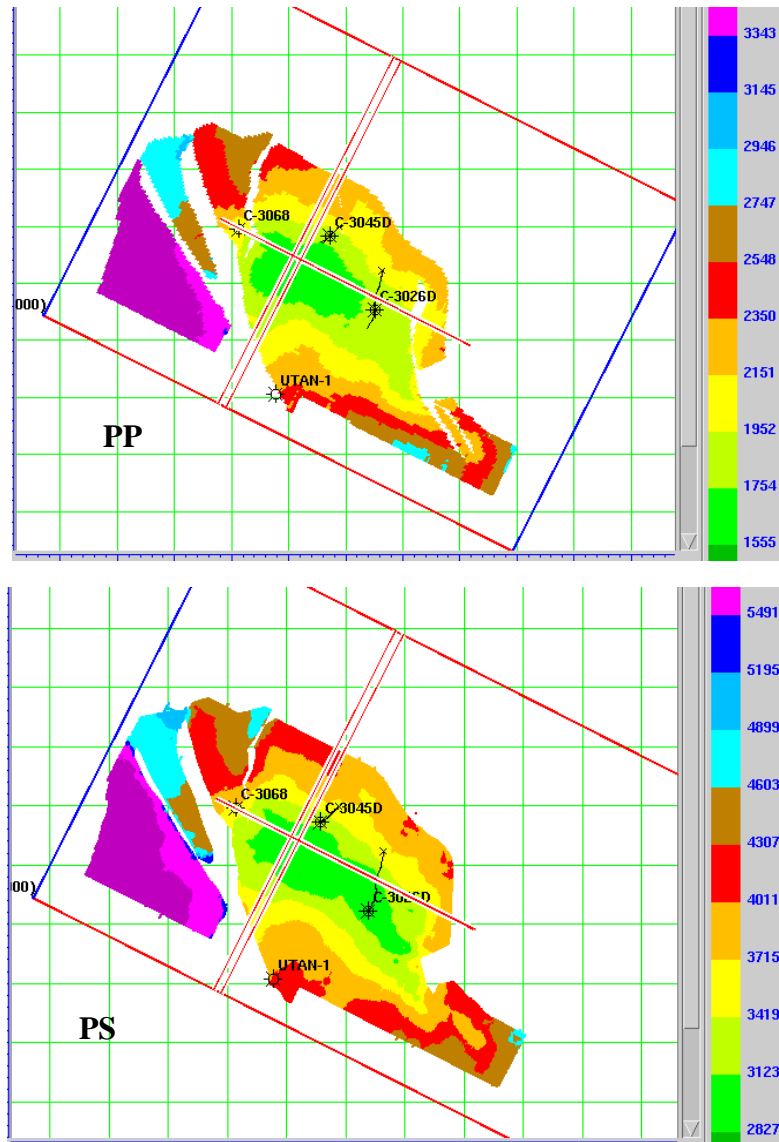
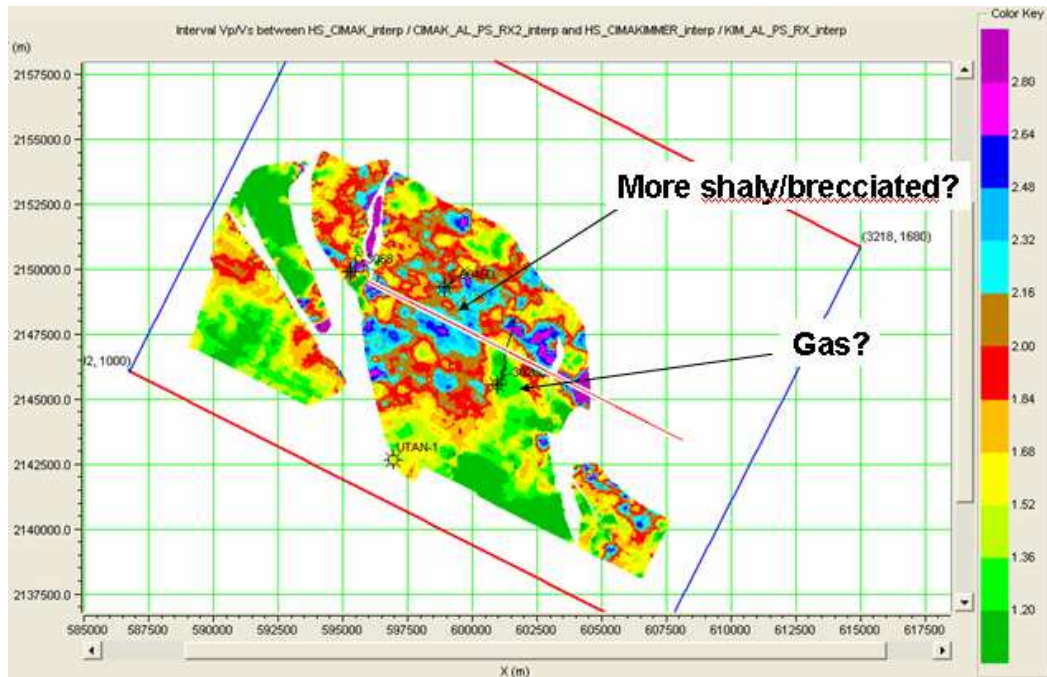


Figure 5.42 *PS* section (inline 2667) with horizons annotated.



**Figure 5.43** *PP* and *PS* time structures interpreted on the top of the allochthonous Kimmerigian. Color represents time in ms.



**Figure 5.44** Interval  $V_p/V_s$  map between allochthonous Cretaceous and Kimmeridgian horizons.

From the  $V_p/V_s$  map, we notice some areas of high values and others with relatively low values. The high values could be interpreted as less consolidated, more fractured, or shalier. The low values could be showing the effects of gas. In addition, we must add that anomalous  $V_p/V_s$  values can be a sign that wavelets are changing significantly or that the picks need to be reconsidered.

#### *Cretaceous Autochthonous*

Let's move deeper to interpret the autochthonous Cretaceous horizon. One anomalous feature can be seen on the *PS* data as the circled area in Figure 5.45. This anticlinal structure is not so evident on the *P*-wave data in Figure 5.46.

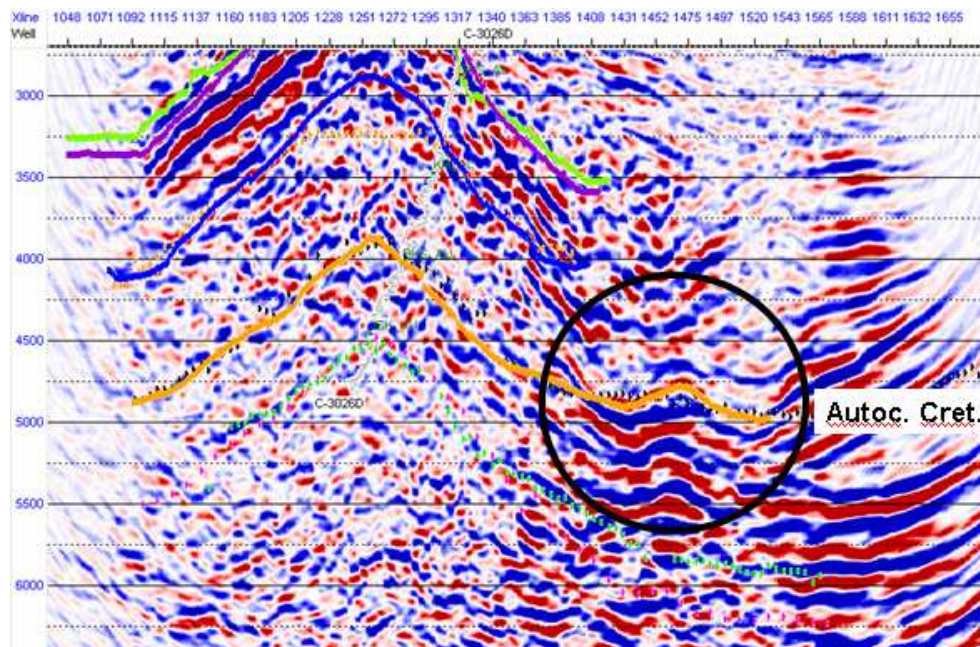


Figure 5.45 Possible deeper structure in evidence on the *PS* section (inline 2667).

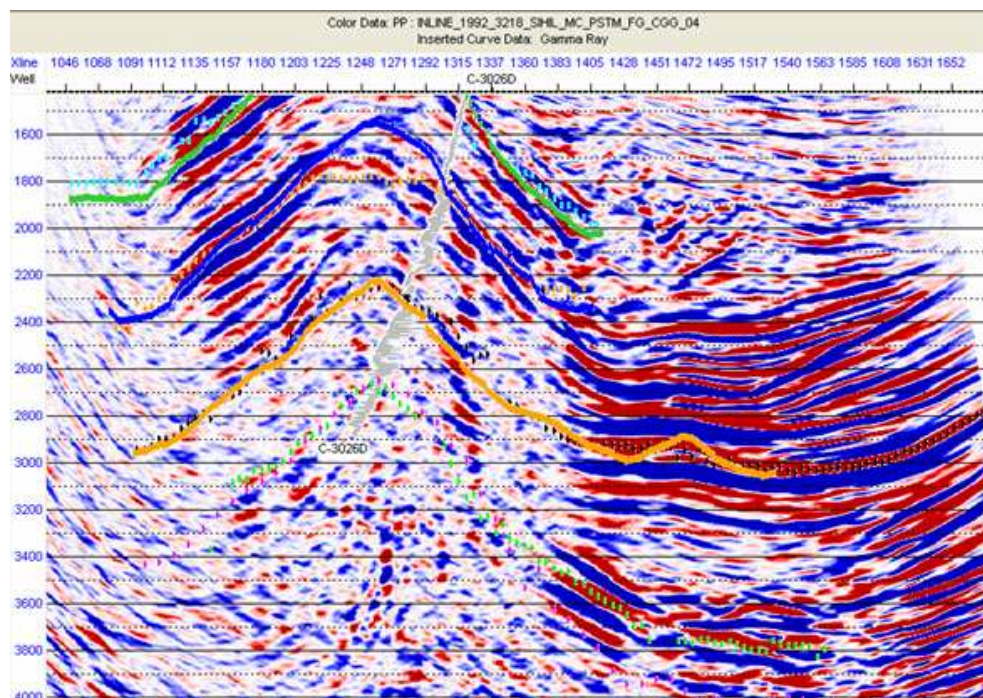
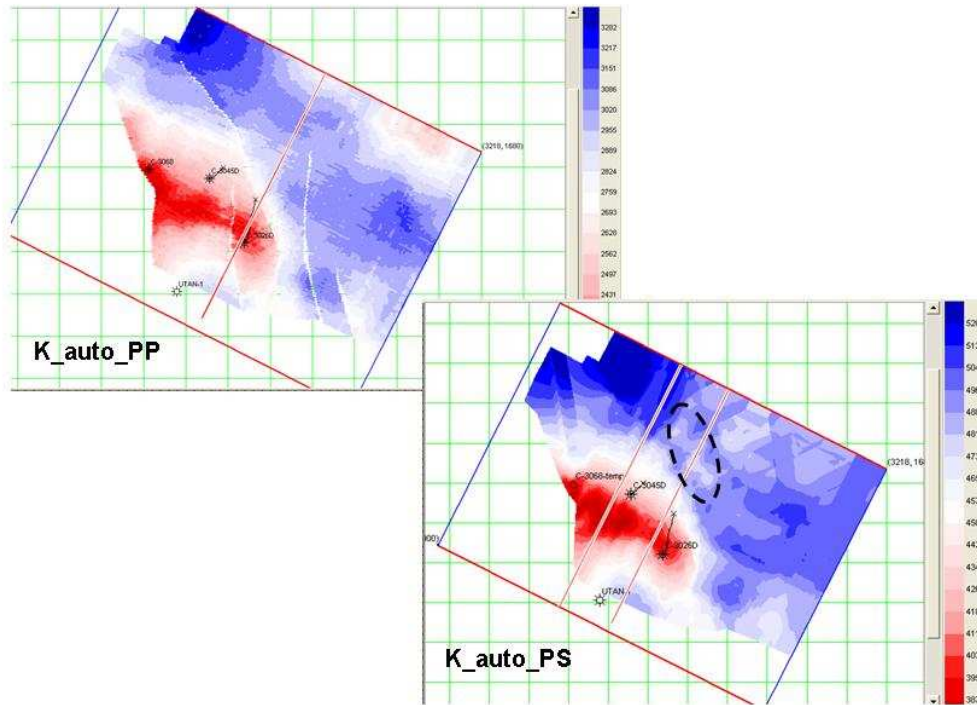


Figure 5.46 Trace of the *PS* horizon superposed on the *P*-wave section. The structure is not as well developed on the *PP* section (inline 2667).

*PS*-time structure map on this horizon also show a fascinating closure, which is not evident on *PP*-time structure map (Figure 5.47).



**Figure 5.47** Time structures on the top of the autochthonous Cretaceous. Note the possible closure on the *PS* time structure.

### *Kimmeridgian Autochthonous*

Now further into the section has us encounter the Autochthonous Kimmeridgian. We see some differences in the *PP* and *PS* structures, but they do provide an overall similarity.

The sections naturally become more difficult to interpret as we go deeper or longer in time. The *P*-wave data show a fairly chaotic region below the Kimmeridgian (Figure 5.48). The *PS* data, while also very noisy, have a pattern that bears some

resemblance to the salt images of the northern areas of the Gulf of Mexico. We have thus postulated the idea of a salt body embedded here (Figures 5.49 and 5.50).

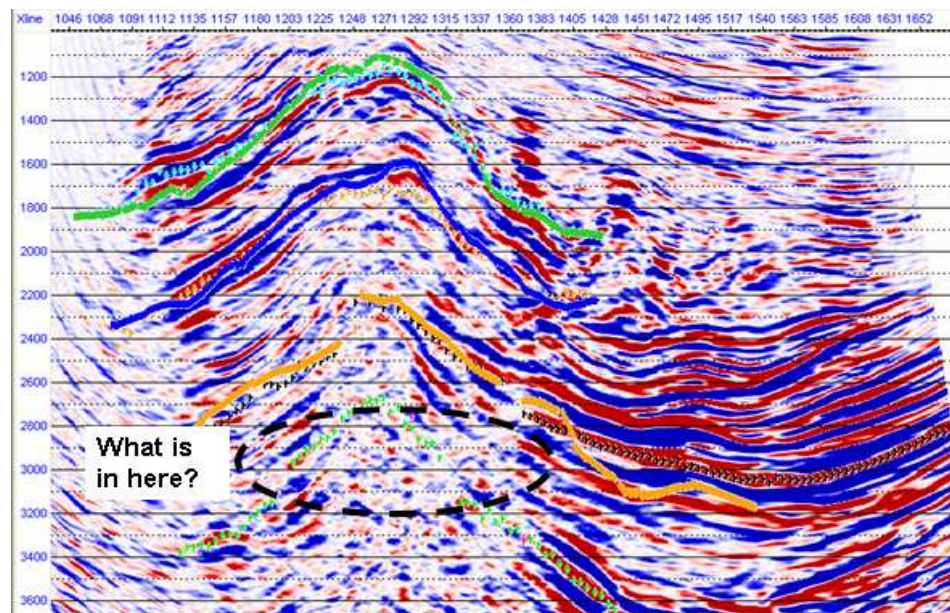


**Figure 5.48** *PP* section (inline 2627) with an ambiguous area in the autochthonous region.

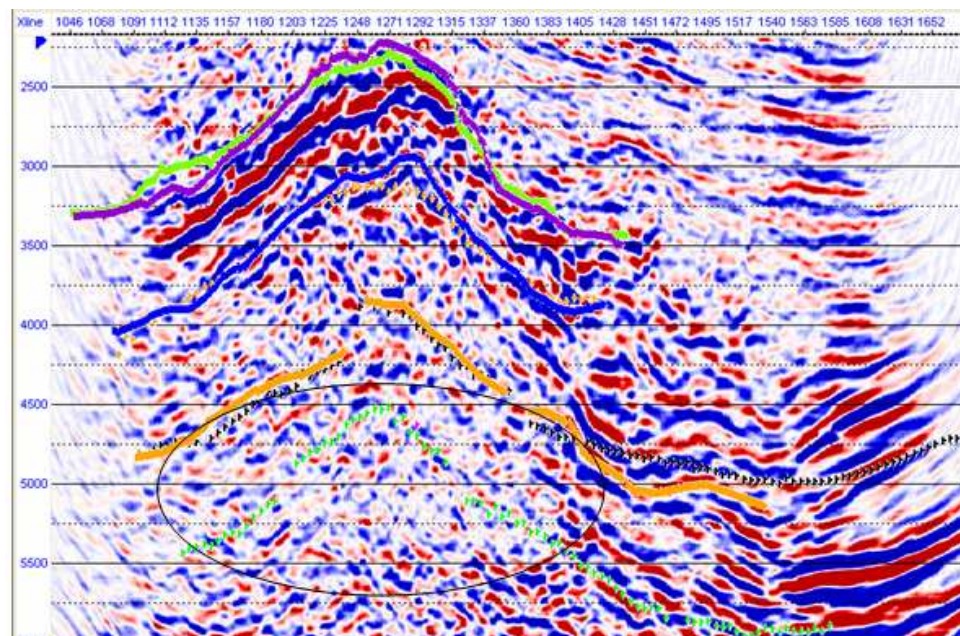


**Figure 5.49** *PS* section (inline 2627) indicating a dim area over a sub-horizontal region.

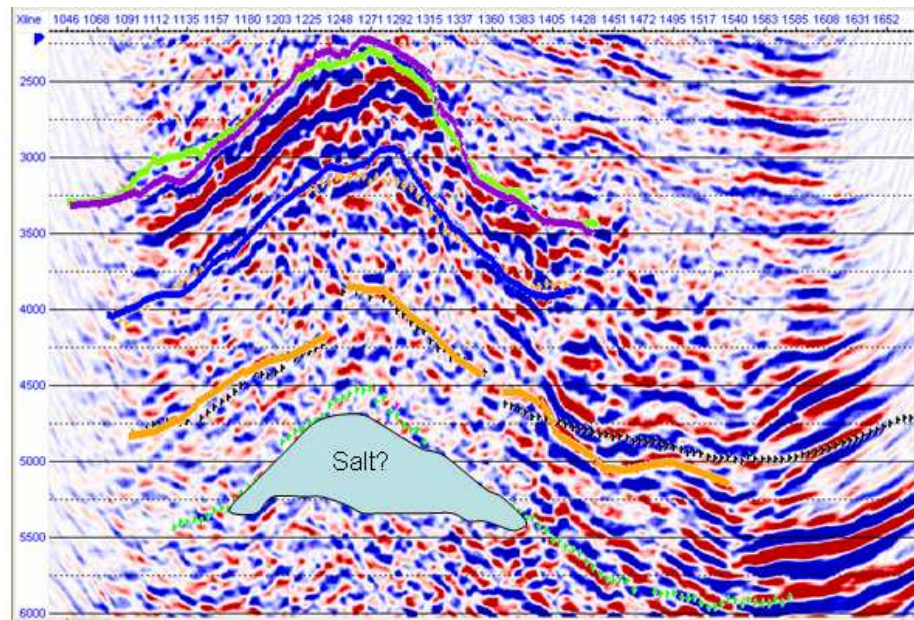


**Figure 5.50** Interpreting the dim area in the previous figure as a salt structure.

### **5.9 Value of the *PS* data**

- Clear image through gas cloud
- More clear image of the top Cretaceous allochthonous
- Structural traps on *PS* seismic data

The *PS* has provided some interesting images of the Cantarell structure that are complementary to or enhancements of the *P*-wave pictures.

1) We see some structural crispness on the top Cretaceous (Akal) likely due to the lack of influence on the *S*-wave by gas saturation.

2) The gas cloud on the *P*-wave data and its corresponding absence on the *PS* may lead to some useful mapping of gas leakage.

3) A new structure, on the north side of Akal, as determined by the *PS* volume may be worth further consideration.

- 4) We see a possible gas/oil contact in Akal that could be verified by log and production information.
- 5)  $V_p/V_s$  values in the southern part of the structure could indicate shaliness or other lithologic change.
- 6) The macroscopic  $V_p/V_s$  values from this study can be used in AVO work (they are not available any other way than by multicomponent analysis).
- 7) A potential salt body has been proposed based on the *PS* images.

### **5.10 Summary**

The Sihil 4C-3D seismic data set provides a very rich set of pictures over the complicated Cantarell geologic structure. We have interpreted the multicomponent seismic data using geologic models, well logs, synthetic seismograms, and VSP. Using the available log and VSP data, we find that Castagna's limestone equation provides a reasonable  $V_p$ -to- $V_s$  map. The synthetic seismograms tie VSP data quite well and correlate with both *PP* and *PS* seismic data. These data help develop a *PS*-to-*PP* time mapping with  $V_p/V_s$  values ranging from 4.5 to 1.9. We correlate the *PS* seismic data as mapped to *PP* time with the *PP* seismic volumes. The shallow horizons are somewhat straightforward to pick, while the deeper structures require more imagination. We picked both allochthonous and autochthonous horizons of the Cretaceous and Kimmeridgian units. Interval  $V_p/V_s$  maps were calculated from these time horizons. We suggest that there are gas effects visible in the *P*-wave sections. The *PS* provide more continuous reflections in these areas (as noted elsewhere, especially in the North Sea). This may provide useful refinement of the structure on the top of the Akal reservoir. In addition, there may be fluid contacts visible in the Akal reservoir. Several new Cretaceous structures are interpreted on the *PS* data.  $V_p/V_s$  values could be interpreted as showing

shaliness or less consolidation in some areas. The lithologic assessments could bear more study. A somewhat imaginative salt structure can be interpreted deeper in the sections.

### **5.11 Recommendations**

The Sihil 4C-3D seismic data are of reasonably good quality. There is a great deal of well log, VSP, and seismic data available in the area. There are numerous outstanding problems in understanding the details of the Cantarell structure, stratigraphy, and its fluid content. There could be some significant new exploration opportunities in the Cantarell region as covered by the Sihil survey. Thus, we would recommend continued analysis of these 4C-3D data. In particular:

- 1) more detailed consideration of interesting leads (e.g., fine time structure over closure regions, time thicknesses, fault mapping);
- 2) further investigate the usefulness of the observed gas effects;
- 3) interpret more horizons and calculate narrower  $V_p/V_s$  values;
- 4) integrate geology with  $V_p/V_s$  values in more detail;
- 5) build a more detailed velocity model for future AVO studies, inversions, and depth conversions;
- 6) do *PP* and *PS* inversions;
- 7) estimate well logs from *PP* and *PS* attributes (inversions and reflectivity volumes) and co-kriging/neural nets;
- 8) after more has been extracted from the time volumes, consider reprocessing the data to depth and for anisotropy.

## Chapter Six: An example of 2D-3C multicomponent seismic interpretation

### 6.1 Introduction

In this chapter, a 2D land multicomponent dataset in the United States is interpreted and analyzed. Due to proprietary and commercial reasons, the location of this survey, the formation and well names, and the target zones are all kept anonymous. The purpose of this study is to investigate the rock physics, particularly  $V_p$ - $V_s$  relationship in this area, to analyze and understand the response of multicomponent seismic data.

This 2D-3C survey was acquired in early 2000. There are three lines, from south to north namely 13S, 13N and 12S, approximately 1 mile apart and about 6.2 mile long for each line (Figure 6.1). The CDP bin size is 55 ft. The source type is unknown. Most of the surface area in the survey is farm land with very small elevation variations and less surface condition changes. Both *PP* and *PS* data used in this study are post-stack migrated datasets. Unfortunately, the field acquisition report and data processing report are not available. The original SEG Y tapes and data loading logs are also not found. The data are exported from Landmark's SeisWorks database as segy files and loaded into Hampson-Russell's ProMC software.

There are a few deep wells with modern electric logs in this area but none of them are on these 2D lines. The nearest deep well having dipole sonic log is J28, drilled in 2009, which is located about one mile south of line 13S. The projected location of well J28 on line 13S is at CDP 156 (Figure 6.1).

There are a few existing (and abandoned) oil and gas fields in vicinity. However, none of the producing fields is on or between these three 2D lines.

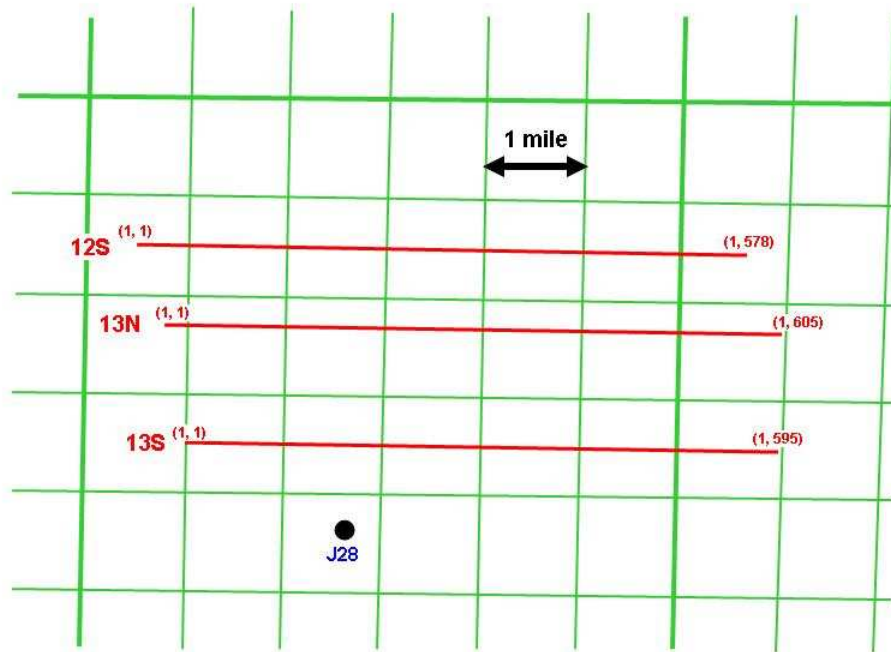


**Figure 6.1** The basemap of three 3C-2D lines and location of well J28. Each grid is one section, which is one mi<sup>2</sup>.

## 6.2 Well log and $V_p$ - $V_s$ relationship

The full logging suite of Well J28 is shown in Figure 6.2. The major formation tops are also posted. Well J28 has TD at about 10122 ft, or 3085 m. One observation is that the P-velocity for most formations is less than 3000 m/s. Only the very short interval close to TD (D2 and below) has velocity greater than 3000 m/s. This slow velocity in a relatively deep section indicates that the sediments likely have a short burial history and this basin is relatively young.

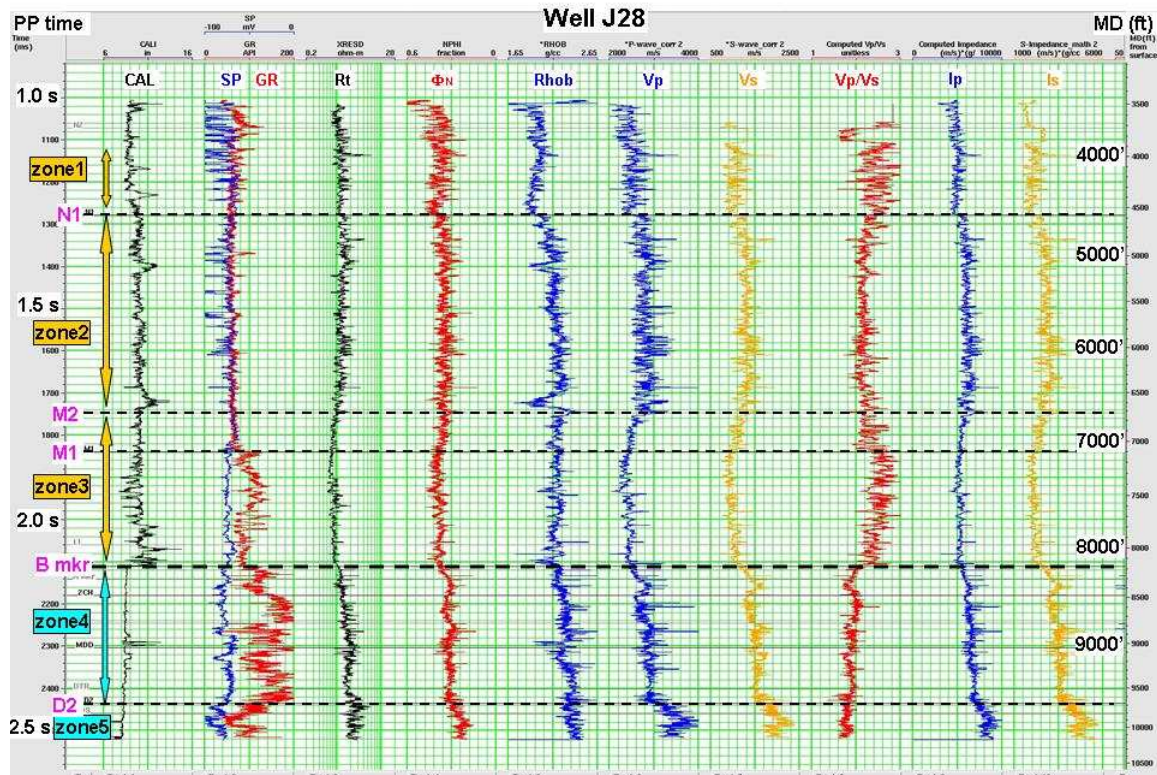


**Figure 6.2** Log curves in well J28 with formation tops posted. Notice the five different zones by log responses.

It is noticed that the column revealed in well J28 could be subdivided into five intervals/zones according to log responses, mainly from GR, SP,  $V_p$  and  $V_p/V_s$ . The definition, thickness and the approximate average value of GR, Density,  $V_p$ ,  $V_p/V_s$  are listed in Table 6.1.

Zone 1 has the average  $P$ -velocity of 2500 m/s,  $V_p/V_s$  about 2.5 and density less than 2.0 g/cc. In conjunction with the oscillating SP, this zone looks like an unconsolidated sandy formation. Zone 2 is similar to zone 1, with more stable  $V_p/V_s$  at 2.2 and slightly higher  $V_p$ , about 2800 m/s, and higher density but less SP response. In zone 3,  $V_p$  drops to 2400 m/s at about 6800' to 8200' (2075 m to 2500 m) interval but  $V_p/V_s$  increases to 2.5.

Zone 4 and zone 5 apparently are quite different from zone 1 to 3, expressed by much higher GR and  $V_p/V_s$  less than 2.0.

The mud log of well J28 indicates that zone 1 and 2 are mainly unconsolidated sand, siltstone and claystone; zone 3 consists shale, claystone, mudstone and siltstone; zone 4 is mainly clay shale, porcelaneous claystone; zone 5 has a mixture of a variety of lithology like clay shale, foraminiferous shale, calcareous porcelanite, porcelaneous chert, limestone and small amount of sandy siltstone.

The general deposition environment for zones 4 and 5 is quiet deep water. For zone 1 to 3, it is shallow water to fluvial and maybe alluvial at very shallow depth.

Zone #	definition	Thickness (ft)	Ave. GR (API)	Ave. $\rho$ (g/cc)	Ave. $V_p$ (m/s)	Ave. $V_p/V_s$
1	3900' – 4602' (N1)	702'	60	1.95	2500	2.5
2	4602' (N1) – 6754' (M2)	2152'	60	2.15	2800	2.2
3	6754' (M2) – 8207' (B mkr)	1453'	90	2.15	2400	2.5
4	8207' (B mkr) – 9707' (D2)	1500'	150	2.30	2800	2.0
5	9707' (D2) – 10122' (TD)	415'	100	2.40	3500	1.9

**Table 6.1 The definition, thickness and average value of GR, density,  $V_p$  and  $V_p/V_s$  for the five zones in well J28.**

As there is no publication on the framework of the general relationship between  $V_p$  and  $V_s$  in this area, it is necessary to check each of the five zones to see that what kind of  $V_p$ - $V_s$  relationship the data may follow. By crossplotting the fairly high quality  $V_p$  and  $V_s$  log, five linear regressions have fit the data points in the form of  $V_s = \mathbf{a} * V_p + \mathbf{b}$ ,

where the coefficient **a** and **b** are shown in Table 6.2. The unit for both  $V_p$  and  $V_s$  are m/s. As a reference, the **a** and **b** for Mudrock line are also listed in this table.

Zone #	definition	thickness	$V_s$ (m/s) = <b>a</b> * $V_p$ (m/s) + <b>b</b>	
			<b>A</b>	<b>b</b>
Mudrock line			0.8621	- 1172
1	3900' – 4602' (N1)	702'	0.8462	- 1101
2	4602' (N1) – 6754' (M2)	2152'	0.7045	- 684
3	6754' (M2) – 8207' (B mkr)	1453'	0.7810	- 902
4	8207' (B mkr) – 9707' (D2)	1500'	0.7212	- 543
5	9707' (D2) – 10122' (TD)	415'	0.6858	- 409

**Table 6.2 The result of linear regression of  $V_p$  versus  $V_s$  for five zones in well J28.**

Although all the five equations are different, we can put them into two groups: zones 1, 2 and 3 look close to Mudrock line; zones 4 and 5 have another trend. To be more illustrative, all data points of  $V_p$  and  $V_s$  in zone 1 to 3 are plotted and the regression redone, giving us the following  $V_p$ - $V_s$  relationship:

$$V_s = 0.7703 V_p - 873 \quad (6.1)$$

Similarly,  $V_p$  and  $V_s$  in zone 4 and 5 are plotted together, and the regression for  $V_p$  versus  $V_s$  is:

$$V_s = 0.7115 V_p - 514 \quad (6.2)$$

Figure 6.3 clearly demonstrates these two distinct trends as we crossplot all the data points in well J28, with Mudrock line and lines of  $V_p/V_s = 1.6, 2.0, 3.0$  superimposed

as reference lines. The two clusters have little overlap area. The shallow trend (zone 1 to 3) follows the Mudrock line quite well, and more or less, can be treated as the local calibration of Mudrock relation. In other words, the shallow part until the formation B-marker in this area is very likely the clastic sand-shale sequence. However, the deep part (zone 4 to 5) below B-marker, which contains the deep-water deposits, can not be represented by Mudrock line and has its own  $V_p$ - $V_s$  relationship (Equation 6.2). It's also different from Castagna (1993) carbonate empirical relationship (Equation 5.5). The  $V_p/V_s$  value for most data in this part is between 1.6 to 2.0.

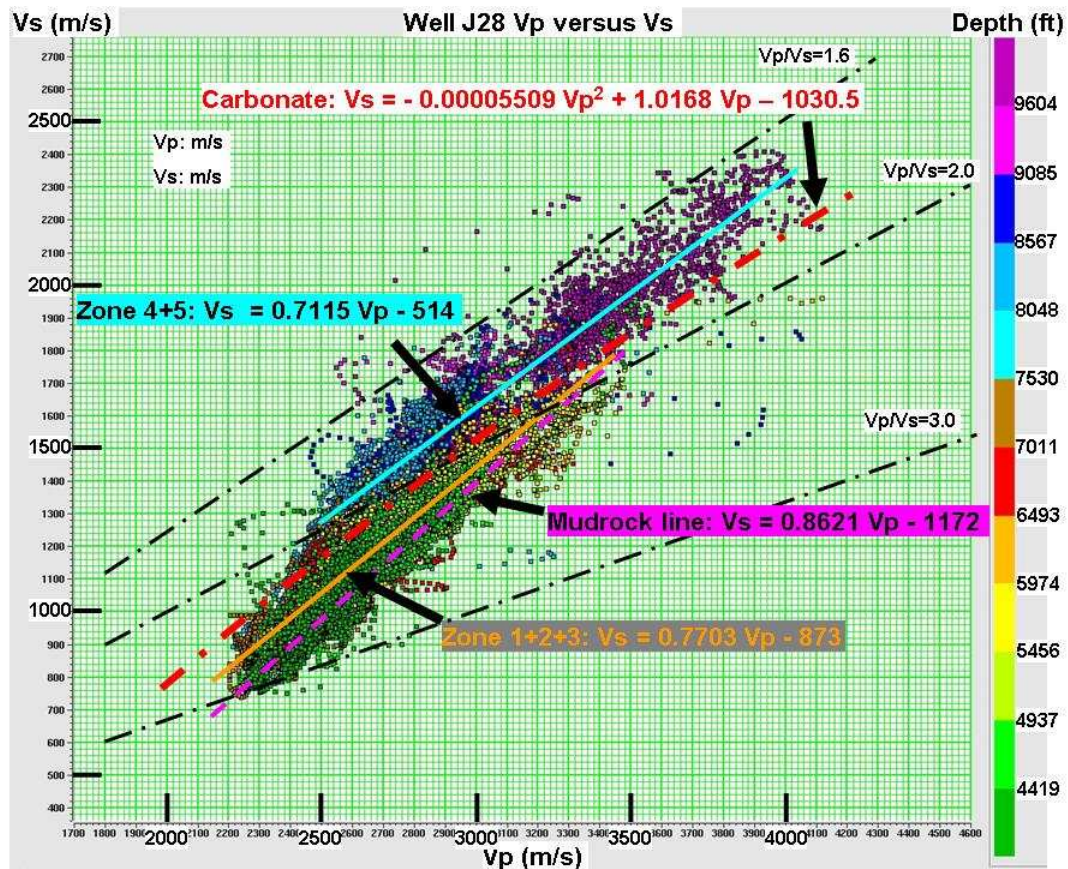
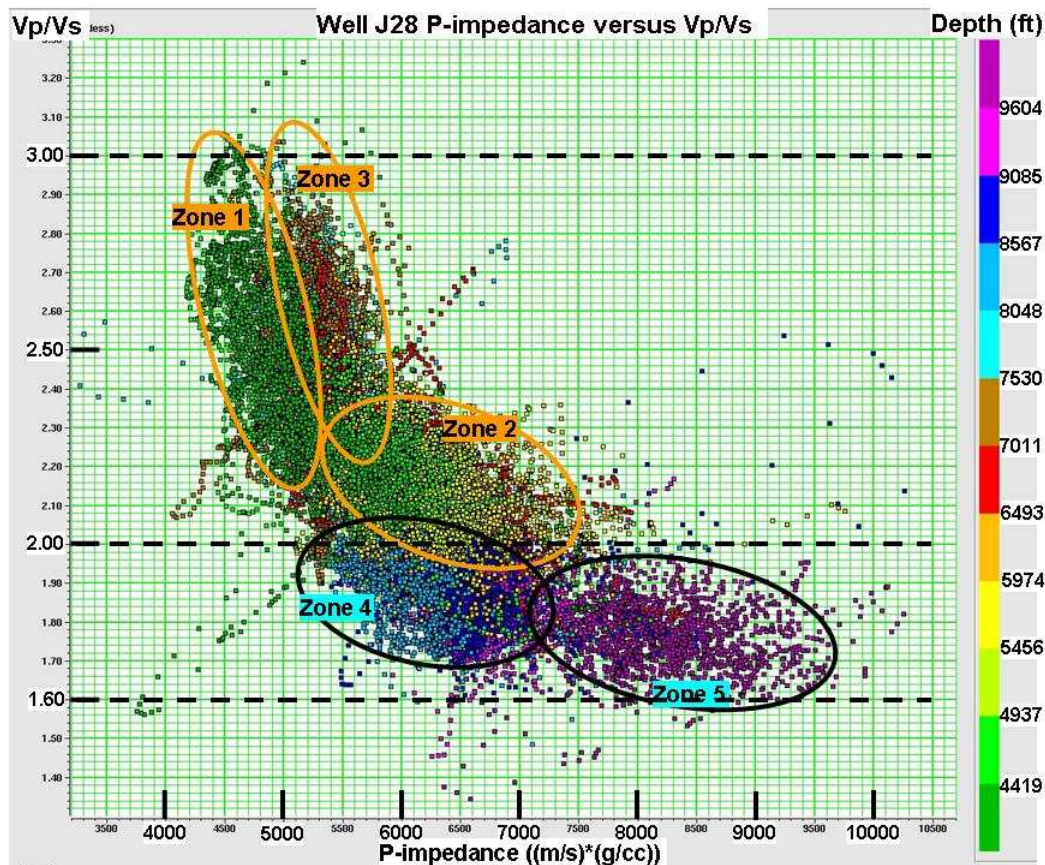


Figure 6.3 Crossplot of  $V_p$  versus  $V_s$  in well J28. The shallow and deep zones show different regression relationship. The Mudrock line and three constant  $V_p/V_s$  lines are also posted for reference. The color key is measured depth.

Another commonly used crossplot to show the lithology or possible separation of different lithology is  $P$ -impedance versus  $V_p/V_s$ . The usefulness of this plot is that both  $P$ -impedance and  $V_p/V_s$  are seismically derivable, which leaves us the possibility of using seismic data to determine the lithology. Figure 6.4 shows the crossplot of  $P$ -impedance versus  $V_p/V_s$  in well J28, with five zones schematically illustrated. Again, the deep-water deposits of zones 4 and 5 have much lower  $V_p/V_s$  than the shallow clastic deposits (zones 1 to 3). For the three shallow zones, zone 3 is an interesting exception: although it is much deeper, it has lower  $P$ -impedance and higher  $V_p/V_s$  than zone 2. The reason needs to be further investigated.



**Figure 6.4** Crossplot of  $P$ -impedance versus  $V_p/V_s$  in well J28. The five zones are easy to recognize in this plot. The color key is measured depth.

### **6.3 Checking *PP* and *PS* seismic data**

The available stacked data are post-stack migrated. Vertical component (*PP*-wave) and horizontal component (*PS*-wave) data of the three 2D lines are loaded into Hampson-Russell's multicomponent seismic interpretation software ProMC. For some reason, all the *PP* data start at about 500 ms and the data above been chopped. The *PS* data start from around 800 ms *PS* time. *PP* and *PS* data for each 2D line are displayed in Figure 6.5 to 6.10.

The *PP* data looks to be typical land seismic data. The subsurface formations are following a gentle monocline dipping to the west. Most of the events are near parallel, and we can see there is a subtle trend of wedging to the east. This indicates that the paleo-topography, which is most likely a gentle slope, is stable and similar for all the sediments deposited under a relative quiet deposition environment. The basement (ranging from *PP* time 2.6 s at the east to 3.4 s at the west end) shows the same dipping direction, and has gentle structures and high angle faults. Within basement, there are not many continuous seismic events. The yellow circle area looks like a ramp.

Looking at the *PS* data of the same line 13S (Figure 6.3), we see the events are there, but with lower frequency content, as usual. The shallow data has stronger amplitude and more events. The continuity of *PS* data decreases little bit at depth, especially in the left side area.

The quality of line 13N and line 12S is not as good as line 13S, especially *PS* data, the lateral continuity is degrading. For this reason, only line 13S is interpreted.

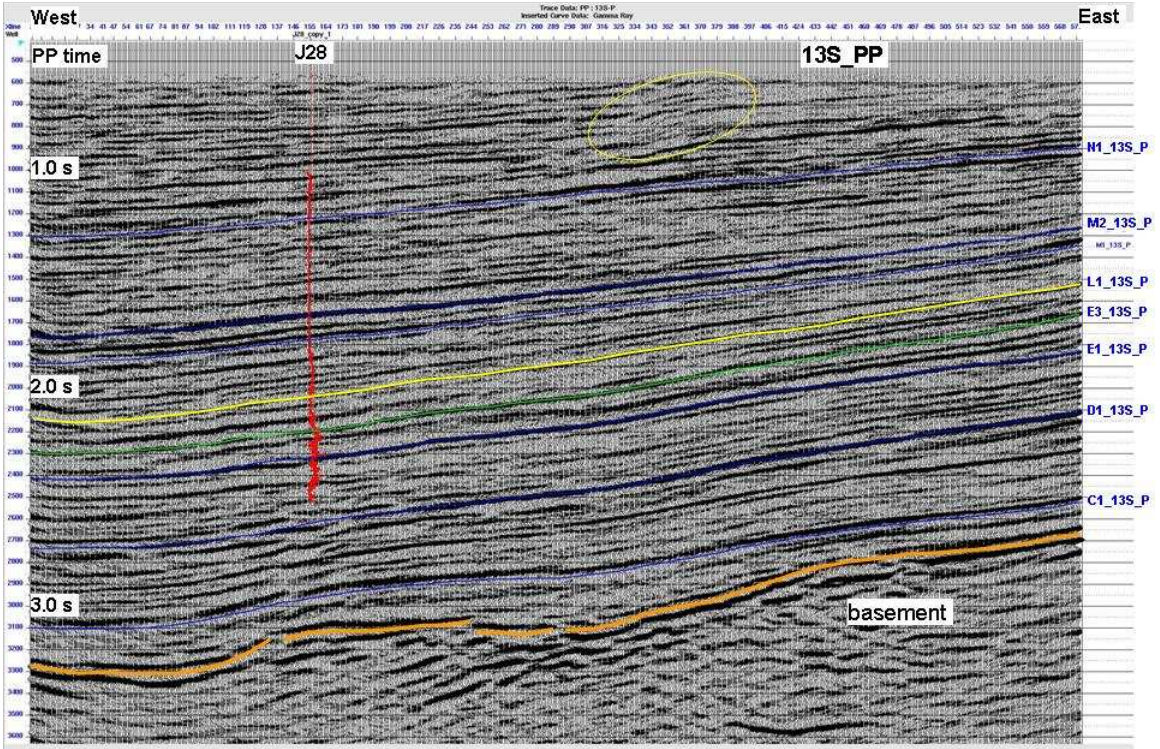


Figure 6.5 PP section of 2D line 13S. Well J28 is projected on this line.

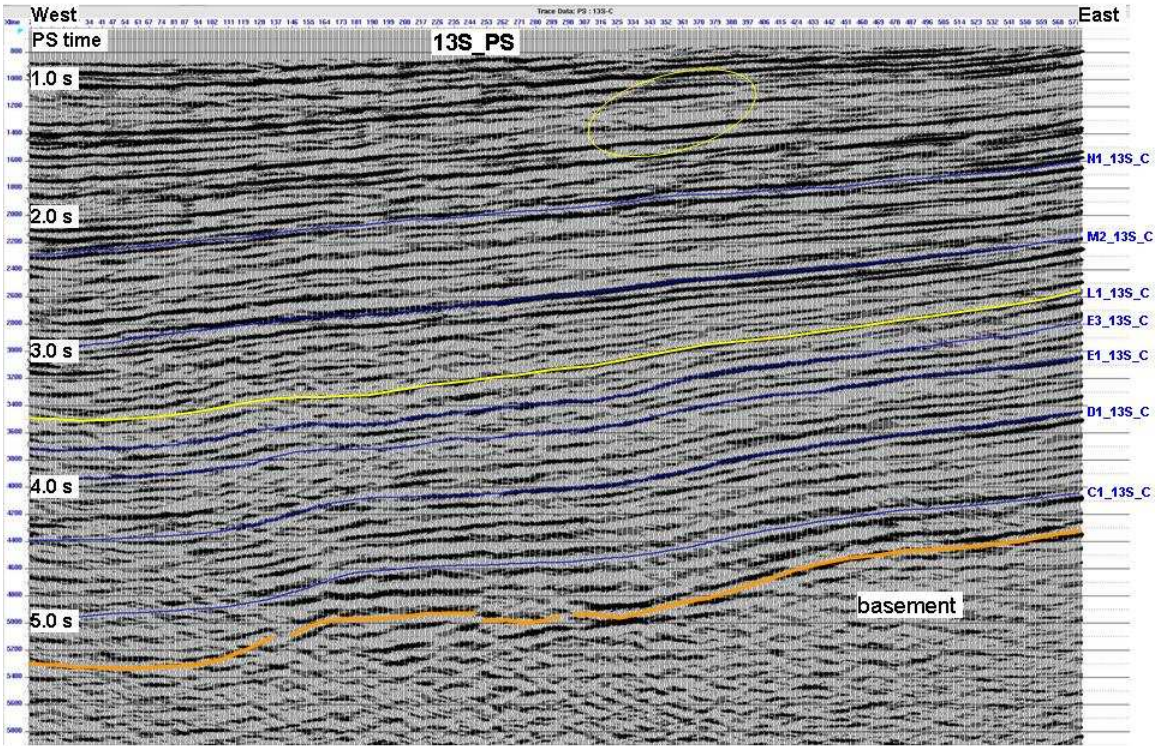


Figure 6.6 PS section of 2D line 13S.

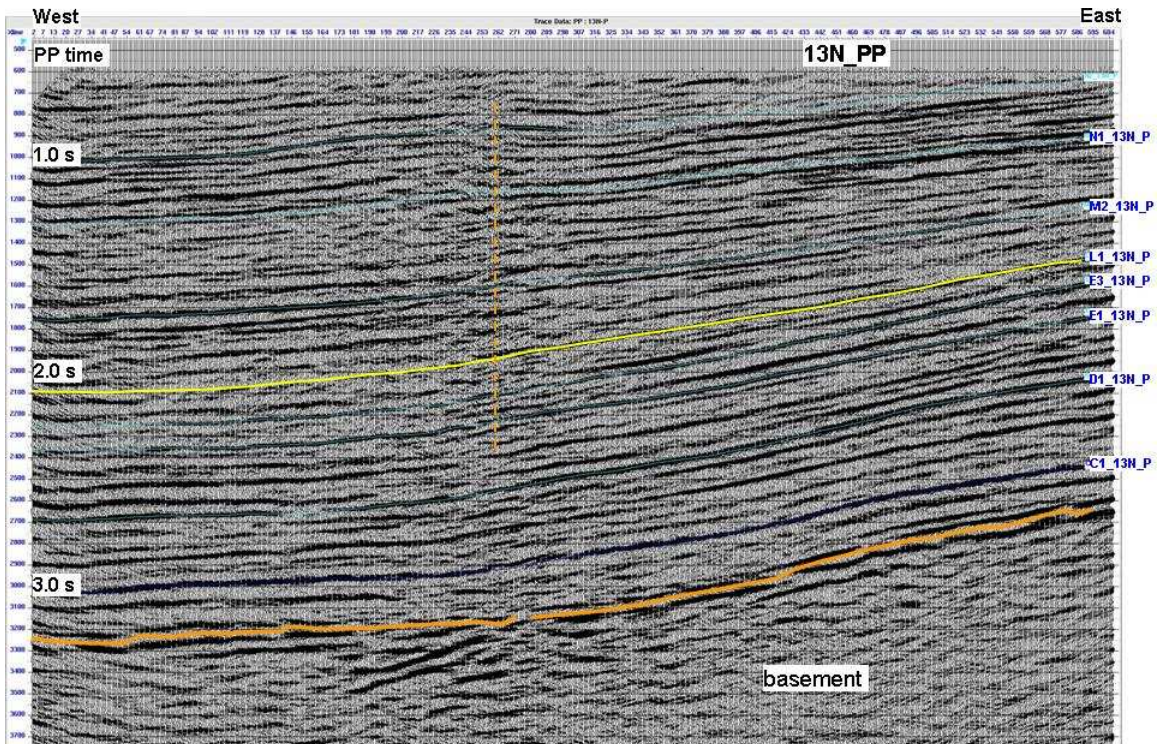


Figure 6.7 PP section of 2D line 13N.

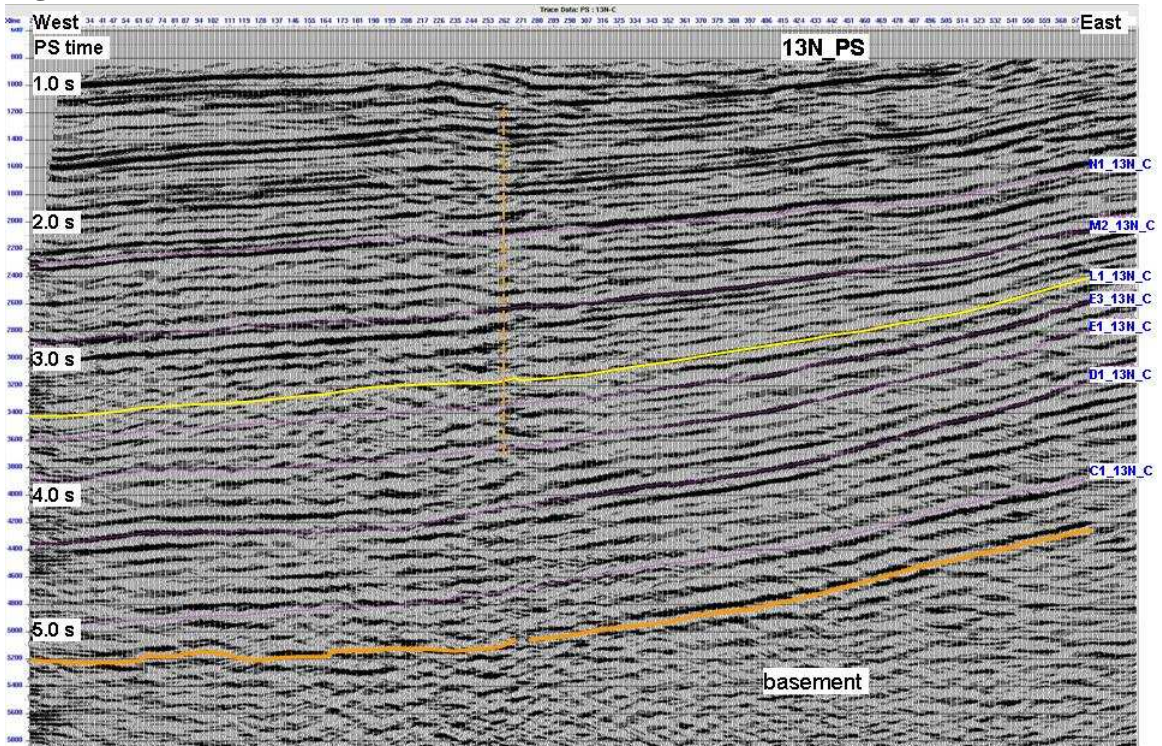


Figure 6.8 PS section of 2D line 13N in its native PS time domain.

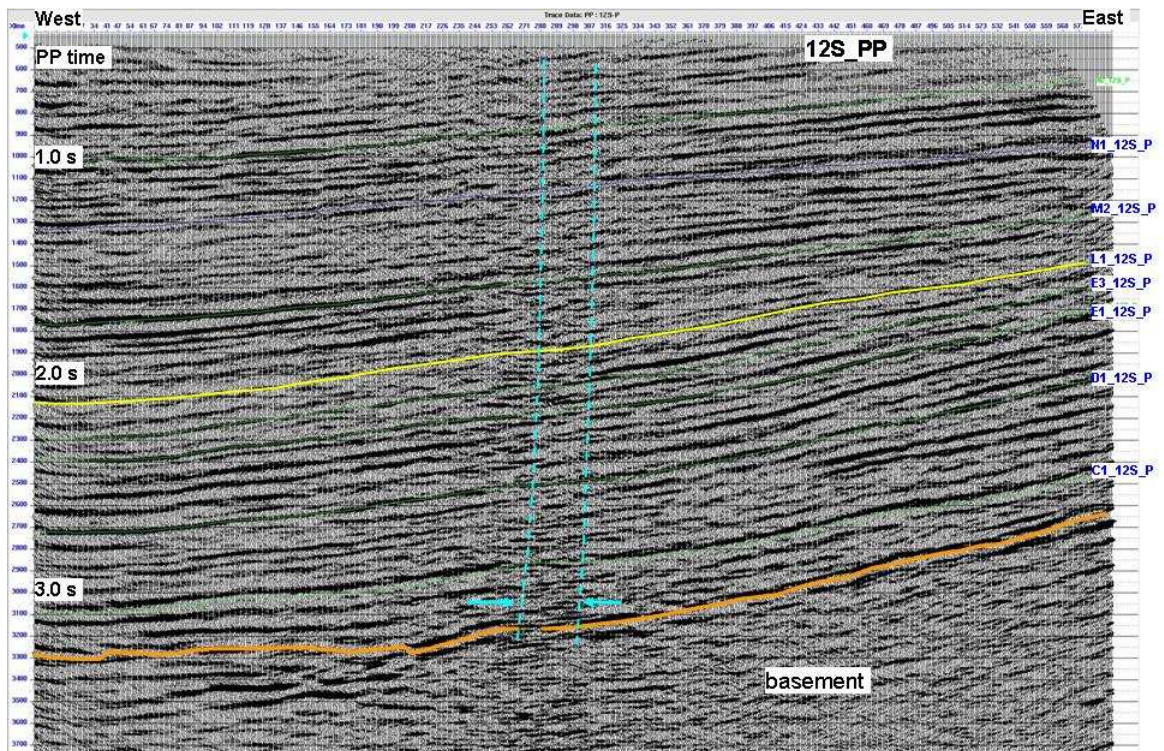


Figure 6.9 PP section of 2D line 12N.

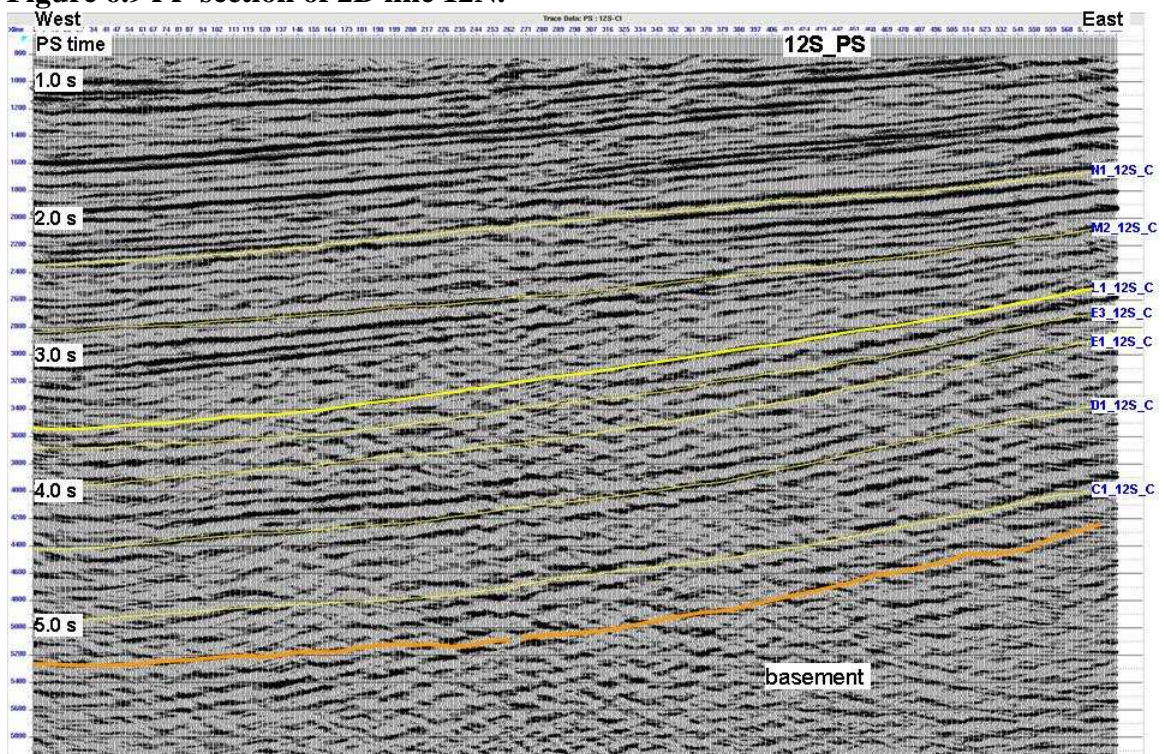
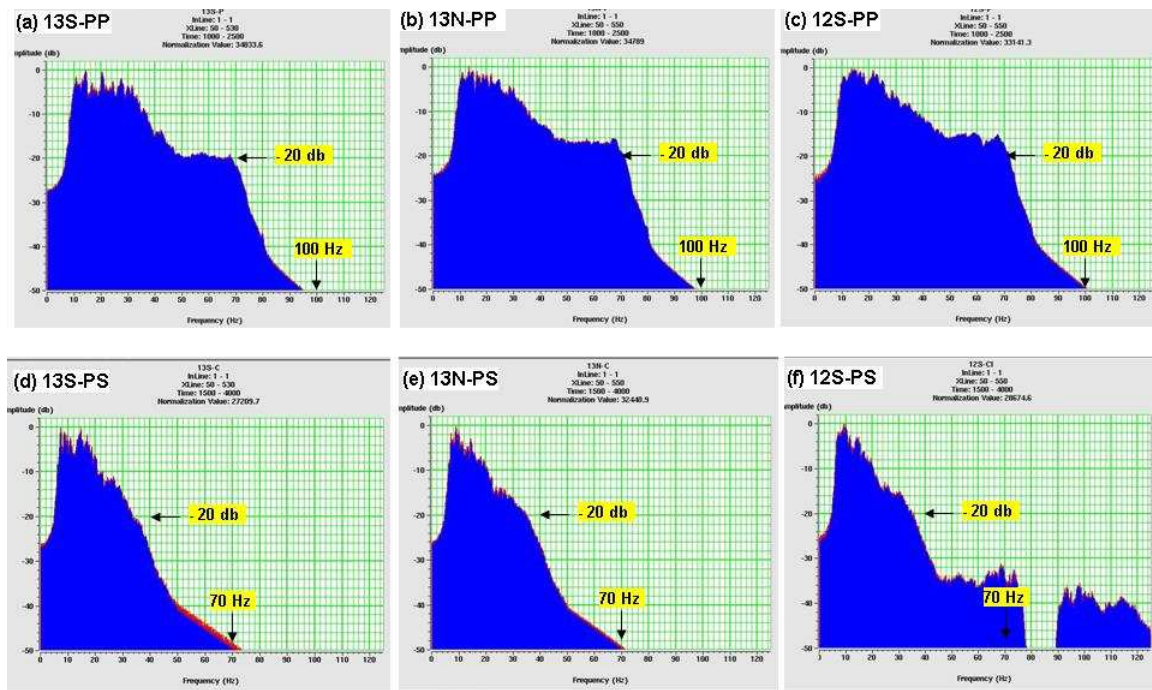


Figure 6.10 PS section of 2D line 12N in its native PS time domain.

*Frequency components: PP and PS*

Frequency is checked for the *PP* and *PS* data of all three 2D lines (Figure 6.11). For *PP* data, the window to calculate the amplitude spectrum is 1000 – 2500 ms in *PP* time. For *PS* data, the time window is 1500 – 4000 ms in *PS* time. As usual, the *PP* data show a higher frequency than *PS* data. The south most line 13S appears to have better quality data for having a frequency plateau at 10 – 40 Hz, meanwhile both line 13N and 12S lost this plateau. *PS* data has the similar trend: the second peak at about 15 Hz from line 13S decreases for line 13N and 12S. All the *PP* data have a shoulder in 50 – 70 Hz, which looks like an over boost in the data processing procedure of frequency balance. *PS* data of line 12S shows a unusual spectrum in the high end of its bandwidth.



**Figure 6.11** Amplitude spectrum of the *PP* data (a) line 13S, (b) line 13N and (c) line 12S, and *PS* data (d) line 13S, (e) line 13N and (f) line 12S.

## 6.4 *PP* and *PS* synthetic seismograms

Using  $V_p$  and density log of well J28, the *P*-wave synthetic seismogram is generated to correlate with *PP*-wave seismic (Figure 6.12). The wavelet used for synthetic is extracted from 41 traces centered at well location (CDP 156) in a *PP*-time window 1000 ms – 2500 ms on *PP* seismic of line 13S.

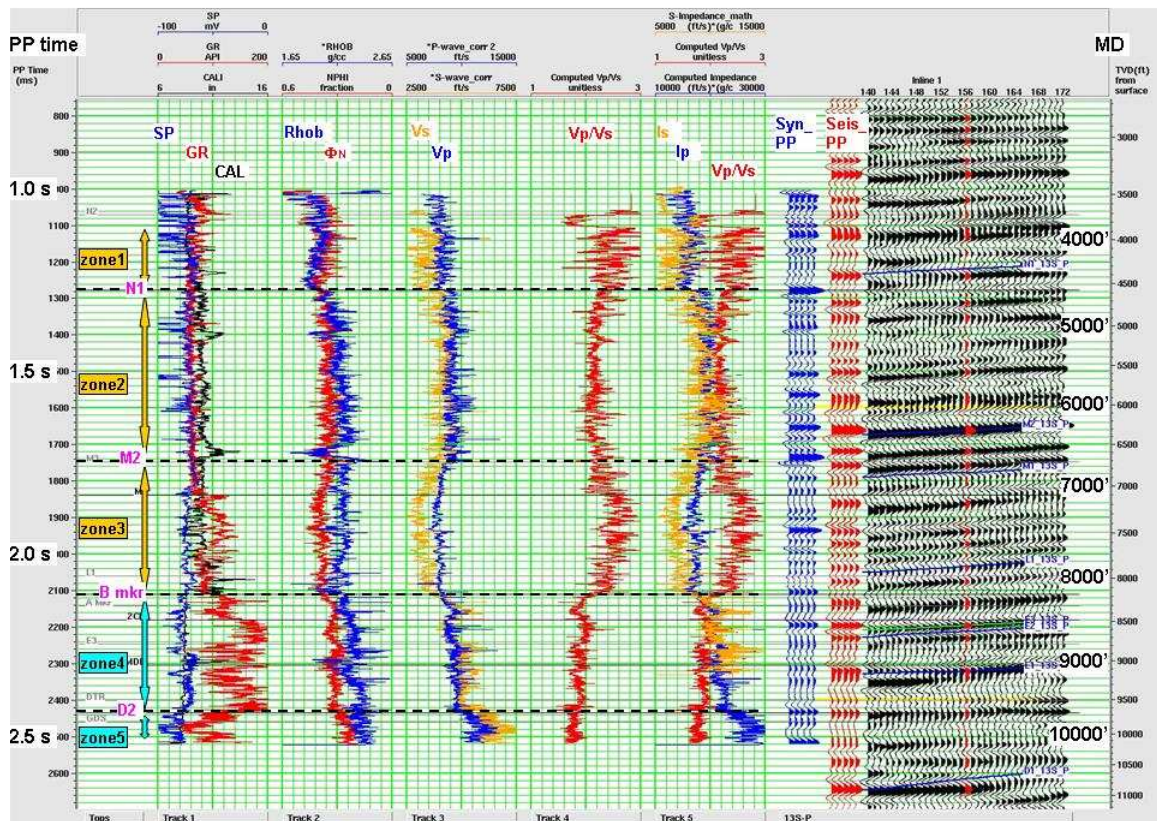
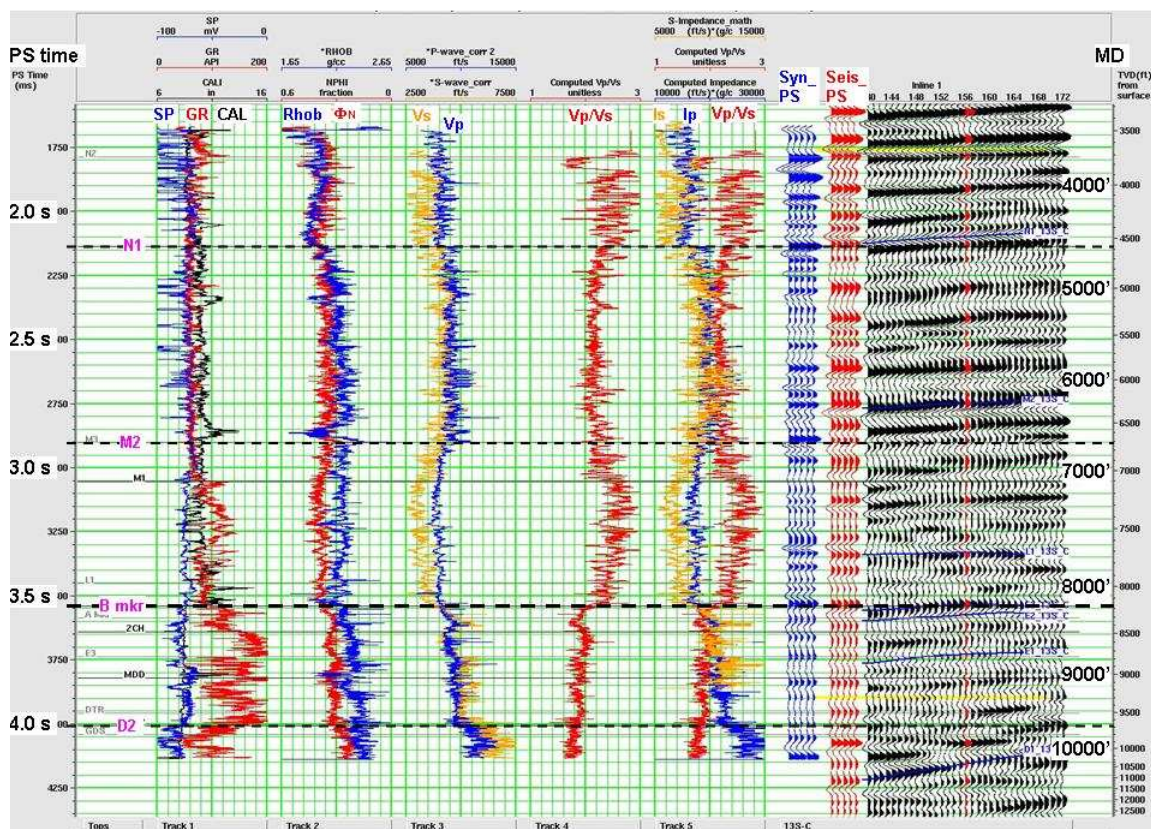


Figure 6.12 Log curves in well J28, the *PP* synthetic and *PP* seismic section.

The *PS*-wave synthetic seismogram is created using  $V_s$  and density log, with the wavelet extracted from 41 traces centered at well location (CDP 156) in a *PS*-time window 1500 ms – 3500 ms on *PS* seismic of line 13S (Figure 6.13).



**Figure 6.13** Log curves in well J28, the *PS* synthetic and *PS* seismic section.

In Figure 6.5 and 6.6, except the basement, all the events on *PP* and *PS* seismic sections don't show strong easy-recognizable signatures or characters as seismic markers. Continuous deposition, lack of unconformities, young sediments, and the distance from well to the 2D seismic line, all are factors when put together, may (or partially) explain the poor correlation between synthetics and surface seismic for both *PP*- and *PS*-wave.

## **6.5 Interpretation and analysis**

Because the correlation between well synthetics and seismic data are not quite conclusive, another criteria for picking key horizons is to pick the most lateral continuous event, on both *PP* and *PS* sections. Actually, the similarity between *PP* and *PS* is quite

high for line 13S, which also increases the confidence of the *PS* seismic interpretation. After the horizons have been picked, the step of horizon matching forced the *PS* to be at the *PP* time of the same set of horizons on *PP* seismic. In turn, the spatially varying  $V_p/V_s$  between two adjacent horizons are achieved (Figure 6.14).

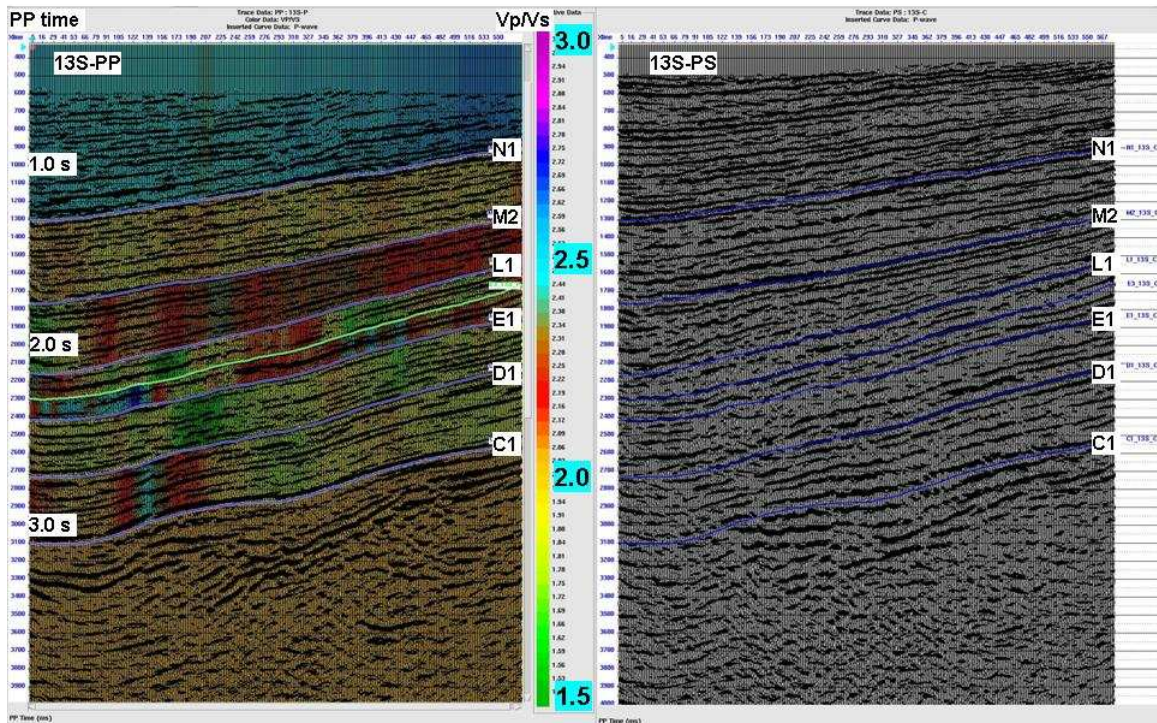


**Figure 6.14** *PP* and *PS* horizon matching of line 13S, in *PP* time domain. The left panel is *PP* data overlapped with color representing  $V_p/V_s$ . The right panel is *PS* data.

The  $V_p/V_s$  is about 2.4 for the shallow formations above horizon N1, about 2.0 for the interval between horizon N1 to M2, and about 2.2 for the zone between horizon M2 to L1, which is corresponding to the average of log measured  $V_p/V_s$  in well J28 of 2.5, 2.2, and 2.5, respectively (Table 6.1), although this well is about 1 mile away from line 13S.

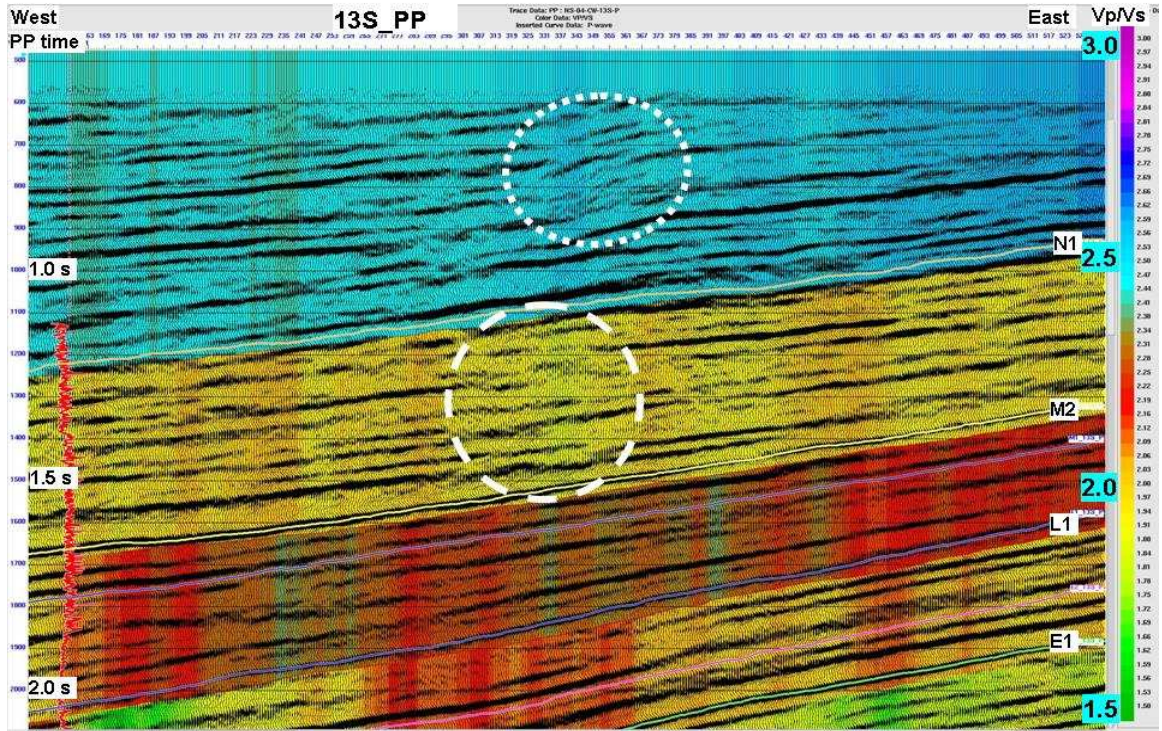


Figure 6.15 PP data of line 13S. Background color is  $V_p/V_s$  from horizon matching.

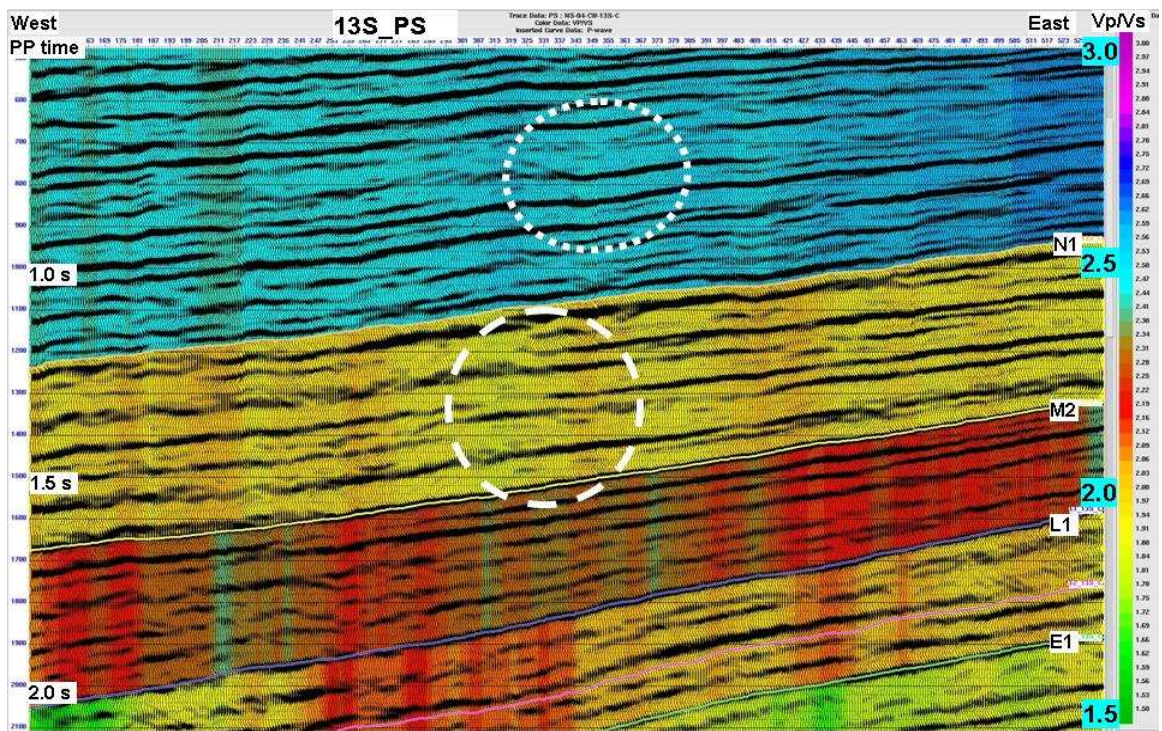


Figure 6.16 PS data of line 13S. Background color is  $V_p/V_s$  from horizon matching.

Another observation is that horizon L1 seems to act as a boundary. Above L1, generally speaking, *PS* data show better continuity than *PP* data (circled areas in Figure 6.15 and Figure 6.16). More obvious at the very shallow portion, above 1.0 second in *PP* time, *PS* data looks have higher frequency and much better definition. In contrast, below horizon L1, the *PP* data have better defined and more continuous events than *PS* data.

## **6.6 Conclusion**

Detailed study in well J28 reveals that there are two distinct trends for  $V_p$ - $V_s$  relationship in this area: formations above B-marker show  $V_p$ - $V_s$  relationship close to Mudrock line, or a local calibration; formations below B-marker, which are deep-water sediments, have a Mudrock-different  $V_p$ - $V_s$  relationship. The deep-water shale and siliceous shale have  $V_p/V_s$  less than 2.0 and approach to 1.6 when getting deeper. The feature of low  $V_p/V_s$  associated with low velocity is different than that of the normal clastic sand-shale sequence.

Three 2D-3C seismic lines are checked. The *PS* data exhibits more continuity in the shallow portion than *PP* data, but worse at depth. At well location, *PP* and *PS* synthetic seismograms have been generated but both have poor correlation with surface seismic. A number of key horizons are interpreted on both *PP* and *PS* section of line 13S, and a  $V_p/V_s$  profile is achieved by *PP* and *PS* horizon matching. The horizon-derived  $V_p/V_s$  corresponds with log-measured  $V_p/V_s$ .

## Chapter Seven: Conclusions and future work

### 7.1 Conclusions

A 3C-3D seismic dataset over Husky Energy's Ross Lake heavy-oil field in south-western Saskatchewan, Canada has been interpreted and analyzed. For these sand-shale dominated consolidated formations, the  $V_p$ - $V_s$  relationship from dipole sonic log in five regional wells corresponds with the Mudrock line very well. We find a reasonably good correlation among synthetic seismograms, VSP (zero-offset and offset for  $PP$ -wave, offset for  $PS$ -wave), and surface seismic data for both  $PP$ -wave and  $PS$ -wave. The  $PS$  synthetic seismogram provides an essential guide to interpret horizons on  $PS$  seismic. In addition, the far-offset VSP-CCP map helps to identify geological formations on  $PS$  seismic data and is another bridge to connect  $PP$  and  $PS$  seismic data.

The low velocity channel sand shows as a thick anomaly on the  $P$ -wave isochron map between the two horizons which are right above and below the target formation. On the  $V_p/V_s$  map calculated from  $PP$  and  $PS$  isochrones, the channel sand is delineated as a low  $V_p/V_s$  anomaly, but with a higher  $V_p/V_s$  break in it, which is interpreted as a shale plug. This interpretation is supported by the result of a horizontal well. Therefore, the  $V_p/V_s$  map indicates the spatial distribution of the reservoir sand, and in turn to provide us further development opportunities.

The impedance inversion from post-stack  $P$ -wave data shows that the oil-bearing sand body has a lower  $P$ -impedance value compared with the surrounding formation, mostly shales. In contrast, the inversion on post-stack  $PS$ -wave data indicates the sand has a slightly higher  $S$ -impedance. For this dataset, the  $V_p/V_s$  value derived from  $P$ - and

$S$ -impedance is generally lower, and the spatial definition of the channel sand is less clear and crisp than that of the  $V_p/V_s$  derived from  $PP$  and  $PS$  isochrons ratio. A detail look at the  $PS$  seismic data combined with the QC of  $PS$ -wave impedance inversion around the producing well points out that the imaging and continuity of  $PS$ -wave data at the reservoir level may need to be addressed in a further revisit of  $PS$ -wave data processing.

Attenuation is a rock property. The in-situ interval  $Q$  values could be calculated from the average  $Q$  values that are determined using spectral-ratio method from the zero-offset VSP experiment, by setting the surface sweep as the reference level. Meanwhile, an indicator, the ratio of first arrival time to the average  $Q$  factor –  $T/Q_{ave}$ , has been established for indicating the quality of  $Q$  estimation, which reveals where the standard spectra-ratio method could come up with stable  $Q$  values and where it couldn't.

In the Ross Lake example, a reliable, continuous interval  $Q_p$  curve has been determined from the downgoing wavefield of the zero-offset  $P$ -wave source VSP. Judged by the indicator  $T/Q_{ave}$ , the  $Q_s$  seems unstable from the  $S$ -wave source VSP data for most of the measured interval. Therefore a  $Q_s$  over large intervals is estimated instead of the high resolution continuous  $Q_s$ . Then, the average value of  $Q_p$ ,  $Q_s$ ,  $V_p/V_s$  and  $V_p$  are estimated for four major geological intervals in this region.

General in Ross Lake area, at depth above 600 m,  $Q_s$  is about half of  $Q_p$ , or 16~17 comparing with 30~38. Below 600 m,  $Q_s$  is about two thirds of  $Q_p$ , or 26~37 comparing with 40~54. The VSP-derived  $Q_p$  curve demonstrates a strong inverse linear relationship with the VSP-derived  $V_p/V_s$  curve, which may help us be able to predict attenuation from  $V_p/V_s$ .

In the Pikes Peak example, similarly,  $Q_p$  has been estimated from the zero-offset VSP using the same method. In general, for the formation at similar depth, its  $Q$  factor is relatively higher compared with the result from Ross Lake. The fact that no obvious correlation between  $Q_p$  and  $V_p/V_s$  in this example may be due to a number of reasons including possibly questionable  $V_s$  log, well bore configuration and near-field effect, etc.

The 4C-3D OBS seismic survey over PeMex's Cantarell/Sihil oilfield is interpreted. This dataset provides a very rich set of pictures over the complicated Cantarell structure. Using the available well logs and VSP data, we find that Castagna's limestone equation provides a reasonable  $V_p$ -to- $V_s$  map for this carbonate reservoir. The synthetic seismograms tie VSP data quite well and correlate with both  $PP$  and  $PS$  seismic data. These data help to develop a  $PS$ -to- $PP$  time mapping with  $V_p/V_s$  values ranging from 1.9 to 4.5. The shallow horizons are easier to pick, while the deeper structures are more interpretive. Interval  $V_p/V_s$  maps were calculated from these time horizons. It's suggested that there are gas effects visible in the  $P$ -wave sections. The  $PS$  data provide more continuous reflections in these areas (as noted elsewhere, especially in the North Sea). For the first time, the definition of the reservoir top for the giant Akal field is clear, based on  $PS$ -wave data. In addition, there may be fluid contacts visible in the Akal reservoir. Several new structures are interpreted on the  $PS$  data.  $V_p/V_s$  values could be interpreted as showing shaliness or less consolidation in some areas. The lithologic assessments could bear more study. A possible salt structure might be interpreted deeper in the sections.

Finally, a 3C-2D seismic survey in the U.S. is interpreted and analyzed. Detailed study of  $V_p$  and  $V_s$  log reveals that there are two distinct trends in this area: the  $V_p/V_s$  relationship for shallow formations follows the Mudrock line quite well but is different

for deep formations, which are deep-water sediments. The  $V_p/V_s$  values for those deep-water shales and siliceous shales are less than 2.0 and approach to 1.6 when getting deeper. The feature of low  $V_p/V_s$  associated with low velocity is different than that of the clastic sand-shale formations.

The *PS* seismic data exhibit more continuity at the shallow portion than *PP* seismic data, but worse at depth. At well location, *PP* and *PS* synthetic seismograms have been generated but both correlated poorly with surface seismic. A number of key horizons are interpreted on both *PP* and *PS* sections of the 2D seismic line 13S, and a  $V_p/V_s$  profile is achieved by *PP* and *PS* horizon matching. The horizon-derived  $V_p/V_s$  corresponds with log measured  $V_p/V_s$ .

In general, through the examples in this dissertation, in conjunction with abundant case studies from other people, we would say the converted-wave data could enhance the *P*-wave seismic data and provide additional information about the subsurface. To maximize the value of *PS*-wave data, it would be beneficial (1) to have high frequency, high signal-to-noise ratio data; (2) to have *PP*- and *PS*-wave seismic data been adequately processed; (3) to understand rock properties and in hence to understand the response of *PP*- and *PS* seismic; and (4) to carefully correlate synthetics and VSPs with *PP* and *PS* seismic data. The road to fully utilizing the elastic wavefield seismology for resource exploration and exploitation needs to continue.

## **7.2 Future work**

Whenever possible, reprocessing seismic data after the initial interpretation is almost always an option, as the reprocessing will be more guided and focused on the

target zones with information from interpretation. Also, an amplitude friendly prestack time migration on the both *PP*-wave and converted-wave data would be helpful to improve the imaging and preserve the amplitude which is critical for impedance inversion.

With the improved converted-wave data, a joint *PP* and *PS* inversion should be done.

Attenuation is an interesting topic. Estimating  $Q_s$  and applied an inverse  $Q$  filter to *PS* seismic would be more necessary than for *PP*-wave seismic.

For the Cantarell/Sihil dataset, adding fault interpretation would be helpful.

As industry's interest on shale reservoir has been growing dramatically in recent years, more work about elastic properties of the siliceous shale, or in particular, the reservoir rocks in shales need to be addressed. Furthermore, to investigate the relationship of  $V_p/V_s$  with shale content, porosity and different phase of porcelanite would be of particular interest with more well data. Also, how to extract the rock properties from multicomponent seismic to help identify reservoirs or sweet spots in shale reservoirs should certainly draw attention in the future. The study of the 2D-3C data in Chapter 6 is just a start.

## References

- Aki, K. and Richards, P. G., 1980, Quantitative seismology: Theory and methods: E. H. Freeman and Sons.
- Aquino, J. A. L., Ruiz, J. M. Flores, M. A. and Garcia, J. H., 2003, The Sihil field: Another giant below Cantarell, offshore Campeche, Mexico, *in* M. T. Halbouty, ed., Giant oil and gas fields of the decade 1990–1999: AAPG Memoir **78**, p. 141–150.
- Bale, R. A. and Stewart, R. R., 2002, The impact of attenuation on the resolution of multicomponent seismic data: CREWES Research Report, vol. **14**, ch. 18, 1-21.
- Batzle, M. L., Han, D. and Castagna, J. P., 1996, Attenuation and velocity dispersion at seismic frequency: Soc. Expl. Geoph., Expanded Abstract, 1687-1690.
- Berg, E., Svenning, B. and Martin, J., 1994, SUMIC: Multicomponent sea-bottom seismic surveying in the North Sea-Data interpretation and applications: SEG Expanded Abstracts, IM1.6.
- Biot, M. A., 1956, Theory of propagation of elastic waves in a fluid saturated porous solid, II, Higher frequency range: J. Acoust. Soc. Am., **28**, 179-191.
- Cary, P., 2001, Multicomponent seismic exploration in Canada – one person’s perspective: CSEG Recorder, Vol. **26**, No. 7, 62-67.
- Castagna, J. P., Batzle, M. L. and Eastwood, R. L., 1985, Relationship between compressional-wave and shear-wave velocities in clastic delicate rocks: Geophysics, **50**, 571-581.
- Castagna, J. P., Batzle, M. L. and Kan, T. K., 1993, Rock physics – the link between rock properties and AVO response:

- Chernikoff, A.O., Garcia, J.H, Schatzinger R.A., 2006, Mesozoic extensional tectonics: its impact on oil accumulations in Campeche Sound, Gulf of Mexico: The Leading Edge, **25**, 1224-1234.
- Christopher, J. E., 1974, The Upper Jurassic Vanguard and Lower Cretaceous Mannville Groups of Southwestern Saskatchewan, Report No. 151, Department of Mineral Resources, Saskatchewan Geological Survey, Sedimentary Geology Division.
- Dvorkin, J. and Nur, A., 1993, Dynamic poroelasticity: a unified model with the squirt and the Biot mechanisms: Geophysics, **58**, 524-533.
- Downton, J. E. and Lines, L. R., 2001, Preliminary results of the AVO analysis at Pikes Peak: CREWES Research Report, vol. **13**.
- Gaiser, J. E., 1996, Multicomponent Vp/Vs correlation analysis: Geophysics, **61**, 1137-1149.
- Gaiser, J. E., Moldoveanu, N., Macbeth, C., Michelena, R. and Spitz, S., 2001, Multicomponent technology: The players, problems, applications, and trends: The Leading Edge, **20**, No. 9, 974-977.
- Gaiser, J. E. and Probert, T., 2006, Significant developments in multicomponent seismic exploration in the last five years: Recent developments in converted PS-wave analysis processing of S-wave splitting and prestack migration: CSEG Recorder, **31**, 60-64.
- Gardner, G. H. F., Gardner, L. W., and Gregory, A. R., 1974, Formation velocity and density – the diagnostic basis for stratigraphic traps: Geophysics, **39**, 770-780.
- Garcia, J. H., Gonzalez, M. C., Zavaleta, J. R., Chernikoff, A.O., and Ploszkiewicz, V., 2005, Structural style of the Gulf of Mexico's Cantarell complex: The Leading Edge, **24**, 136-138.

- Gregory, A. R., 1977, Aspects of rock physics from laboratory and log data that are important to seismic interpretation, *in* Seismic Stratigraphy – Application to hydrocarbon exploration: Memoir **26**, Am. Assn. Petr. Geol.
- Haase, A. B. and Stewart, R. R., 2006, Intrinsic and apparent seismic attenuation in VSP data: CSPG/CSEG/CWLS Ann. Natl. Mtg., Calgary, Abstract, 267.
- Haase, A.B., and Stewart, R.R., 2010, Near-field seismic effects in a homogeneous medium and their removal in vertical seismic profile attenuation estimates: Geophysical Prospecting, Vol. **58**, No. 6, 1023-1032.
- Hargreaves, N. D. and Calvert, A. J., 1991, Inverse Q filtering by Fourier transform: Geophysics, **56**, 519-527.
- Hernandez, J. G., Castillo, M. G., Ruiz, J. Z., Chernikoff, A. O. and Ploszkiewicz, V., 2005, Structural style of the Gulf of Mexico's Cantarell complex: The Leading Edge, **24**, 136-138.
- Hons, M. S. and Stewart, R. R., 2009, Geophone and MEMS Accelerometer Comparison at Spring Coulee, Alberta: Presented at the CSPG/CSEG/CWLS Ann. Mtg., Calgary.
- Hulten, V., 1984, Petroleum geology of Pikes Peak heavy oil field, Waseca formation, Saskatchewan: Canadian Society of Petroleum Geologist, 9, 441-454.
- Johnston, D. H. and Toksöz, M. N., 1981, Definitions and terminology, *in* Toksöz, M. N. and Johnston, D., H., eds., Seismic wave attenuation: Soc. Expl. Geophys., 1-5.
- Klimentos, T., 1995, Attenuation of P- and S-waves as a method of distinguishing gas and condensate from oil and water: Geophysics, **60**, 447-458.
- Kjartansson, E., 1979, Constant Q wave propagation and attenuation: J. Geophys. Res., **84**, 4737-4748.
- Lawton, D. C., and Howell, C. T., 1992, P-SV and P-P synthetic stacks: 62nd Ann. Internat. Mtg., Soc. Expl. Geophys., Expanded Abstracts, 1344-1347.

- Li, S, Henderson, C. M. and Stewart, R. R., 2004, Well log study and stratigraphic correlation of the Cantuar Formation, southwestern Saskatchewan: CREWES Research Report, vol. **16**, 1-18.
- Lynn, H. and Spitz, S., 2006, Pau 2005: The Leading Edge, **25**, 950–953.
- MacLeod, M. K., R.A.Hanson, Bell, C. R. and McHugo, S., 1999, The Alba Field ocean bottom cable seismic survey: Impact on development: The Leading Edge, **18**, no. 11, 1306-1312.
- Magoon, L. B., Hudson, T. L., and Cook, H. E., 2001, Pimienta–Tamabra -- A giant supercharged petroleum system in the southern Gulf of Mexico, onshore and offshore Mexico, in C. Bartolini, R. T. Buffler, and A. Cantu-Chapa, eds., The western Gulf of Mexico basin—Tectonic, sedimentary basins, and petroleum systems: AAPG Memoir, vol. **75**, p. 83 - 125.
- Nahm, J. W. and Duhon, M. P., 2003, Interpretation and practical application of 4C-3D seismic data, East Cameron gas fields, Gulf of Mexico: The Leading Edge, **22**, 300–309.
- Margrave, G. F., Lawton, D. C., and Stewart, R. R., 1998, Interpreting channel sands with 3C-3D seismic data: The Leading Edge, **17**, 509–513.
- Mitra, S., Figueroa, G. C., Garcia, J. H., and Alvarado, A. M., 2005, Three-dimensional structural model of the Cantarell and Sihil structures, Campeche Bay, Mexico: AAPG Bulletin, v. **89**, no. 1, pp. 1–26.
- Nahm, J. W. and Duhon, M. P., 2003, Interpretation and practical applications of 4C-3D seismic data, East Cameron gas fields, Gulf of Mexico: The Leading Edge, 300-309, 4.
- Newrick, R. T., Lawton, D. C. and Spratt, D. A., 2001, Seismic velocity anisotropy analysis at Pikes Peak, Saskatchewan, Canada: SEG San Antonio, 2001 Expanded Abstracts.

- Pickett, G. R., 1963, Acoustic character logs and their applications in formation evaluation: *J. Petr. Tech.*, **15**, 650-667.
- Russell, B. and Hampson, D., 1991, Comparison of poststack seismic inversion methods: Presented at the Ann. Intl. Mtg., Soc. Explor. Geophys., Expd. Abst., 876-878.
- Rutledal, H., Ertresvag, E. T. and Berg, O. E., 2000, Interpretation and analysis of the 1997 3D multicomponent seismic survey covering a part of the Oseberg field in the North Sea: 70th Ann. Internat. Mtg., Soc. Expl. Geophys., Expanded Abstracts, 570–573.
- Santiago, J., and A. Baro, 1992, Mexico's giant fields, 1978–1988 decade, in M. T. Halbouty, ed., *Giant oil and gas fields of the decade 1978– 1988: AAPG Memoir* **54**, p. 73– 99.
- Soubotcheva, N., 2006, Reservoir property prediction from well logs, VSP and multicomponent seismic data: Pikes Peak heavy oilfield, Saskatchewan: M.Sc. Thesis, University of Calgary, Department of Geology and Geophysics.
- Stainsby, S. D. and Worthington, M. H., 1985,  $Q$  estimation from vertical seismic profile data and anomalous variations in the central North Sea: *Geophysics*, **50**, 615-626.
- Stewart, R. R., Huddleston, P. D. and Kan, T. K., 1984, Seismic versus sonic velocities: A vertical seismic profiling study: *Geophysics*, **49**, 1153-1168.
- Stewart, R. R. and Bland, H. 1997, An approximate relationship between  $R^{ps}$  and  $R^{ss}$ : CREWES Research Report, vol. **9**, ch. 12, 1-4.
- Stewart, R. R., Gaiser, J. E., Brown, R. J. and Lawton, D. C., 2002, Converted-wave seismic exploration: *Methods: Geophysics*, **67**, 1348–1363.
- Stewart, R. R., Gaiser, J. E., Brown, R. J. and Lawton, D. C., 2003, Converted-wave seismic exploration: *Applications: Geophysics*, **68**, 40–57.

- Stewart, R. R., 2009, The measure of full motion: Multicomponent seismic exploration and its value: 79th Annual International Meeting, SEG, Expanded Abstracts, 4243–4248.
- Tatham, R. T., 1982, Vp/Vs and lithology: *Geophysics*, **47**, 336–344.
- Tonn, R., 1991, The determination of seismic quality factor Q from VSP data: A comparison of different computational methods: *Geophys. Prosp.*, **39**, 1-27.
- Vanbeselaere, N. A., 1995, Regional Cross-sections of the Mannville Group - Southwest Saskatchewan, phase I: Geological Survey of Canada, Ottawa.
- Vazquez, M. G., Garcia, G. M., Maya, F., Ruiz, C. F. T., Berg, E. W., Vuillermoz, C., and Fyhn, A., 2005, Improved Sihil image from 4C full azimuth node data: Presented at the Ann. Intl. Mtg., Soc. Explor. Geophys., Expd. Abst., 983-986.
- Wang, Y., 2002, A stable and efficient approach of inverse Q filtering, *Geophysics*, **47**, 657–663.
- Wang, Y., 2003, Quantifying the effectiveness of stabilized inverse Q filtering: *Geophysics*, **68**, 337-345.
- Watson, I., 2004, Integrated geological and geophysical reservoir analysis: M.Sc. Thesis, University of Calgary, Department of Geology and Geophysics.
- White, R. E., 1992, The accuracy of estimating Q from seismic data: *Geophysics*, **57**, 1508-1511.
- Wong, F. Y. F., Anderson, D. B., O'Rourke, J. C., Rea, H. Q. and Scheidt, K. A., 2001, Meeting the challenge to extend success at the Pikes Peak steam project to areas with bottom water: 2001 SPE Annual Technical Conference and Exhibition, New Orleans, 30 September - 3 October.
- Xu, C., Stewart, R. R. and Osborne, C. A., 2001, Walkaway VSP Processing and Q estimation: Pikes Peak, Saskatchewan: CSEG Ann. Natl. Mtg., 2001 Expanded Abstracts.

- Xu, C. and Stewart R.R., 2004, Using 3D Multi-component Seismic Data, Logs and VSP to Interpret a Sand-Shale Oil Reservoir: 66th EAGE Mtg., Expanded Abstracts.
- Xu, C. and Stewart, R. R., 2004, Identifying channel sand versus shale using 3C-3D seismic data, VSPs and horizontal well logs: 74th Ann. Internat. Mtg., Soc. Expl. Geophys., Expanded Abstracts, **23**, 374-377.
- Xu, C. and Stewart, R. R., 2005, Delineating a sand reservoir using inversion of 3C-3D seismic data: 75th Ann. Internat. Mtg., Soc. Expl. Geophys., Expanded Abstracts, **24**, 995-998.
- Xu, C. and Stewart, R. R., 2006, Seismic attenuation (Q) estimation from VSP data and  $Q_p$  versus  $V_p/V_s$ : 76th Ann. Internat. Mtg., Soc. Expl. Geophys., Expanded Abstracts, **25**, 1938-1942.
- Xu, C. and Stewart R.R., 2006, Delineating a sand channel using 3C-3D seismic data: Ross lake heavy oilfield, Saskatchewan: Recorder, Vol **31**, 2006 Special Edition, pg. 86 – 89.
- Xu, C. and Stewart R.R., 2006, Seismic attenuation (Q) estimation from VSP data: Recorder, Vol. **31**, no. **7**, pg. 57 – 61.
- Zou, Y., Bentley, L. R. and Lines, L. R., 2002, Time-lapse seismic modelling of the Pikes Peak field: CREWES Research Report, **14**.

## **Appendix A: Seismic tomography of Carbonate robbles**

### **A.1 Abstract**

A multicomponent seismic survey was conducted on a Mayan pyramid ruin at Chan Chich, Belize, central America in June, 2000. The purpose of this survey was to test whether a hammer seismic technique could propagate energy through the carbonate-rubble and mortar pyramid (40 m x 40 m at the base) and if this energy could be used to make images of the interior of the structure. To this end, ten 3-component geophones were planted, with 2 m spacing, on one side of the pyramid. Source points were acquired around the corner on an adjacent side of the pyramid at a 4 m spacing – giving a geometry like that of a VSP on its side. The sledge-hammer source was struck about 20 times per shot point. We analyze the VSP-type dataset here by picking first-break arrivals from 60 seismic traces and performing a traveltime inversion to estimate the velocities inside the pyramid. Finally, a velocity contour map is given with resolution and reliability analysis. We find that the near-surface of the pyramid has velocities about 100~200 m/s while the interior has higher velocities (500 m/s to 700 m/s). There is evidence of a low velocity region amongst the higher velocity areas.

In March 2001, a phase II seismic survey was acquired on the same Chan Chich pyramid ruin. As part of the seismic study, a tomography-purpose 3-component geophone line was laid along same elevation contour as year 2000's survey. There are 27 hammer-sledge sources, as well as 20 geophones, both with 2.5 m spacing. The sledge-hammer source was tapped about three times per shot point this time. The three-component datasets and amplitude spectrum were analysed, and the first-break arrivals were picked from the vertical component seismic traces. Then, the same

traveltime inversion was performed to estimate the velocities inside this pyramid. Compared with year 2000 result, the inversion result shows similar velocity structure but greater coverage, which is that the near-surface of the pyramid has velocities about 100~200 m/s while the interior has higher velocities (500 m/s to 700 m/s).

There was also undertaken another tomography survey on further pyramid: Ma'ax Na, which is smaller than Chan Chich. The inversion result shows there is a high velocity core surrounded by low-velocity materials, and the north and south outer parts close to the trenches demonstrated lower velocity.

## **A.2 Introduction**

In June 2000, a multicomponent seismic survey on a Maya pyramid ruin was acquired at the Chan Chich archaeological site in Belize, Central America. This carbonate rubble and mortar pyramid has rounded corners and a soft-soil surface covered by tropical jungle. The pyramid has an about 40 m by 40 m base and stands some 18 m high. A unique seismic dataset was acquired: five hammer-seismic sources are located on one side of the pyramid, juxtaposed with ten 3-component geophones planted on the adjacent, perpendicular side. The 3-C receivers are planted at a 2 m horizontal spacing along the contour line of 2 m above the base of the pyramid. The shots are on the adjacent perpendicular side of the pyramid with a nominal 4 m spacing. An exception is that the shot #6 is in between receiver #1 and #2. This survey geometry is thus like a VSP on the side of the pyramid (Figure A.1). We use these data, via a straight-line generalized traveltime inversion, to estimate the velocity structure inside the pyramid.

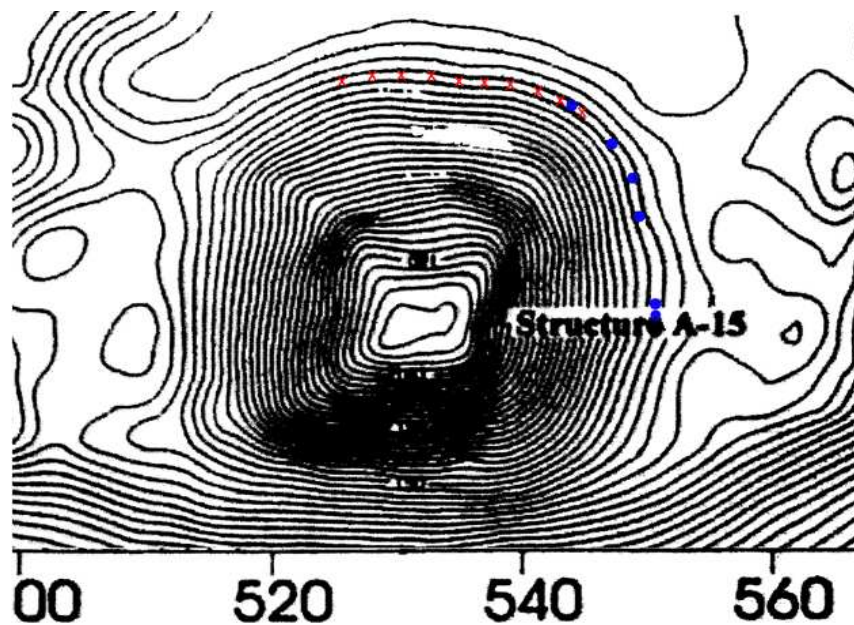


**Figure A.1** Topographic contour map of the pyramid. The pyramid is about 40 m by 40 m at its base. Annotations are in metres. The blue dots indicate shots and the red “x”s denote geophone locations.

Encouraged by the result of year 2000, a revisit was made to the same Chan Chich pyramid in March 2001. This time, a geophone line containing 20 three-component geophones with 2.5 m spacing is laid along the same contour line. The sledge-hammer source is a stack of three strikes per shot point. There are 27 shots located at the same elevation of the receiver line, with the spacing of 2.5 m. The geometry is shown in Figure A.2. Therefore, there are  $27 \times 20 = 540$  traces in total. We use these data, via the same travelt ime inversion method, to estimate the velocity structure inside the pyramid.

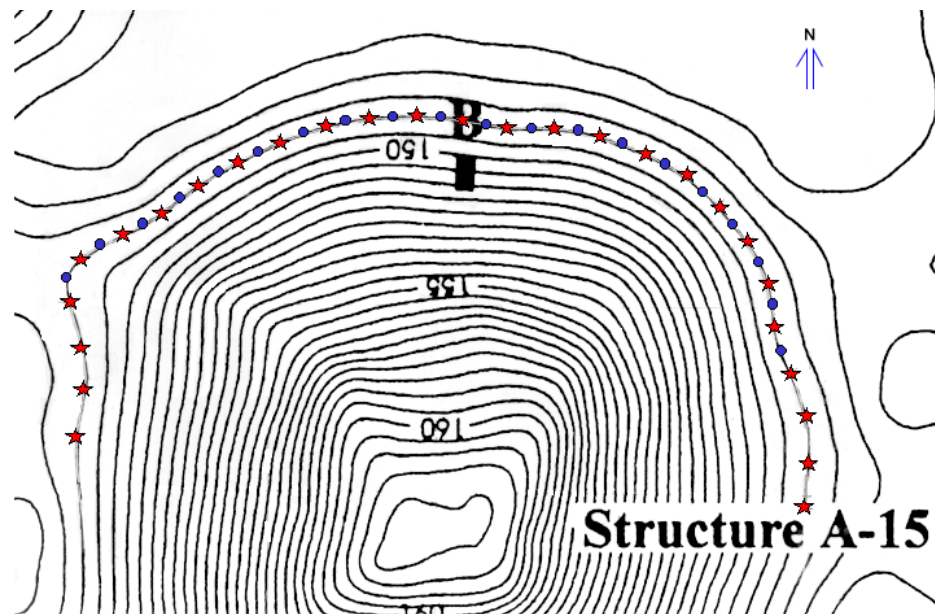


**Figure A.2 Topographic contour (in meters) map of the Chan Chich pyramid. The blue dots indicate receiver locations and the red stars denote shot locations.**

### **A.3 Data analysis**

#### ***A.3.1 Chan Chich 2000 data***

By viewing the raw three-component seismic data, we find that the vertical component data show generally good quality and contain consistent first breaks. Some reflections are visible, especially above 150 ms, with different apparent slopes (Figure A.3). Channel #5 is dead and channel #1 is noisy. Unfortunately, the H1 component data have six dead channels out of 10 geophones. The H2 component data have only one dead channel (#2), but it seems not as high quality as the vertical component. Figure A.3 shows the data with a 150 ms window AGC.

	Vertical	H1	H2
Dead trace #	5	1, 4, 5, 8, 9, 10	2
Bad trace #	1	None	None

**Table A.1 Trace editing of the vertical and two horizontal channels.**

The first positive peak on the vertical component trace is picked as the first arrival and also displayed on the H1 and H2 traces (Figure A.3). Due to no or unreliable data, interpolation is applied to pick the first break on channels #5 and #1.

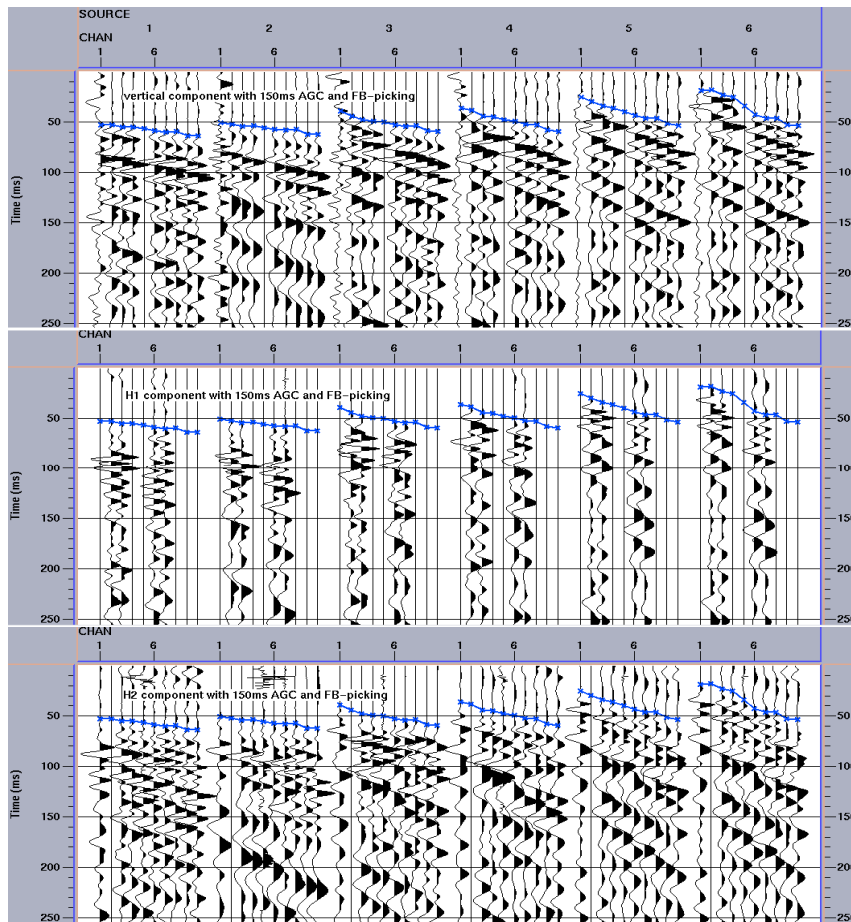


**Figure A.3 Display of Vertical (V), horizontal-X (H1) and horizontal-Y (H2) components shot gather with the first-break picks.**

The hammer-seismic source produces a fairly broadband signal from about 5 Hz to 155 Hz. Figure A.4 shows the amplitude spectrum of shot #1. Five other shots show similar spectra.

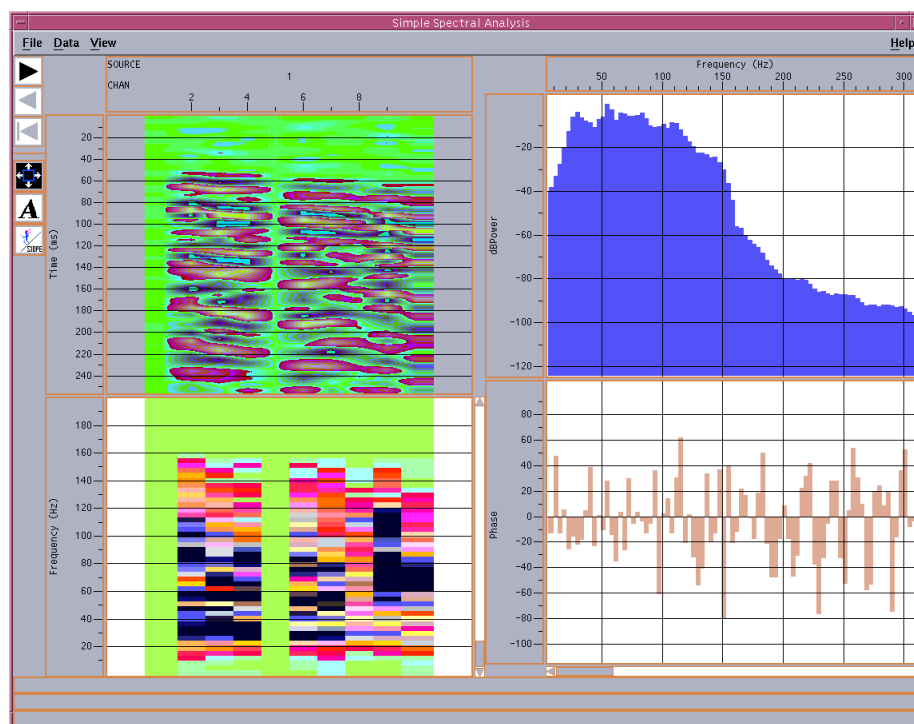


**Figure A.4 Display of amplitude spectrum for shot #1 of Chan Chich 2000 data.**

### *A.3.2 Chan Chich 2001 data*

In general, year 2001 data has relative higher quality and less dead traces than year 2000 data. Checking the raw three-component seismic data, we find that again the vertical component shows better quality, clear events and consistent first breaks. Figure A.5 shows the three component data with a 200 ms window AGC. We picked first breaks on vertical component data, showing as red lines, and also displayed on H1 and H2 data, showing as green lines. It is observed that always the vertical component detects the earliest wave, even if the shot is in between two geophones.

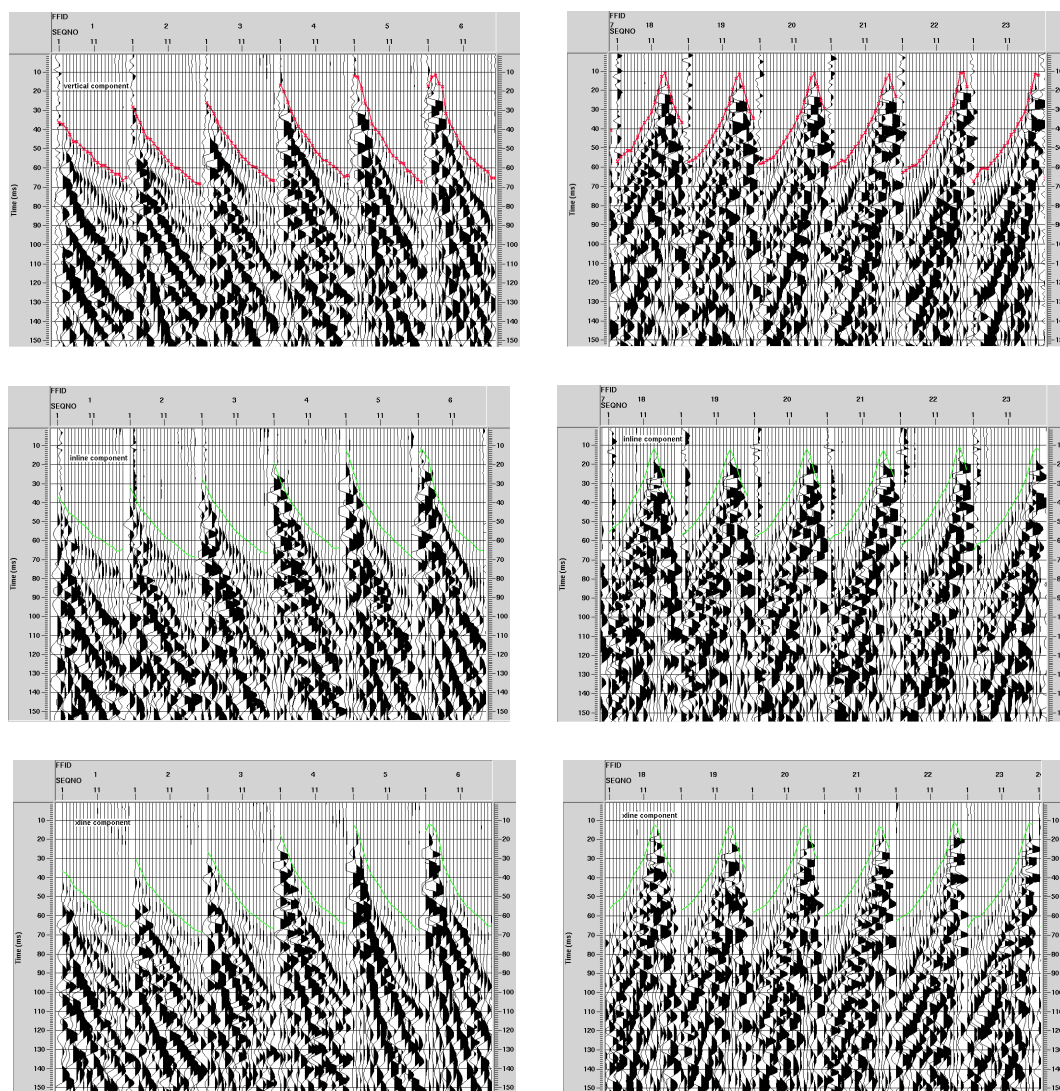


**Figure A.5 Display of vertical (V, top row), horizontal-inline (H1, middle row) and horizontal-crossline (H2, bottom row) shot gathers with 200ms AGC.**

This time, the three-fold hammer seismic source also creates a fairly broadband signal up to about 160 Hz. As an example, Figure A.6 displays the amplitude spectrum of shot #19. The other shots show similar spectra.

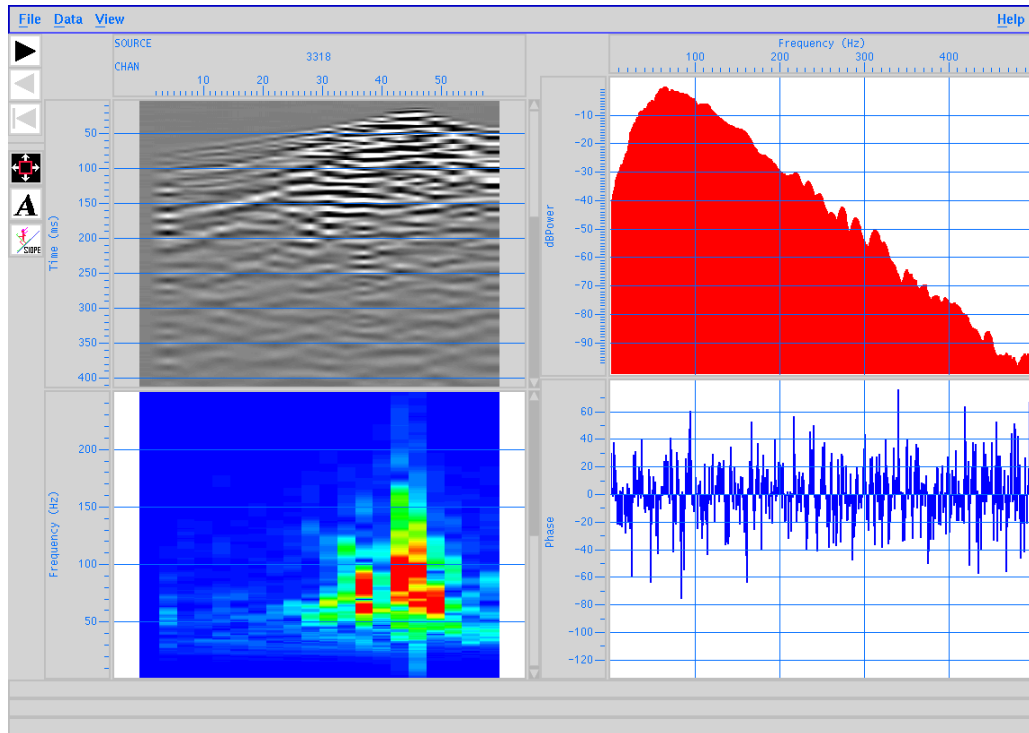


**Figure A.6** Display of amplitude spectrum for shot #19 of Chan Chich 2001 data.

#### **A.4 Travelttime inversion**

We assume straight-line ray-paths and thus cast the tomographic travelttime inversion as a system of linear equations:

$$t_i = \sum_j D_{ij} \cdot s_j , \quad (\text{A.1})$$

where  $t_i$  is total travelttime of  $i^{\text{th}}$  shot-receiver pair,  $s_j$  is slowness of  $j^{\text{th}}$  grid, and  $D_{ij}$  is the distance of  $i^{\text{th}}$  ray traveling in  $j^{\text{th}}$  grid. Each shot-receiver pair builds one equation.

Expressed in matrix form, it is:

$$\mathbf{t} = \mathbf{D} \cdot \mathbf{s} \quad (\text{A.2})$$

#### A.4.1 Year 2000 data

First, we need to determine how many bins or pixels there should be. To keep the problem over-determined, the number should not exceed 60. If we set  $dx = dz = 4$  m, there will be 7 rows and 6 columns, or a total of 42 pixels – about half of which will be intersected. So, we use 4 m by 4 m pixels. With the same bin size, different origin positions result in different inversion systems. Figure A.7 shows one type of grid, which x-axis ranges from -3 m to 21 m, and y-axis ranges 0 m to 27 m. The matrix D has a somewhat different distribution if we shift the x coordinator, i.e. by 1 m to right direction.

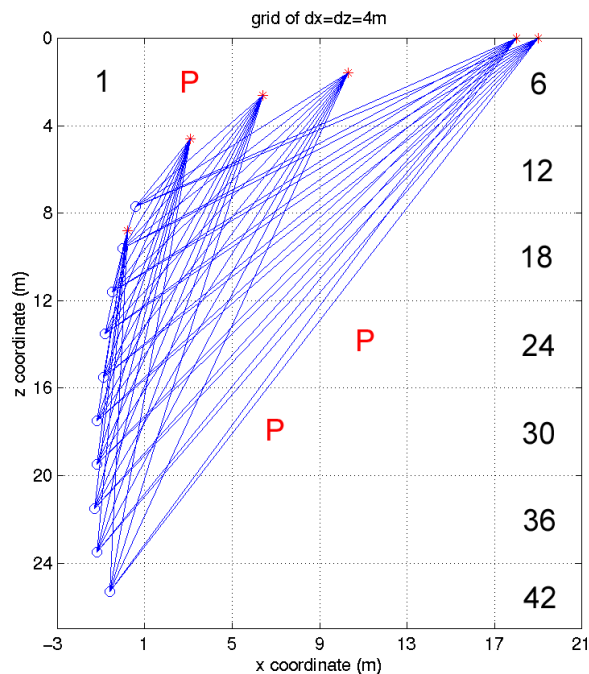


**Figure A.7 Grid with x range (-3 ~ 21 m) and bin size  $dx=dz=4$ m. Red (\*) symbols represent shot points as well as blue (o) symbols denote receiver points. The number in bins indicates the sequential number of these bins.**

To solve the model parameter  $s_{inv}$  (slowness vector), two methods are used: singular value decomposition (SVD) and conjugate-gradient (CG). In SVD, the stabilization factor is  $1.0e-6$  in the following computation.

The inversion results from these two methods are shown in table A.2. There are several negative slowness values that are unphysical. Looking closely, most of the velocity values from the two methods are close. A comparison between the picked first arrivals from data and from inversion (SVD method) is made (Figure A.8). The final velocity contour map is shown in Figure A.9.

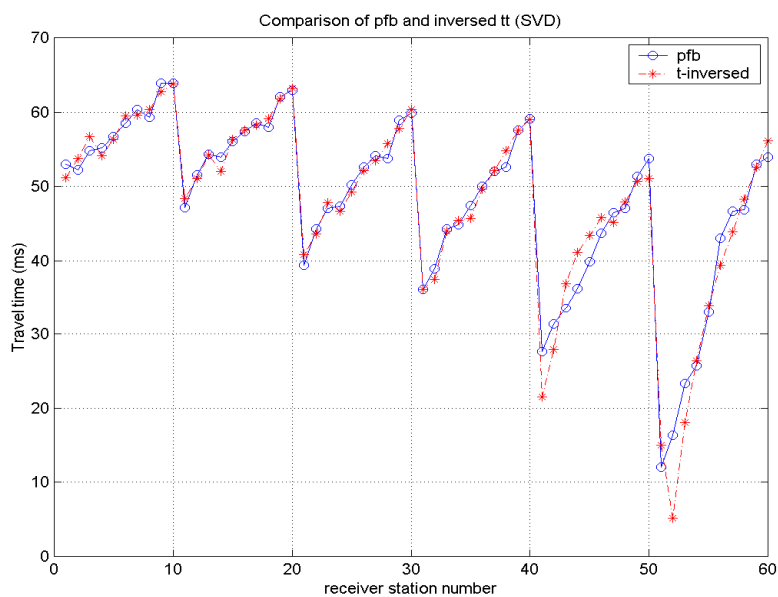


**Figure A.8 Comparison of the observed first-break times and calculated times from inversion-estimated slowness model.**

Result of Conjugate-gradient method:

flag = 1  
relres = 5.9710e-05  
iter = 20

s_tomo =						v_tomo = 1.00E+03 *					
0	1.8654	2.8750	-0.9216	1.1590	1.4969	0	0.5361	0.3478	0	0.8628	0.668
13.197	4.1034	5.0379	2.6536	2.1589	0	0.0758	0.2437	0.1985	0.3768	0.4632	0
6.1904	1.2759	2.2507	2.4109	0	0	0.1615	0.7838	0.4443	0.4148	0	0
3.8548	2.6031	2.2932	0.9422	0	0	0.2594	0.3842	0.4361	1.0613	0	0
2.3702	1.5228	0.9502	0	0	0	0.4219	0.6567	1.0524	0	0	0
2.2005	2.8322	0	0	0	0	0.4544	0.3531	0	0	0	0
1.9927	0	0	0	0	0	0.5018	0	0	0	0	0

Result of SVD:

s_tomo =						v_tomo =					
0	14.636	2.8557	-0.6943	1.2660	1.4996	0	68.3266	350.1739	0	789.9092	666.8497
12.835	3.9986	4.8449	2.5044	1.7397	0	77.9147	250.0899	206.4042	399.3031	574.8036	0
6.2566	1.4062	2.2625	3.5164	0	0	159.8300	711.1178	441.9879	284.3788	0	0
3.8406	2.6596	1.6463	2.9190	0	0	260.3742	375.9926	607.4177	342.5782	0	0
2.3330	1.4889	-1.1786	0	0	0	428.6312	671.6187	0	0	0	0
2.1841	3.4308	0	0	0	0	457.8452	291.4811	0	0	0	0
2.0046	0	0	0	0	0	498.8464	0	0	0	0	0

**Table A.2 Inversion result from CG (top) and SVD (bottom).**

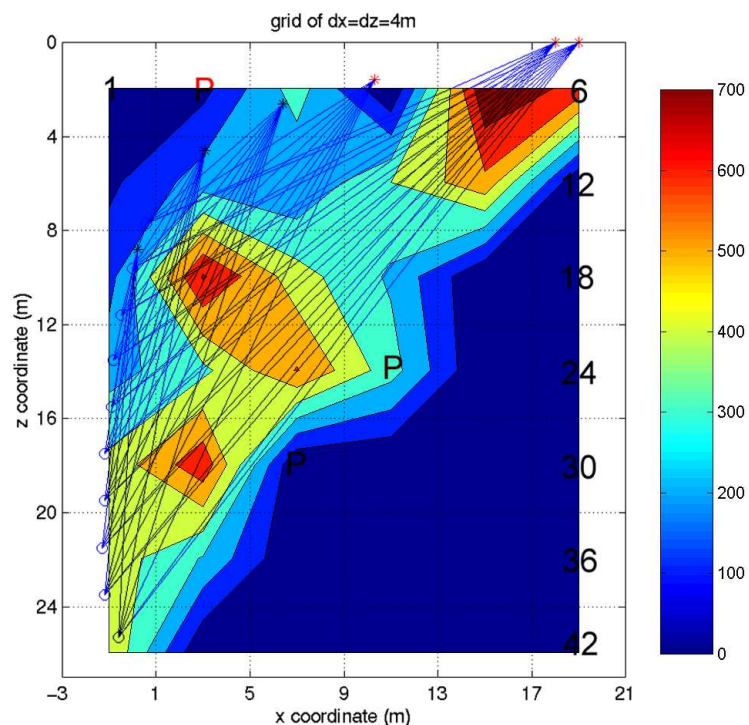


**Figure A.9 Displays of the final velocity (m/s) maps calculated by the SVD method.**

#### *A 4.2 Year 2001 data*

From year 2000 result, we could reasonably assume the average velocity along this elevation slice is about 500 m/s. For 150 Hz signal, the wavelength is about 3~4 meters. Considering the size of this pyramid is 40 m by 40 m, we can use straight-line to describe the ray-path for first arrivals, without losing the validation.

We omit the last four shots and use 23 shots to do inversion. Therefore, there are  $23 \times 20 = 460$  equations. Using same method, we inverted the newly recorded data.

Based on the year 2000 survey's velocity estimation and signal frequency, grid size of 4 m is a reasonable start. The geometry is demonstrated in Figure A.10, we call the north-south direction as x direction, from 0 m to 24 m, and east-west direction as z, from 0 m to 40 m. There are 10 rows (x) and 6 columns (z), with total of 60 grids.

Given the coordinates of the shots and receivers, the matrix of distance D is calculated. In this case,  $dx = dz = 4$ , the size of D is  $460 \times 60$ . The matrix D is defined as soon as the grid is defined.

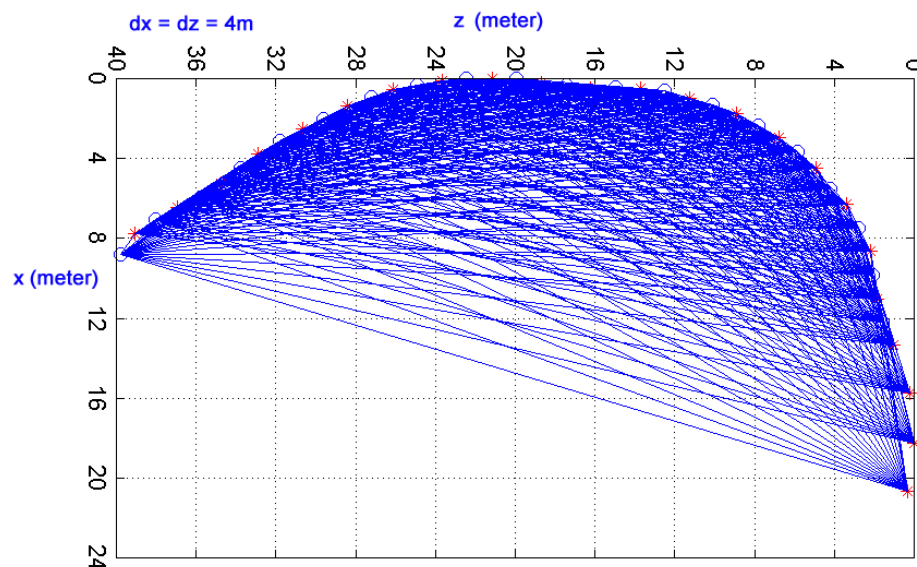


**Figure A.10** Grid with x range (0~24) m and bin size  $dx=dz=4m$ . Red (\*) symbols represent shot points as well as blue (o) symbols denote receiver points.

Method of singular value decomposition (SVD) is used here to solve the model parameter  $s_{inv}$  (slowness vector), then convert into velocity in m/s. Figure A.11 shows picked first breaks (blue circle), calculated travel time from inverted slowness (red stars) and the difference between them  $\Delta t = t_{inv} - t_{FB}$  (green line). We see that, for the most part, the green line varies around the zero line within  $\pm 5$  ms.

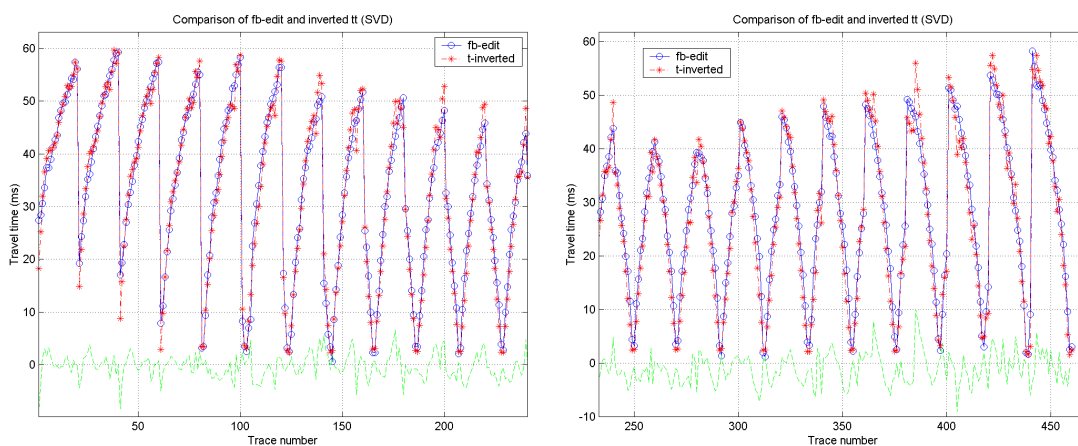
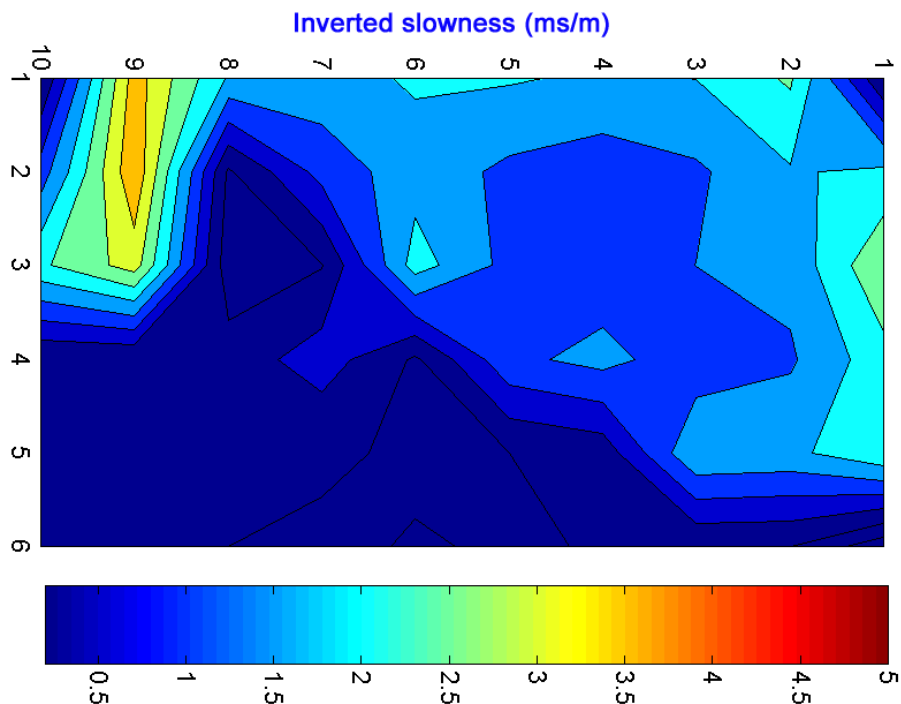


**Figure A.11** Comparison of the observed first-break times and calculated times from inversion-estimated slowness model.

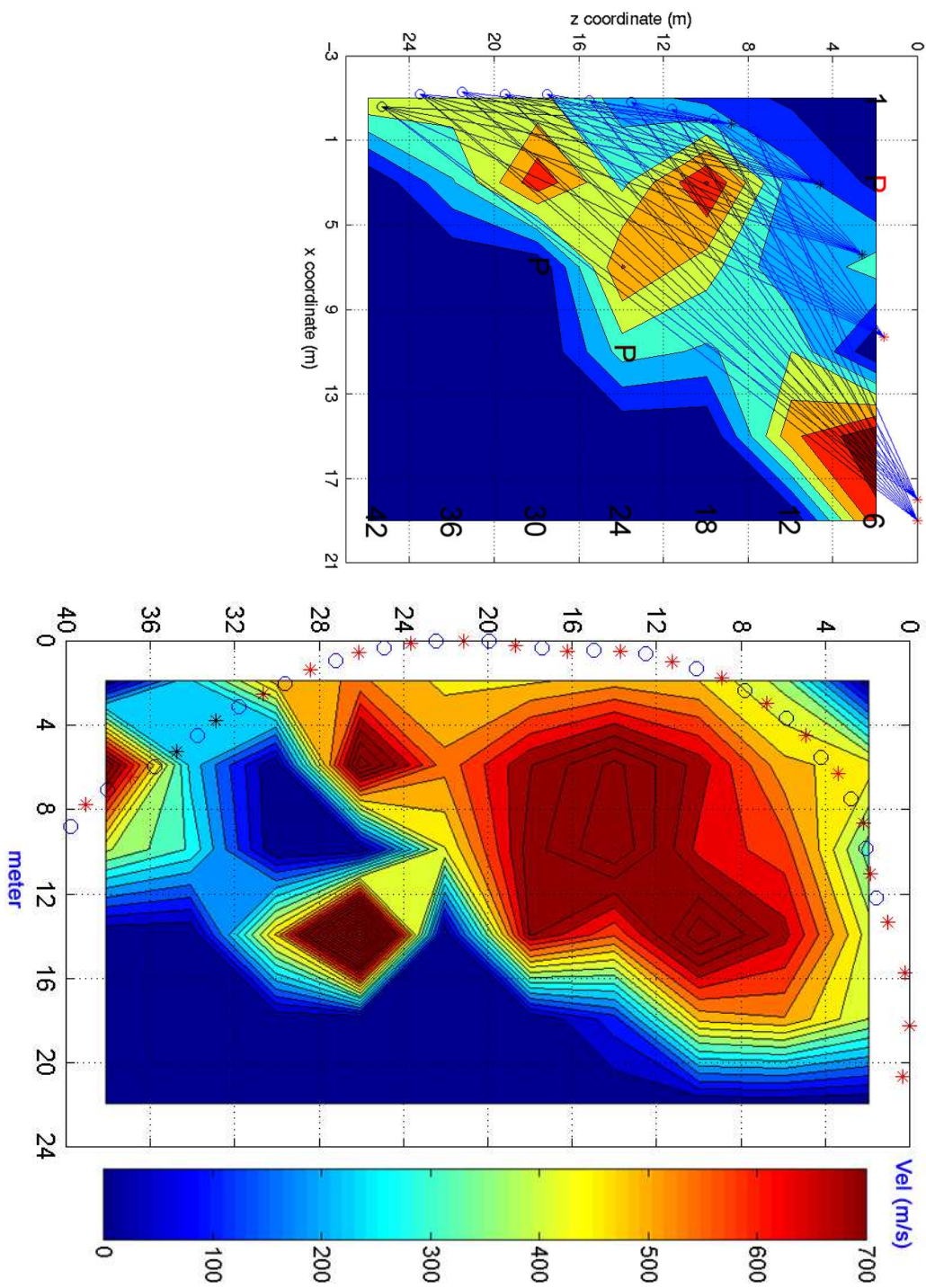
s_tomoC23 = (ms/m)						
0	2.1064	2.9508	2.3190	2.4605	-0.8456	
2.5808	1.9542	1.6406	1.4343	1.8541	0.0000	
2.0095	1.4184	1.5038	1.1712	1.9679	0.0000	
1.9218	1.2055	1.1617	1.6750	8.7979	0.0000	
2.0492	1.3861	1.3364	1.3680	-0.0000	-0.0000	
2.0609	1.7878	2.2233	-0.0749	-0.0000	0.0000	
1.8125	1.1769	-0.0254	0.7614	0.0000	-0.0000	
1.9353	-0.0693	-0.2868	2.0000	0	0	
3.7272	3.9162	3.2257	0	0	0	
0	1.2203	2.4104	0	0	0	
v_tomoC23 = (m/s)						
0	474.75	338.89	431.22	406.42	0	
387.48	511.72	609.55	697.20	539.34	0	
497.65	705.04	664.97	853.85	508.15	0	
520.34	829.53	860.82	597.02	113.70	0	
488.00	721.45	748.27	731.00	0	0	
485.22	559.35	449.78	0	0	0	
551.72	849.68	0	1313.4	0	0	
516.72	0	0	500.00	0	0	
268.30	255.35	310.01	0	0	0	
0	819.50	414.86	0	0	0	

**Table A.3 Inversion result of year 2001 data using SVD method.**

The inversion result shows there are several negative unphysical slowness values. For display purpose, the velocity values of those negative slowness grids are set to 0. The final contour map are shown in Figure A.12 and A.13.



**Figure A.12 Inverted slowness of year 2001 data, unit is ms/m.**



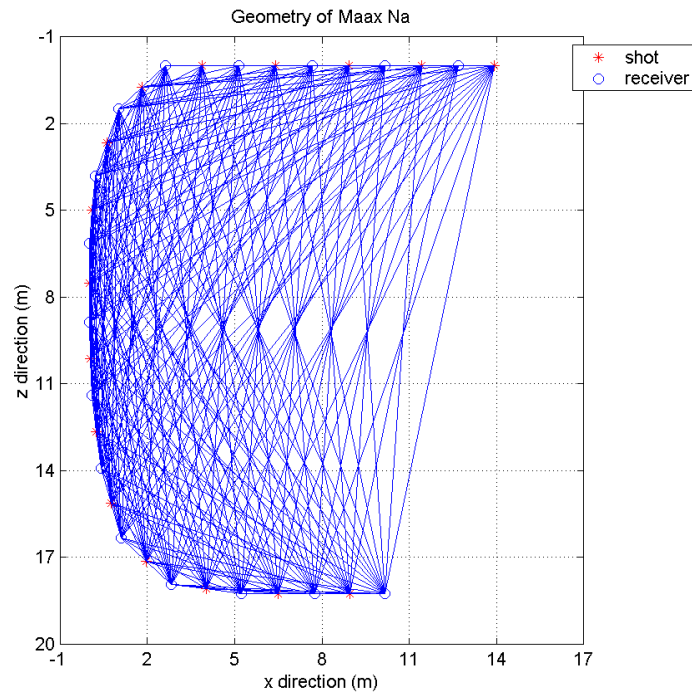
**Figure A.13 Comparison of the final velocity (m/s) maps calculated by the SVD method between year 2000 (upper) and year 2001 (lower).**

Figure A.13 shows the comparison of the estimated velocity structure between year 2000 and year 2001 data. Year 2001's result demonstrates bigger coverage and similar velocity profile.

#### ***A.4.3 2001 Ma'ax Na data***

In year 2001 survey, a tomography purpose seismic line also was laid on the second pyramid called Ma'ax Na with the size about 28 m by 28 m at base and 15 m high, which is smaller than Chan Chich pyramid. This three-component line has the same configuration as on Chan Chich: 20 geophones with 2.5 m spacing, hammer-sledge shots in the middle of the adjacent two receivers at 2.5 m shot spacing. By observing the data, the last four geophones show inconsistent first arrivals, possibly due to the coupling condition. So, we use first 16 geophone and first 16 shots to perform the inversion.

Following the same procedure as before, first breaks are picked from the vertical component data. The geometry is shown in Figure A.14, with bin size of 3 m.



**Figure A.14 Geometry of Ma'ax Na survey.**

The constraints for inversion are: (1) if the fold in a bin is less than 5, the slowness of this bin will be set to 0; (2) For the bin whose fold is greater than 5, if the inverted slowness less than 1 ms/m, set it to 1 ms/m, which means the highest velocity will be set to 1000 m/s.

The inversion results are shown in Figure A.15 and A.16. Although the time difference between picked first arrival and the calculation from inverted velocity is relatively bigger, we still can have a reasonable velocity profile of this pyramid.

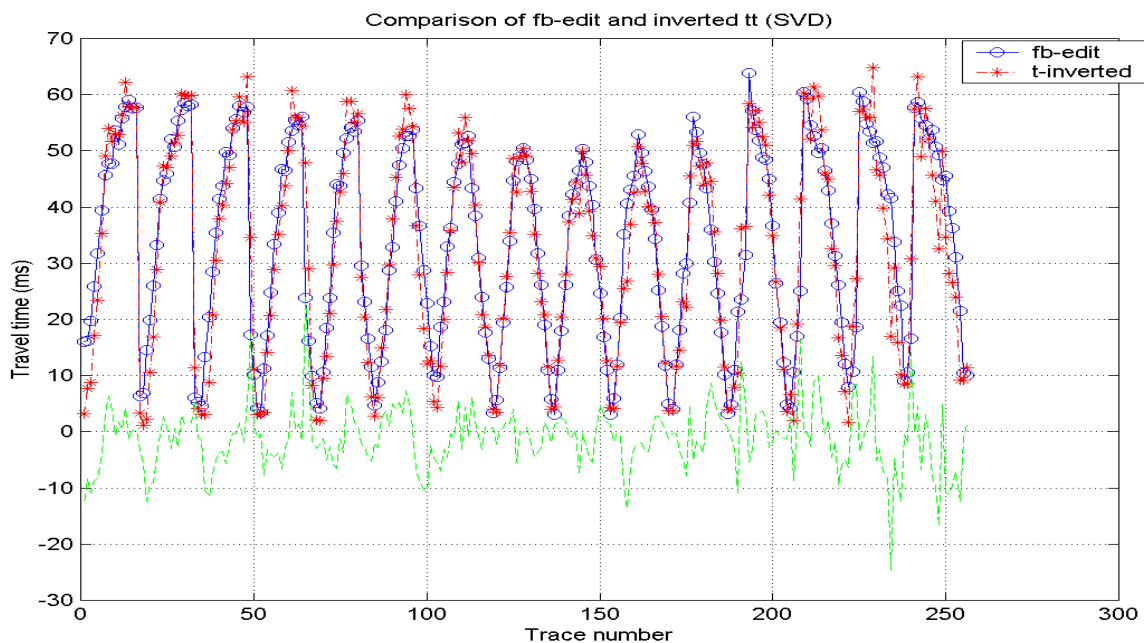


Figure A.15 Comparison of the observed first-break times and calculated times from inversion-estimated slowness model.

s\_tomo\_edt =

5.4733	1.5673	2.4460	3.2995	2.6364	0
3.5026	4.3202	4.2187	4.5673	4.9340	0
2.9276	1.9958	1.6648	2.5666	1.0000	0
3.4036	2.3260	1.0000	1.0000	0	0
2.9787	3.2623	3.1170	2.4663	0	0
3.1438	4.8018	5.7110	7.5984	0	0
2.5611	5.8271	6.7807	9.4462	0	0

v\_tomo\_edt =

1.0e+003 ×

0.1827	0.6380	0.4088	0.3031	0.3793	0
0.2855	0.2315	0.2370	0.2189	0.2027	0
0.3416	0.5010	0.6007	0.3896	1.0000	0
0.2938	0.4299	1.0000	1.0000	0	0
0.3357	0.3065	0.3208	0.4055	0	0
0.3181	0.2083	0.1751	0.1316	0	0
0.3905	0.1716	0.1475	0.1059	0	0

Table A.4 Inversion result of Ma'ax Na pyramid data using SVD method.

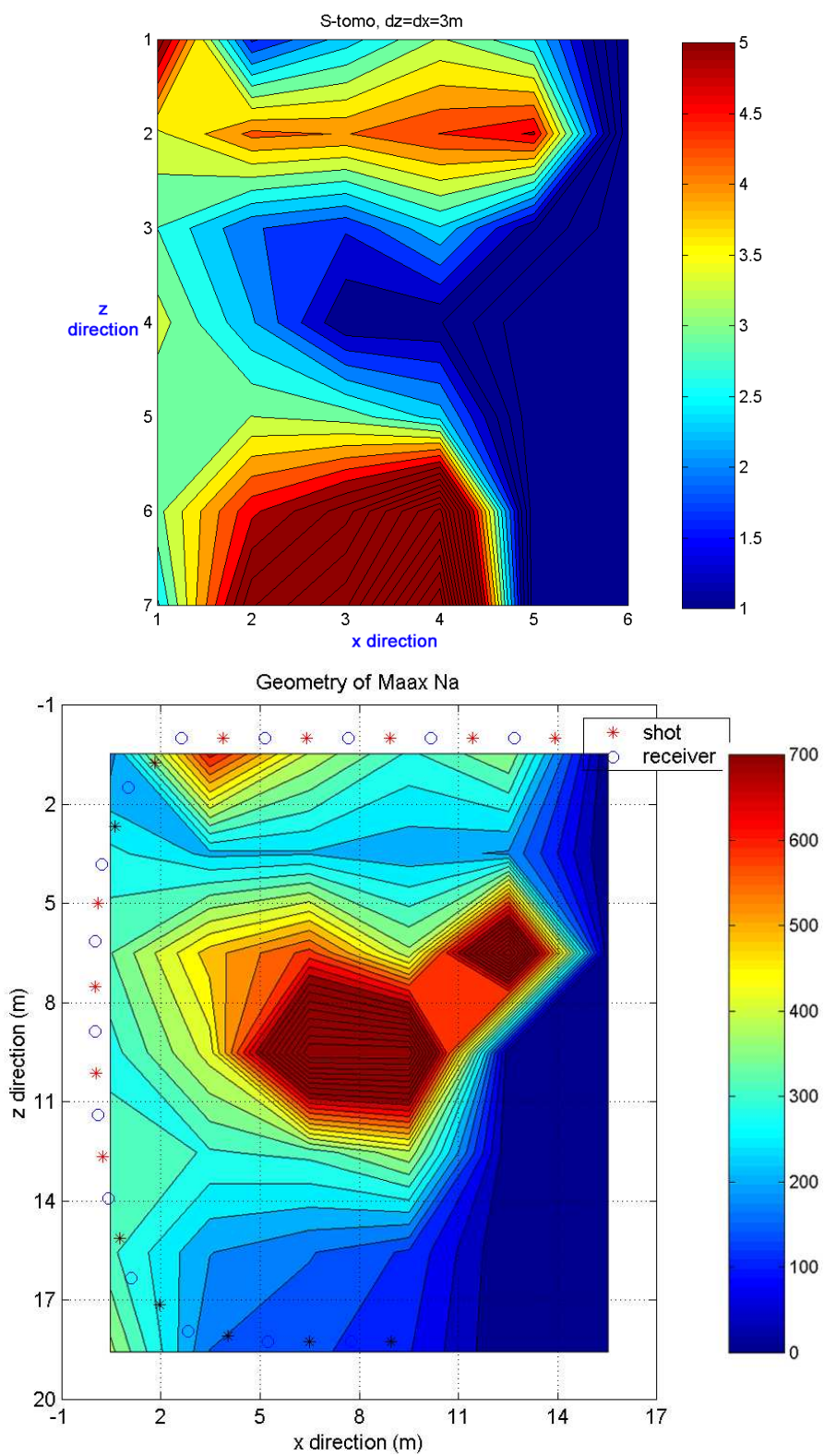


**Figure A.16** Inverted slowness (upper) and velocity (lower) structure of Ma'ax Na.

### **A.5 Conclusion**

Using singular value decomposition, we solve the slowness vector in this tomographic travelttime inversion based on the straight-line ray-paths.

The inversion result of year 2000 Chan Chich data is complete with uniqueness, resolution and reliability analysis. The velocity profile shows that the surface velocity is about 100~200 m/s, and the inner part has higher velocity about 500 m/s, even 700 m/s somewhere. There is a lower velocity area between the two high velocity peaks.

The velocity profile inverted from year 2001 Chan Chich data shows the similar result with year 2000 data, that the surface velocity is about 200 m/s, and the inner part has higher velocity about 600~700 m/s.

Ma'ax Na pyramid also has similar velocity structure: the outer part is about 100~200 m/s, and there is a high velocity core about 700 m/s or even high.

The proper constrain or weight needs to be invoked to make inverted slowness greater than 0.